The Star-formation History of the Universe and its Drivers

David R. S. G. Sobral

Institute for Astronomy
School of Physics and Astronomy

University of Edinburgh
Doctor of Philosophy

September 2011

Abstract

Determining the cosmic star formation history of the Universe is fundamental for our understanding of galaxy formation and evolution. While surveys now suggest that the "epoch" of galaxy formation occurred more than 6 billion years ago, our measurements still suffer from significant scatter and uncertainties due to the use of different indicators, dust extinction and the effects of cosmic variance in the current samples. Furthermore, understanding galaxy formation and evolution require us to go much beyond simply determining the star formation history of the Universe with high accuracy: what are the physical mechanisms driving the strong evolution that we observe? How does star formation depend on stellar mass and environment and how does that change with cosmic time?

This thesis presents both a completely self-consistent determination of the star formation history of the Universe (based on a single, sensitive and well-calibrated star formation indicator up to redshift $z \sim 2.3$: the Hα luminosity) and investigates its drivers by exploring large area surveys (probing a range of environments and overcoming cosmic variance) obtained with the High-redshift Emission Line Survey (HiZELS). HiZELS is a panoramic extragalactic survey using the WFCAM instrument on the 3.8-m UK Infrared Telescope (UKIRT) which utilizes a set of existing and custom-made narrow-band filters in the J, H and K bands to detect emission line galaxies (main targets are Hα emitters at $z = 0.84$, $z = 1.47$ and $z = 2.23$) up to $z \sim 9$ over square degree areas of extragalactic sky.

Detailed measurements of the Hα luminosity function and its evolution with redshift are presented, revealing a significant luminosity evolution. The clustering properties of Hα emitters at high-redshift are quantified and investigated for the first time, revealing that these distant galaxies reside in Milky-Way type dark matter haloes at $z \sim 1$. Mass and environment are found to have important and inter-dependent roles on star formation at high-z and the results are able to reconcile previously contradictory results in the literature. Furthermore, by conducting a novel double-narrow band survey at $z = 1.47$, the relationship between the [OII]$_{3727}$ and Hα emission lines is studied in detail and directly compared to $z \sim 0$, showing no significant evolution in the dust properties of star-forming galaxies, despite the very strong luminosity evolution. Finally, this thesis also presents the widest search for very distant Lyα emitters at $z \sim 9$.

Declaration

The data and results presented in this thesis were obtained by me, except where specifically indicated in this thesis. These results have been published, or will be published soon, in Monthly Notices of the Astronomical Society in five different first author papers:

- Sobral, D. et al., 2009a, MNRAS, 398, 75
- Sobral, D. et al., 2009b, MNRAS, 398, L68
- Sobral, D. et al., 2010, MNRAS, 404, 1551
- Sobral, D. et al, 2011a, MNRAS, 411, 675
- Sobral, D. et al, 2011b, MNRAS, *submitted*, arXiv:1109.1830

I declare that this thesis has not been submitted, in full or in part, for any degree or diploma or other qualification at this or any other University.

This thesis was written by myself and it is the outcome of my own work, except where specifically indicated in the text.

David Sobral

Edinburgh, September 2011

Acknowledgements

Firstly, I would like to thank Philip Best, my supervisor, for the great help, opportunities and both freedom to pursuit my ideas and guidance he has always provided since the very beginning of my PhD. His suggestions, challenges and critical spirit have been an incredible source of motivation, pushed me towards a unique learning experience and have taught me more than a Thesis could possibly contain or cover.

I'm extremely grateful to have worked in the Institute for Astronomy (IfA) and to have been in contact with so many great people. In particular, I would really like to thank Michele Cirasuolo, Ross McLure, Jim Dunlop, Karina Caputi and Edo Ibar (among many others) for the many general high-redshift discussions; Peder Norberg, Wing-Fai Thi, Jack Mayo, Brendan Jackson, Berian James and Duncan Forgan (among others) for extremely interesting discussions across virtually all astronomy areas, and George Mamatsashvili, Henry Pearce, Hanna Parker, Neil Phillips, for other helpful discussions and debates. I would also like to thank John Peacock (now Head of the IfA) and Alan Heavens for their role as Postgraduate Coordinators during the years I spent at the IfA, and for the knowledge transmitted during the first year reading group.

I would also like to thank Ian Smail for the many suggestions and comments on my work and James Geach for many discussions and for guiding me through my first observing run on Mauna Kea. I would also like to thank José Afonso, Rui Agostinho, João Lin Yun and Aprajita Verma for various helpful discussions and particularly because they all played an important role in both motivating me towards astronomy and astronomical research.

I also wish to highlight the crucial role and unique capabilities of UKIRT and the Joint Astronomy Center (JAC) staff in delivering the extremely high-quality data which allowed the studies presented in this thesis to be conducted, and the synergies that can be explored between UKIRT, Subaru and other telescopes. In particular, I would like to thank Andy Adamson, Tom Kerr and Luca Rizzi and the TSSs Jack, Tim and Thor – for both the great support and help during the many observing runs on UKIRT, but also for always feeling observers welcomed both at the telescope and at the JAC.

I would also like to thank Tomo Goto for hosting me at the Institute for Astronomy in Hawaii and David Sanders, Len Cowie, Lisa Kewley, Ester Hu and many other IfA-Hawaii astronomers for exciting and interesting discussions over a wide range of topics. I would also like to thank Peter Capak for hosting me on a visit to Caltech and for many discussions on the COSMOS data-set. I would also like to thank Masami Ouchi, Sebastien Foucaud and Chun Ly for helpful comments and discussions.

I fully acknowledge both the UKIDSS UDS, Subaru-SXDS and the COSMOS teams for their tremendous effort towards assembling the extremely high-quality and unique multi-wavelength data-sets that have been explored to gain a more detailed view on the studies conducted in this thesis.

Furthermore, none of this work would have been possible without the great support from all my family; my wife Catarina, my parents, sister, grandparents and friends. Obrigado!

Finally, I would like to thank the Fundação para a Ciência e Tecnologia (FCT) in Portugal (Ministério da Ciencia e Ensino Superior) for the funding thoughout my PhD (Ref: SFRH / BD / 36628 / 2007) and also to dedicate this thesis to the memory of Tim Garn.

Contents

1 Intro **1**

1.1 Cosmology and Cosmography . . . 1

1.1.1 General Relativity . . . 1

1.1.2 Redshift . . . 3

1.1.3 Line-of-Sight Co-moving Distance . . . 4

1.1.4 Transverse Co-moving Distance . . . 4

1.1.5 Angular Diameter Distance . . . 5

1.1.6 Luminosity Distance . . . 5

1.1.7 Co-moving Volume . . . 5

1.1.8 Look-back Time . . . 5

1.2 Galaxy Formation: the first stars and galaxies . . . 6

1.2.1 Semi-analytical modeling . . . 7

1.2.2 The First Light: Population III . . . 8

1.2.3 Searching for the First Galaxies . . . 9

1.3 Star formation rate density . . . 11

1.3.1 Measuring Star formation: Star formation indicators . . . 11

1.3.2 Initial Mass Function . . . 12

1.3.3 Ultraviolet Continuum . . . 14

1.3.4 Emission lines: Hα, [OII] and others . . . 15

1.3.5 Far-Infrared Continuum . . . 17

1.3.6 Radio . . . 19

1.3.7 Gamma-ray bursts and X-rays . . . 19

1.3.8 AGN *versus* star formation . . . 20

1.4 The Star Formation History of the Universe . . . 22

1.4.1 Comparison of different Star Formation indicators . . . 22

1.4.2 What is driving the Star formation History? . . . 23

1.5 An Answer: narrow-band surveys + Hα . . . 24

1.6 Thesis Outline . . . 25

2 HiZELS **27**

2.1 Overview and Goals . . . 27

2.2 WFCAM: Filters and General Characteristics . . . 28
2.3 Observation Techniques . . . 29
2.4 Reduction Summary . . . 30
2.5 The Data Reduction Pipeline: PfHiZELS . . . 31
2.6 Main Tasks . . . 32
2.7 Cross-check of pipeline performance . . . 33
2.8 Catalogue Production . . . 34
2.9 Narrowband excess selection . . . 35
2.10 Fields . . . 36
2.10.1 UKIDSS UDS . . . 37
2.10.2 COSMOS . . . 37

3 The nature of star-forming galaxies at $z = 0.84$ 39

3.1 Observations . . . 39
3.1.1 Source Extraction and Survey Limits . . . 40
3.2 Selection . . . 40
3.3 Complete sample . . . 41
3.4 Photometric redshift analysis . . . 42
3.5 Selecting Hα emitters at $z = 0.84$ . . . 44
3.6 Spectroscopic redshifts and selection robustness . . . 45
3.6.1 Narrowband-K and H matches . . . 47
3.7 Results . . . 47
3.8 Hα luminosity function at $z = 0.84$ . . . 47
3.8.1 [NII] flux contamination correction . . . 48
3.8.2 Completeness correction . . . 48
3.8.3 Extinction Correction . . . 49
3.8.4 Filter profile corrections . . . 50
3.8.5 Fully corrected luminosity function . . . 51
3.9 The star formation rate density at $z = 0.84$ . . . 53
3.9.1 AGN contamination . . . 53
3.9.2 Star formation rate density . . . 54
3.10 The morphology of Hα emitters . . . 56
3.10.1 Morphology with *HST* imaging . . . 56
3.10.2 Morphology–Hα luminosity relations . . . 58
3.10.3 Redshift evolution of the morphology relations . . . 59
3.11 Summary and Conclusions . . . 61

4 The clustering and evolution of Hα emitters at $z \sim 1$ **63**

4.1 Introduction and Motivation . . . 63

4.2 Data and Samples . . . 65

4.2.1 The sample of Hα emitters from HiZELS . . . 65

4.2.2 The random sample . . . 66

4.3 The Clustering Properties of Hα emitters . . . 67

4.3.1 The two-point $\omega(\theta)$ correlation function at $\mathbf{z = 0.84}$ . . . 67

4.3.2 Robust error estimation and the effect of cosmic variance . . . 68

4.3.3 AGN contamination . . . 70

4.3.4 Real-space correlation . . . 71

4.4 The clustering dependences on galaxy properties . . . 74

4.4.1 Hα luminosity/ Star-formation rate . . . 74

4.4.2 Rest-frame continuum luminosity . . . 78

4.4.3 Morphological class . . . 79

4.4.4 Hα luminosity versus rest-frame K luminosity . . . 80

4.5 The Clustering of Hα emitters across cosmic time . . . 81

4.5.1 The clustering of Hα emitters at $\mathbf{z = 0.24}$ . . . 81

4.5.2 The clustering of Hα emitters at $\mathbf{z = 2.23}$ . . . 82

4.5.3 The clustering evolution of Hα emitters since $\mathbf{z = 2.23}$ . . . 83

4.5.4 The dark matter host halo-$\mathbf{L^*_{H\alpha}}$ relation . . . 84

4.6 Summary and Conclusions . . . 85

5 The Roles of Mass and Environment at $z \sim 1$ **87**

5.1 Introduction and Motivation . . . 87

5.2 Samples and Properties . . . 89

5.2.1 The sample of robust Hα emitters at $\mathbf{z = 0.84}$ . . . 89

5.2.2 The underlying population samples . . . 89

5.2.3 The potential Hα emitters at $\mathbf{z = 0.84}$ with EW< 50 Å . . . 90

5.2.4 Morphological classification with *HST* imaging . . . 92

5.2.5 Stellar mass estimates . . . 92

5.2.6 Local density estimates . . . 94

5.2.7 The clustering-density relation and interpretation . . . 94

5.2.8 Confirmed clusters and groups in COSMOS and UDS . . . 96

5.3 Mass-dependences and downsizing . . . 97

5.4 The Environment of Hα emitters . . . 100

5.5 The nature of star formation and the mass-environment view . . . 103

5.5.1 The star-forming fraction in the 2-D mass-environment space . . . 103

5.5.2 The mass-SFR-environment dependence . . . 105

5.5.3 The colours of star-forming galaxies in the 2-D mass-environment space 106
5.6 Discussion 108
5.6.1 Comparison with other studies 109
5.6.2 The role of the star formation mode: potential mergers vs. non-mergers 111
5.7 Summary and Conclusions 112

6 Star formation at $\mathbf{z = 1.47}$ 114

6.1 Introduction and Motivation 114
6.2 Data and Samples 116
6.2.1 Near-infrared NB_H imaging with UKIRT 116
6.2.2 NB_H Source Extraction and Survey Limits 117
6.2.3 Optical NB921 imaging with Subaru 117
6.3 SELECTION 118
6.3.1 Narrowband excess selection 118
6.3.2 The samples of narrow-band emitters 119
6.3.3 Distinguishing between different line emitters 121
6.3.4 The dual narrow-band approach at $z = 1.47$ 124
6.3.5 Selecting Hα and [OII] $\mathbf{z = 1.47}$ emitters 126
6.4 Hα and [O**II**] Luminosity functions 127
6.4.1 Contribution from adjacent lines 127
6.4.2 Individual line completeness 128
6.4.3 [OII] selection completeness 130
6.4.4 Volume: Hα and [OII] surveys 131
6.4.5 Filter Profiles: volume and line ratio biases 131
6.4.6 Extinction Correction 133
6.4.7 Hα Luminosity Function at $z = 1.47$ and Evolution 133
6.4.8 The [OII] Luminosity function at $z = 1.47$ and Evolution 134
6.4.9 Evolution of the Hα and [OII] Luminosity Functions 135
6.4.10 The star formation rate density at $z = 1.47$ 136
6.5 The matched Hα-[OII] view 138
6.5.1 A SDSS sample at $\mathbf{z \sim 0.1}$ 138
6.5.2 Calibrating [OII]/Hα line ratio as a dust extinction probe 139
6.5.3 [OII]-Hα luminosity correlation at $z = 1.47$ and $z \sim 0.1$ 141
6.5.4 Mass as a dust-extinction indicator 144
6.5.5 Predicting $A_{H\alpha}$ dust-extinction with colours 146
6.5.6 Discussion of emission-line ratios 147
6.6 Conclusions 148

7 Bright Lyα emitters at $z \sim 9$ **150**

7.1 Motivation and background . . . 150

7.2 Search for Candidates . . . 151

7.3 Candidates, testing and follow-up observations . . . 151

7.4 Lyα luminosity function at $z \sim 9$ . . . 152

7.5 Comparison with models and future surveys . . . 153

7.6 High redshift Lyα searches and cool galactic stars . . . 154

7.7 Summary . . . 156

8 Conclusions **157**

8.1 On-going and Future Research . . . 160

A The underlying populations **164**

A.1 Completeness and contamination . . . 164

A.2 The effect of varying photo-z cuts . . . 166

B Stellar Mass Estimates **169**

List of Figures

1.1 N-body Simulations: Millennium Simulation . . . 7
1.2 The first stars and galaxies: simulations . . . 9
1.3 Spectra of the most distant galaxies . . . 10
1.4 Observing a HII region . . . 12
1.5 Most popular Initial Mass Functions (IMFs) . . . 13
1.6 Spectra of stars with different masses . . . 15
1.7 Recombination in hydrogen atoms: emission lines . . . 16
1.8 Emission lines: signatures of recent star formation . . . 17
1.9 Spectral energy distribution of star-forming galaxies . . . 18
1.10 The Optical versus Infrared view of M81 . . . 18
1.11 HII region within the Milky Way . . . 20
1.12 AGN-Star formation separation . . . 21
1.13 Star formation History of the Universe . . . 23
1.14 The independent mass and environmental quenching at $z = 0$ . . . 24

2.1 Observing at UKIRT . . . 28
2.2 WFCAM focal plane . . . 29
2.3 WFCAM broad and narrow-band filters . . . 30
2.4 Example of excess sources in COSMOS . . . 34
2.5 Colour-magnitude diagrams: selection of potential emitters in COSMOS . . . 36
2.6 UDS Coverage and comparison with other Fields . . . 38

3.1 Selection of NBJ emitters in both COSMOS and UDS . . . 41
3.2 Photometric and spectroscopic redshift analysis: NBJ . . . 43
3.3 Colour-colour separation of NBJ emitters . . . 44
3.4 Line recovery and detection completeness . . . 49
3.5 Hα luminosity function at $z = 0.84$ and evolution . . . 52
3.6 Hα luminosity function parameters evolution . . . 53
3.7 Emission-line diagnosis: AGN contamination . . . 54
3.8 The star formation history of the Universe: the Hα and the overall view . . . 55
3.9 Different morphological types in the Hα sample . . . 56
3.10 Morphology-Hα luminosity relations at $z = 0.84$ . . . 57

3.11 Morphology-dependent Hα luminosity functions at $z = 0.84$ . . . 58
3.12 Morphology-Hα luminosity (scaled) relations at different cosmic times . . . 60

4.1 The on-sky distribution of sources in COSMOS and UDS . . . 65
4.2 The 2-point angular correlation function . . . 68
4.3 The area-depenent uncertainty of the correlation function . . . 69
4.4 The 2-point correlation function and the best power-law fit . . . 72
4.5 The angular correlation function for samples with different Hα luminosities . . . 75
4.6 The dependence of the clustering length on Hα luminosity . . . 75
4.7 Clustering dependences on K, B luminosity and morphological class . . . 78
4.8 The 2-D M_K-log $\mathrm{L}_{\mathrm{H}\alpha}$ space . . . 80
4.9 The evolution of the clustering length for Hα emitters . . . 82
4.10 A single relation between Hα luminosity and DM halo mass for the last 10 Gyrs . . . 84

5.1 The clustering-local density empirical relation and environmental calibration . . . 95
5.2 COSMOS and UDS: on-sky distribution and local density fields . . . 96
5.3 The dependence of star formation rates on stellar mass . . . 97
5.4 Star-forming fraction as a function of stellar mass . . . 98
5.5 Star-forming fraction as a function of stellar mass for different specific star formation rate cuts . . . 99
5.6 The fraction of star forming galaxies and SFRs as a function of environmental density 101
5.7 The environmental dependence of the merger rate in star-forming galaxies at $z = 0.84$ 102
5.8 The role of the environment in shaping the Hα luminosity function . . . 102
5.9 The environment-mass correlation and the 2-D view on the star-forming fraction . . . 104
5.10 Merger fraction as a function of mass-environment and the dual view without mergers 105
5.11 The dependence of the median SFR on environment for different masses . . . 106
5.12 The 2-D environment-mass dependence of colours and comparison with underlying sample 107

6.1 A comparison between narrow-band filter profiles . . . 115
6.2 Selection of potential emitters with UKIRT and Subaru . . . 118
6.3 Example of the double narrow-band technique . . . 119
6.4 The distribution of photometric redshifts of both samples . . . 122
6.5 Spectroscopic redshift distribution . . . 122
6.6 The BRiK colour-colour separation . . . 124
6.7 Colour-colour separation of higher redshift galaxies . . . 125
6.8 Photometric redshift distribution of matched sample of emitters . . . 126
6.9 Line ratio distributions and survey limits . . . 127
6.10 H band distribution of sources used for recovery simulations . . . 129
6.11 Completeness as a function of line flux . . . 129
6.12 Fraction of sources as a function of line flux . . . 130

6.13 A study of the potential profile biases 132
6.14 The Hα luminosity function evolution 134
6.15 The evolution of the OII luminosity function 136
6.16 The star formation history of the Universe 137
6.17 Calibrating OII/Hα line ratios as dust extinction probes using the Balmer decrement . 140
6.18 Evaluating potential metallicity trends and biases in the calibration 141
6.19 Relation between observed luminosities at both redshifts 142
6.20 line ratios 143
6.21 Extinction - stellar mass relation 146
6.22 The relation between $A_{H\alpha}$ and colour 147

7.1 Observed Lyα luminosity functions and the best constraints at $z \sim 7-9$ 153
7.2 The near-IR spectra of cool T-dwarf stars and the colour excess recovered with NB filters in the J, H and K bands 155

A.1 Completeness and contamination of underlying sample as a function of photo-z cut . . 166
A.2 Testing environmental trends with different photo-z samples 167
A.3 Testing the mass trends with different photo-z samples 168

B.1 Comparison between different stellar mass estimations 170

Chapter 1

Introduction

1.1 Cosmology and Cosmography

No matter where we look at in the Universe, we cannot escape its immense structure and diversity. From our solar system to galaxies, clusters and super-clusters of galaxies, the Universe reveals a complex pattern on almost every scale we have observed. In fact, it is only when we observe the truly large-scale structure, or look sufficiently back in time, that we realise that the Universe is, in fact, relatively close to being homogenous and isotropic. On the other hand, by studying the Universe as it was thousands of millions of years ago, we rapidly understand that its structure is immensely dynamic and always evolving. Thus, the triumph of Cosmology over the past century has been to model with accuracy what we see and observe in our Universe, particularly with the Λ Cold Dark Matter model.

1.1.1 General Relativity

Einstein's field equations describe how energy, being equivalent to mass, affects space and time, making use of the covariance principle (according to the Lorentz transformations). The field equations are:

$$R_{\mu\nu} - \frac{R}{2} g_{\mu\nu} + \Lambda g_{\mu\nu} = -\frac{8\pi G}{c^4} T^{\mu\nu} \tag{1.1}$$

where $R_{\mu\nu}$ is the Ricci tensor (the contraction of the curvature tensor), R its contraction (the curvature scalar), $g_{\mu\nu}$ is the metric tensor and $T^{\mu\nu}$ is the energy-momentum tensor. Finally, Λ is the cosmological constant, G is Newton's gravitational constant and c is the speed of light.

Assuming that the Universe is homogeneous and isotropic, one gets a simplification of the metric of the Universe. It may be described by the line element ds of the Robertson-Walker metric in polar coordinates $x^{\mu}=(t, r, \theta, \psi)$ as:

$$ds^2 = dt^2 - a(t)^2 \left[\frac{dr^2}{1-kr^2} + r^2(d\theta^2 + \sin^2\theta d\phi^2) \right] \tag{1.2}$$

where $a(t)$ is the scale factor (time dependent) which describes an expanding Universe. The curvature of space, k, may be set to 0, +1 or −1 by choosing an appropriate scaling of r.

One may describe matter in the Universe as a continuous ideal fluid consisting of particles (such as galaxies) which have a mean matter density $\rho(t)$ and a pressure $P(t)$. Evaluating for today ($t = t_0$), one can introduce the following constants:

$$a_0 = a(t_0), \qquad H_0 = \frac{\dot{a}(t_0)}{a(t_0)}, \qquad \rho_0 = \rho(t_0), \qquad q_0 = -\frac{\ddot{a}(t_0)a(t_0)}{\dot{a}(t_0)^2} \tag{1.3}$$

where q_0 is the deceleration parameter and H_0 is the Hubble constant (Hubble, 1929). Today, the Universe seems to be matter-dominated, which means $\rho_{rad} \sim 0$. Using all this, one may evaluate the curvature of space expressed in the above constants:

$$\frac{k}{a_0^2} = H_0 \left(\frac{3}{2}\frac{\rho_0}{\rho_{cr}} - q_0 - 1 \right) \tag{1.4}$$

where

$$\rho_{cr} = \frac{3H_0^2}{8\pi G} \tag{1.5}$$

is the critical density. Finally, it is important to introduce the density parameters:

$$\Omega_M = \frac{\rho_0}{\rho_{cr}} = \frac{8\pi G\rho_0}{3H_0^2}, \qquad \Omega_\Lambda = \frac{\Lambda}{3H_0^2}, \qquad \Omega_k = 1 - \Omega_M - \Omega_\Lambda. \tag{1.6}$$

The cosmological parameters H_0, Ω_m, Ω_Λ and k are subject to numerous measurements and the combination of many experimental measurements have now placed strong constraints on the cosmological parameters. The best estimates have been derived from the type Ia supernovae magnitude-redshift relation (Perlmutter et al., 1999; Kowalski et al., 2008; Amanullah et al., 2010), from the power spectrum of the cosmic microwave background (CMB) with WMAP (Spergel et al., 2003; Dunkley et al., 2009; Komatsu et al., 2009), from the large-scale structure (e.g. Tegmark et al., 2006; Percival et al., 2007), and from galaxy clusters (e.g. Rozo et al., 2010). The combined measurements indicate that the energy density of the Universe is split between dark energy ($\Omega_\Lambda = 0.728 \pm 0.016$), dark matter ($\Omega_C = 0.227 \pm 0.014$) and baryonic matter ($\Omega_b = 0.0456 \pm 0.0016$) – and therefore $\Omega_M = 0.273 \pm 0.016$ – and with $H_0 = 70.4 \pm 1.4$ km s^{-1}Mpc^{-1}. Given this cosmological model, the Universe is 13.75 ± 0.11 Gyrs old. Indeed, it is clear today that the baryonic matter we can see directly (as stars or illuminated by stars) or indirectly (absorption) accounts for at most $\frac{1}{10}$ of Ω_M (Springel et al., 2005). The dynamic properties of galaxies and galaxy clusters and the effects of gravitational lensing agree well with such a result, while the discovery of the Bullet cluster (1E 0657-56 Markevitch et al., 2002) and subsequent study (e.g. Markevitch et al., 2004) clearly points towards the existence of *dark matter*, which, to date, we have not been able to clearly identify.

For simplicity, throughout this thesis, a "F737" cosmology will be used (also designated by concordance cosmology), with parameters which are very close to the best estimates, meaning:

$$k = 0, \qquad H_0 = 70 \text{ km.s}^{-1}\text{Mpc}^{-1}, \qquad \Omega_M = 0.3, \qquad \Omega_\Lambda = 0.7. \tag{1.7}$$

The Hubble constant H_0 has been mentioned before, but it is worth expressing it in terms of observable parameters. It is a constant of proportionality between recession speed v and distance d in the expanding Universe:

$$v = H_0 d. \tag{1.8}$$

The subscripted 0 refers to the present epoch, as in general H changes with time. H_0 has inverse time dimensions, but it is usually written as:

$$H_0 = 100h \text{ km.s}^{-1}\text{Mpc}^{-1}, \tag{1.9}$$

where h is a dimensionless number. As referred before, we assume h=0.7, which is in good agreement with recent observations. The inverse of the Hubble constant is the Hubble time $t_H = \frac{1}{H_0}$ and the speed of light c times the Hubble time is defined as the Hubble distance $D_H = \frac{c}{H_0}$. These are the quantities that set the scale of the Universe.

With an expanding Universe, computing distances turns out to be slightly more complex than in a simple euclidean non-expanding Universe. In fact, this expansion (and possible curvature) makes distances between co-moving objects change constantly.

1.1.2 Redshift

One of the most common ways to describe large astronomical distances is by the concept of redshift. Observations show that for distances larger than $\sim$ Mpc the more distant an object is, the more its light is shifted to longer wavelengths, first noted by Lemaître (1927), although this finding is usually attributed to Hubble (1929). Absorption and emission lines of atoms and molecules (for which one can determine the rest-frame wavelength) are commonly used to measure a redshift. The redshift effect may be explained in two ways. One may interpret it as the Doppler effect that affects light due to the movement of the source relative to the observer. The other way to look at it is a general expansion of space which stretches the light wave (cosmological redshift). The redshift, z, is defined as:

$$z = \frac{\lambda_0 - \lambda_\epsilon}{\lambda_\epsilon} \tag{1.10}$$

where λ_0 is the observed wavelength and λ_ϵ is the wavelength of the photon in the rest-frame of the source. The redshift is related to the scale factor $a(t)$ of the Universe:

$$1 + z = \frac{a(t_0)}{a(t_\epsilon)} \tag{1.11}$$

where $a(t_0)$ is the size of the Universe at the time the light from the object is observed, and $a(t_\epsilon)$ is the size at the time it was emitted. Redshift is independent of cosmology, but it definitely does not correspond to a distance one could measure with a ruler. To obtain a distance measure in a proper length scale, one needs to take spacetime into account, for which there are many ways, as defined in the next sections.

1.1.3 Line-of-Sight Co-moving Distance

As light needs time to get from an object to the observer, one can define a distance that may be measured between the observer and the object with a ruler at a given cosmological time: the proper distance. The proper distance evaluated for today is called the *co-moving distance*. To obtain this quantity, one can consider a beam of light emitted along the line of sight between the object and the observer. It is emitted at the time t_e from the object and is received by the observer today, i.e., at $t = t_0$. The light thus runs a distance $c \times dt$, which is stretched as the Universe expands. Integrating all those small distances leads to the line-of-sight co-moving distance:

$$D_C = \int_{t_e}^{t_0} c \frac{a_0}{a(t)} \mathrm{d}t. \tag{1.12}$$

The co-moving distance between two nearby objects in the Universe is the distance between them which remains constant with epoch if the two objects are moving with the Hubble flow. The total line-of-sight co-moving distance D_C from us to a distant object is computed by integrating the infinitesimal δD_C contributions between nearby events along the radial ray from $z = 0$ to the object. On the other hand, by defining the function:

$$E(z) = \sqrt{\Omega_M (1+z)^3 + \Omega_k (1+z)^2 + \Omega_\Lambda}, \tag{1.13}$$

the total line-of-sight co-moving distance is then given by integrating those contributions:

$$D_C = D_H \int_0^z c \frac{dz'}{E(z')}, \tag{1.14}$$

where D_H is the Hubble distance.

As most of the distance measurements can be derived from the line-of-sight co-moving distance, it can be considered as a fundamental way of measuring distances in cosmology. Nevertheless, the previous integral does not have, in general, an analytical solution, thus a numerical solution is normally needed to solve it.

1.1.4 Transverse Co-moving Distance

The co-moving distance between two events at the same redshift (distance between two objects separated on the sky by some angle $d\theta$) is $D_M d\theta$ and the transverse co-moving distance D_M is equal to the co-moving (D_C) distance if we assume a flat Universe.

1.1.5 Angular Diameter Distance

The angular diameter distance, D_A is defined as the ratio of an object's physical transverse size to its angular size (in radians). It is used to convert angular separations in telescope images into proper separations at the source. It is famous for not increasing indefinitely as z $\rightarrow \infty$. In fact, it turns over at z$\sim$ 1 and thereafter more distant objects actually appear larger in angular size (for a fixed physical size). Angular diameter distance is related to the transverse co-moving distance by:

$$D_A = \frac{D_M}{1+z}. \tag{1.15}$$

1.1.6 Luminosity Distance

The luminosity distance, D_L is defined by the relationship between the bolometric flux S and the bolometric luminosity L:

$$D_L = \sqrt{\frac{L}{4\pi S}}. \tag{1.16}$$

This is related to the transverse co-moving distance and angular diameter distance by:

$$D_L = (1+z)D_M = (1+z)^2 D_A. \tag{1.17}$$

1.1.7 Co-moving Volume

The co-moving volume V_C is the volume measure in which the number densities of non-evolving objects locked into Hubble flow are constant with redshift. The co-moving volume element in a solid angle $d\Omega$ and for a redshift interval dz is:

$$dV_C = D_H \frac{(1+z)^2 D_A^2}{E(z)} d\Omega dz, \tag{1.18}$$

where D_A is the angular diameter distance at redshift z. Once again, assuming a flat Universe simplifies the calculations and thus the total co-moving volume, all-sky, out to redshift z is given by:

$$V_C = \frac{4\pi}{3} D_M^3. \tag{1.19}$$

1.1.8 Look-back Time

The lookback time t_L to an object is the difference between the age t_0 of the Universe now (at observation) and the age t_e of the Universe at the time the photons were emitted (according to the object). It is used to predict properties of high-redshift objects with evolutionary models, such as passive stellar evolution for galaxies, and is given by:

$$t_L = t_H \int_0^z \frac{dz'}{(1+z')E(z')}. \tag{1.20}$$

1.2 Galaxy Formation: the first stars and galaxies

Galaxies are likely to have formed as a result of gravitational collapse due to instabilities caused by density perturbations in the early Universe. The first ones probably began forming at $z \sim 20 - 50$ ($\sim 50 - 200$ Myrs after the Big Bang), when the first dark matter potential wells formed and allowed gas to fall into them, cool and ultimately form stars and galaxies (e.g. Tegmark et al., 1997). These density perturbations are observed as fluctuations in the Cosmic Microwave Background (Smoot et al., 1992; Bennett et al., 1996; Spergel et al., 2007). Inflation (Guth, 1981), the concept that the Universe underwent a rapid period of expansion at an early age, is probably the best natural candidate for these seed fluctuations. The inflationary expansion would have both amplified and frozen quantum fluctuations in the density field. The collapse of these density perturbations can then continue in either one of two ways: top down or bottom up (hierarchical) formation (White and Frenk, 1991; Lacey and Cole, 1993; Baugh et al., 1996). The way in which galaxies form depends greatly on the cosmological parameters defined before and the nature of the matter involved.

As mentioned before, matter is often divided into two groups: baryonic matter and dark matter. The latter has a non-luminous nature, thus one can only infer its existence by gravitational effects on stars in galaxies, or on galaxies in clusters, even thought it is thought to have a major role in structure formation and evolution. So far, several dark-matter candidates have been proposed, yet none has been confirmed. Nevertheless, cold dark matter (CDM) seems to be one of the best candidates. CDM consists of massive particles which are non-relativistic at the point at which they decouple from the rest of matter and radiation (in the early Universe). N-body simulations can be used to model the history of dark matter in the Universe (e.g. Springel et al., 2005) by finding numerical solutions to the coupled equations of the gravitational interactions of N particles (of dark matter). These simulations are the roots for current cosmological simulations.

Running CDM simulations reveals a Universe which develops in a bottom-up scenario (see Figure 1.1). This means that stars form early and galaxies form first, before developing into clusters and super-clusters by a series of complicated merging episodes. Given the consensus on cosmological parameters, the most popular current models are refered to as Λ-CDM models (De Lucia and Blaizot, 2007; Li et al., 2007).

The most accurate computational method for solving the physics of galaxy formation is through direct simulation (see Benson, 2010). With this approach, the fundamental equations of gravitation, hydrodynamics and, in some cases, radiative cooling and transfer, are solved for a large number of points. Dark matter can be easily modeled in this way (since it responds only to the gravitational force), but dark matter alone is insufficient, and baryonic material must be added in to the mix. This, of course, makes the problem much more complicated. Numerous simulation codes are now able to include star formation and feedback from supernovae explosions, while some even attempt to follow the formation of supermassive black holes in galactic centers. However, for galaxy scale simulations the real physics of these processes is happening on scales well below the resolution of the simulation.

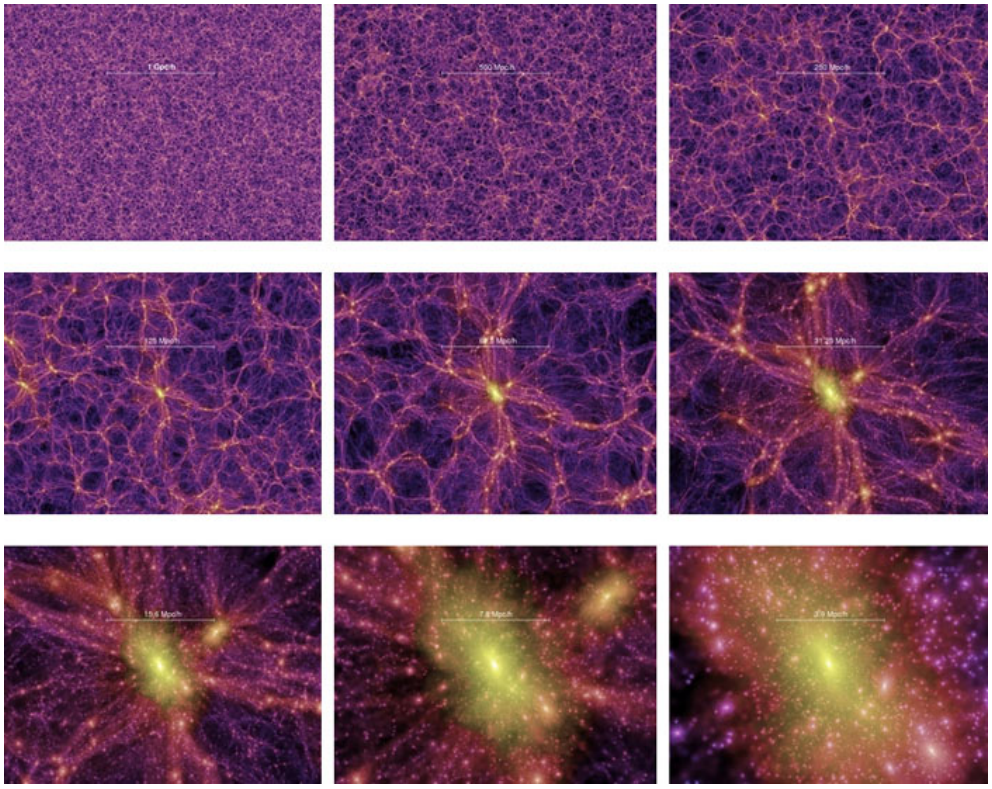

Figure 1.1: A view of the Millennium Simulations (Springel et al., 2005) at different scales, revealing the structure predicted nowadays, which matches well most of the observations done so far.

1.2.1 Semi-analytical modeling

Semi-analytic modeling (for a review, see e.g. Baugh, 2006) builds upon N-body simulations, but takes a phenomenological approach to galaxy formation modeling by treating the various physical processes associated with galaxy formation using approximate, analytic techniques. In practice, it contains both precision-calibrated estimates of the abundance of dark matter haloes, their assembly and merger trees, but also explores empirical scaling relations/prescriptions for gas cooling, star formation, feedback, chemical evolution, galaxy mergers and sizes. An unique advantage of this semi-analytic approach is that it is truly computationally inexpensive, particularly when compared to full hydrodynamic simulations; this allows for very large samples to be generated and compared to observed populations. The final step required to connect the theoretical predictions to observations requires the production of a synthetic spectral energy distribution for each model galaxy, i.e. the amount of energy emitted by the galaxy as a function of wavelength or frequency, which also needs detailed modeling. Semi-analytical models predict the complete star formation history of a galaxy, taking into account all mergers between the progenitors of the galaxy, star formation in bursts triggered by mergers and quiescent star formation in galactic disks; this information is then combined with a stellar population synthesis model to compute a composite stellar population for the whole galaxy (e.g. Bruzual and Charlot, 2003).

The semi-analytical models currently provide the most detailed and complete predictions for the

properties of the galaxy population in cold dark matter universes. The modular framework of the models means that it is straightforward to revise the description of the various phenomena, as required to reproduce the results of more detailed (and expensive) numerical simulations or as motivated by the need to reproduce new observations. One of the great advantages of semi-analytical modelling is that facets of the model can easily be varied or switched on and off to gain a better appreciation of which ingredients have the most bearing on a particular observation.

However, there are still some problems within these models. Whilst they fit the general observations well, implying that the ingredients of the model are essentially correct, there are some classes of objects which are hard to be properly explained (at least not within one single model/approach). For example, these models typically under-predict the number of Lyman break galaxies and sub-mm galaxies at high-redshift (although models such as Baugh et al. (2005) are able to predict those well). These problems are not necessarily fundamental: there are sufficient dark matter haloes produced to house these massive galaxies at high redshift. In fact, global properties such as the global star-formation rate and the total co-moving stellar mass are reasonably well matched as a function of redshift. However, it is clear that the physical mechanisms for star-formation or their evolution are not yet fully understood. One particular example is the fact that there is enough stellar matter predicted at high redshift, but not in the form of large, red spheroids. It may be that feedback mechanisms that allow the quenching of star-formation should be introduced to solve these problems and AGN may drive this feedback (c.f. Bower et al., 2006; Best et al., 2006). Furthermore, it may also be that the initial mass function (IMF, see 1.3.2) was different at earlier times. In fact, by assuming a top-heavy IMF at earlier epochs, Lacey et al. (2011) show (using the Baugh et al. model) that it is possible to solve most of the typical short-comings of these models and to obtain results which are in broad agreement with observations. While the IMF may have been top-heavy at high look-back times and is has evolved with cosmic time, it is also possible that it simply depends on star formation rate (Gunawardhana et al., 2011), or that we are still missing a significant part of the complicated physics.

1.2.2 The First Light: Population III

The formation of the first stars probably happened at redshift z $\sim$ 20 and is thought to have marked an extremely important transition in the history of the Univese. Structure started forming very early in the Universe, mostly driven by dark matter, but as the Universe continued expanding and cooling down there were no new sources of light and, until the first generation of stars formed, the Universe went through its "dark ages". With the formation of the first luminous objects though, the Universe was rapidly transformed into an increasingly complex, hierarchical system, due to the energy and heavy element input from the first stars and accreting black holes (Barkana and Loeb, 2001). Those stars are thought to have formed just $\sim$ 200 Myr after the Big Bang, when the primordial gas was first able to cool and collapse into dark matter mini-halos with masses of $\sim 10^6$ $M_\odot$ (Figure 1.2). Those stars formed in a very different environment when compared with the present star-formation. In fact, due to the lack of metals, the cooling mechanisms were so ineffective (the main cooling mechanism is

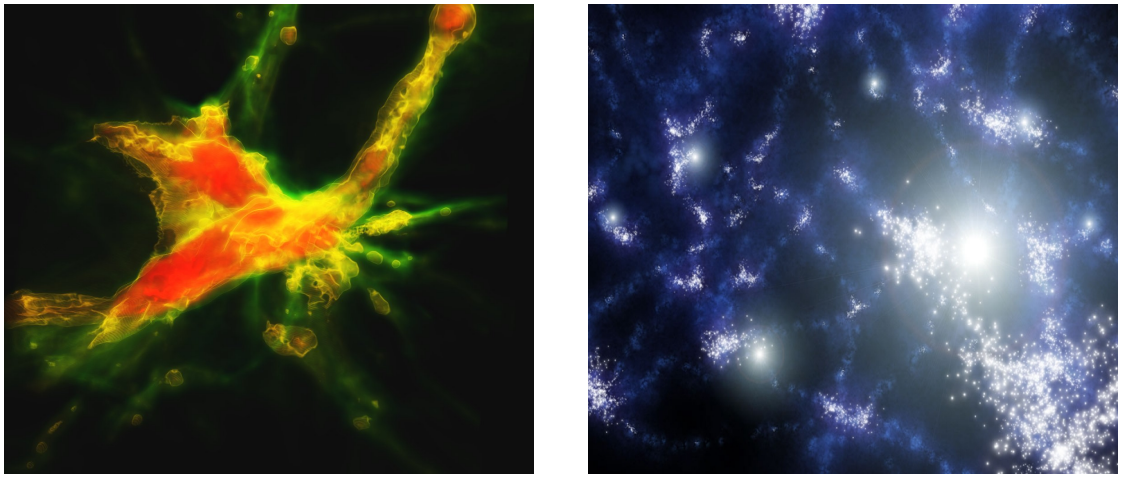

Figure 1.2: The *left* panel shows a simulated galaxy at $z = 10$, sites of the first star-formation episodes in the Universe (from Yoshida et al., 2008); the *right* panel presents an artist impression of the first stars – the *metal-free* population III. These stars are expected to have been very massive (∼100 times as massive as the sun) and extremely short-lived, contributing significantly to the re-ionization of the Universe (credit: NASA/JPL-Caltech/R. Hurt).

through H_2 molecules) that the result is believed to be the production of stars with $\sim$ 100-1000 $M_\odot$. It is still not clear whether those very massive objects would be able to fragment into smaller ones, although recent studies have shown that it is not likely to happen (Bromm and Larson, 2004). Whilst being so massive, they are expected to have been extremely luminous (and extremely short-lived), thus being able to effectively (and possibly quickly) contribute to the re-ionization of the Inter-Galactic Medium (IGM). Finally, some authors have suggested that the first clouds to collapse could also result in the direct formation of the first black holes (Begelman, 2008) with masses of ~ 10 $M_\odot$ which could then grow quite rapidly. This can then explain how it is possible to find very massive black holes at very high redshift (z $\sim$ 6-7), as those would act as seeds for the formation of such objects (c.f. Cattaneo et al., 2009, and references herein).

1.2.3 Searching for the First Galaxies

One of the most important questions in astronomy is "when did the first stars and galaxies form?". Observations of the most distant galaxies offer one of the greatest possible constraints on structure formation, allowing models of early galaxy formation and evolution to be tested, refined or refuted. Over the last decade, considerable manpower and telescope time has been dedicated towards this goal (see Ellis, 2008; Robertson et al., 2010): galaxies have been robustly identified out to redshift $z \sim 7$, just 750 Myr after the Big Bang (Misawa et al., 2006), a Gamma Ray Burst (GRB) has been detected even further away, at $z \approx 8.3$ (Tanvir et al., 2009), and, even more recently, a galaxy has been spectroscopically confirmed at $z = 8.55$ (Lehnert et al., 2010), although at a relatively low signal-to-noise. The most recent progress (including the galaxy followed-up by Lehnert et al., 2010) is a direct result of the great success of the recently refurbished HST/WFC3, which truly opened a window to

the early epochs in galaxy formation, allowing the robust selection of $z \sim 7-8$ very faint candidates (c.f. Bouwens et al., 2010; McLure et al., 2010; Bunker et al., 2010). The sample of very-high redshift galaxies is therefore growing rapidly.

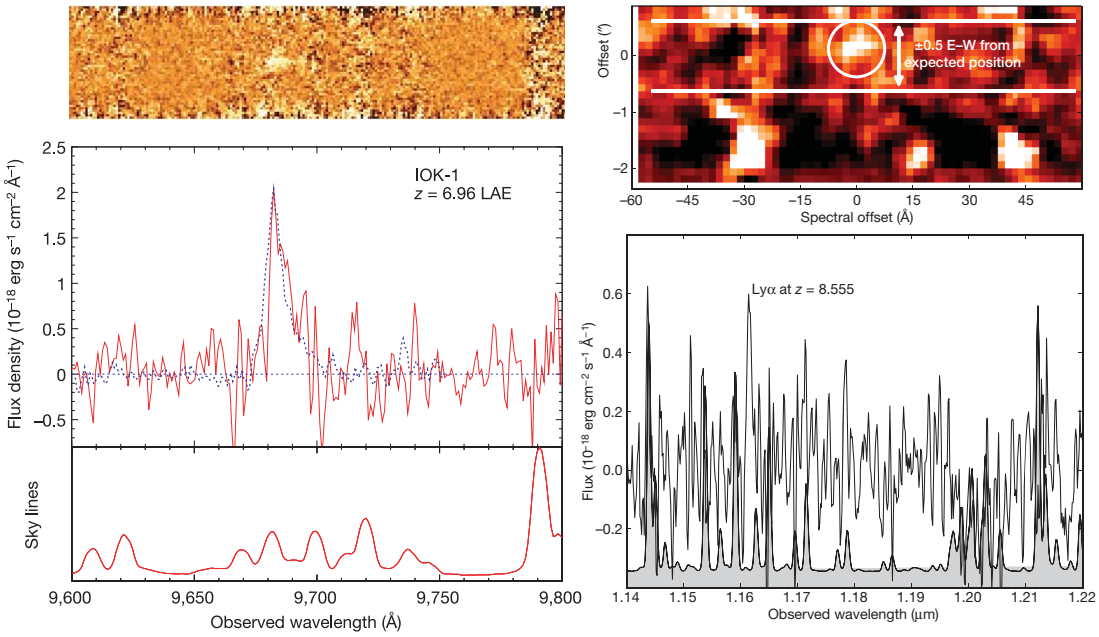

Figure 1.3: Spectrum of the most distant galaxies ever detected and confirmed at z=6.96 (IOK-1) taken from Iye et al. (2006) and z=8.55 taken from Lehnert et al. (2010). The bottom panels show the removed OH sky emission lines, while top panels show the 2-D and 1-D spectra.

Making the additional step out to redshifts of $z \sim 9$ and even earlier epochs is of the upmost importance because it not only offers much tighter constraints on the first star formation or AGN activity of the Universe, but also allows the re-ionisation epoch of the Universe to be studied. As the mean fraction of neutral hydrogen in the intergalactic medium increases, the Lyα emission from these star-forming galaxies will be strongly attenuated, with dramatic consequences for the shape of the Lyα luminosity function or the fraction of Lyα emitters (e.g. Stark et al., 2010), although the precise details may depend upon the level of local ionization of the intergalactic medium by the star-forming galaxies (e.g. Haiman and Cen, 2005). Little evolution is seen in the Lyα luminosity function between $z \sim 3$ and $z \sim 6$, suggesting that the Universe was effectively fully ionized by $z = 6$ (e.g. Malhotra and Rhoads, 2004; Ouchi et al., 2008), although hints of evolution have been found at the bright end of the luminosity function beyond $z \sim 6$ (e.g. Kashikawa et al., 2006; Ota et al., 2008; Ouchi et al., 2010). Still, the re-ionisation epoch is widely believed to occur around $z \sim 9$, with this being supported by several models and observations; the latest results from the Cosmic Microwave Background (e.g. Dunkley et al., 2009; Komatsu et al., 2009) show that the bulk of the re-ionisation occurred at $z = 11.0 \pm 1.4$ (1σ). However, it should be noted that the CMB can only provide the time of re-ionisation assuming it happens through a step-function process; therefore, the best current measurement is likely to be an estimate of the mid-point of re-ionisation, but it does not reveal how long the process actually lasted.

Table 1.1: Main Sequence lifetimes and typical masses for O, B, A, F and M stars.

Star	$M_\odot$	Lifetime	Star	$M_\odot$	Lifetime
O3	60	3 Myr	A5	3	0.3 Gyr
O7	30	11 Myr	F5	1.5	3 Gyr
B4	10	30 Myr	M7	0.1	1 Tyr

1.3 Star formation rate density

Understanding the basic features of galaxy formation and evolution requires measuring the star-formation rate density, ρ_{SFR}; this provides a measurement of how many stars (in units of mass) per unit volume the Universe was forming at a particular epoch. Understanding its evolution with cosmic time unveils the star formation history of the Universe and how it assembled its stellar mass all the way from the first galaxies to the present-day. To achieve this, one needs to detect and quantify star-formation activity over large volumes and over the bulk of the cosmological time.

1.3.1 Measuring Star formation: Star formation indicators

Most of the baryonic mass in a galaxy is in the interstellar medium. Eventually, this can build clouds of gas, where structure can form due to turbulence and/or activity of other stars. Random turbulent processes can then lead to regions which are dense enough to collapse under their own weight; these can then form stars. In the solar neighborhood, and within our Galaxy, it is possible to observe the new-born stars and star-forming regions individually, as sufficiently high resolution imaging is relatively easy to obtain. However, as soon as one "leaves" our own galaxy, and, particularly, the local group, the distances to new-born stars become so large that it is extremely difficult to probe star formation, not only on a star-by-star basis, but also in an individual cloud-by-cloud or star-forming region to region basis. For the bulk of the population of very distant galaxies, the best we one can do – even with the high-resolution of the Hubble Space Telescope – is to obtain an average star formation rate across each galaxy using different star formation rate tracers which reveal the *signatures* of recent star-formation.

The "current" star formation rate (SFR) of a galaxy is a fundamental parameter for our understanding of galaxy evolution. It is possible to find a wide range of signatures of the existence (or deaths) of very massive stars, and therefore, in practice, there are several ways we can estimate star formation rates, with these *tracers* being at different wavelengths. These tracers include: the continuum ultraviolet (UV) radiation, directly radiated by massive stars; major emission lines in the visible (such as Hα and [OII]), resulting from atoms re-combining after being ionized by the intense UV radiation; far-infrared emission from dust grains heated by the UV emission; radio emission from the supernova explosions of the massive stars – these indicators are discussed in Section 1.3.3 through to Section 1.3.7.

Figure 1.4: HII regions are associated with intense star-formation. This image shows an HII region within our galaxy (the Rosette Nebula – NGC 2237-9) with the Hα emission shown in red – this is a result of the strong ionizing radiation from massive stars. Credit: Robert Gendler.

Ideally, the use of different star formation tracers would provide consistent answers to most of the questions that remain unanswered. Unfortunately, with different star formation tracers suffering different biases and selection effects, having different sensitivities and probing stars with slightly different masses (and at different stages of their evolution), significant discrepancies are found. These problems are also amplified by the effects of cosmic variance in most of the current samples. Another significant issue is the difficulty in correcting for extinction, especially for UV and optical wavelengths, which can lead to large systematic uncertainties in the star formation densities derived from measurements in these wavebands, not only because of the difficulty of correcting for what surveys detect, but especially for those galaxies that surveys miss.

No single indicator provides a perfect view of the evolution of the star-formation rate density; each has its biased view, together with advantages and disadvantages. Moreover, because recent star formation indicators are, in practice, only probing the existence (or recent deaths) of the most massive stars, estimating the real recent star formation activity requires one to account for all the stars formed, including the lower-mass stars. The latter is achieved by using the Initial Mass Function.

1.3.2 Initial Mass Function

Probing star formation in distant galaxies and trying to obtain a reliable star-formation rate is not an easy task. As the following sections describe, the really *distinct* signature of recent star-formation activity comes from newly born massive stars (which are short-lived). Can we extrapolate the signature of those massive stars to lower mass stars and determine the total star formation rate? Yes, if we

know the initial mass function.

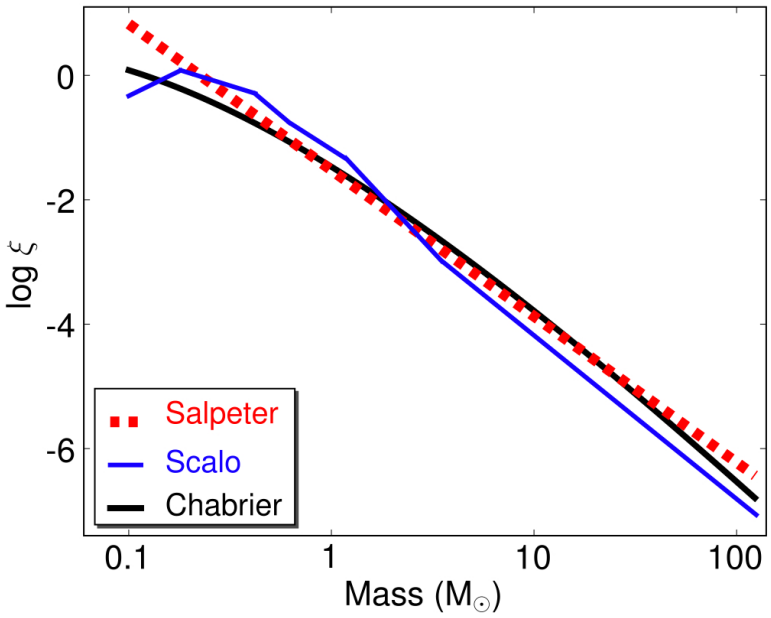

Figure 1.5: A comparison between three widely used IMFs: Salpeter (1955), Scalo (1986) Chabrier (2003), showing that the differences are mostly noticeable at the high and very low masses.

The initial mass function, IMF, is an empirical function that tries to describe the mass distribution of stars as a function of their theoretical initial mass that led to their formation. It is often represented by $\xi(M)$ and is frequently written as simple power law:

$$\xi(M) = cM^{-(1+x)} \tag{1.21}$$

In general, however, $\xi(M)$ is assumed to extend from a lower to an upper cutoff, normally chosen to be $M_1 = 0.1\mathrm{M}_\odot$ and $M_2 = 100\mathrm{M}_\odot$.

There are many different IMFs which are used in the literature; some of the most widely used are plotted in Figure 1.5. The different slopes of the considered laws produce different spectral energy distributions. The Scalo (1986) and Miller and Scalo (1979, not shown) relations, for example, are relatively flat at low masses and less rich of massive stars with respect to the Salpeter (1955) IMF, as they allow x to vary in different mass ranges. Salpeter (1955), on the other hand, implies a large number of massive stars, producing an excess of UV flux, whereas the Scalo (1986) law generates too many solar mass stars, making the spectrum too red to match observed colours. The Chabrier IMF lies mostly in between Salpeter (1955) and Scalo (1986), predicting less low mass and high mass stars than Salpeter (1955), but more stars at both ends than Scalo (1986).

Several studies have been done in our galaxy, where we can probe star-forming regions in detail. These have shown that the IMF remains fairly constant for all the regions studied, i.e., for each star-forming region, the fraction of stars forming with a given mass as a function of the initial mass of the cloud does not change considerably. Therefore, for years now, astronomers have assumed a constant IMF which has been empirically determined.

Nevertheless, while the constancy of the IMF within our galaxy seems to valid, the same might not be true for star-forming regions in other galaxies, particularly when one looks at star formation in very massive or/and very young galaxies at high-redshift. Regardless of that limitation/uncertainty, star formation rates all rely on assuming a certain IMF to account for low-mass stars produced in star formation episodes in galaxies.

1.3.3 Ultraviolet Continuum

Massive stars are characterized by a very intense UV light (see Figure 1.6). On the other hand, as these stars are very short-lived (see Table 3.3, showing that the lifetime scales as $\sim M^{-3}$), the amount of UV light can then be used as an "instantaneous" star formation rate (SFR) tracer. In order to avoid contamination by older stars, the optimal wavelength range is 125-250 nm, longward of the Lyα forest. These wavelengths are inaccessible from the ground for local galaxies (z<0.5) but one can easily observe these in the redshift range 1-5. The conversion between UV flux over a given wavelength interval and the SFR can then be derived using synthesis models. Assuming a constant SFR over time-scales long enough when compared to the lifetimes of dominant UV emitting population ($\sim$10-50 Myr), and using a Salpeter (1955) IMF with mass limits 0.1 and 100 $M_\odot$ yields:

$$\mathrm{SFR}(M_\odot \mathrm{year}^{-1}) = 1.4 \times 10^{-28}\ L_\nu\ (\mathrm{ergs.s}^{-1}\mathrm{Hz}^{-1}). \tag{1.22}$$

Unfortunately, UV is very sensitive to extinction and to the form of the IMF. Typical extinction corrections in the integrated UV magnitudes are $\approx$1-3 mag, but these can be even higher for very dusty galaxies.

While UV luminosity is commonly used as a SFR indicator, the luminosity at rest-frame u-band wavelengths ($\lambda \sim 3600$ Å) is similarly dominated (in starburst galaxies) by young stellar populations, and in the absence of UV measurements it may be used as a SFR indicator. However, using u-band as a SFR indicator is more problematic than UV; it is harder to assign a simple scaling factor to derive a SFR due to the strong dependence on the evolutionary timescale. From synthetic galaxy spectra it can be seen that the u-band luminosity varies from about a factor of 10 lower than the UV luminosity at the onset of a burst of star formation to almost equivalent on later times.

Given this sensitivity of the u-band luminosity (L_u) to the starburst age and the assumed star formation history, a more complex calibration is in general likely to be necessary. This may take the form of a nonlinear dependency on L_u to reflect the rapid change of L_u with respect to L_{UV} during the first 10^8 yr of a starburst and to account for the presence of old stellar populations that are likely to contribute significantly to L_u in less luminous systems. More quiescent or low-luminosity SF systems have a relatively larger contribution to their u-band luminosity from old stellar populations (they are, on average, redder than more luminous galaxies), and this causes a linear calibration from luminosity to SFR to result in an overestimation.

While recent star-formation activity is likely to produce large quantities of energy, initially released by the massive young stars, a significant portion of that energy is actually absorbed and re-emitted

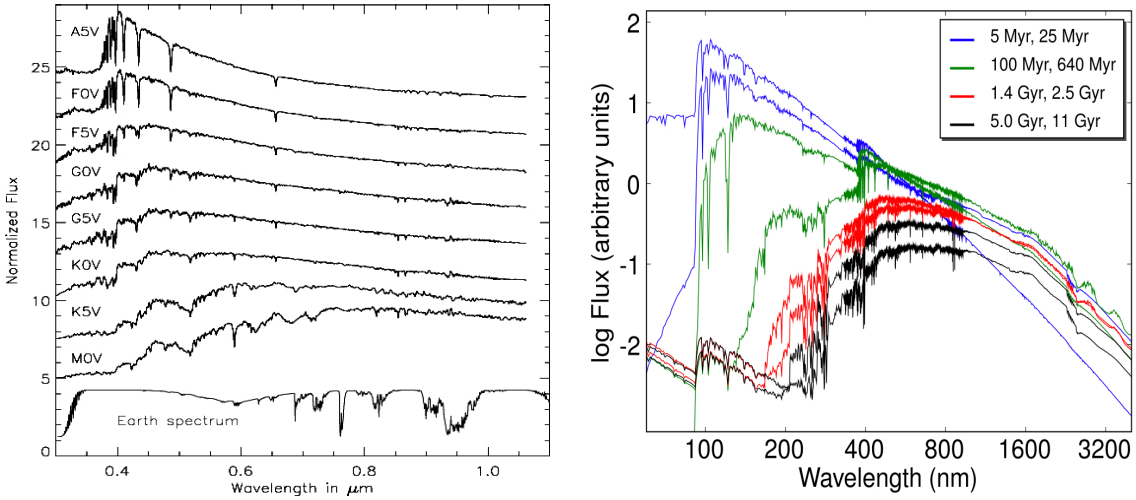

Figure 1.6: The *left* panel presents spectra for typical stars with decreasing mass from the top to the bottom and a comparison with Earth's spectrum, showing that only the most massive stars contribute significantly to the UV flux. The *right* panel presents the spectral energy distribution of an instantaneous burst of star formation seen at different ages. This evolves strongly at UV wavelengths due to the evolution and death of the most massive stars, emphasizing that at $\sim 100 - 250$ nm the UV emission is completely dominated by short-lived massive stars.

through a large variety of physical processes, including emission lines. Therefore, while the UV luminosity is the only *truly direct* star-formation indicator, the advantages of the following SF tracers can, in many cases, make them a better choice than UV.

1.3.4 Emission lines: Hα, [OII] and others

As discussed above, UV is very sensitive to extinction and to the form of the IMF, and typical extinction corrections in the integrated UV magnitudes can easily reach ≈3 (mag). On the other hand, most of the absorbed UV energy is then re-emitted by several different processes, including recombination lines. Only stars with masses of > 10 M$_\odot$ and lifetimes of < 20 Myrs contribute significantly to the integrated ionizing flux, so the emission lines provide a nearly instantaneous measure of the SFR, independent of the previous star formation history. With most of the baryonic matter being in the form of Hydrogen, this is the element that tends to absorb most of the UV photons and become ionized. The subsequent recombination of hydrogen atoms then happens through a broad range of processes (see Figure 1.7). One of the most common ways implies the emission of photons of the Paschen series. Hα photons are also emitted quite effectively. Hα is a sensitive star formation indicator which can be calibrated using UV radiation from local galaxies. Despite that, it is still affected by extinction, which one can account for by measuring the flux of Hβ, for example. This works due to the existence of a standard Hα to Hβ ratio for photo-ionisation, thus measuring the observed ratio probes the effective extinction. Nevertheless, this is a hard task, as Hβ is often weak and hard to detect or measure. For solar abundances and the same Salpeter IMF (0.1 to 100 M$_\odot$), the calibrations of Kennicutt et al.

(1994) and Madau et al. (1998) yield:

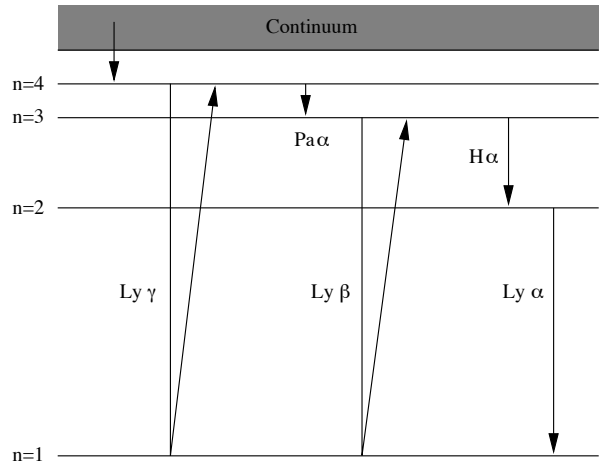

Figure 1.7: A schematic view on some of the recombination emission lines for hydrogen, with Hα ending up being one of the strongest.

$$\mathrm{SFR}(\mathrm{M}_{\odot}\mathrm{year}^{-1}) = 7.9 \times 10^{-42}\ \mathrm{L}_{\mathrm{H}\alpha}\ (\mathrm{ergs\,s}^{-1}). \tag{1.23}$$

Large Hα surveys have been published since de 1970's (Cohen, 1976; Kennicutt and Kent, 1983; Romanishin, 1990; Gavazzi et al., 1991; Gallego et al., 1995; Yan et al., 1999; Tresse et al., 2002; Glazebrook et al., 2004; Doherty et al., 2006) up to z$\sim$1.3, using both spectroscopic surveys and also the technique of narrow-band imaging (see Chapter 2). Hα also permits the mapping of star formation in nearby galaxies at high resolution, even with smaller telescopes. Nevertheless, it is still sensitive to uncertainties in the IMF, along with the assumption that all of massive star formation is traced by ionized gas. Several studies, such as Kennicutt (1983) or Afonso et al. (2000) have used integrated Hα and radio fluxes of galaxies to derive a mean extinction A(Hα) = 0.8-1.1 mag. Studies of large samples of individual HII regions in nearby galaxies yield similar results, with typical A(Hα) = 0.5-1.8 mag (Caplan et al., 1996). As mentioned before, Paschen and Brackett lines are also involved in the recombination process, and thus can potentially be used as SFR tracers. However, they are typically 1-2 orders of magnitude weaker than Hα, thus they can only be used for the brightest emitters.

The Hα line is redshifted out of the visible window for z >0.5, so bluer lines which can trace SFR can be very important (see Figure 1.8). Unfortunately, the other Balmer lines are poor SFR diagnostics, as they are both weak and very stellar-absorption dependent, but other elements, such as oxygen, can play an important role. In fact, one of the strongest emission features in the blue is the [OII]$_{\lambda\lambda 3727}$ doublet emission line (forbidden). Luminosities of forbidden lines are not directly coupled to the ionizing luminosity, and their excitation is sensitive to abundance and the ionization of the gas. Despite that, the excitation of [OII] is sufficiently well-behaved and it can be empirically calibrated using Hα as a quantitative SFR tracer. As [OII] falls into the visible window out to redshifts of about 1.6, it can easily be used for large surveys up to that redshift. Only the hottest stars have sufficient UV flux to ionize oxygen atoms, therefore the [OII] flux is mostly due to O and B stars. Rates of

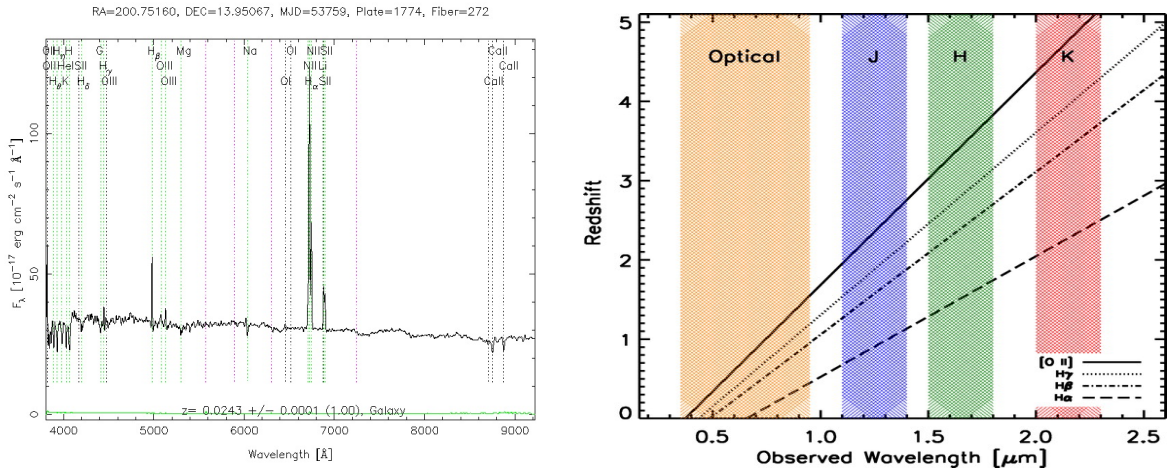

Figure 1.8: *Left*: A typical spectrum of a low-redshift starburst galaxy, showing strong Hα, Hβ and [OII] emission lines. At higher redshifts, these lines move to higher wavelengths and can only be observed in specific windows (*right*), with the Hα line being the first to go beyond the K band, at z$\sim$2.5.

star-formation come from folding in the well-known lifetimes of those stars. Adopting the same IMF and calibrating using Hα emission results in:

$$\mathrm{SFR}(\mathrm{M}_{\odot}\mathrm{year}^{-1}) = (1.4 \pm 0.4) \times 10^{-41}\ \mathrm{L}_{[\mathrm{OII}]}\ (\mathrm{ergs\,s}^{-1}) \tag{1.24}$$

where the uncertainty indicates the range between blue emission-line galaxies (lower limit) and samples of more luminous spiral and irregular galaxies (upper limit). Observed luminosities must still be corrected for extinction, and, due to the way the relation was computed, the extinction that needs to be applied is that estimated at Hα, and not [OII]. Unfortunately, SFRs derived by this method are less precise than those using Hα, especially because the line ratio between the two lines varies from galaxy to galaxy. However, it is very useful, especially for a consistency check on SFRs derived with other methods.

1.3.5 Far-Infrared Continuum

A large fraction of the bolometric luminosity of a galaxy is absorbed by interstellar dust and re-emitted in the thermal IR at wavelengths of roughly 10-300μm (see Figure 1.9). The involved cross-section is strongly peaked in the UV, implying that the far infrared (FIR) emission can be a sensitive tracer of the young stellar population and SFR. In fact, the efficiency of this method depends on the contribution of young stars to heating the dust and on the optical depth of the dust in star-forming regions. The simplest physical situation occurs when young stars dominate the radiation field in the UV-visible and the dust opacity is high everywhere. In this case, the FIR luminosity measures the bolometric luminosity of the star-formation *burst*. In such a limiting case, the FIR luminosity is an excellent SFR tracer, providing a calorimetric measure of the SFR. Such conditions roughly hold, at least in the dense circum-nuclear starbursts that power many IR-luminous galaxies, though the physics become

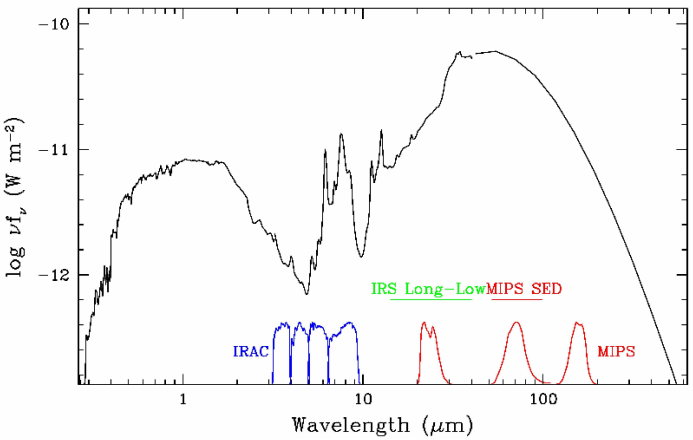

Figure 1.9: The spectral energy distribution of a typical star-forming galaxy. The interstellar dust absorbs the UV light from young stars and radiates like a blackbody in the mid-infrared, with that radiation being typically strong enough to be detected and measured.

more complex when dealing with disks of normal galaxies. In fact, the FIR spectra of galaxies contain both a *warm* component associated with dust around star-forming regions ($\sim \lambda_{peak} = 60$ μm) and a *cooler*, *infrared cirrus* component at longer wavelengths which is associated with more extended dust heated by the interstellar radiation field. In blue galaxies, both spectral components may be dominated by young stars. However, for red galaxies, where the composite stellar continuum drops off steeply in the blue, dust heating from the visible spectra of older stars may be important.

The relation between the global FIR emission and the consequent SFR has been a controversial subject. On the one hand, it is true that for late-type galaxies, where dust heating from young stars is expected to dominate the 40 to 120 μm emission, the FIR luminosity correlates well with other SFR tracers such as the UV continuum and Hα luminosities (Buat and Xu, 1996). On the other hand, early-type galaxies often exhibit high FIR luminosities, but much cooler, cirrus-dominated emission.

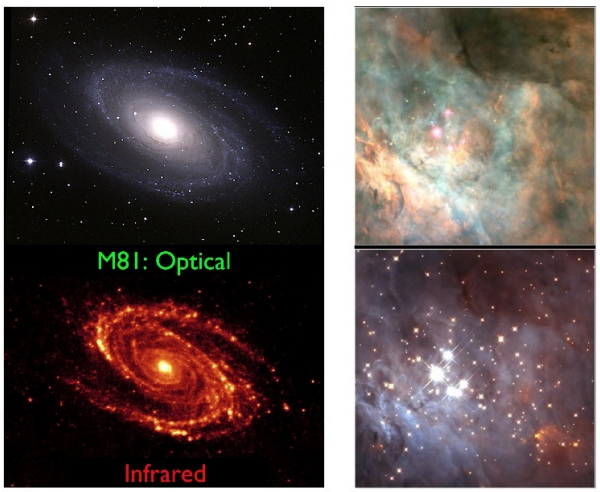

Figure 1.10: The optical *versus* infrared view of M81 and a star-forming region showing how dust extinction can alter the view of the exact same objects. *Credit*:$NASA/JPL/ESA$.

Despite the problems one finds when calibrating the FIR as a SFR tracer, the truth is that it should provide an excellent measure of the SFR in dusty circum-nuclear star-bursts. Calibrations published by Kennicutt (1998) using the same IMF as before yields the relation:

$$\mathrm{SFR}(\mathrm{M}_{\odot}\mathrm{year}^{-1}) = 4.5 \times 10^{-44}\ \mathrm{L}_{\mathrm{FIR}}\ (\mathrm{ergs\,s}^{-1}) \tag{1.25}$$

where $\mathrm{L}_{\mathrm{FIR}}$ is obtained by integrating over the full, mid and far-IR spectrum (8 to 1000 μm). Nevertheless, for starbursts, most of the emission will happen in the 10 to 120 μm range. In practice, obtaining the far-IR integrated spectrum implies SED fitting using the most commonly-used bands, where the 24 μm (MIPS) and the sub-mm bands are powerful (and essential) tools.

1.3.6 Radio

Long-wavelength SFR estimates are insensitive to dust obscuration, increasing their attraction for SFR investigations, but they are not without limitations. Radio luminosity can be generated by AGN as well as star formation processes, and indeed the majority of apparently bright radio sources are AGNs. By selecting for star formation directly from optical spectroscopic features, however, one can eliminate this potential source of confusion. The detailed physics involved in the connection between SF and radio emission is still poorly understood, despite numerous attempts. Still, neglecting AGN contribution, there are two main components of the radio continuum emission in star-forming galaxies: thermal *bremsstrahlung* from ionized hydrogen in HII regions and nonthermal synchrotron emission from cosmic-ray electrons (from supernovae events) spiraling in the magnetic field of the galaxy. Thermal radio emission presents a spectrum $\sim \nu^{-0.1}$, whereas non-thermal emission presents a steeper spectrum with $\sim \nu^{-0.8}$.

Because radio is essentially not affected by extinction, it is often regarded as a good SFR tracer (although not an *instantaneous* tracer, as it mostly probes supernovae events, and thus it can be considered a *delayed* SFR indicator), especially for the most obscured, dusty galaxies (c.f. Condon, 1992). However, it is not very sensitive.

Radio emission is also well correlated with the FIR emission (Dickey and Salpeter, 1984; Helou et al., 1985; de Jong et al., 1985), even though the broad range of different physical processes involved would not imply it. In fact, it has proven to be one of the tighter relations in astronomy, and recently, studies such as Ibar et al. (2008) or Ivison et al. (2010) have shown that it holds up to the ∼highest redshifts for which it is possible to perform these studies.

1.3.7 Gamma-ray bursts and X-rays

We have seen before that it is possible to infer the formation rate of massive stars from their death rate, since their lives are short. While it is not possible to detect ordinary core-collapse supernovae at high redshift, long-duration gamma-ray bursts, which have been shown to be associated with a special class of core-collapse supernovae, have been detected beyond $z \sim 8$. Therefore, assuming that

it is possible to match the number of these GRBs with an average star-formation rate density at a particular epoch, one can try to obtain a star-formation history of the Universe based on them. Nevertheless, while the calibration is not easy to obtain, GRBs are also too rare to provide the same amount of information as all the other SFR indicators described before.

On the other hand, binary systems with two very massive stars can evolve to form high-mass X-ray binaries, which are generally more powerful than supernovas and their remnants. There are actually two types of X-ray binaries: low mass X-Ray binaries (LMXBs), which contain a neutron star or a black hole as the primary object, together with a star of less than 2.5 $M_{\odot}$, and high-mass X-ray binaries (HMXBs) with a secondary object of more than 2.5 $M_{\odot}$. This results in very different lifetimes, together with a significant difference in the accretion – stars in HMXBs have strong stellar winds and thus the primary can accrete mass from this wind alone. Also, as HMBXs present lifetimes of 10^5-10^7 years, they can, in principle, be used as a good recent star formation indicator. The X-ray emission from HMXBs can penetrate thick columns of gas and dust to give an unobscured view of the star-formation activity.

However, for distant galaxies, it is not really possible to distinguish between the X-ray contribution of LMXBs and HMXBs. Still, using some other star-formation indicator to select apparent star-formation dominated galaxies, and remove AGN contamination, one can in principle assume that most of the X-ray flux is coming from HMXBs and not from LMXBs (which are related to the mass of the galaxy) and in some cases obtain an X-ray based star-formation rate.

Figure 1.11: HII regions are associated with intense star-formation. This image shows a HII region within our galaxy (Image by *Steve Mandel*).

1.3.8 AGN *versus* star formation

Active galactic nuclei (AGN) are galaxies which host an accreting super-massive black hole in their nucleus. These emit across the whole electro-magnetic spectrum, and some of them are particularly

strong in the radio. One can distinguish between various types of AGN. Quasars (Quasi Stellar Objects) present strong emission lines, some of them broad (as they are produced near the nucleus, where the gas is moving faster). Seyfert galaxies are fainter, and also present strong emission lines: Seyfert I presents both broad emission lines (the permitted emission lines) and forbidden (narrow) emission lines, while Seyfert II present only narrow emission lines. These two classes of Seyferts are believed to be a single class of objects and can be unified by assuming they are being observed at different angles (Antonucci, 1993).

While the energy sources of AGN and (pure) star-forming galaxies are very different, without a careful analysis, the signatures of both sources can easily be mixed up: both AGN and star formation can produce high UV fluxes, strong emission lines, far-IR and radio emission. Thus, in order to correctly measure star formation rates, and obtain a good estimation of the number density of star-forming galaxies, it is necessary to separate AGN-powered from star-forming-powered emission. The latter can be done by different means, such as emission-line ratios (probing the differences in the hardness of steepness of the UV), dust temperatures (using mid-infrared colours), looking for very high radio power or high-luminosity X-ray emission, or fitting the entire spectral energy distribution to star-forming and AGN-like templates (c.f. Figure 1.12).

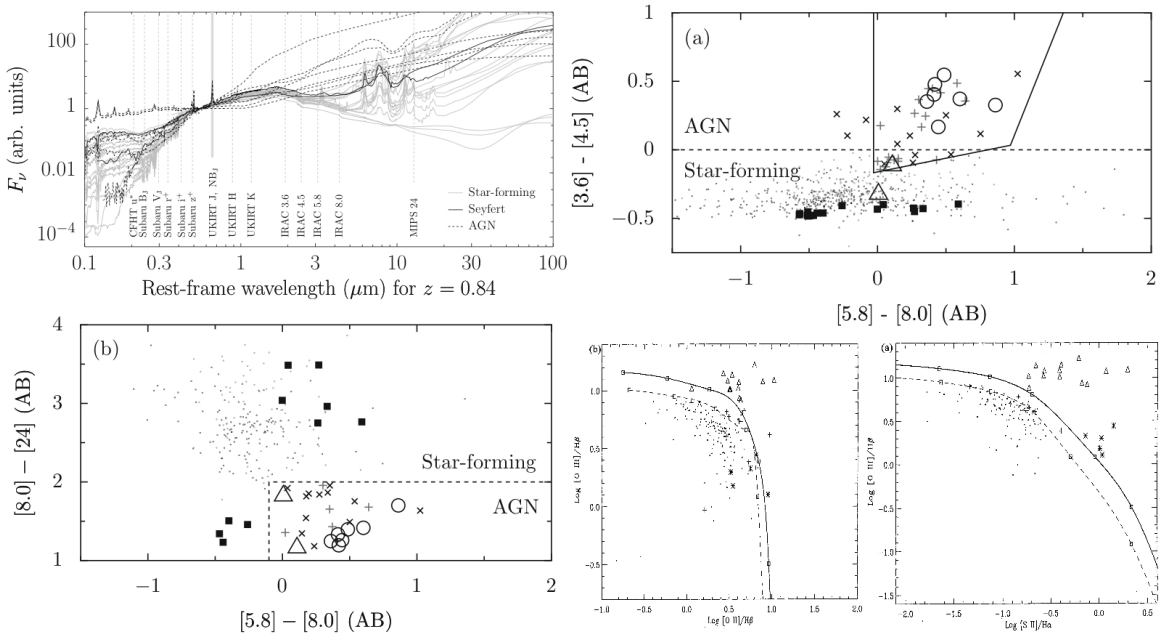

Figure 1.12: *Top − left*: Differences in the SEDs of AGNs and star-forming galaxies can be used to separate the two populations; such differences can also investigated using mid-infrared colours (*top-right* and *bottom-left* panels; adapted from Garn et al., 2010). *Bottom-right*: Due to the difference in the slope of the UV ionizing radiation produced by AGN and star-forming galaxies, ratios of relatively strong emission lines can also be used to distinguish between AGN and star-forming galaxies (adapted from Rola et al., 1997).

1.4 The Star Formation History of the Universe

Understanding the basic features of galaxy formation and evolution implies unveiling the volume-averaged star formation rate as a function of epoch, $\rho_{\rm SFR}$, its distribution function within the galaxy population, and the variation with environment. At the present, surveys of the star-formation rate as a function of epoch suggest that the star-formation rate density rises as $(1+z)^4$ out to at least z$\sim$1 (Lilly et al., 1996; Connolly et al., 1997; Hogg et al., 1998a; Haarsma et al., 2000; Hopkins, 2004; Hopkins and Beacom, 2006) indicating that most of the stars in galaxies today formed at z $>$ 1 with the peak occurring around that cosmic time (see Figure 1.13). However, determining the precise redshift where the star-formation rate peaked is not trivial, especially when different star-formation indicators give different measures of the integrated star-formation rate density. Nevertheless, the star-formation rate density seems to flatten at z $\sim$ 2 and thus it is likely that the majority of stars seen today were formed between z $\sim$ 1 and z $\sim$ 3 (e.g. Madau et al., 1996; Connolly et al., 1997; Hughes et al., 1998; Yan et al., 1999; Hopkins and Beacom, 2006; Geach et al., 2008; Shim et al., 2009). Indeed, z$\sim 2-2.5$ appears to be an important era in the evolution of many populations, such as Quasi Stellar Objects (QSOs) and sub-millimeter galaxies, which may be intimately linked to the formation of massive galaxies. However, it is still not completely certain if the evolution of $\rho_{\rm SFR}$ reaches a peak around z $\sim$ 1.5 and decreases significantly thereafter (e.g. Madau et al., 1996) or whether it stays flat to much higher redshifts (e.g. Steidel et al., 1999; Haarsma et al., 2000; Yüksel et al., 2008; Geach et al., 2008).

1.4.1 Comparison of different Star Formation indicators

No single star-formation indicator is ideal to probe all cosmic epochs. Nevertheless, the use of different star formation tracers ought to present a consistent picture which would allow us to answer most of the key questions. Unfortunately, when they are combined the result is far from ideal, with a large scatter in the resultant measurements (e.g. see Hopkins, 2004). These problems are amplified by the effects of cosmic variance in the current samples, which are normally based on small-field surveys. Another reason for the uncertainty in the star-formation history and the discrepancy between tracers seems to be the difficulty in correcting for extinction (especially for UV and optical wavelengths). In fact, when one does not correct for that, there is a clear discrepancy between values of $\rho_{\rm SFR}$ estimated from radio and FIR and those estimated from Hα and UV. Even when simple extinction corrections are made, however, systematic differences seem to persist between estimates of SFR or $\rho_{\rm SFR}$ made at differing wavelengths. This can be seen in the distribution of SFRs for individual objects in studies of local galaxies (e.g. Cram et al., 1998), in a multiwavelength studies (e.g. Sullivan et al., 2001; Wijesinghe et al., 2011; Kurczynski et al., 2010), or, more globally, in the redshift dependence of $\rho_{\rm SFR}$ (Haarsma et al., 2000). Several efforts have been made to address this concern. A detailed investigation of some of these issues is presented in Adelberger and Steidel (2000), with particular emphasis on obscuration at UV wavelengths. Other authors have refined a technique for correcting UV luminosities for attenuation using rest-frame luminosities alone (e.g. Meurer et al., 1999), with

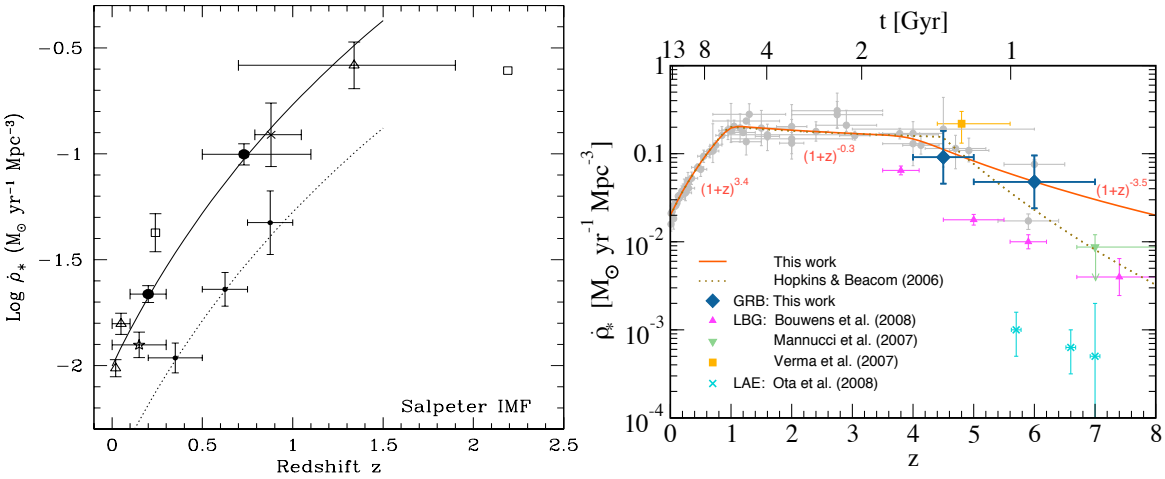

Figure 1.13: Evolution of star formation rate density as traced by present surveys of Hα emitters (Tresse et al., 2002, *left*). This shows the star formation density estimated from reddening-corrected Hα observations (whereas the point at z$\sim$2 is from Moorwood et al., 2000), except for the three small diamonds which are UV-observations from Lilly et al. (1996). The solid line is a fit $\sim (1+z)^{4.1}$ to the Hα data at $z < 1.5$, while the dotted line shows the same relation fit to the UV data points (systematically low). The *right* figure shows the evolution of star formation rate density as traced by present surveys using several SF tracers, including estimates from gamma-ray bursts (from Yüksel et al., 2008).

the method being based on an observed correlation between the FIR-UV flux ratio and the UV spectral slope. More recently, and using a sample of local galaxies, Kennicutt et al. (2009) show that combining Hα with far-infrared fluxes provides much more reliable measurements than any of the individual indicators on their own.

1.4.2 What is driving the Star formation History?

Knowing the global average star formation rate is not enough to fully understand the nature and distribution of star-forming galaxies at high redshifts. In fact, recent results are showing that star formation in the most massive galaxies is happening earlier than in lower mass galaxies, a process known as *downsizing* (Cowie et al., 1996). In addition to that, star formation rates of galaxies are probably highly influenced by the environment in which they reside (e.g. Dressler, 1980; Butcher and Oemler, 1984). In the local Universe, many studies have now demonstrated in detail that star formation is strongly dependent on the environment (e.g. Lewis et al., 2002; Gómez et al., 2003). While clusters of galaxies seem to be primarily populated by passively-evolving galaxies, star-forming galaxies are mainly found in less dense environments. Furthermore, there is a natural connection between mass and environment: higher density environments will tend to have more massive galaxies, and, therefore, to which extent are mass-downsizing and the environmental trends related? Using the very large samples now available in the local Universe, studies such as Peng et al. (2010) have now clearly showed that both mass and environment seem to play important and separable roles

in quenching star-formation (see Figure 1.14), and thus neither seems to be truly fundamental and driving the other.

How important is the build-up of stellar mass, and of galaxies into groups and clusters for the decline in cosmic star formation rate since z∼1 until the present? How do these environmental and mass dependencies change with cosmic time? When did they start to be noticeable, and how do they affect the evolution of galaxies, clusters and the star formation rate density of the Universe as a whole? How much of the evolution of the cosmic star formation rate density is associated with the evolution of (isolated) star-forming galaxies and how much is driven by galaxy merger activity?

In order to properly answer such questions it is mandatory to conduct observational surveys at high redshift, which can then be used to test theoretical models of galaxy evolution. However, such surveys can only be carried out provided that we have the right tools for both selecting significant samples of star-forming galaxies, and measuring how much star-formation is on-going in each of those.

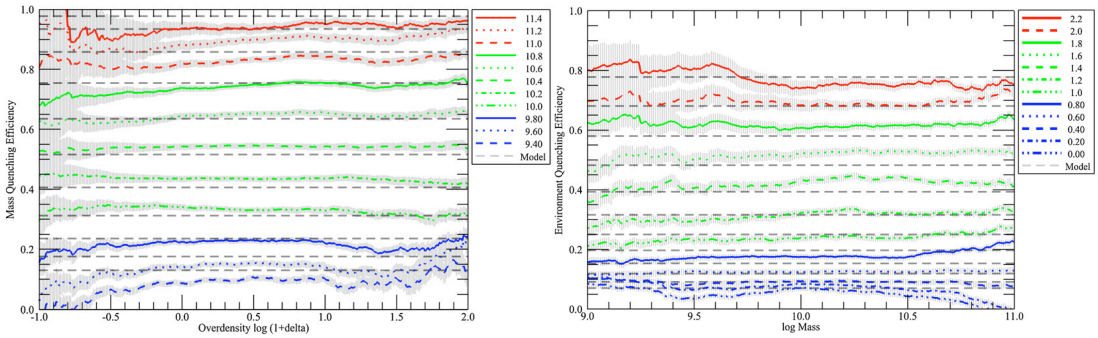

Figure 1.14: Observed values of the relative mass-quenching efficiency (fraction of galaxies at a given mass which would be forming stars in a reference environment, but which are progressively quenched, i.e., red, in denser environments; c.f. Peng et al., 2010) as a function of environment for different galaxy masses (left) and of the relative environment-quenching efficiency as a function of mass for different environments (right; fraction of galaxies residing in a given environment which would be forming stars in a reference mass, but which are progressively quenched, i.e., red, at higher masses; c.f. Peng et al., 2010). The fact that these are essentially flat reveals that mass and environmental trends are separable and both important, at least locally. Figure from Peng et al. (2010).

1.5 An Answer: narrow-band surveys + Hα

As seen before, no single indicator provides a "perfect" view of the evolution of the star-formation rate density (e.g. Kewley et al., 2004), but using different tracers is not the solution either. Thus, what one ideally requires is a star-formation indicator that can be applied from the present to z∼3, selecting large samples, relatively immune to dust extinction and with sufficient sensitivity. The last of these is important to ensure that the derived star-formation rate distribution doesn't require large extrapolations for faint sources below the sensitivity limit. Hα luminosity is probably the best candidate to achieve these goals and it is bright enough that surveys with a sensitivity of about

(or below) $10\,M_{\odot}yr^{-1}$ can be done with current instrumentation, even at z∼2. This contrasts with the equivalent star formation rate limit for dust-independent tracers such radio, far-infrared or sub-millimeter surveys which vary from 100 to 1000 $M_{\odot}yr^{-1}$ at the same redshift. A summary of the Hα star-formation history is presented in Figure 1.13, taken from Tresse et al. (2002).

Narrow-band emission-line surveys are very effective for obtaining Hα-derived star-formation rates for large and robust samples of galaxies. Moreover, with the "rise" of large-format imaging cameras in the optical and in the near-infrared, narrow-band filters can be used to undertake deep and unbiased surveys for emission-line objects in large volumes at the most important redshifts (out to z∼2.5). The surveys identify the sources on the basis of the strength of their emission line and thus represent (broadly) a star-formation rate-selected sample, while they also select very narrow redshift slices. Hence, by using a set of narrow-band filters, it is possible to apply a single technique to target Hα emitters across a wide range of redshifts, gathering representative samples at each epoch with a uniform selection. Those samples are powerful tools for tracing the evolution in the star-formation rate density across the expected peak of star-formation in the history of the Universe.

Recently, several attempts to find Hα emission at high redshift have been made using near-infrared narrowband surveys, but these have been done in small areas. At the typical limit, $F_{H\alpha} \sim 10^{-16}$ erg s^{-1} cm^{-2}, only a few $z \sim 2$ galaxies have been found. Villar et al. (2008) have presented results of $\sim$ 100 Hα emitters at $z \sim 0.84$, using narrow-band J imaging. However, many detections are not robust enough to claim any major and robust improvement for determining the SFR at that epoch, as $\sim$ 50 % of the detections are below the 3 σ level. Furthermore, the survey only probes a total area of 0.2 square degrees and thus the effect of cosmic variance cannot be ignored. In this thesis I will present an improvement over previous studies (such as Villar et al., 2008) by taking advantage of the large area coverage of the Wide Field Camera (Casali et al., 2007) on the 3.8-m United Kingdom Infrared Telescope (UKIRT) and two excellent fields for conducting this study in a large and deep area: COSMOS and UKIDSS UDS (for further details regarding these fields see Chapter 2).

Large Hα surveys covering $z = 0 - 3$ can also provide a powerful tool for measuring the growing influence of environment on star-forming galaxies, and determine how the characteristic stellar mass of star-forming galaxies changes with epoch. Such observations would also provide key tests of current galaxy formation models (e.g. Baugh et al., 1998; Benson et al., 2000; Baugh et al., 2005).

1.6 Thesis Outline

This thesis is organized in the following way: Chapter 2 presents the general WFCAM characteristics and the HiZELS survey, its goals and the data-reduction pipeline. Chapter 2 also presents the observations and the basics of data reduction and the narrow-band technique for selecting potential emission-line galaxies. Chapter 3 presents the sample of over 700 Hα emitters at $z = 0.84$ in two fields, and uses the large sample to compute the Hα luminosity function and investigate its evolution from $z = 2.23$. Chapter 3 also details the morphological nature of these star-forming galaxies and

presents morphology-Hα luminosity relations. Chapter 4 presents a detailed clustering analysis of the sample, including the dependence of the clustering on Hα luminosity and other galaxy properties, and investigates the evolution of the clustering properties of Hα emitters over the last 11 Gyrs. Chapter 5 investigates the detailed roles of mass and environment at $z \sim 1$ and reconciles previous contradictory results in the literature. Chapter 6 presents the results from a double narrow-band emission-line survey for both Hα and [OII] emission lines at $z = 1.47$, comparing the evolution seen in both lines/luminosity functions, investigating [OII]/Hα line ratios as a function of galaxy properties and looking for redshift evolution. Chapter 7 describes the widest-area search for $z \sim 9$ Lyα emitters. Finally, Chapter 8 presents the conclusions and a brief discussion of open questions and future research directions.

Chapter 2

HiZELS

2.1 Overview and Goals

HiZELS is a panoramic extragalactic survey using the WFCAM instrument on the 3.8-m UK Infrared Telescope (UKIRT), having been allocated over 50 nights on UKIRT during 2007–2012. The survey uses a set of existing and custom-made narrow-band filters in the J, H and K bands to detect emission line galaxies at z = 1-9 over $\sim$ 7 square degrees of extragalactic sky, mostly in the UKIRT Infrared Deep Sky Survey (UKIDSS) Deep Extragalactic Survey (DXS) regions. Strong emission line galaxies include both star-forming galaxies and systems where Active Galactic Nuclei (AGN) contribute to significant line emission. The $H_2(S_1)$ narrow-band filter is used to target Hα emitting galaxies at z=2.23. In addition, custom narrow-band filters have been made. The J and H narrow-band filters target the [OII] emission line at 3727Å and the [OIII] line at 5007Å, in galaxies at the same redshift as the $z = 2.23$ Hα survey, and, even more importantly, they deliver identically-selected Hα samples at $z = 0.84$ and $z = 1.47$, respectively. The comparisons between the luminosity function, the clustering and variation with environment of these Hα-selected samples across z=0.8-2.2 will yield unique constraints on the evolution of star-forming galaxies. More speculatively, the J-band filter is sensitive to Lyα emission from galaxies at z=8.90 and could detect a few such sources if some of the current theoretical predictions are correct.

The primary HiZELS' goals are to:

- Measure the cosmic star formation history of the Universe using a single well-understood star formation indicator out to beyond the expected peak in the star formation history at z$\sim$2.

- Determine the clustering of star forming galaxies, and investigate any evolution in the shape or normalization of the Hα luminosity function with environment and morphology.
- Study the host galaxy properties of star forming galaxies across a wide range of redshifts to investigate how the star formation history of a galaxy depends upon its mass and environment.
- Identify the highest redshift known galaxies in the Universe, and use these to study the epoch of re-ionization.
- Compare the star formation properties of the Hα-selected galaxies with those selected in other multi-wavelength data-sets.

2.2 WFCAM: Filters and General Characteristics

The Wide Field Infrared Camera (WFCAM; Figures 2.1 and 2.2 Casali et al., 2007) is a near-IR wide-field camera for UKIRT. It consists of four 2048x2048 detectors with a pixel scale of 0.4″ and so covers a sky area of nearly 0.2 square degrees in a single pointing. The detectors are separated by nearly a full detector width, such that with four macro-stepped pointings a contiguous sky area of about 0.8 square degrees can be observed (see Figure 2.2). It has been designed specifically to carry out large-scale survey observations. Most of WFCAM observing is devoted to the UKIRT Infrared Deep Sky Survey (UKIDSS; Lawrence et al., 2007) and to four large Campaign Projects, of which HiZELS is one.

Figure 2.1: *Left* Observing at UKIRT, with the 4 monitors displaying raw frames coming out of the 4 different WFCAM cameras. *Right* A view of UKIRT inside the dome.

A typical observing night at UKIRT with WFCAM produces around 200 GB of data. A quick data processing at the telescope provides near real-time data quality assessment and initial science results, though the raw data is transfered to CASU at Cambridge for full off-line processing, and from there to the WFCAM Science Archive at the WFAU in Edinburgh. The WFCAM Science Archive is the primary data source for both UKIDSS results and PATT project data. Nevertheless, in our case, we do our own reduction (see reduction sections below), as CASU data reductions were optimised

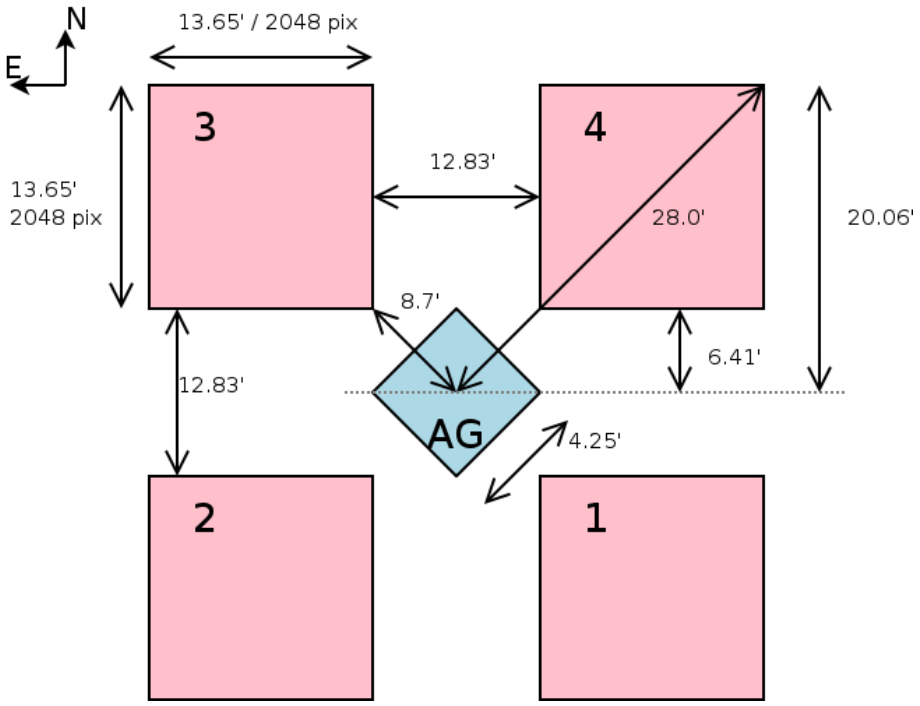

Figure 2.2: WFCAM schematic representation of its focal plane with the 4 cameras. Each paw-print probes an area of about 0.2 square degrees.

for broad-band data-sets (the vast majority of non-HiZELS observations) and performed relatively badly for narrow-band data-sets (although one should note that the CASU performance in reducing narrow-band imaging has improved greatly since 2007-08).

2.3 Observation Techniques

Observations conducted with WFCAM on UKIRT follow a basic procedure, in order to maximize its scientific use. However, some steps are specific to each Science program.

When conducting infra-red observations from the ground, one needs to be aware of the brightness of the sky. Obviously, sky subtraction is fundamental to obtain the data, but it is particularly difficult (when compared to the visible), as sky emission is both strong (orders of magnitude brighter than typical sources) and highly variable.

In order to be able to build flat frames, to perform a good sky subtraction, minimize artifacts and the effect of cosmic rays, many short exposures of the same sky region are obtained, and these are jittered (i.e. they cover slightly different regions of the sky, with small offsets). This jittering procedure (one can think of many different ways of doing this, from a simple A-B-A-B to many (~ 10 or more) different positions in the sky with a ∼few arcsec offsets in both X and Y) for conducting near-IR imaging is very effective in minimizing most of the problems one has to deal with imaging, and particularly in the near-IR.

Specific to HiZELS is the need to obtain imaging in two filters per band: a broad- and a narrow-

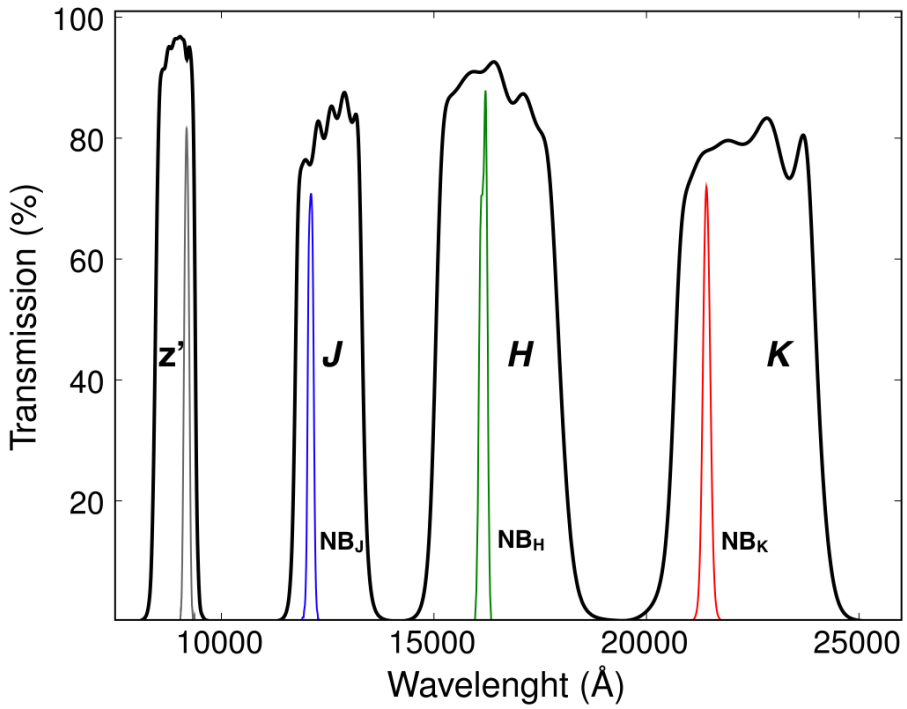

Figure 2.3: Total filter transmissions of the z, J, H and K broad band filters on WFCAM, UKIRT and total filter transmissions of the NB921 (see Chapter 6), J, H and K narrow-band filters used to look for emission-line sources.

band filter (see Figure 2.3), in order to be able to detect emission-lines and obtain reliable fluxes by subtracting the continuum that is still picked up by the narrow-band filter. While the broad and narrow filters have relatively similar central wavelengths (but not the same, and therefore small colour corrections are needed – see Section 2.9), their FWHMs are typically in the ratio 10:1, and therefore it is necessary to adjust the exposure times to take this into account. In practice, for HiZELS, broad band imaging is obtained with single 10 s exposures and narrow-band imaging with 100 s exposures, jittered with the same jitter pattern (small offsets in X and Y over 14 different positions).

2.4 Reduction Summary

Dark frames were median combined for each observing night and the individual science frames were then dark subtracted. Secondly, frames were median combined in each jitter sequence without correcting for the applied small offsets, to produce a rough first pass flat-field frame. The latter is then used to produce a badpixel mask for that particular sequence of frames. Each frame is then flattened, and a badpixel mask is produced for each frame, by searching for read-out problems and adding those to the more general badpixel mask.

Although the sky dominates the signal, objects which are too faint to detect on the raw frames still contribute and mean that the first pass flat field has slightly higher values at their locations. In order to produce better flats (so that the contribution from sources becomes negligible), SExtractor (Bertin

and Arnouts, 1996) was used to produce source masks, using the flattened combined frames from the first pass. These masks were used to filter out pixels significantly contaminated by sources, and, by combining masked frames for a given sequence, ultimately used to produce improved flat fields. The latter flats are used to flatten the data.

A world coordinate system is fitted to each frame by querying the USNO A2.0 catalogue. This fits, on average, $\sim$ 100 objects and rotates images appropriately, for each WFCAM camera. Frames are then de-jittered and co-added with SWarp (Bertin, 1998), which performs a background mesh-based sky subtraction optimized for our data. It should be pointed out that WFCAM frames suffer from significant cross-talk artifacts, which manifest themselves as toroidal features at regular (every 128) pixel intervals from sources, in the read-out direction. Furthermore, as these are linked to a "physical" location, they can only be removed from the source catalogue.

Narrow band and broad band images are photometrically calibrated by matching $11 < m_J(m_H) < 16$ stars from the 2MASS All-Sky catalogue of Point Sources (Cutri et al., 2003) which are unsaturated in narrow-band frames. As the custom filter lies in the J (or H) band, it is possible to check the zero-point offsets to be applied to the narrowband frames directly from the broadband calibration, taking into account the relative widths of the filters, such that the offset between the zeropoints is $-2.5log\frac{\Delta\lambda_{BB}\times\Delta t_{BB}}{\Delta\lambda_{NB}\times\Delta t_{NB}}$, where BB and NB refer to the broad and narrow band frames. On the other hand, it is easy to confirm that BB-NB $\sim$ 0 as expected, using the photometry of bright stars. Based on the photometric calibration, the magnitude calibration should be good to $< 3\%$ (from the scatter), when compared to 2MASS. For convenience, narrow and broad band images are then leveled (in flux), leading to the same zero-points in both.

2.5 The Data Reduction Pipeline: PfHiZELS

The Pipeline for HiZELS (PfHiZELS) is a top level python script written by me which calls all the other necessary scripts in order to implement a complete reduction for our WFCAM data. Also, it allows the user to run a selection of tasks for certain dates or fields. It has been built upon a rudimentary set of scripts developed by Jim Geach in Durham (see below for a complete description of the improvements and for a description of what was completely new; key: ** new, * major modifications, () little or no changes), which were improved, optimised and linked so that they can be run either in a general sequence, a user-selected sequence, or still just on their own. Apart from that, many new tasks and scripts were written and developed, including several science-analysis tools such as removing the frames regions with very poor signal, aligning narrow-band frames with the broad-band frames, flux leveling, and an automated way to run SExtractor, producing a complete catalogue of the sources for the entire field(s).

The pipeline is mostly written in Python, taking advantage of packages such as numpy, pyfits, and numarray (along other general packages). It also uses separate software packages such as SExtractor (Bertin and Arnouts, 1996), SWarp and WCStools. It was written so that it can be run in almost any

computer.

2.6 Main Tasks

The latest version of the pipeline implements the following reduction steps (chosen by the user; ** new, * major modifications, () little or no changes):

Book-keeping

- Adjust to computer, set paths and directories **
- Data download from the raw WFCAM archive to a specific directory **
- Decompress and organize the downloaded data *
- Reset astrometry in headers
- List observations **

First-pass

- Find dark frames, median combine them, dark subtract the raw frames *
- Separate the frames by field within each night **
- Combine frames in each calculated jitter pattern to make first pass flat fields *
- Flatten the frames *
- Use first pass flat field to make a bad pixel mask together with an individual bad-pixel mask for each frame (looking for read-out effects) *

Masking and Second-pass

- Use flattened frames to make a mask for each frame using SExtractor *
- Make a second pass flat using unmasked pixels only **
- Flatten the raw frames **

Astrometry, Sky Subtraction and Co-adding

- Run WCStools to get good astrometry in each frame
- Sort frames according to object, filter and exposure time in appropriate folders **
- Mask bad pixels from frames **
- Make an exposure map **
- Median combine frames using SWarp after sky subtraction **

Photometry and Catalogue Production

- Calculate Zero Point and level broad and narrow band images using 2MASS *
- Extract sources and produce a final catalogue removing cross-talk artifacts *

It should be noted that the pipeline was designed to be able to run all the tasks in a row, without any human intervention (the last tasks being the exception, as they must be checked and confirmed due to their importance for the production of good results), though it can be run by tasks, separately. Also, the individual scripts that the top-level script calls can all be used for other purposes, individually.

One of the main aims of having a fully functional pipeline is to provide completely systematic and repeatable reductions for different datasets reduced in different locations. However, doing that can be quite problematic. Because each computer/operating system/location has its own definitions, paths and software, incompatibilities arise very often. Thus, having a simple and working solution for dealing with those problems is very important. With this in mind, the very first book-keeping step was introduced in the general pipeline. It can set most of the parameters, paths and directories for the user, to assure that the remaining scripts will run without major problems. This zero-script will run on any machine with any version of python, and will will output notices regarding the best versions of the software called by the pipeline. The user is then free to follow the recommendations, or just try to use the local versions of all software.

2.7 Cross-check of pipeline performance

When writing a pipeline for dealing with such a large amount of data as we did, it is important to check whether the automated reduction is producing results with the quality needed for our science goals. Thus, a thorough look into each tasks' products was done, together with a direct comparison with a detailed IRAF reduction in one field (COSMOS).

When comparing the final results with the IRAF-based reduction, we find that the pipeline is at least comparable, and in some aspects even better, whilst it is also much less time-consuming (to a factor of 10 less), and completely automated. A detailed visual inspection of both final reduction products reveals that there were no major differences across most of the images. However, the pipeline reduction was able to reduce cross-talk issues, and to deal better with very bright objects which saturate on the individual frames.

Source extraction and catalogue production (see Section 2.8) was done for both sets of data. The aim was to compare how similar the photometry would be for the different reduction methods and how that would affect the final results. In the end, it was easy to conclude that the average change in magnitude was lower than ~ 0.01 mag, with a small standard deviation (~ 0.06 mag) at the faint end. Moreover, the selection of potential line emitters also yielded very similar results, with over 95 % of sources common to both data-sets and the same photometric redshift distribution.

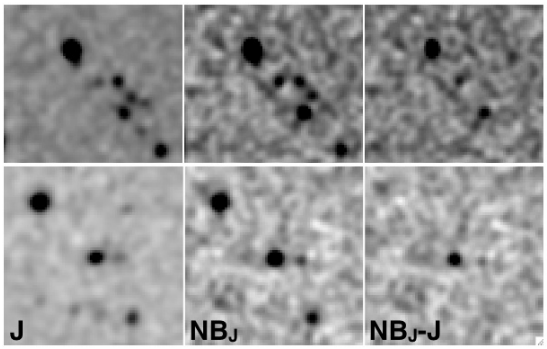

Figure 2.4: Two narrow-band excess objects selected from the NB_J imaging with different colour significances (upper panels), and a strong isolated emitter (lower panels). Images are $\sim 20'' \times 20''$.

2.8 Catalogue Production

Sources were extracted using SExtractor (Bertin and Arnouts, 1996). Optimal parameters were found by running a large number of different extractions which converged to a set of parameters that allowed the extraction of all obvious sources down to the 3-σ limit in each frame and minimized the extraction of noise/artifact features. The extraction included an optimized sky subtraction, and fixed photometry apertures of $3''$ (diameter) were used. Several tests were done using SExtractor in dual mode (using frames in one band to detect the sources and measuring on the other band) and single mode. The first option was used for fields where data were taken in both bands and so the frames were extremely well-registered, while for fields where UKIDSS data were used for the broad-band, the extraction was done on both bands independently, followed by a match using a simple $2.0''$ criteria. In the small number of cases where there was more than one match, a careful local astrometry solution was calculated based on nearby sources clearly identified in both bands and the correct source was then clear in all cases (the correct match was always the original closest). Furthermore, tests were run on COSMOS frames (a field where HiZELS data were taken in both bands) to show that both options produce comparable samples, and so this is not likely to produce any significant difference between the extraction in different fields. Narrowband sources with no clear broad-band detection were retained but there are few of these as the broad-band coverage is generally significantly deeper than the narrow-band. As the observations often have slightly different FHWMs, different total exposure times, and because each WFCAM chip has slightly different properties, objects were extracted down to each chip's limit and the analysis is done on a chip-by-chip basis.

In order to clean spurious sources from the catalogue (essential to remove cross-talk artifacts), the frames were visually inspected showing that sources brighter than ~ 12 mag are surrounded by large numbers of artifacts detected within "bright halos", as well as cross-talk, while fainter sources (up to 16 mag) show only cross-talk features. Sources fainter than 16 mag do not produce any detectable cross-talk at the typical depth of the observations. Cross-talk sources and detections in the halo regions were removed from the catalogue separately for each frame, which greatly simplifies their identification (Geach et al. 2008).

When combining the catalogues from each individual WFCAM chip into a global catalogue for each field, sources detected in regions with less than 85% of the total integration time were removed; this still ensures a complete overlap between frames. When a source was catalogued in more than one final image, the catalogue entry with a higher exposure time was selected.

2.9 Narrowband excess selection

Emission line systems are initially selected according to the significance of their ($BB-$NB) colour, as they will have ($BB-$NB) > 0. However, true emitters need to be distinguished from those with positive colours due to scatter in the magnitude measurements and this is done by quantifying the significance of the narrowband excess. The parameter Σ quantifies the excess compared to the random scatter expected for a source with zero colour (Bunker et al., 1995). In other words, a source can be considered to have a genuine narrow-band excess if:

$$c_{NB} - c_{BB} > \Sigma\delta \tag{2.1}$$

where $c_{\rm NB}$ and c_{BB} are the (normalized) counts for the NB and BB bands (see Section 2.4), respectively, and δ is the combined photometric error:

$$\delta = \sqrt{\pi r^2(\sigma^2_{\rm NB} + \sigma^2_{BB})}, \tag{2.2}$$

where r is the radius of the apertures used and $\sigma_{\rm NB}$ and σ_{BB} are the standard deviation per pixel (in normalized counts per pixel) measured in the NB and BB individual images, respectively. The approach is similar to a standard signal-to-noise selection. Colour and Σ significances are related by:

$$BB - {\rm NB} = -2.5\log(1 - \Sigma\delta 10^{-0.4(ZP-{\rm NB})}), \tag{2.3}$$

where ZP is the zeropoint of both frames, assuming that the sky variation is the dominant feature contributing to the errors in photometry. This has been tested by measuring counts in randomly placed apertures (~ 10000 for each frame), confirming the hypothesis.

As the NB filter does not generally fall at the centre of the BB filter, objects with different colours may have non-zero BB-NB colours due to differential contribution of their continuum emission. This will affect the selection of emission line objects, but can be corrected for by considering the broad-band colours of each source; these will be discussed for each BB+NB filter combination separately in the relevant chapters.

The flux of an emission line, $\rm F_{line}$, and the equivalent width, $\rm EW_{line}$, can then be expressed as:

$${\rm F_{line}} = \Delta\lambda_{NB}\frac{f_{NB} - f_{BB}}{1 - (\Delta\lambda_{NB}/\Delta\lambda_{BB})} \tag{2.4}$$

and

$${\rm EW_{line}} = \Delta\lambda_{NB}\frac{f_{NB} - f_{BB}}{f_{BB} - f_{NB}(\Delta\lambda_{NB}/\Delta\lambda_{BB})} \tag{2.5}$$

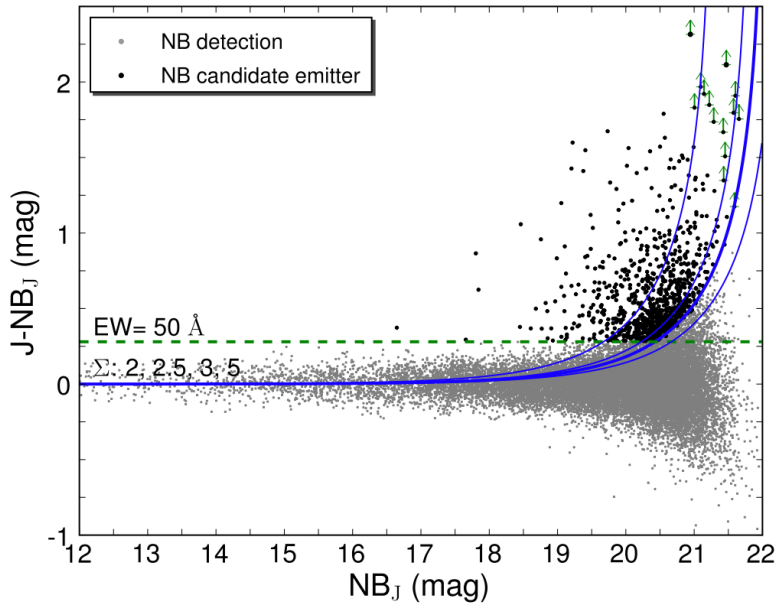

Figure 2.5: Example of the narrow-band emitters selection, showing $> 3\sigma$ detections in the NB$_J$ image. The curves represent Σ significances of 5, 3, 2.5 and 2, respectively, as defined in the text (for an average depth). The dashed line represents an equivalent width cut of 50Å. Candidate narrow-band emitters are plotted in black. Emitters with no clear J-band detection are assigned a 3-σ upper limit.

where $\Delta\lambda_{NB}$ and $\Delta\lambda_{BB}$ are the widths of the broad and narrow-band filters, and f_{NB} and f_{BB} are the flux densities measured for each band. EW$_{\rm line}$ is simply the ratio of the line flux and continuum flux density.

The selection of emission-line candidates is done imposing two conditions. Firstly, the NB sources are considered candidate emitters if they present a colour excess significance of $\Sigma > 2.5$. Secondly, only NB detections with a sufficiently high EW are selected (see Figure 2.5). This is done to avoid including bright foreground objects with a large significance and a steep continuum across the BB (e.g. van der Werf et al., 2000), and was chosen to reflect the general scatter around the zero colour a bright magnitudes. A comparison with spectroscopic data (see Section 3.6) indicates that these criteria maximise the completeness of the sample without introducing a significant number of false emitters. Figure 2.5 shows an example of a colour-magnitude diagram with the selection criteria. Figure 2.4 presents two examples of emitters.

2.10 Fields

Chosing the best targets is essential towards achieving the survey goals, especially because we intend to complement our observations with deep multi-wavelength data. This allows us to either confirm redshifts or estimate them photometrically. Most importantly, these high-quality data allow us to provide very good estimates of fundamental galaxy properties such as masses, colours and morphologies, at the same time that they allow us to select and study underlying populations. For those reasons,

COSMOS (Scoville et al., 2007; Capak et al., 2007) and UKIDSS-UDS (Lawrence et al., 2007) were the primary two fields targeted by HiZELS, and all data in this thesis were taken in those fields.

2.10.1 UKIDSS UDS

The UDS is a 0.8 square degree field centered on the Subaru-XMM Deep Survey (J0218-05), with a wealth of multiwavelength data (see Figure 2.6). The current UKIRT data release for the ESO community is DR8, released in October 2010. Data Release 3 was made World public in July 2009, and is used for the bulk of this thesis. The latest release (near-infrared data taken on UKIRT) reaches 25 mag in both J and H, and 24.5 in K (5σ in AB). Depth estimations are based on noise measurements within randomly placed 2" apertures across the entire field.

The field has deep Subaru imaging data with 5σ (AB) limiting magnitudes of 27.5 (B), 26.7 (V), 27.0 (R), 26.8 (i), 26.9 (z). These data have been obtained using 5 separate Suprime-cam pointings which largely overlap the UKIDSS field between them (see Figure 2.6). The field has also been targeted by a wide range of telescopes and instruments, which is briefly presented now (from short to long wavelengths). X-ray data, as part of the SXDS, is available from the XMM-Newton Survey Science Centre in the 2XMM. There are 7 contiguous fields with a total exposure of 400 ks covering most of the area. U-band data from CFHT Megacam have also been obtained. Further data include Spitzer observations as part of SWIRE. Much deeper data has recently been obtained from a Spitzer Legacy survey, with 292 hours of observation using IRAC and MIPS, reaching 24 mag (AB) at 3.6 and 4.5 μm (5σ). Submillimetre data are also available from the SHADES survey of the central region of the UDS field and the field is the location of the SCUBA2 cosmology Legacy Survey. There are also VLA radio data at 1.4 GHz to a depth of 12-20 μJy per beam. Finally, a large redshift survey is currently underway at the VLT (an ESO Large Programme) to obtain redshifts for a representative sample of 4500 galaxies at $z > 1$ using the VIMOS and FORS2 spectrographs.

2.10.2 COSMOS

COSMOS is a Hubble Space Telescope (HST) Treasury Project which covers a 2 square degree equatorial field with the Advanced Camera for Surveys (ACS). It is the largest survey that HST has ever done, utilizing 10% (640 orbits) of its observing time over the course of two years (HST Cycles 12 and 13). The COSMOS field has now been targeted by a wide range of telescopes and instruments and data have been obtained in more than 30 bands, from the shortest (X-rays) to the longest (radio) wavelengths, clearly making this field the best well-studied $\sim 1-2\,\mathrm{deg}^2$ field.

The field has been observed in 20 Suprime-cam (on the Subaru telescope) broad-, medium- and narrow-bands. The 5σ (AB) limiting magnitudes of the broad-band imaging are: 27.4 (B), 27.2 (V), 26.9 (R), 26.9 (i), 26.3 (z), and the imaging data cover the full HST coverage. The COSMOS field also has very deep u band data, obtained with Megacam on the CFHT, reaching a 5σ depth of 26.5 AB; it also has full FUV (1500 Å) and NUV (2300 Å) coverage from GALEX (reaching depths of ~ 26 AB).

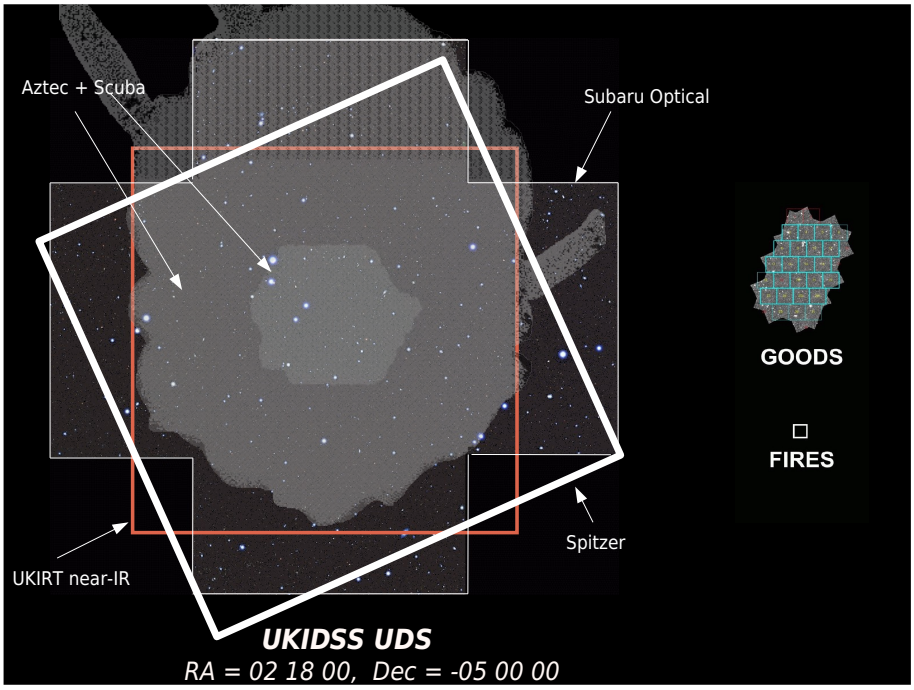

Figure 2.6: UDS Coverage and comparison with other fields.

Near-infrared data is available from WFCAM on UKIRT (J$\sim$ 23.7, 5σ, AB) and from WIRCAM (H and K $\sim$ 24, 5σ, AB). The field has deep IRAC data in the four bands, reaching $\sim$ 24 AB in the 3.6 μm band. X-ray, radio and submillimetre data has also been obtained in the field, together with a very large spectroscopic survey (zCOSMOS, Lilly et al. 2009), targeting over 20 000 galaxies.

Chapter 3

The nature of star-forming galaxies at $z = 0.84$

This Chapter presents the results of deep narrow-band imaging using the NB_J filter at $\lambda = 1.211\mu$m, as part of HiZELS, over $\sim 0.7\,\mathrm{deg}^2$ of the SXDF Subaru-XMM–UKIDSS Ultra Deep Survey (Lawrence et al., 2007) field (UDS), and $\sim 0.8\,\mathrm{deg}^2$ in the Cosmological Evolution Survey (Scoville et al., 2007; Koekemoer et al., 2007) field (COSMOS). This corresponds to an area coverage which is ~ 8 times larger and twice the depth of the survey by Villar et al. (2008), the best previous emission-line survey at $z \sim 1$. The results presented in this Chapter are published in Sobral et al. (2009a).

3.1 Observations

Both fields were observed with WFCAM on UKIRT using a set of custom narrow-band J filters ($\lambda = 1.211\mu$m, $\Delta\lambda = 0.014\mu$m), during 2007 January 13–17 and February 13,14 & 16 for the COSMOS field and October 19–24 for UKIDSS UDS. WFCAM's standard "paw-print" configuration of four 2048×2048 $0.4''\,\mathrm{pixel}^{-1}$ detectors offset by $\sim 20'$ can be macrostepped four times to cover a contiguous region of $\sim 55' \times 55'$ (Casali et al., 2007). For each field (COSMOS and UDS) 4 paw-prints, or $\sim 0.8\,\mathrm{deg}^2$ were mapped with narrowband exposures of $\sim 21\,\mathrm{ks\,pixel}^{-1}$. The seeing varied between 0.8–1.0$''$ during the observing nights, and conditions were photometric. The NDR (Non Destructive Read) mode was used for all narrow-band observations to minimise the effects of cosmic rays in long exposures. The observations were obtained following a 14-point jitter pattern for UDS (to match the UKIDSS observing strategy) and a 9-point jitter sequence for COSMOS. Broad-band J-band observations were also obtained in the COSMOS field, but were not necessary for the UDS due to the

availability of UKIDSS data. A summary of the observations is given in Table 3.1.

Data reduction was done using PfHiZELS (see Chapter 2).

3.1.1 Source Extraction and Survey Limits

The survey is made up of a mosaic of eight WFCAM pointings (4 each for UDS and COSMOS), i.e., $8 \times 4 \times 13.7' \times 13.7'$ tiles. The UKIDSS UDS J-band image does not overlap entirely with the full narrow-band image, leading to a total overlapping area of $0.70\,\mathrm{deg}^2$, while for COSMOS the overlap is $0.78\,\mathrm{deg}^2$.

Sources were extracted using SExtractor (Bertin and Arnouts, 1996) in dual mode (see Chapter 2), for the COSMOS field (where data were taken in both bands and so the frames were extremely well registered), and single mode for UDS (where UKIDSS data was used for the J band), followed by a match using a simple $2.0''$ criteria. In 11 cases there was more than one match; for these, a careful local astrometry solution was calculated based on nearby sources clearly identified in both bands and the correct source was then clear in all cases (the correct match was always the original closest). Objects were extracted down to each chip's limit, which was then confirmed using Monte Carlo simulations (see Chapter 2 and Section 7.5). Cross-talk sources and detections in the halo regions were removed from the catalogue separately for each frame, which greatly simplifies their identification (see Chapter 2). Catalogue sources detected in regions with less than 85% of the total integration time were removed and when a source was catalogued in more than one final image, the catalogue entry with a higher exposure time was selected.

The average 3-σ depth of the entire set of NB_J frames is 21.6 mag, with J depths being $J = 23.4$ mag (UKIDSS UDS DR3) and $J = 22.7$ mag (COSMOS). The narrow-band imaging detects a total of 21773 objects in COSMOS across $0.76\,\mathrm{deg}^2$ and 15449 in UDS across $0.68\,\mathrm{deg}^2$. These areas include the removal of regions in which cross-talk and other artifacts caused by bright objects are located; see Chapter 2.

3.2 Selection

Emission line systems are initially selected according to the significance of their $(J - \mathrm{NB}_J)$ colour, as they will have $(J - \mathrm{NB}_J) > 0$. However, true emitters need to be distinguished from those with positive colours due to scatter in the magnitude measurements and this is done by quantifying the significance of the narrowband excess (see Chapter 2).

As the NB_J filter does not fall at the centre of the J-band, objects with redder colours will tend to have a negative $(J - \mathrm{NB}_J)$ colour, while bluer sources will have $(J - \mathrm{NB}_J) > 0$. This will affect the selection of emission line objects, but can be corrected for by considering the broad-band colours of each source. To do this, $(J - \mathrm{NB}_J)$ was plotted as a function of $(z - J)$ (COSMOS) or $(J - K)$ (UDS) colour and a linear fit was derived, determining trends with a slope of $(J - \mathrm{NB}_J) \sim 0.06(J - K)$ for UDS and $(J - \mathrm{NB}_J) \sim 0.11(z - J)$ for COSMOS. This was then used to correct the J magnitudes and

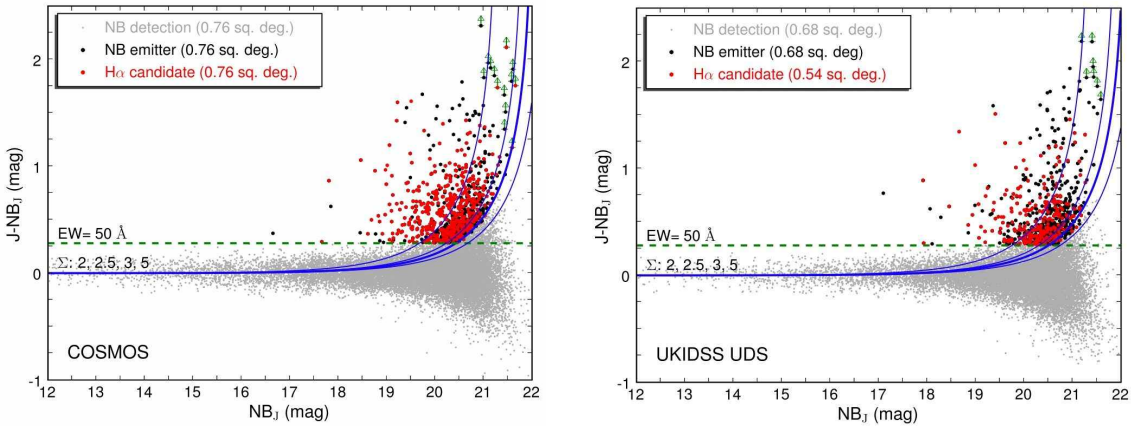

Figure 3.1: Colour-magnitude plots for COSMOS (left panel) and UDS (right panel) showing all $> 3\sigma$ detections in the NB$_J$ image. The curves represent Σ significances of 5, 3, 2.5 and 2, respectively, as defined in the text (for an average depth). The dashed line represents an equivalent width cut of 50Å. All selected narrow-band emitters are plotted in black, while candidate Hα emitters (selected using photometric redshifts from Mobasher et al. 2007 for COSMOS and Cirasuolo et al. 2008 for UDS) are plotted in red. Emitters with no clear J-band detection are assigned a 3-σ upper limit.

thus the resultant $(J-\mathrm{NB}_J)$ colours. Sources with no z or K data – either because they are too bright or too faint – were corrected assuming a median colour (based on sources at similar magnitudes).

The selection of emission-line candidates is done imposing two conditions. Firstly, the NB$_J$ sources are considered candidate emitters if they present a colour excess significance of $\Sigma > 2.5$. Secondly, only NB$_J$ detections with $\mathrm{EW_{line}} > 50$Å (corresponding to $(J-\mathrm{NB}_J) > 0.3$) are selected. This is done to avoid including bright foreground objects with a large significance and a steep continuum across the J band (e.g. van der Werf et al., 2000), and was chosen to reflect the general scatter around the zero colour a bright magnitudes. A comparison with spectroscopic data (see Section 3.6) indicates that these criteria maximise the completeness of the sample without introducing a significant number of false emitters. Figure 3.1 shows the colour-magnitude diagrams with the selection criteria for COSMOS and UDS, respectively. Figure 2.4 presents two examples of emitters.

3.3 Complete sample

Narrow-band detections below the 3-σ threshold were not considered. When there was no $> 3\sigma$ J-band detection, a 3-σ upper limit for the $(J-\mathrm{NB}_J)$ colour was computed, as shown in Figure 3.1. The average 3-σ line flux limit over both fields is $8 \times 10^{-17}\,\mathrm{erg\,s^{-1}\,cm^{-2}}$. The complete sample has 1517 excess sources out of all 37222 NB$_J$ detections in the entire area, with 824 being detected in COSMOS (corresponding to 1084 emitters per deg^2) and 693 in UDS (1020 emitters per deg^2). The potential emitters were all visually inspected in both J-band (when detected) and NB$_J$, and 48 were removed from the sample as they were flagged as spurious. The majority of these (34) correspond to artifacts caused by bright stars that are on the edges of two or more frames simultaneously. The

Table 3.1: Observation log for the NB_J and J observations of the COSMOS and UKIDSS UDS fields.

Field	Filter	R.A. (J2000)	Dec. (J2000)	Int. time (ks)	FHWM ($''$)	Dates (2007)	m_{lim} (3σ)
COSMOS 1	NB_J	10 00 00	+02 10 30	19.7	1.0	14–16 Jan	21.7
COSMOS 2	NB_J	10 00 52	+02 10 30	21.6	1.0	13, 14 Jan	21.6
COSMOS 3	NB_J	10 00 00	+02 23 44	19.0	0.9	15–17 Jan	21.7
COSMOS 4	NB_J	10 00 53	+02 23 44	17.2	0.9	15, 17 Jan, 13–16 Feb	21.6
COSMOS 1	J	10 00 00	+02 10 30	5.7	0.9	14–16 Jan	22.8
COSMOS 2	J	10 00 52	+02 10 30	6.9	1.0	13, 14 Jan	22.8
COSMOS 3	J	10 00 00	+02 23 44	5.7	0.9	15–17 Jan	22.8
COSMOS 4	J	10 00 53	+02 23 44	5.1	0.9	15, 17 Jan, 13–16 Feb	22.6
UDS NE	NB_J	02 18 29	−04 52 20	21.2	1.0	18, 20 Oct	21.6
UDS NW	NB_J	02 17 36	−04 52 20	22.6	1.0	19, 21 Oct	21.7
UDS SE	NB_J	02 18 29	−05 05 53	20.0	1.0	19 Oct	21.5
UDS SW	NB_J	02 17 38	−05 05 34	22.5	1.0	20, 21 Oct	21.6

remaining 14 sources removed were low S/N detections in noisy regions of the NB_J image.

3.4 Photometric redshift analysis

In order to select Hα emitters at $z = 0.84$, one needs to separate them from other line emitters at different redshifts. The detection of Hβ and [OIII] 5007 emitters at $z \sim 1.4$–1.5 is expected, together with [OII] 3727 at $z = 2.23$ and other emission lines. Multi-wavelength data, photometric and spectroscopic redshifts available for both COSMOS (Mobasher et al., 2007; Lilly et al., 2009) and UDS (Cirasuolo et al., 2010) are therefore used to distinguish between different emission lines and also to evaluate how robust the emitter selection criteria are. In order to do this, photometric redshifts for the emission line candidates were taken from the photometric redshift catalogues for COSMOS and UDS (Mobasher et al., 2007; Cirasuolo et al., 2010). For UDS, the overlap with the photometric redshift catalogues reduces the area coverage to $0.54\,\mathrm{deg}^2$ due to the required overlap with Subaru optical data and further masking around bright stars: 133 sources are "lost" as they are in the excluded area. In addition, for 14 sources photometric redshifts are not available in the catalogues due to i/K_s magnitude limits (3 in COSMOS, 11 in UDS): while these appear to be real sources (although there is a chance they are spurious), they are likely to be at redshifts higher than $z = 0.84$ and so are excluded from this analysis of Hα emitters. The photometric redshift matches result in a final sample of 1370 excess sources (821 in COSMOS, 549 in UDS) meeting all of the selection criteria across a total of $1.30\,\mathrm{deg}^2$.

The photometric redshifts in COSMOS are particularly good for selecting Hα emitters at $z = 0.84$

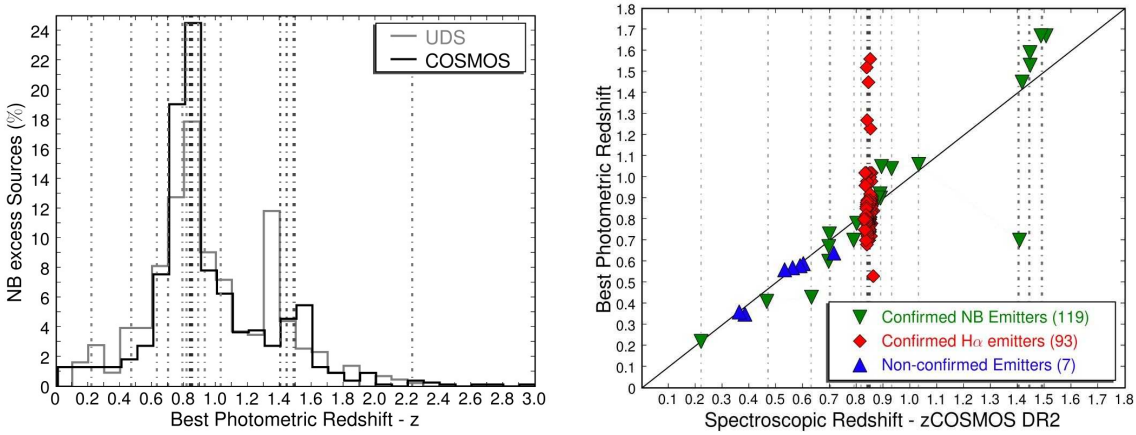

Figure 3.2: The left panel shows the photometric redshift distribution (peak of the probability function for each source) for the selected excess sources for COSMOS and UDS. Both distributions peak at $z \sim 0.85$, as expected, thus implying that the great majority of the selected sources are Hα emitters. The right panel shows the best photometric redshifts plotted against the spectroscopic redshifts for the emitters with accurate redshifts (reliability $> 95\%$) measured in the z-COSMOS DR2 dataset. Dash-dotted lines indicate the redshifts at which emission lines are matched with the NB$_J$ filter and these are the same in both figures (the width of the lines scales with the fraction of confirmed emitters; see Table 3.2 for more details). The great majority of potential emitters is confirmed to be real and only a small fraction ($\sim 6\%$) was not confirmed.

as the available data are ideal to probe the 4000Å break at that redshift. The deeper near-infrared data used in the UDS photometric redshifts provide better accuracy for higher redshift sources, and are accurate enough to probe the proportion of $z \sim 1.4$–1.5 [OIII] 5007 and Hβ emitters. Photometric redshifts for COSMOS present $\sigma(\Delta z) = 0.03$, where $\Delta z = (z_{phot} - z_{spec})/(1 + z_{spec})$. The fraction of outliers, defined as sources with $\Delta z > 3\sigma(\Delta z)$, is lower than 3%, based on results from z-COSMOS (see Section 3.6). For UDS, the photometric redshifts have $\sigma(\Delta z) = 0.04$, with 2% of outliers.

Figure 3.2 shows the photometric redshift distribution for the selected narrow-band emitters in COSMOS and UDS, demonstrating very good agreement between the two fields, despite the completely different photometric analyses – done with different codes, bands and by completely independent teams. Both samples peak at $z \sim 0.85$, implying that the majority of the narrow-band excess sources are indeed Hα emitters. In addition to this, there is another peak at $z \sim 1.4$–1.5 in UDS and the same – but at a slightly higher photo-z – in COSMOS. This is interpreted as a significant population of [OIII] 5007 emitters at $z \sim 1.4$ and/or Hβ emitters at $z \sim 1.5$. However, the photometric redshifts are not accurate enough to clearly distinguish between these two populations, and thus the slight difference between UDS and COSMOS might be just caused by the use of different bands and methods giving different performance at $z > 1$.

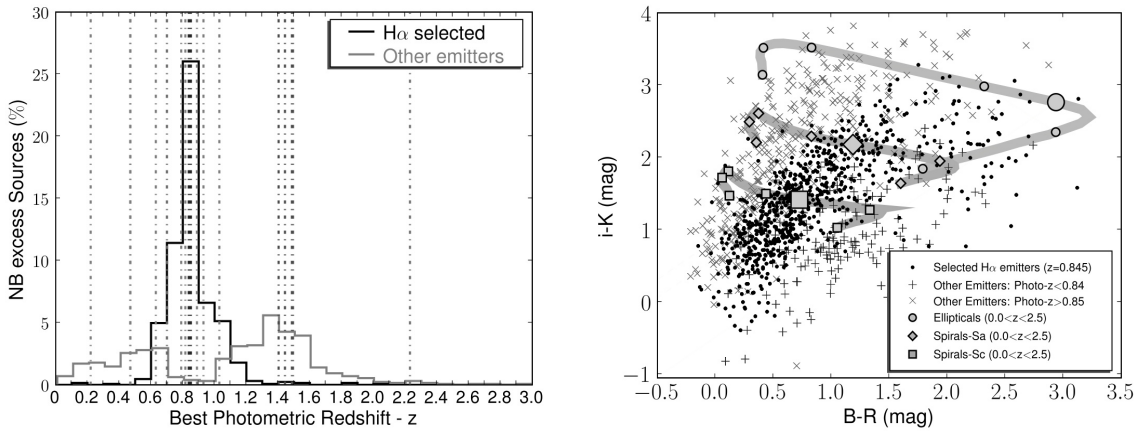

Figure 3.3: The left panel shows the photometric redshift distribution (peak of the probability function for each source) for the selected Hα emitters (see Section 3.5) and the remaining emitters, with the spectroscopically confirmed lines plotted as in the left panel of Figure 3.2. The right panel presents a BRIK colour-colour diagram, clearly distinguishing the high-redshift emitters from the low-redshift emitters, and also the Hα emitters from these two populations. Overlaid on the plot are evolutionary tracks for different galaxy models, drawn from Poggianti (1997); small symbols on the tracks mark steps of 0.5 in redshift from 0 to 2.5, whilst the larger symbol indicates z=0.84. The observed colours for the H-alpha emitters are consistent with them being mostly star-forming galaxies at z=0.84, whilst the colours of the other emitters also lie in the expected regions.

3.5 Selecting Hα emitters at $z = 0.84$

The sample of candidate Hα emitters at $z = 0.84$ is derived by considering not only the best-fit photometric-redshift for each source, but also more extensive information contained within the photometric redshift probability distribution. In particular, the Hα candidates are defined to be those sources with $z_{min} < 0.845 < z_{max}$ (where z_{min} and z_{max} are the 1-σ redshift limits of the principle peak in the photometric redshift probability distribution). For COSMOS, the photometric redshift selection produces a sample of 477 potential Hα emitters, while for UDS the same procedure yields 270 sources (see Section 3.4 for details).

While it is true that this selection can potentially introduce some biases, a careful comparison of the selected Hα emitters and the remaining emitters shows no evidence for such an effect. The emission line equivalent width distributions of the selected Hα and non-Hα emitters are statistically indistinguishable. The sample of non-selected emitters does contain objects which have slightly fainter magnitudes (and correspondingly fainter emission lines) than the selected Hα emitters, but the colours of these fainter galaxies are clearly consistent with them simply being at higher redshift (e.g. [OIII], Hβ or [OII] emitters): they are typically detected at a $\sim$20-30 σ (or higher) level in the optical images, and thus it should not be any inaccuracy in the photometric redshifts which affects their selection. One can also see that the photometric redshift distribution in Figure 3.3 (left panel) is clearly different between the selected Hα emitters and the remaining emitters, revealing both a population of lower and higher redshift. The right panel of Figure 3.3 also reveals that the Hα selected emitters present colours

which clearly distinguish them from the low-z and higher-z samples of emitters – they also occupy a region in the colour-colour diagram where one expects to find star-forming galaxies at z=0.84. Finally, as examined below, spectroscopic redshifts for $\sim$ 25% of the sample in COSMOS show that only a negligible fraction of the Hα emitters are being missed by the photometric redshift selection.

3.6 Spectroscopic redshifts and selection robustness

Both COSMOS and UDS have large spectroscopic surveys underway, but only a limited fraction of those spectroscopic redshifts is currently available. Nevertheless, for the z-COSMOS survey (Lilly et al., 2009) Data Release 2 (DR2), the match with the sources detected on the NB$_J$ frames yields 4600 sources (using a 1.0$''$ match criteria), of which 138 (each matching only one z-COSMOS source) have been selected as excess sources and hence potential emitters. Twelve of these have unreliable or non-existent redshift determinations. Of the remaining 126, the vast majority (119) have redshifts which place an emission line within the NB$_J$ filter (see Table 3.2 for the detailed list of emitters), confirming the narrow-band excess as an emission line. For the other 7 sources, it was not possible to identify any emission line falling into the NB$_J$ filter. Spectra for these sources were analysed in order to look for potential errors in the redshift determination. In fact, while redshifts for 5 of them are very robust, one source, identified as $z \sim 0.4$, seems better fitted by being at $z = 0.85$ (with [OII] 3727 being detected, while the fit at lower redshift assumes an emission line where fringing starts to become an issue in the spectrum). The remaining source contains one emission line (identified as [OII] 3727) but with a low signal to noise (S/N$<$ 2.0). These 7 sources all have a colour excess significance $\Sigma = 2.5$–3.0, and at least the 5 robust cases represent the galaxies expected to be randomly scattered into the candidate emitter list at these low Σ values. All of the candidate emitters with $\Sigma > 3.0$ were confirmed to be real. It is also worth noticing that z-COSMOS DR2 is highly biased towards $z < 1$ sources, which means that its completeness for potential interlopers (which are more likely to be in this redshift range) is very high, while at the same time it misses most of the emitters at higher redshift. Therefore, the contamination rate within the sample of emitters (i.e., the fraction of non-emitters) is likely to be lower than $\sim$ 6%, even down to $\Sigma = 2.5$.

Tests regarding the selection criteria used were also done by selecting samples with different colour significances and different equivalent width cuts, and comparing the matches for each selection criteria with z-COSMOS DR2. As expected, the number of potential interlopers declines rapidly with an increasing colour significance threshold, but so does the sample size. The sample with the largest number of real emitters whilst returning a low ratio between potential interlopers and real emitters is obtained using $\Sigma \sim 2.5$ and an equivalent width cut of $\sim$ 50Å, therefore indicating that the selection criteria used are producing reliable results.

Table 3.2 compares the spectroscopic selection of line emitters with the selection from the photometric redshift catalogue. It can be seen that 88 of the 93 Hα emitters are correctly identified ($\sim$ 95% completeness). On the other hand, 2 non-Hα emitters (with fluxes which do not deviate significantly

Table 3.2: Spectroscopic redshifts matches (from z-COSMOS DR2) for the narrow-band excess objects. The first column of the table indicates the emission line producing the narrow-band excess, based on the accurate spectroscopic redshifts which place such lines within the narrow-band filter. The remaining columns present the mean redshift, the number of emitters and the number of those selected as Hα using the photometric redshift selection (see Section 3.4).

Emission Line	λ (Å)	$< z >$	Number	Selected as Hα
Hα	6563	0.845	93	88
Hβ	4861	1.49	2	0
[OIII]	5003	1.42	4	1
HeI	5876	1.04	1	0
[OI]	6363	0.89	4	0
[SII]	6717	0.79	2	1
[ArIII]	7135	0.70	3	0
[OII]	7325	0.63	1	0
HeII	8237	0.47	1	0
CI	9830	0.22	1	0
Unidentified			7	0

from the median) were found in the photometric redshift selected sample (implying a $\sim 98\%$ reliability), with one of those being a [SII] 6731 emitter. Because this line is very close to Hα it is very difficult to completely distinguish these emitters with photometric redshifts alone. However, as seen by the sample which has been presented, the total contamination by these will be very small ($< 2\%$). The spectroscopic data were used to improve the Hα catalogue, removing the 2 non-Hα emitters and including those 5 which had not been selected by the photometric redshifts. These few sources present mean and median fluxes slightly higher than the rest of the sample, suggesting that some bright Hα emitters could be lost by a photometric redshift selection, due to the emission line contribution to the broad-band fluxes. However, as the brighter Hα emitters are likely to contain strong emission lines in the visible ([OII] 3727, Hβ and [OIII] 5007), these targets should have a very high completeness in z-COSMOS, so this can be interpreted as an upper limit. As these emitters are introduced into the sample, no further specific correction was applied.

While 93 Hα emitters are confirmed using z-COSMOS, there are 72 z-COSMOS galaxies with a spectroscopic redshift which should place the Hα line in the NB$_J$ filter. The failure to select these as narrow-band excess sources means that they have a weak or absent Hα emission line. These present a mean colour $(J - \mathrm{NB}_J) = 0.1$ corresponding to a mean measured Hα flux lower than the survey limit ($3 \times 10^{-17}\,\mathrm{erg\,s^{-1}\,cm^{-2}}$ and a mean EW of 20Å). The brightest source has $J = 19$ mag. These are likely to be very faint emitters for which a completeness correction is applied later (see Section 7.5). The [OII] 3727 line fluxes from z-COSMOS galaxies confirms this: where they are detected they yield similar line fluxes to the ones that would be estimated for Hα. On the other hand, some of these

sources have a negative $(J - \mathrm{NB}_J)$ colour. By applying similar selection criteria used for emitters, it seems that at least 2 Hα absorbers would be selected.

3.6.1 Narrowband-K and H matches

By design, the custom-built narrow-band filters make it possible to look for line detections in multiple bands to refine redshift estimates. Currently, data are available in $\mathrm{H_2S_1}$ for COSMOS (Geach et al. 2008) and NB_H and $\mathrm{H_2S_1}$ for UDS (see Chapter 6)

For COSMOS, it was possible to match 3 sources between excess sources catalogs (J and K), confirming a $z = 2.23$ redshift for those emitters. This shows that the line being detected in NB_J is [OII] 3727.

For UDS, 18 sources were matched between the NB_H and NB_J. These have photometric redshifts consistent with either being Hα emitters at $z \sim 1.5$ or Hα emitters at $z = 2.23$, thus meaning that the line detected in the J band is Hβ or [OII] 3727 (respectively) for these emitters. At least 2 of these are also selected as emitters in the NB_K filter, which confirms $z = 2.23$ for them. In addition, there are another 6 matches between the K and the J narrow-band filters, indicating that those sources are at $z = 2.23$ as well. Four of these 24 matched sources were found in the photometric redshift-derived Hα catalog and were thus removed as the evidence points towards these being at higher redshift.

3.7 Results

A total of 743 candidate $z = 0.84$ Hα emitters are detected over $1.30\,\mathrm{deg}^2$ down to an average observed line flux limit of $8 \times 10^{-17}\,\mathrm{erg\,s^{-1}\,cm^{-2}}$. This sample will now be used to evaluate the Hα luminosity function and estimate the star formation rate density at $z = 0.84$. The morphological mix of these Hα emitters in the COSMOS field will then be investigated, together with their evolution as a function of luminosity and redshift, and their contribution to the total luminosity function and star formation rate density.

3.8 Hα luminosity function at $z = 0.84$

In order to calculate the luminosity function of Hα emitters, line fluxes are converted to luminosities by applying:

$$L_{\mathrm{H}_\alpha} = 4\pi \mathrm{D}_\mathrm{L}^2 \mathrm{F}_{\mathrm{H}_\alpha} \tag{3.1}$$

where $\mathrm{D_L}$ is the luminosity distance, 5367 Mpc at $z = 0.84$.

The estimate of the source density in a luminosity bin of width $\Delta(\log L)$ centered on $\log L_c$ is given by the sum of the inverse volumes of all the sources in that bin. Therefore, the value of the source density in that bin is

$$\phi(\log(L_c)) = \frac{1}{\Delta(\log L)} \sum_{|\log \frac{L_i}{L_c}| < \frac{\Delta(\log L)}{2}} \frac{1}{\Delta(V_{\rm filter})}. \quad (3.2)$$

Here, i refers to sources and c to the center of each bin. The volume probed is calculated taking into account the survey area and the narrow-band filter width (initially assumed to be a top-hat function across 1.2037–1.2185μm; see Section 3.8.4 for a refined approach), resulting in a co-moving volume of $7.4 \times 10^4\,{\rm Mpc}^3$ (UDS) and $1.04 \times 10^5\,{\rm Mpc}^3$ (COSMOS). As detailed before, this takes into account the removed area due to the presence of bright stars and consequent artifacts, along with noisy areas.

The luminosity functions presented here are fitted with a Schechter function defined by the three parameters: α, ϕ^* and L^*:

$$\phi(L)dL = \phi^*(L/L^*)^\alpha \exp(-L/L^*)d(L/L^*). \quad (3.3)$$

3.8.1 [NII] flux contamination correction

When computing line fluxes and equivalent widths for the Hα line, one must note that the adjacent [NII] lines at 6548 and 6583Å will also contribute to both quantities, increasing them both. In order to account for this, the relation between the flux ratio $F_{[NII]}/F_{H\alpha}$ and the total measured equivalent width EW(Hα+[NII]) derived by Villar et al. (2008) is used. This shows that the fractional [NII] flux contribution decreases with increasing EW. The relation between $y = \log(F_{[NII]}/F_{H\alpha})$ and $x = \log(\,{\rm EW(H}\alpha + [{\rm NII}]))$ can be approximated by $y = -5.78 + 7.63x - 3.37x^2 + 0.42x^3$ for EW > 50Å. This results in a correction lower than the conservative 33% used by some authors (e.g. Geach et al. 2008), with the median being 25% for this sample with EW > 50Å.

3.8.2 Completeness correction

Fainter sources and those with weak emission lines might be missed and thus not included in the sample; this will result in the underestimation of the number of emitters, especially at lower luminosities. Furthermore, the completeness rate is highly affected by the selection criteria ($\Sigma > 2.5$, EW > 50Å, $\sigma > 3$). To address this problem, a series of simulations was conducted. First, the recovery rate has been studied as a function of magnitude for objects in the same frame, using a Monte Carlo method. For this, 10 different galaxies (both real – taken from the narrow-band images in UDS and COSMOS – and simulated) were used. These were introduced (20 for each run, in any given image) with different input magnitudes into the science frames and then detected using the same extraction parameters as the main catalogues. The recovery rate and the recovered magnitude were then studied. The latter follows the input magnitude reasonably well down to the 3-σ limit. The recovery rate, while varying slightly with the type of galaxy used (the artificial and point-like objects, for example, showed a much higher recovery rate at fainter levels than real galaxies), falls off sharply fainter than ${\rm NB}_J \sim 21$. Similar simulations were also done for the J band images.

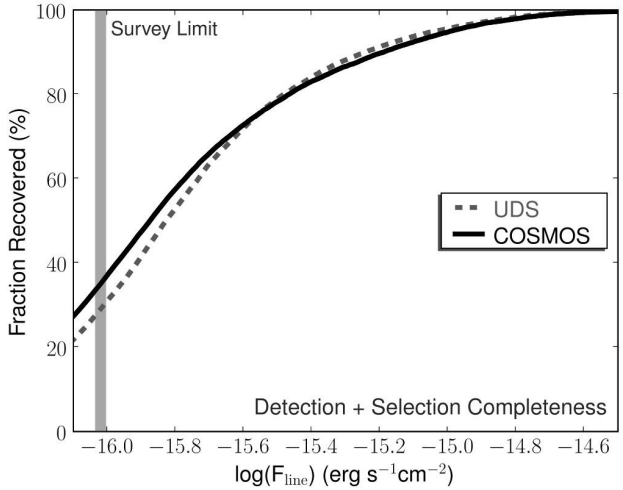

Figure 3.4: The total completeness function used for COSMOS and UDS resulting from several simulations to address the effects of selection and detection. This confirms a $\sim$ 30% completeness at a flux limit of $\sim 10^{-16}\,\mathrm{erg\,s^{-1}\,cm^{-2}}$.

This information alone cannot be used to correct the luminosity function, as faint narrow-band sources don't necessarily have faint Hα lines and vice-versa. To address this, a second series of simulations were performed to investigate the selection completeness of faint emission lines within detected galaxies. For this, narrow-band detections not classified as emitters were considered not to have any emission line. For each of those sources ($\sim$ 21000 for COSMOS and $\sim$ 15000 for UDS) a line flux (in steps of $5 \times 10^{-18}\,\mathrm{erg\,s^{-1}\,cm^{-2}}$ up to $5 \times 10^{-15}\,\mathrm{erg\,s^{-1}\,cm^{-2}}$) was added to both NB_J and J-band magnitudes, and the selection criteria were applied to the revised magnitudes for each line flux to study the recovery rate. This outputs a colour selection completeness for each line flux. Finally, a combined completeness correction was done combining both simulations described. The combined completeness function, which is used to correct the luminosity function on a bin to bin basis, is shown in Figure 3.4. Slightly higher completeness rates at the same flux level have been claimed in Villar et al. (2008), for shallower data, but it should be pointed out that these authors use a combination of selection criteria which is significantly different from those used in this study. Furthermore, they only consider the colour-selection completeness, neglecting the detection completeness, and on the other hand, they use sources detected down to just 0.8σ in NB_J (instead of the 3-σ limit used in this work), and with a lower EW ($\sim$ 15Å) cut; therefore, the results presented here are likely to be more reliable than those by Villar et al. (2008).

3.8.3 Extinction Correction

It is well-known that the Hα emission line is not immune to dust extinction, although it is considerably less affected than Lyα or the UV continuum. Measuring the extinction for each source can in principle be done by several methods, ranging from spectroscopic analysis of Balmer decrements to a comparison between Hα and far-infrared determined SFRs. For now, however, a conservative $\mathrm{A}_{H\alpha} = 1$ mag is

Table 3.3: The Hα luminosity function. Superscript numbers in the column titles indicate the corrections made in each stated value: 1 – extinction correction ($A_{H\alpha} = 1$ mag) and [NII] correction as a function of total measured EW; 2 – completeness correction; 3 – filter profiles biases correction.

$\log(L_{H\alpha})$ (erg s^{-1})	# Sources[1]	$\log(\Phi)^1$ (Mpc^{-3})	$\log(\Phi)^{1,2}$ (Mpc^{-3})	$\log(\Phi)$ final^{1,2,3} (Mpc^{-3})	$\Delta\log(\Phi)^{1,2,3}$ (Mpc^{-3})
41.7 (41.65–41.75)	101	−2.25	−1.77	−1.77	0.14
41.8 (41.75–41.85)	133	−2.13	−1.78	−1.74	0.10
41.9 (41.85–41.95)	132	−2.13	−1.88	−1.83	0.10
42.0 (41.95–42.05)	110	−2.20	−2.04	−1.96	0.10
42.1 (42.05–42.15)	79	−2.35	−2.23	−2.12	0.11
42.2 (42.15–42.25)	69	−2.41	−2.32	−2.24	0.11
42.3 (42.25–42.35)	39	−2.66	−2.59	−2.48	0.14
42.4 (42.35–42.45)	24	−2.87	−2.81	−2.68	0.18
42.5 (42.45–42.55)	14	−3.10	−3.06	−2.92	0.22
42.6 (42.55–42.65)	9	−3.30	−3.26	−3.11	0.27
42.7 (42.65–42.75)	8	−3.50	−3.45	−3.35	0.28
42.9 (42.75–43.05)	6	−4.05	−4.04	−4.02	0.37

used, which is the same correction adopted in most of the similar studies done before (e.g. Fujita et al., 2003; Ly et al., 2007; Geach et al., 2008). This same correction is also applied to all other datasets being compared here, when possible, in order to give consistency between all studies and search for evolution. Section 3.9.1 shows that this correction should not be too far from the actual mean extinction for the entire sample.

3.8.4 Filter profile corrections

The narrow-band filter transmission function is not a perfect top-hat (as assumed earlier), and thus the real volume probed varies as a function of intrinsic luminosity: luminous Hα emitters will be detected over a larger volume than the fainter ones because they can be detected in the wings of the filters (although they will be detected as fainter sources in these cases). Low luminosity sources will only be detected in the central regions of the filter and thus the effective volume will be smaller.

In order to correct for this when deriving the Hα luminosity function, a further set of simulations was run. Firstly, the luminosity function was computed with the corrections described above and the best fit was assigned. This was then assumed to be the true luminosity function, allowing the generation of a set of $\sim 10^5$ Hα emitters with a flux distribution given by the measured luminosity function, but spread evenly over the redshift range $z = 0.81$–0.87 (assuming no cosmic structure variation or evolution of the luminosity function over this narrow redshift range). The top-hat filter model was then confirmed to recover the input luminosity function perfectly. Next, the true filter

profiles were used to study the recovered luminosity function. These simulations showed that the number of brighter sources is underestimated relative to the fainter sources. A mean correction factor between the input luminosity function and the one recovered (as a function of luminosity) was then used to correct each bin. The simulation was run again with the new luminosity function, confirming that the recovered luminosity function is very similar to the input luminosity function.

The filter profiles were also checked against the spectroscopic redshift distribution from z-COSMOS DR2. By distributing the artificial Hα emitters to reproduce the luminosity function, one can predict the redshift distribution of observed sources for each filter. Those matched well the redshift distribution of the z-COSMOS emission line sample, although this sample only contains ~ 100 emitters at the moment.

3.8.5 Fully corrected luminosity function

The final $z = 0.84$ Hα luminosity function is presented in Figure 3.5 and in Table 3.3. The raw luminosity function, without correcting for incompleteness and filter profile biases (correcting only for [NII] contamination and $A_{H\alpha} = 1$ mag of extinction), is also shown. The errors are Poissonian in each bin, combined with an uncertainty on the correction factor assumed to be 10% of the applied correction. Luminosity functions are also computed separately for the two observed fields (Figure 3.5) with these being compared with the combined luminosity function. Both luminosity functions are generally consistent within the errors, although there seems to be a slightly higher density at $z = 0.84$ in COSMOS. The on-sky distribution of the Hα emitters in the COSMOS and UDS fields is far from homogeneous: they are highly clustered and several high-density regions can be found (a detailed clustering analysis is presented in Chapter 4). Assuming a standard angular correlation function for the Hα emitters, parameterised as $w(\theta) = A\theta^{-0.8}$ (with θ in arcsec), then for a value of $A \approx 1$ (typical for galaxies like these), and following Peebles (1975), the cosmic variance in the number of emitters expected in a 1.3 deg^2 sky area due to clustering is estimated to be roughly double the pure Poissonian errors. This leads to (1σ)uncertainties of $\sim 12\%$ on the total number of detected Hα emitters; the corresponding uncertainties for the individual fields are $\sim$15% for UDS and $\sim$13% for COSMOS. These are fully consistent with the actual differences in number densities found. Even for an extremely clustered population, with $A \sim 10 - 15$, the source count variations would not be larger than $\sim 20\%$ on fields of this size. Given this, and the consistency between the COSMOS and UDS fields (and also the results of Villar et al 2008), it is safe to say that the results derived are largely robust against cosmic variance.

Also plotted in Figure 3.5 are other published Hα luminosity functions at different redshift; these demonstrate a significant evolution with redshift, linked to an increase of the number density of both faint and bright emitters at least up to $z \sim 1$. To quantify this evolution a Schechter function is fitted to the combined $z = 0.84$ luminosity function, which yields: $\phi^* = 10^{-2.28\pm0.10}\,\mathrm{Mpc}^{-3}$, $\alpha = -1.65 \pm 0.15$ and $L^* = 10^{42.26\pm0.05}\,\mathrm{erg\,s}^{-1}$. These parameters, and a comparison with the best fits for COSMOS and UDS separately, can be found in Table 3.5. The best fit parameters indicate a steeper faint end

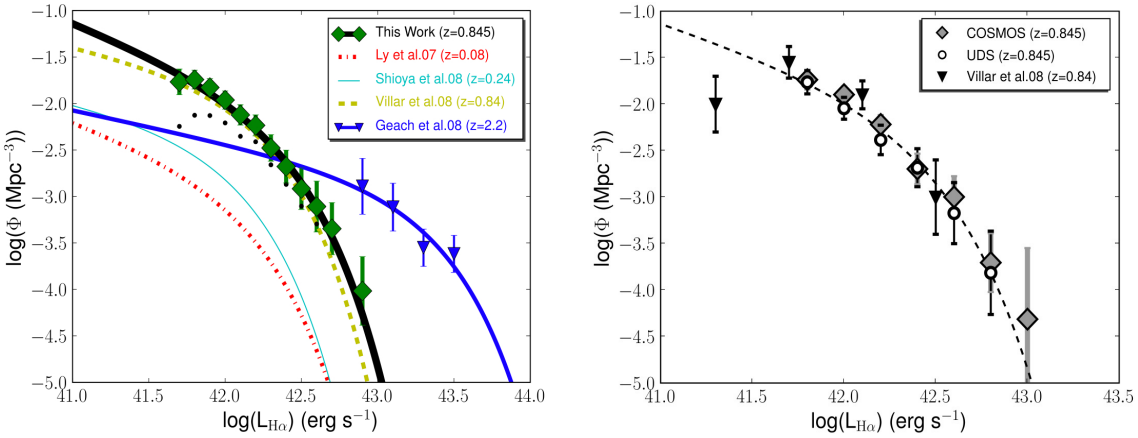

Figure 3.5: The left panel shows the Hα luminosity function (corrected for [NII] contamination, completeness, extinction and filter profile biases) with the best fit Schechter function given by $\phi^* = 10^{-2.28\pm0.10}\,\mathrm{Mpc}^{-3}$, $\alpha = -1.65 \pm 0.15$ and $L^* = 10^{42.26\pm0.05}\,\mathrm{erg\,s}^{-1}$. Small black dots present the derived luminosity function with corrections for [NII] and extinction ($A_{H\alpha} = 1$ mag) only. Other luminosity functions (corrected for $A_{H\alpha} = 1$, except for $z = 0.08$ and $z = 0.24$ where the extinction corrections from the authors were used) from narrow-band surveys of Hα emitters at different redshifts are presented for comparison, showing a clear evolution with cosmic time up to at least $z \sim 1$. The derived Hα luminosity function for each separate field (COSMOS and UKIDSS UDS) is presented in the right-hand panel, with a comparison with data points from Villar et al. (2008) – assuming the same dust extinction as applied in the present study. There seems to be a slightly higher density of sources in COSMOS, but both luminosity functions agree well with the combined fit (dashed line).

slope at $z = 0.84$ than the canonical $\alpha = -1.35$ usually assumed; similarly steep faint-end slopes for the luminosity function of star-forming galaxies have recently been found from UV studies (e.g. Bouwens et al., 2008). These authors have argued for an increase in the faint-end slope of star-forming galaxies with redshift. However, evidence for a steep faint-end slope in the Hα luminosity function ($\alpha \sim -1.6$) has been found even at $z = 0.08$ by Ly et al. (2007) as well as in other Hα studies at higher redshifts, $z \sim 0.2$–1.3 (e.g. Hopkins et al., 2000; Fujita et al., 2003; Dale et al., 2008). Figure 3.6 shows the best-fit α for Hα luminosity functions derived at $z = 0.02$–1.3. This reveals no clear evidence of evolution of the faint-end slope with cosmic time; indeed, rather than having a random distribution, the values of α seem to cluster into two groups with $\alpha \sim -1.6$ or $\alpha \sim -1.3$. The origin of these discrepant results is unclear, but cosmic variance may play an important role.

Figure 3.6 also shows the variation of L^* and ϕ^* of the Hα luminosity function out to $z \sim 2$. To derive these values, only LFs of Hα surveys which were fitted with the "canonical" α=−1.35 or that had their data points published (those were then refitted by fixing α=−1.35) were used, in order to reduce degeneracies and allow a direct comparison between results. It should be noted that some degeneracy will still remain between L* and ϕ^* values. Figure 3.6 shows a strong evolution in L^*, increasing by at least an order of magnitude from the local Universe (Gallego et al. 1995) to $z = 2.23$ (Geach et al. 2008). The evolution of ϕ^* is somewhat different: while it appears to increase from $z = 0$ up to $z = 0.84$ (this work and Villar et al. 2008) by one order of magnitude, it would then

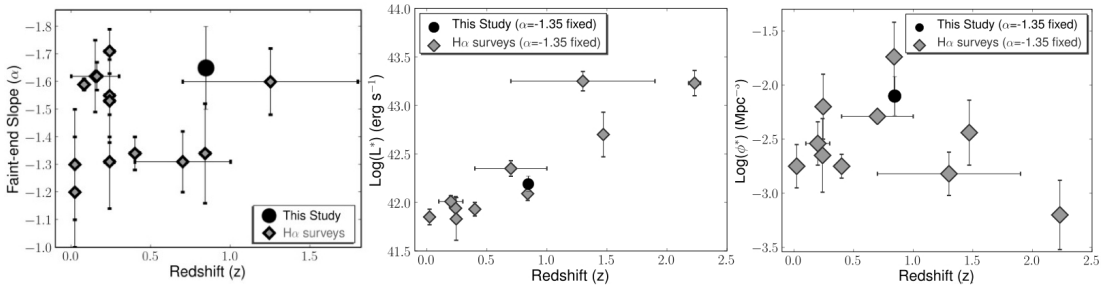

Figure 3.6: The evolution of the best-fit Schechter function parameters of the Hα luminosity function for Hα surveys. The left panel presents the best-fit values for the faint end slope, α, which appear to fall into two distinct groups with $\alpha \sim -1.6$ and $\alpha \sim -1.3$, with little evidence for any redshift evolution. The middle and right-hand panels show the evolution of L^* and ϕ^* as calculated by fixing $\alpha = -1.35$. L^* appears to evolve strongly with redshift out to $z > 2$, whereas ϕ^* might peak at $z \sim 1$ and then decline. Fixing the faint-end slope at $\alpha = -1.65$ yields a similar result.

need to fall at $z > 1$ to be consistent with the higher redshift data of Yan et al. (1999) and Geach et al. (2008). Note that the increased value of ϕ^* at $z = 0.84$ does not arise just due to the degeneracy between ϕ^* and L^*: a value of $\phi^* = 10^{-2.9}\,\mathrm{Mpc}^{-3}$ for the current data-set can be strongly rejected, having a probability $< 10^{-6}$. The evolution of L^* and ϕ^* is therefore revealing important details of the evolution of the Hα luminosity function: from $z \sim 0$ to $z \sim 1$ it seems to be driven by an increase in the number density of both bright and faint emitters, with an increasing population of bright emitters at higher redshift then being responsible for a stronger evolution in L^*. These results are also consistent with studies done using 24 μm data (e.g. Caputi et al., 2007). The evolutionary trends do not change if α is fixed at a higher value ($\alpha = -1.65$ for example).

3.9 The star formation rate density at $z = 0.84$

3.9.1 AGN contamination

The Hα luminosity function previously derived used all the Hα emitters from the survey, and while most of such sources are likely to be star-forming galaxies, some of these can also be AGN. Spectra from z-COSMOS DR2 were used to explored this. A visual inspection of the 93 available spectra was done to confirm additional emission lines ([OII] 3727, [OIII] 5007 and Hβ) and the assigned redshift. The line fluxes were then measured using an IDL script. Although the comparison of those lines with the Hα line fluxes is influenced by many factors (e.g. Hα/[NII] ratio, exact location of the Hα line within the filter profile, fraction of emission line light falling into z-COSMOS slit) it is noteworthy that both the mean ratio of Hα/[OII] 3727 = 2.27 and the ratio of Hα/Hβ = 4.16 are consistent with an Hα extinction of ~ 1 mag or slightly higher.

In order to estimate the AGN contamination, the [OII] 3727/Hβ and [OIII] 5007/Hβ line ratios were used; these have been widely used to separate AGN from star-forming galaxies (e.g. Rola et al.,

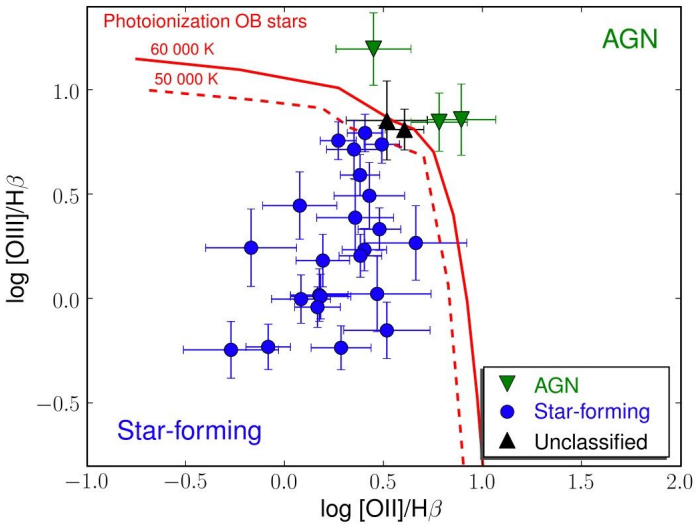

Figure 3.7: Line ratios from the z-COSMOS spectra of the $z = 0.845$ Hα sample. These show that the great majority of the sample is composed of star-forming galaxies (82%), as expected, with 11% showing evidence for being AGN contaminants and 7% being unclassified. The red curves represent the maximum line ratios for a star-forming galaxy (from OB stars with effective temperatures of 60000 K (solid line) and 50000 K (dashed line)).

1997). Only spectra with all lines being detected at S/N > 3.0 were used, which results in a sample of 28 galaxies, mainly due to the low S/N at longer wavelengths where [OIII] 5007 and Hβ are found. Figure 3.7 shows data-points for the line ratios, while the curves represent maximum line ratios for a star-forming galaxy (from OB stars with effective temperatures of 60000 K and 50000 K). From the sample of 28 Hα emitters, 23 seem to be clear star-forming galaxies, while 3 are likely to be AGN contaminants. A $\sim 15\%$ AGN contamination is thus estimated, consistent with that found in other Hα studies. The AGN are found to have Hα fluxes typical of the rest of the sample.

3.9.2 Star formation rate density

The observed Hα luminosity function can be used to estimate the average star formation rate density, ρ_{SFR}, at $z = 0.84$. To do this, the standard calibration of Kennicutt (1998) is used to convert the extinction-corrected Hα luminosity to a star formation rate:

$$\mathrm{SFR}(\mathrm{M}_{\odot}\mathrm{year}^{-1}) = 7.9 \times 10^{-42}\ \mathrm{L}_{\mathrm{H}\alpha}\ (\mathrm{ergs}^{-1}). \tag{3.4}$$

This assumes continuous star formation, Case B recombination at $T_e = 10^4$ K and a Salpeter initial mass function ranging from 0.1–100 $\mathrm{M}_{\odot}$. All measurements of ρ_{SFR} include a correction of 15% for AGN contamination and an extinction correction $\mathrm{A}_{H_\alpha} = 1$ mag, except where the authors only presented their own extinction corrected luminosity function.

In Section 3.8.5 a significant evolution in the observed Hα luminosity function was observed. The left panel of Figure 3.8 shows how this translates into an evolution in ρ_{SFR} as a function of redshift, for

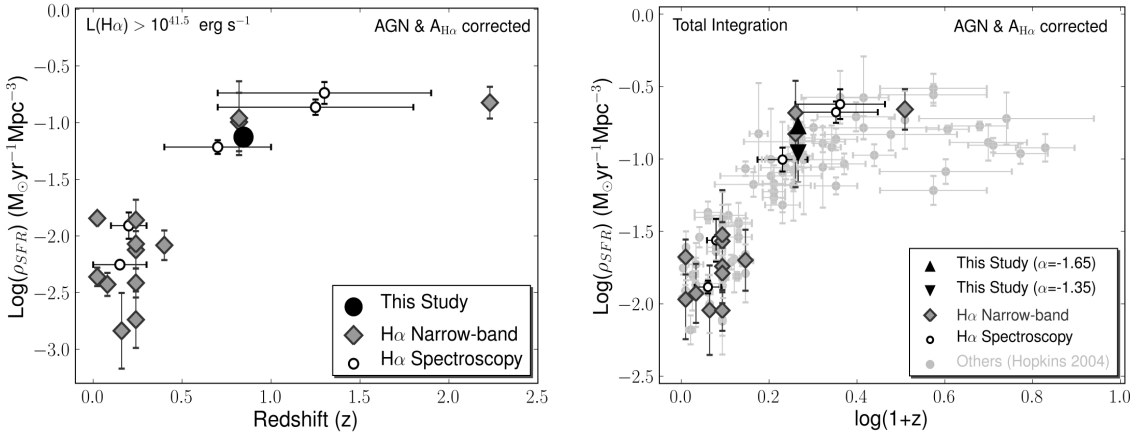

Figure 3.8: The evolution of the star formation rate density as a function of redshift based on Hα – down to the limit of this survey (left panel) and by integrating the entire luminosity function (right panel). The right panel also includes data from all other star-formation tracers, as detailed in the Hopkins (2004) compilation. Both panels show a clear rise in ρ_{SFR} up to at least $z \sim 0.9$–1.0, slightly steeper than the canonical $(1+z)^4$ rise, followed by a flattening out to at least $z \sim 2.2$. Hα data points refer to (in order of increasing mean redshift) Gallego et al. (1995; $z = 0.02$), Pérez-González et al. (2003; $z = 0.02$), Ly et al. (2007; $z = 0.08$), Sullivan et al. (2000; $z = 0.15$), Dale et al. (2008; $z = 0.16$), Tresse & Maddox (1998; $z = 0.20$), Shioya et al. (2008; $z = 0.24$), Fujita et al. (2003; $z = 0.24$), Dale et al. (2008; $z = 0.24$), Morioka et al. (2008; $z = 0.24$), Ly et al. (2007; $z = 0.24$), Ly et al. (2007; $z = 0.4$), Tresse et al. (2002; $z = 0.7$), Villar et al. (2008; $z = 0.84$, 1 mag extinction – higher ρ_{SFR} – and author's extinction correction), this study ($z = 0.845$), Hopkins et al. (2000; $z = 1.25$), Yan et al. (1999; $z = 1.3$), Geach et al. (2008; $z = 2.23$).

luminosity functions which have been integrated down to $\mathrm{L_{H\alpha}} > 10^{41.5}\mathrm{erg\,s^{-1}}$ (the limit of this survey). The measurement at $z = 0.84$ presented in this study ($0.07 \pm 0.02\,\mathrm{M_\odot\,yr^{-1}\,Mpc^{-3}}$) demonstrates a strong rise in ρ_{SFR}, when compared to the local Universe (Gallego et al., 1995; Pérez-González et al., 2003; Ly et al., 2007) and low redshift measurements (e.g. Tresse and Maddox, 1998; Sullivan et al., 2001; Dale et al., 2008; Morioka et al., 2008; Westra and Jones, 2008; Shioya et al., 2008; Sumiyoshi et al., 2009), as suggested by other smaller surveys done at similar redshifts (e.g. Tresse et al., 2002; Villar et al., 2008). This rise seems to be slightly steeper than $\rho_{SFR} \sim (1+z)^4$. When compared to higher redshift (e.g. Geach et al. 2008), the observations also support a flattening in ρ_{SFR} around $z \sim 1$, up to at least $z = 2.23$. A rise and subsequent flattening of the star formation rate density out to $z \sim 2$ has therefore been accurately measured using a single star formation tracer. Cosmic evolution of dust reddening corrections may alter the results slightly but would have to be very strong to change the overall conclusions.

Figure 3.8 also presents the same evolution, but now integrating the entire luminosity function. Caution should be used in interpreting this figure as it involves extrapolating all the luminosity functions and it is critically dependent on the assumed faint-end slope (see Chapter 6). For this study, for example, $\rho_{SFR} = 0.17 \pm 0.11\,\mathrm{M_\odot\,yr^{-1}\,Mpc^{-3}}$ using the measured value of $\alpha = -1.65$, but if one adopts $\alpha = -1.35$, ρ_{SFR} is reduced to $0.11 \pm 0.06\,\mathrm{M_\odot\,yr^{-1}\,Mpc^{-3}}$. Measurements obtained from a set of other star-formation indicators compiled by Hopkins (2004) are also shown for comparison

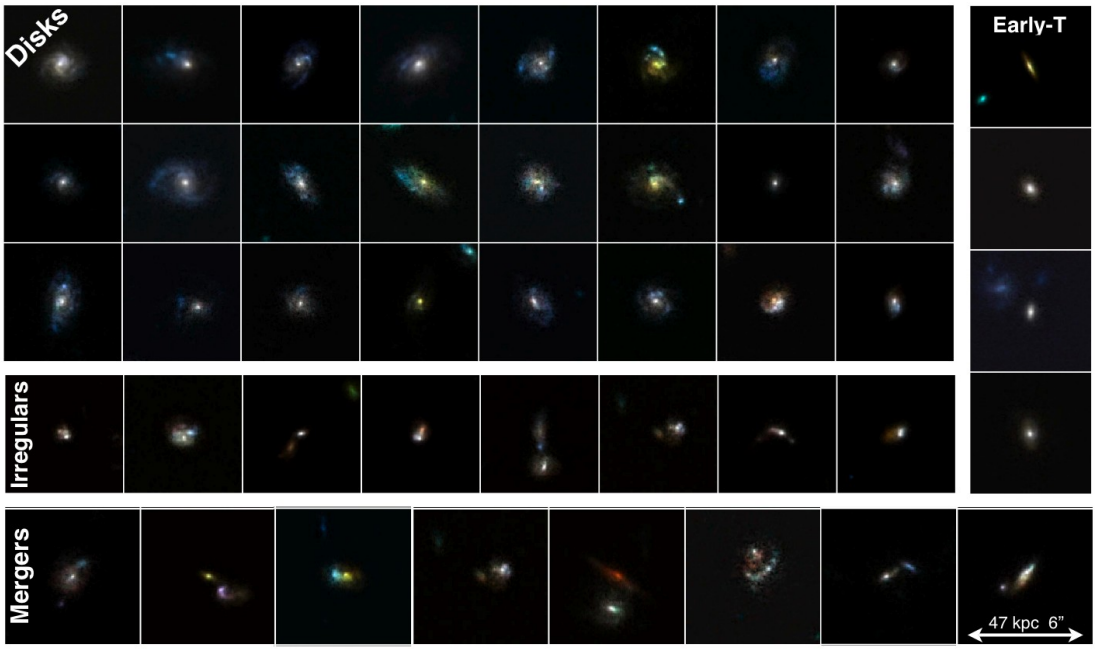

Figure 3.9: *HST* imaging of examples of the sample of Hα emitters at $z = 0.84$ in the COSMOS field, organized into the visual morphological classes described in Section 3.10.3. These include large and small spirals, mergers and irregulars. The thumbnails are all $6'' \times 6''$ corresponding to 47×47 kpc at $z = 0.84$.

(corrected by a common extinction factor consistent with the Hα extinction correction applied here). This confirms the same rise seen using only Hα and the possible flattening at $z \sim 1$.

3.10 The morphology of Hα emitters

3.10.1 Morphology with *HST* imaging

The COSMOS field has sensitive *Hubble Space Telescope* (*HST*) ACS F814W coverage which provides detailed morphological information on the Hα sample. These data are used to study the morphologies of the selected star-forming galaxies. This morphological information can be greatly enriched with colour information, and thus the ACS images are combined with deep Subaru data in Brz bands to produce a pseudo-true colour image. The Subaru images are first registered and transformed to match the *HST* images using IRAF and PYTHON scripts. The *HST* image is then used to define the luminance of the true colour image. In this way colour and morphological information were derived on ~ 500 Hα emitters with sufficient detail that a visual morphology analysis could be undertaken. Figure 3.9 presents some examples of these.

All of the galaxies within the sample were visually classified. In order to compare those results with morphologies obtained in an automated way (by ZEST, kindly supplied by Claudia Scarlata, Scarlata et al. (2007)), 4 morphological classes were used: 1) Early-types, 2) Disks/spirals, 3) Irregulars, and 4) Unclassified. Table 3.4 shows the comparison between ZEST and the visual classification, while

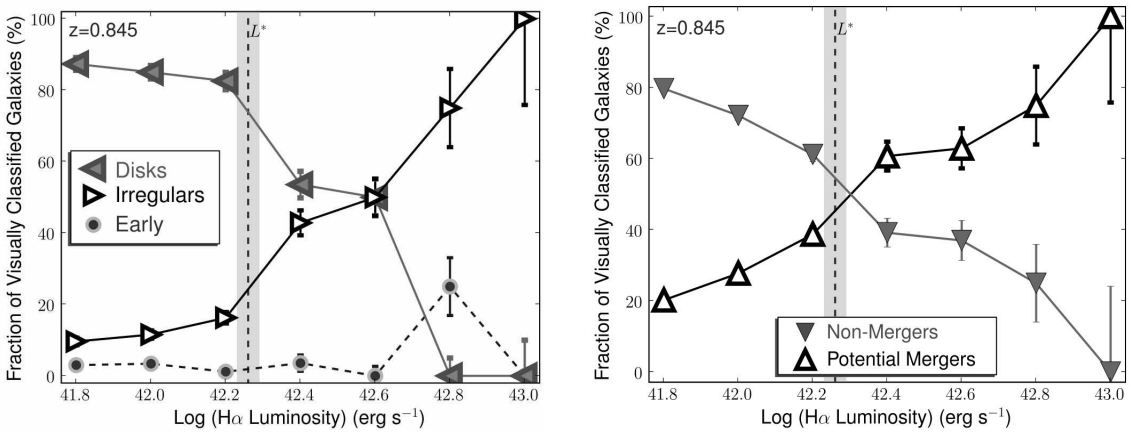

Figure 3.10: Morphological class fractions (left panel) and merger fractions (right panel) as a function of Hα luminosity at $z = 0.84$. These show clear Hα luminosity dependences, with the fraction of irregulars and mergers rising with increasing luminosity. The vertical line indicates the value of L^* derived from the best total Schechter function fit with $\alpha = -1.65$.

Figure 3.9 shows examples of each morphological type. In general, a very good agreement between the visual classifications and ZEST was obtained. The main difference is that visual classification was able to reduce the number of unclassified galaxies. Also, visually, it was possible to improve the distinction between disks and irregulars by using the colour information – distinguishing between multiple bulges and bright spiral arms – which resulted in a sightly lower fraction of irregulars in the visual classification.

Due to a considerable number of sources showing evidence of merging activity, the sample was also classified independently into merger classes. A source is classified as a merger when: 1) it presents a clearly disturbed morphology or disturbed disk which is inconsistent with being that of a normal disk galaxy; or 2) the source presents more than 1 bright point-like source and the colour information is inconsistent with one of those being a spiral arm; or 3) there are two or more galaxies which are very close (< 15 kpc). By applying these criteria, a visual classification was done, where each source was classified at least twice. In the end, 3 merger classes where used to classify all sources: the consistent non-mergers (non-mergers); those galaxies classified at least once as probable mergers (potential mergers); and galaxies always classified as mergers (mergers). The distribution of mergers within the previous morphological classifications and the total numbers can be found in Table 3.4 and examples of classified galaxies can also be found in Figure 3.9.

From a total of 477 Hα emitters, 381 are disks (80%), with 68 being classified as irregulars (14%), 14 are early-types (3%) and a total of 14 (3%) are unclassified as these are too faint. Furthermore, 24% of the sample seems to be populated by clear mergers, with the total merger fraction being estimated as 28 ± 4%; almost all irregulars fall into this class.

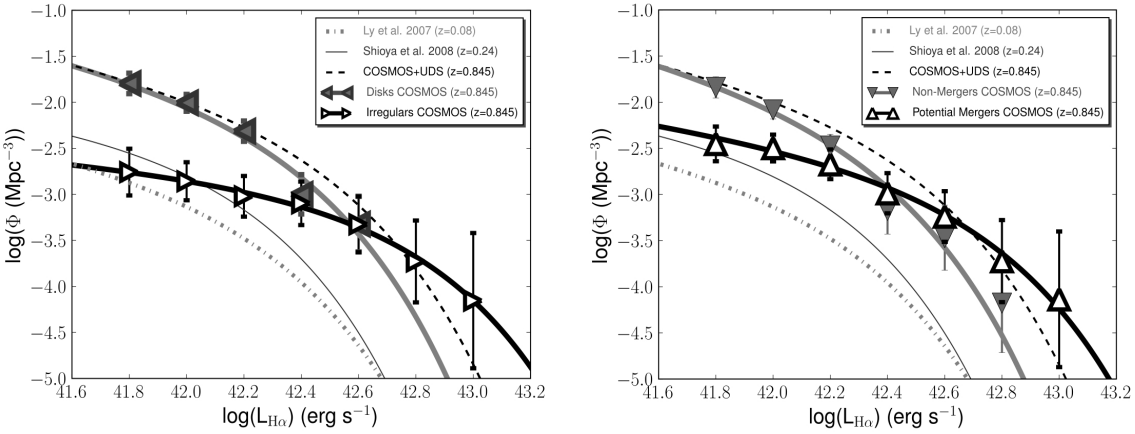

Figure 3.11: The computed luminosity functions and the best fits for different visual morphologies. The dash-dotted line refers to the $z = 0.08$ LF (Ly et al. 2007), with the solid line being that at $z = 0.24$ (Shioya et al. 2008), and the dashed line is the best fit for the combined UDS+COSMOS luminosity function at $z = 0.84$. The brightest bin for both irregulars and potential mergers seems much higher than in the combined luminosity function due to the COSMOS field having a higher space density of bright sources (c.f. Figure 3.5).

Table 3.4: Visual morphology classifications compared to the automated classifications obtained by ZEST (Scarlata et al. 2007) for the Hα emitters at z=0.84. The two agree very well. Differences arise mostly from using colour information for the visual classifications, while ZEST only uses the *HST F*814*W* imaging. The final rows of the table give the distribution of visual morphologies for different merger classes.

Visual Class	ZEST Early	ZEST Disks	ZEST Irregulars	ZEST Unclassified	Visual Total	Visual N-mergers	Visual Mergers
Early	7	3	0	4	14 (3%)	12	2
Disks	2	301	15	63	381 (80%)	297	84
Irregulars	0	10	44	14	68 (14%)	1	67
Unclassified	0	2	0	12	14 (3%)	0	0
Total	9 (2%)	316 (67%)	59 (12%)	93 (19%)	477 (100%)	310 (67%)	153 (33%)

3.10.2 Morphology–Hα luminosity relations

The left panel of Figure 3.10 presents the fraction of galaxies classified into each morphology as a function of Hα luminosity. There is a clear evolution of morphological type with increasing Hα luminosity. While at low star-formation rates, disks dominate the sample completely ($> 85\%$), at higher Hα luminosities ($L > L^*$) irregulars become more significant, reaching 100% in the highest luminosity bin. With the large sample presented in this work it is possible to derive independent luminosity functions for each of those morphological classes. Those can be seen in Figure 3.11 with the best fit Schechter function parameters tabulated in Table 3.5. They illustrate well the different contributions to the total Hα luminosity function by disks and irregulars. Irregulars present a remarkably flat lu-

Table 3.5: The Hα Luminosity function and ρ_{SFR} for different subsets of the data. $\rho_{SFR\ >41.5}$ results from integrating the Hα luminosity function down to $10^{41.5}\,\mathrm{erg\,s^{-1}}$. A 15% AGN correction is made to all ρ_{SFR} measurements.

Sample	$\log\phi^*$ ($\mathrm{Mpc^{-3}}$)	$\log L^*$ ($\mathrm{erg\,s^{-1}}$)	α	$\rho_{SFR\ >41.5}$ ($\mathrm{M_\odot\,yr^{-1}\,Mpc^{-3}}$)
Total: COSMOS+UDS	−2.28±0.10	42.26±0.05	−1.65±0.15	0.07±0.01
UDS	−2.34±0.16	42.25±0.10	−1.70±0.22	0.06±0.02
COSMOS	−2.26±0.12	42.28±0.07	−1.68±0.18	0.08±0.02
COSMOS: Disks	−2.17±0.13	42.12±0.06	−1.65±0.22	0.055±0.020
COSMOS: Irregulars	−3.26±0.23	42.58±0.14	−1.27±0.21	0.015±0.008
COSMOS: Non-mergers	−2.32±0.14	42.16±0.09	−1.71±0.21	0.05±0.02
COSMOS: Potential Mergers	−2.99±0.13	42.50±0.10	−1.47±0.20	0.03±0.01

minosity function, only falling at the highest luminosities, while disks demonstrate a steeper faint end and a much lower space density at the bright end. Overall disks are the dominant contributors to the total ρ_{SFR}, with a large number of galaxies producing stars at rates $< 10\,\mathrm{M_\odot\,yr^{-1}}$.

As mentioned before, almost all of the irregulars show clear evidence of merging activity. In fact, separating non-mergers from likely mergers (mergers, together with potential mergers weighted by 0.5), a very similar behaviour is found (Figure 3.10). While non-mergers dominate at faint luminosities, the contributions from the two populations cross over at $L \sim L^*$, with mergers dominating the bright-end of the luminosity function. The luminosity functions for non-mergers and potential mergers are presented in Figure 3.11. This reveals that non-mergers present the typical disk luminosity function found before, but mergers have a steeper luminosity function than the irregulars. This means that while irregulars on their own are only important in the bright end of the LF, mergers seem to play a dominant role at the bright end (accounting for$\sim$ 60% of the ρ_{SFR} there) together with a non-negligible contribution even at the faintest luminosities. Overall, mergers account for $\sim$ 20% of the total ρ_{SFR} at $z = 0.84$.

The relations which have been presented were found to be very robust, with the same results being obtained regardless of the use of the visual or ZEST classifications, and independently of the [NII] correction – a constant correction also produces the same dependences.

3.10.3 Redshift evolution of the morphology relations

One can compare the morphological mix for the Hα sample at $z = 0.84$ with that found at lower redshifts. In the local Universe, the morphologies of the Hα emitters seem to be somewhat different, with visual morphologies from Vitores et al. (1996) indicating that disks are 88% of the sample, while early-type galaxies increase their importance (9%) and irregulars drop to only 3%. At $z = 0.24$ the narrow-band Hα emitters of Shioya et al. (2008) in the COSMOS field can be more directly compared

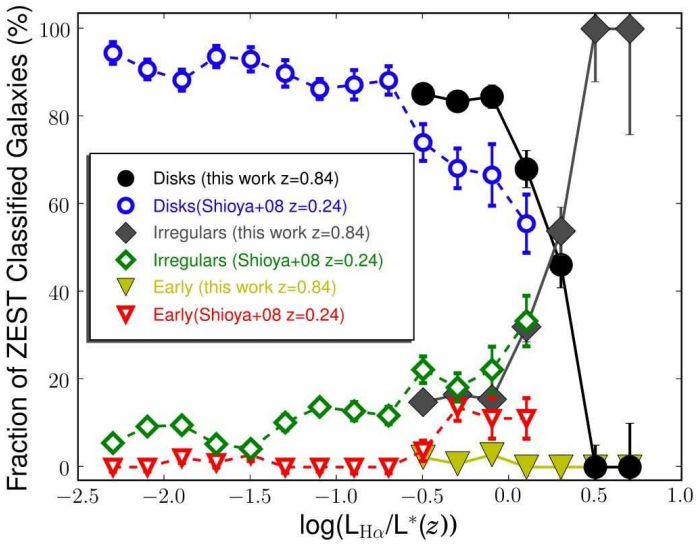

Figure 3.12: Morphology class fractions as a function of Hα luminosity for $z = 0.24$ (Shioya et al. 2008) and this study. These results find the same morphological dependence at both epochs consistent with an evolution in L^* ($\log(L) \sim 0.4$). Morphologies were obtained in an automated way by ZEST (Scarlata et al. 2007) for both samples.

to the $z = 0.84$ sample, using ZEST morphologies for both (although noting that the rest-frame wavelength of the images is different between the two studies – rest-frame B band at $z = 0.84$ and rest-frame R band at $z = 0.24$ – which could introduce a small bias). In the ZEST classifications at $z = 0.24$, disks are still dominant (89%), ∼10% of the galaxies have an irregular morphology, and elliptical galaxies account for only 1% of the sample. These results seem to show that while disks are always the dominant population ($> 80\%$) up to $z \sim 1$, there is a significant increase in the irregular fraction from 3% at $z = 0$ to 10% at $z = 0.24$ and 15% at $z = 0.84$.

The ZEST classifications for the Shioya et al. (2008) sample can also be compared with those for the $z = 0.84$ sample to see if there is any evolution in the morphology–Hα luminosity relations. Thus Figure 3.12 presents the comparison between $z = 0.24$ and $z = 0.84$ with the luminosities scaled by L^*. A very similar variation in morphological mix with Hα luminosity is found at $z = 0.24$, with the irregular fraction increasing from $\sim$ 10% to $\sim$ 35% with increasing luminosity and with the disk fraction having the opposite behaviour, decreasing from $\sim$ 90% to $\sim$ 60%. The relatively good agreement between the data at these two different redshifts and the fact that the switch-over luminosity appears to be at the same L/L^* at both redshifts seems to point towards a rather simple L^* evolution driving the morphology–Hα luminosity relation. However, the Shioya et al. (2008) sample is not able to probe the brightest sources and thus there are no low redshift data to directly compare the complete dominance of irregulars at $L > 3L^*$.

The disk fraction at $z = 0.24$ appears to be slightly lower than the disk fraction at $z = 0.84$ (for the bins which can be directly compared). Curiously, this is due to an apparent rise in the fraction of early-types. However, this might be simply reflecting classification errors between the two epochs. At least some of the very faint galaxies which have been unclassified at $z = 0.84$ (even after visual

classification) are likely to be early-types which are just too faint to be seen at $z = 0.84$, but sufficiently bright at $z = 0.24$ to be classified.

3.11 Summary and Conclusions

Deep near-infrared narrow-band imaging has been obtained, allowing the selection of line emitting galaxies down to an effective flux limit of $F_{H\alpha} \sim 10^{-16}\,\mathrm{erg\,s^{-1}\,cm^{-2}}$. This has resulted in the largest and deepest survey of emission line selected star forming galaxies at $z \sim 1$, detecting 1517 potential line emitters over an area of $\sim 1.4\,\mathrm{deg}^2$ in the COSMOS and UDS fields, with 1370 having quality multi-wavelength data available in a region of $1.3\,\mathrm{deg}^2$. For Hα emission line objects this survey probes a co-moving volume of $\sim 1.8 \times 10^5\,\mathrm{Mpc}^3$ at $z = 0.84$ down to a star formation rate of $\sim 3\,\mathrm{M_\odot\,yr^{-1}}$ (with an $A_{H\alpha} = 1\,\mathrm{mag}$ extinction correction).

Photometric redshifts for COSMOS and UKIDSS UDS (Mobasher et al. 2007; Cirasuolo et al. 2008) clearly show that the majority of the selected emitters are Hα emitters at $z \sim 0.84$ with a secondary population of [OIII] 5007/Hβ emitters at $z \sim 1.4$–1.5. Almost 120 emitters were confirmed spectroscopically, from which 93 are Hα at $z = 0.84$. The contamination within the sample of emitters is estimated to be lower than $\sim 6\%$, and the contamination within the Hα sample is much lower ($\sim 0\%$) based on the current samples. A total of 743 Hα selected emitters (based on their photometric and spectroscopic redshifts) was obtained in the two fields. These were used to calculate the luminosity function after correcting for [NII] flux contamination, extinction, incompleteness and filter profile biases. The morphologies of these emitters were also investigated. The main conclusions of this work are:

- The Hα luminosity function at $z = 0.84$ found is well fitted by a Schechter function with $\phi^* = 10^{-2.28\pm0.10}\,\mathrm{Mpc^{-3}}$, $\alpha = -1.65 \pm 0.15$ and $L^* = 10^{42.26\pm0.05}\,\mathrm{erg\,s^{-1}}$. This demonstrates a strong evolution in the Hα luminosity function compared to lower redshifts and agrees reasonably well with previous smaller studies at $z \sim 1$.

- The evolution of the Hα luminosity function can be described by an increase in ϕ^* and L^*, at least out to $z \sim 1$, with L* then continuing to rise up to $z \sim 2$ but ϕ^* peaking around $z \sim 1$ and then decreasing at higher redshifts.

- The integrated luminosity function is used to estimate the cosmic star formation rate density, (ρ_{SFR}) at $z = 0.84$: $0.07 \pm 0.02\,\mathrm{M_\odot\,yr^{-1}\,Mpc^{-3}}$ (corrected for 15% AGN contamination and integrated down to $2.5\,\mathrm{M_\odot\,yr^{-1}}$).

- An accurate determination of the cosmic evolution of ρ_{SFR} has been made using a single star formation tracer (Hα) from $z = 0$ to $z = 2.23$. This shows a strong rise up to $z \sim 1$ followed by a flattening out to $z \sim 2.2$.

- Hα emitters at $z = 0.84$ are mostly morphologically classed as disks in the rest-frame B-band

$(82 \pm 3\%)$. Irregulars account for $15 \pm 2\%$ of the sample and early-type galaxies are only $3 \pm 1\%$. Apparent mergers are a significant fraction of the sample $(28 \pm 4\%)$.

- A strong morphology–Hα luminosity relation is found at z=0.84, with the fraction of irregulars rising steadily with luminosity and the fraction of disks falling. Mergers/non-mergers present the same behaviour, and L^* (from the total sample) seems to define a critical switch-over luminosity between the two populations.

- Mergers dominate the bright end of the total Hα luminosity function at $z = 0.84$ and $\sim 20\%$ of the total ρ_{SFR} is due to their activity.

- A similar morphology–Hα luminosity relation is found at lower redshift ($z = 0.24$), consistent with a simple L* evolution.

These results suggest that the evolution of both the Hα luminosity function and ρ_{SFR} change significantly in nature beyond $z \sim 1$, and that it is entirely plausible that this is driven by the different evolutionary behaviour of two different populations of star forming galaxies. Out to $z \sim 1$, the integrated ρ_{SFR} at each redshift is produced predominantly by disk galaxies; it is therefore the evolution of these disk galaxies, rather than that of major mergers, which drives the strong decrease in the cosmic star formation rate density from redshift one to the current epoch – this is in line with other recent results (e.g. Lotz et al., 2008). At these redshifts, the evolution in ρ_{SFR} arises predominantly from an evolution in the characteristic space density of the Hα luminosity function (ϕ^*; which seem to evolve by a factor of a few between $z = 0$ and $z = 0.84$), rather than a strong evolution in L^*. With their relatively quiescent star formation activity, the disk galaxies dominate the Hα luminosity function at low luminosities, and are thus responsible both for the ϕ^* evolution and for setting the faint-end slope of the luminosity function.

In contrast, irregular and merging galaxies appear to dominate the Hα luminosity function above L^*, at $z = 0.84$ (and also at $z = 0.24$), being responsible for more than 50% of the non-extrapolated ρ_{SFR} (integrated down to $2.5\,\mathrm{M}_\odot\,\mathrm{yr}^{-1}$). The evolution of these systems controls the bright end of luminosity function, and thus the cosmic evolution of L^*. The continued strong evolution of L^* between $z = 0.84$ and $z = 2.23$, and the decrease in ϕ^*, suggests an increasing importance of merger-driven star formation activity beyond $z \sim 1$, especially as the irregular Hα luminosity function seems to be very similar to the one found at $z = 2.23$ by Geach et al. (2008) when taking into account an L^* evolution. This is consistent with recent results such as Shi et al. (2009a). The completed HiZELS survey will provide statistically significant samples of Hα emitters at $z = 1.47$ and $z = 2.23$ and so provide a direct test of this suggestion.

Chapter 4

The clustering and evolution of Hα emitters at $z \sim 1$

4.1 Introduction and Motivation

While measuring ρ_{SFR} as a function of cosmic time is fundamental for our understanding of galaxy formation and evolution, there are other aspects of the nature and evolution of star-forming galaxies – such as the clustering and environment properties – which can only be unveiled if one goes beyond such quantity. Fortunately, large-scale narrow-band imaging surveys can also be explored to measure the clustering properties of large samples of galaxies and its evolution with cosmic time, along with possible dependences such as luminosity, morphology, star-formation rate and/or stellar mass.

In a Universe dominated by cold dark matter, galaxies are found in dark matter halos with a structure determined by universal scaling relations (e.g. Navarro et al., 1996). Since baryons trace the underlying distribution of dark matter, measurements of the clustering of baryonic matter can be used to extract typical dark-matter halo masses (Mo and White, 1996; Sheth et al., 2001) and to suggest links between populations found at different epochs.

Wide surveys of the nearby Universe (e.g. 2dF, SDSS; Colless et al., 2001; York et al., 2000) have now assembled extremely large samples of galaxies which can be explored to study their clustering properties in great detail. Using those data, several studies have found that the amplitude of the two-point correlation function rises continuously with galaxy luminosity (e.g. Norberg et al., 2001; Zehavi et al., 2005; Li et al., 2006). They also reveal that the most rapid increase occurs above the characteristic luminosity, L^*. Red galaxies are found to be more clustered than blue galaxies, but the correlation amplitude of the latter population also increases continuously with blue or infrared

luminosities (e.g. Zehavi et al., 2005). This seems to indicate that both star-formation rate (SFR, traced by ultraviolet/blue light) and stellar mass (traced by near-infrared light) are important for determining the clustering of different populations of galaxies. Other studies have used morphological classifications. Skibba et al. (2009), for example, took advantage of the largest sample of visually classified morphologies to date (from SDSS) to clearly reveal that although early-type galaxies cluster more strongly than discs, once the analysis is done at a fixed colour and luminosity no significant difference is found; this confirms previous results (e.g. Beisbart and Kerscher, 2000; Ball et al., 2008) for the nearby Universe.

Understanding when these trends were created and how they evolved with cosmic time is a key input to galaxy formation models and to our general understanding of how galaxies formed and evolved. The first clustering studies of different populations of galaxies beyond the local Universe (e.g. Efstathiou et al., 1991; Fisher et al., 1994; Brainerd et al., 1995; Le Févre et al., 1996), although pioneering, were mostly limited by the lack of information on the redshifts for their samples. Fortunately, those problems are now starting to be effectively tackled by larger and deeper surveys. Such surveys have recently led to robust clustering studies of specific populations of sources at moderate and high redshift such as AGN (e.g. da Ângela et al., 2008), sub-mm galaxies (e.g. Blain et al., 2004; Weiß et al., 2009), luminous red and massive galaxies (e.g. Wake et al., 2008), or star-forming galaxies such as Hα emitters, Lyman-break galaxies or Lyman-α emitters (e.g. Geach et al., 2008; McLure et al., 2009; Shioya et al., 2009). A dependence of the clustering on galaxy luminosity has also been identified beyond the local Universe (e.g. Giavalisco and Dickinson, 2001). In particular, Kong et al. (2006), Hayashi et al. (2010) and, more recently, Hartley et al. (2008) found a clear dependence of the clustering amplitude on near-infrared luminosity for $z \sim 1-2$ "BzK" selected galaxies, indicating that already in the young Universe the most massive galaxies were much more clustered than the least massive ones. These results mean that although different studies have been combined to suggest links between the same population at different redshifts, or between different populations at different epochs, interpreting these requires a great deal of care, since luminosity limits typically increase significantly with redshift and are different for different populations.

Narrow-band surveys have a great potential for determining the clustering properties of large samples of galaxies and their evolution with cosmic time. Such surveys probe remarkably thin redshift slices ($\Delta z \approx 0.02$), which not only provides an undeniable advantage over photometric surveys that can be significantly affected by systematic uncertainties, but also allows the study of very well-defined cosmic epochs. Additionally, the selection function is well-understood and easy to model in detail, a feature that contrasts deeply with that of current large high-redshift spectroscopic redshift surveys. Narrow-band surveys also populate the redshift slices they probe with high completeness down to a known flux limit, in contrast to spectroscopic surveys which are typically very incomplete at any single redshift and present the typical pencil-beam distribution problems. Finally, narrow-band surveys can select equivalent populations at different redshifts, making it possible to really understand the evolution with cosmic time, avoiding the biases arising from comparing potentially different populations.

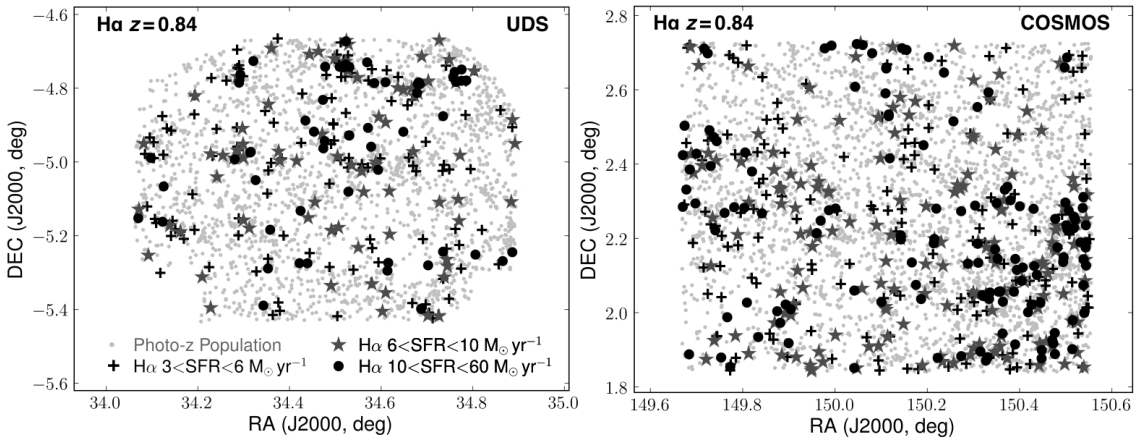

Figure 4.1: The on-sky distribution of the Hα emitters found at $z = 0.84$ in the UDS (left panel) and COSMOS (right panel) fields, together with a photometric redshift selected sample at the same redshift. Both panels/boxes cover the same angular/physical area, corresponding to $\approx 29 \times 29\,\mathrm{Mpc}$ at $z = 0.84$. The Hα emitters are plotted in 3 different symbols corresponding to different star-formation rates (see key in left panel).

This Chapter presents a detailed clustering study of the sample of narrow-band selected Hα emitters at $z \sim 1$ (c.f. Chapter 3); the results have also been published in Sobral et al. (2010).

4.2 Data and Samples

4.2.1 The sample of Hα emitters from HiZELS

This Chapter uses the HiZELS large sample of Hα emitters at $z = 0.845$ presented in Chapter 3, but uses improved photometric redshifts for COSMOS and UDS. Those incorporate a higher number of bands, deeper data and accounting for possible emission-line flux contamination of the broad-bands (c.f. Cirasuolo et al., 2010; Ilbert et al., 2009, Cirasuolo et al. in prep.); these further confirm the robustness and completeness of the selection done in the previous Chapter. The Hα sample used for the analysis in this Chapter is slightly modified on the basis of the new photometric redshifts. In particular, the sample in UDS now contains 257 Hα emitters over 0.52 deg^2. The very small reduction in area simply results from the overlap with deep mid-infrared data used for deriving the new improved photometric redshifts – this reduction places 3 sources from the initial sample outside the coverage. The remaining 6 sources excluded from the sample were removed on the basis that the new photometric redshifts clearly place those sources at $z \approx 2.2$ (2) and $z \approx 1.45$ (4) (they are therefore identified as candidate [OII] 3727 and [OIII] 5007/Hβ emitters, respectively). For COSMOS, the sample of Hα emitters is the same (477 emitters over 0.76 deg^2), since the new photometric redshifts do not change any of the classifications (noting that spectroscopic data had already been used to produce a cleaner sample).

As the samples were obtained in two of the best studied square degree areas, a wealth of multi-

wavelength data are available. These include deep broad-band imaging from the ultra-violet (UV) to the infrared (IR) – including deep *Spitzer* data. These data make it possible to compute rest-frame luminosities for the sample of Hα emitters at $z = 0.84$. Here, rest-frame B luminosities (M_B) are estimated by using i^+-band data (probing 4152.6 Å at $z = 0.84$) obtained with the Subaru telescope in both UDS and COSMOS. This is obtained by applying an aperture correction of -0.097 mag (to recover the total flux for magnitudes measured in 3 arcsec apertures) and a galactic extinction correction of -0.037 to i^+ magnitudes (Capak et al., 2007). It is assumed that all sources are at a luminosity distance of 5367 Mpc ($z = 0.845$); this yields a distance modulus of 43.649. Rest-frame K luminosities (M_K) are computed following Cirasuolo et al. (2010) by assuming the same luminosity distance and interpolating using deep 3.6 μm and 4.5 μm *Spitzer* data.

Furthermore, the COSMOS field has been imaged by ACS/HST, and the sample of Hα emitters has been morphologically classified both automatically, with ZEST (Scarlata et al., 2007), and visually, as detailed in Chapter 3. The sample has also been investigated for AGN contamination, using emission-line diagnostics, and in Garn et al. (2010) making use of a wide variety of techniques.

Figure 5.2 presents the distribution of the Hα emitters at $z = 0.84$ for the UDS and COSMOS fields. The panels visually indicate how these emitters cluster across these two regions of the sky relative to a simple photometric redshift selected population at the same redshift, selected with $0.82 < z_{\rm photo} < 0.87$.

4.2.2 The random sample

Random catalogues are essential for robust clustering analysis and an over- or under-estimation of the clustering amplitude can easily be obtained if one fails to produce accurate random catalogues. These are produced by generating samples with 100 times more sources than the real data and by distributing those galaxies randomly over the geometry corresponding to the survey's field-of-view. This takes into account both the geometry of the fields and the removal of masked areas (due to bright stars/artefacts) – see discussion of masked regions in Chapter 3 for more details.

While the survey is fairly homogeneous in depth, there are some small variations from chip to chip and field to field reaching a maximum of ~ 0.2 mag ($\rm NB_J$ of 21.5 to 21.7 mag). This corresponds to a maximum variation in luminosity [in $\log_{10}(L)$] of ~ 0.1. The observed luminosity function presented in Chapter 3 shows that going deeper by 0.1 in $\log_{10}(L)$ increases the number count by ~ 20 per cent. This can have an effect on estimating the clustering although simulations indicate that this is smaller than the measured errors. The final random catalogues were created reproducing source densities varying in accordance with the measured depths and the number counts.

4.3 The Clustering Properties of Hα emitters

4.3.1 The two-point $\omega(\theta)$ correlation function at $z = 0.84$

In order to evaluate the two-point angular correlation function, the minimum variance estimator suggested by Landy and Szalay (1993) is used:

$$\omega(\theta) = 1 + \left(\frac{N_R}{N_D}\right)^2 \frac{\mathrm{DD}(\theta)}{\mathrm{RR}(\theta)} - 2\frac{N_R}{N_D}\frac{\mathrm{DR}(\theta)}{\mathrm{RR}(\theta)}, \tag{4.1}$$

where $\mathrm{DD}(\theta)$ is the number of pairs of real data galaxies within $(\theta, \theta + \delta\theta)$, $\mathrm{DR}(\theta)$ is the number of data-random pairs and $\mathrm{RR}(\theta)$ is the number of random-random pairs. N_R and N_D are the number of random and data galaxies in the survey. Errors are computed using the Poisson estimate (Landy and Szalay, 1993):

$$\Delta\omega(\theta) = \frac{1 + \omega(\theta)}{\sqrt{\mathrm{DD}(\theta)}}. \tag{4.2}$$

The angular correlation function is computed for the entire sample of Hα emitters[1], as well as for COSMOS and UDS separately, and it is found to be very well-fitted by a power law with the form $A\theta^{\beta}$ with θ in arcsec. The power-law fit is obtained by determining $\omega(\theta)$ 2000 times using different random samples and a range of bin widths ($\Delta \log\theta = 0.1 - 0.3$, randomly picked for each determination) and by performing a χ^2 fit to each of these (over $5 < \theta < 600$ arcsec, corresponding to 38.2 kpc to 4.5 Mpc at $z = 0.845$; these correspond to angular separations for which fitting $\omega(\theta)$ with one single power-law is appropriate; see details in Section 4.3.4). The results are shown in Figure 4.2 and presented in Table 4.1; they imply $A = 14.1 \pm 3.9$ and $\beta = -0.79 \pm 0.06$ for the entire sample (the errors present the 1σ deviation from the average). This reveals a very good agreement with the fiducial value, $\beta = -0.8$.

Recent studies (e.g. Ouchi et al., 2005) have found a transition between small and large-scale clustering (corresponding to one and two-halo clustering, respectively) at high redshift, manifested as a clear deviation from the power-law at small scales (smaller than ≈ 50 kpc for Lyman-break galaxies at $z \sim 4$, for example). While there is no definitive evidence for the one-halo term for the Hα sample presented here (especially for separations larger than $\sim 5''$ – corresponding to 38 kpc), for smaller separations the results are consistent with a departure from the power-law, but only at $\approx 1\sigma$ level. Therefore, a larger sample is required to reliably determine $\omega(\theta)$ down to the smallest scales and constrain the contribution of the one-halo term.

The best power-law fit seen in Figure 4.2 also reveals a good agreement both at small and larger scales between the COSMOS and UDS fields (see also Table 4.1); the UDS field presents a slightly higher clustering amplitude, but consistent within 1σ (fixing $\beta = -0.8$). Note that the Hα luminosity function derived in Chapter 3 for each field also revealed a good agreement between the two fields.

[1] Due to the finite area probed, the measured clustering amplitude will be underestimated by an amount C (known as the integral constrain; c.f. Roche et al., 2002) which depends on the assumed true power-law and the probed area. This is estimated as $C = 0.0023$ for the entire survey area and it only represents ≈ 0.01 per cent change in A, but it is still included, since this becomes significant for obtaining $\omega(\theta)$ at large separations; c.f. Figure 4.4.

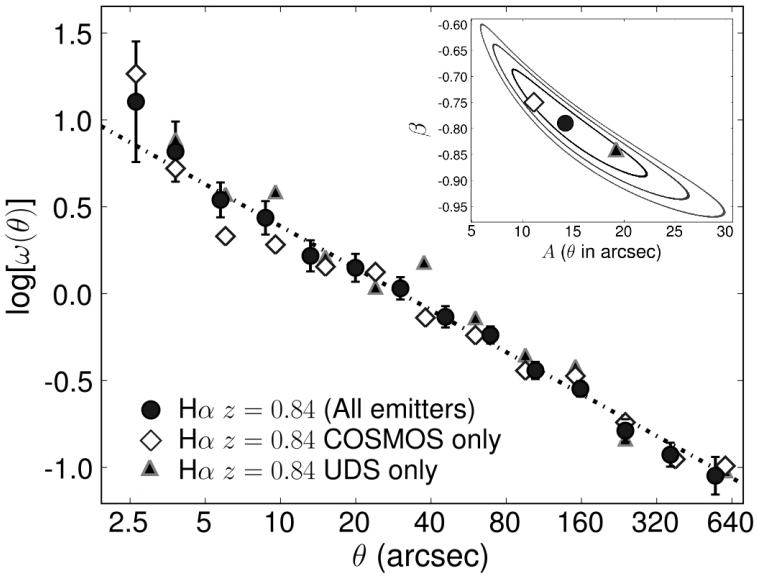

Figure 4.2: The two-point angular correlation function for the entire sample and for the COSMOS and UDS fields separately for angular separations up to 600 arcsec, and the 1σ , 2σ and 3σ co-variance contours when fitting both A and β for the entire sample compared to the results of each field. These results show a very good agreement between COSMOS and UDS, revealing that Hα emitters in completely different regions of the sky cluster with comparable amplitude and power law-slope. The results also show that there is no clear departure from the power-law for this sample of Hα emitters down to $5''$, implying that the 2-halo contribution to $\omega(\theta)$ seems to be dominant for scales larger than $\sim$50 kpc, but there is tentative evidence of a significant 1-halo contribution to $\omega(\theta)$ for smaller scales.

These results are consistent with $\sim 0.6-0.8$ deg^2 fields being sufficient to overcome most of the effects of cosmic variance when conducting clustering analysis with narrow-band surveys at $z \sim 1$ – although the agreement could be caused by chance.

4.3.2 Robust error estimation and the effect of cosmic variance

The survey covers 1.3 deg^2 in two completely independent fields; this is a fundamental advantage over smaller surveys which only probe one single field, as it allows, in principle, a reliable estimate of possible errors due to cosmic variance. In order to achieve this, $\omega(\theta)$ is estimated over randomly picked square areas of different sizes (from 0.05 deg^2, corresponding to the area probed by one WFCAM chip, up to 0.5 deg^2) in COSMOS and UDS. The minimum number of emitters ranges from 15 to 65 within the smaller areas used (0.05 deg^2). Either 100 or 1000 randomly chosen regions are considered for each area (100 for 0.3-0.5 deg^2 and 1000 for smaller areas) and a power law is fitted to each $\omega(\theta)$ determination by fixing $\beta = -0.8$. For each area, the standard deviation on the amplitude A is used to quantify the uncertainty. The results are shown in Figure 4.3 and demonstrate that the measured standard deviation is effectively reduced with area. The error in A (per cent) can be approximated by a power law of the form $20 \times \theta^{-0.35}$ with θ in deg^2; extrapolating this suggests an error slightly lower than $\sim$ 20 per cent for the total area of the survey, and also agrees with the small difference found

Table 4.1: The power-law fit parameters which best describe $\omega(\theta)$ for Hα emitters at $z = 0.845$, resulting from computing $\omega(\theta)$ 2000 times. These were obtained over $5 < \theta < 600$ arcsec, corresponding to 38 kpc to 4.5 Mpc at $z = 0.845$, avoiding both the possible one-halo clustering contribution (at the smallest scales) and the break of the Limber's approximation (at the largest scales). Note the degeneracy between A and β in Figure 4.2. $A_{\beta=-0.8}$ is obtained by fixing $\beta = -0.8$, the fiducial value and in excellent agreement with what has been found for the entire sample with or without possible/likely AGN contamination. An error of 20 per cent is added in quadrature to the random error in $\Delta A_{\beta=-0.8}$ to account for cosmic variance for the entire sample (or 25 per cent when considering just one sub-field – COSMOS or UDS, c.f. Section 4.3.2).

Sample ($z = 0.84$)	**Number** #	**A** (θ in arcsec)	β	$A_{\beta=-0.8}$ (θ in arcsec)
All Emitters	734	14.1 ± 3.9	-0.79 ± 0.06	14.2 ± 3.1
No AGN	660	13.6 ± 4.4	-0.78 ± 0.07	14.1 ± 3.0
No likely AGN	700	15.4 ± 4.0	-0.81 ± 0.06	14.6 ± 3.2
COSMOS	477	11.1 ± 3.0	-0.75 ± 0.08	13.8 ± 3.7
UDS	257	19.2 ± 8.9	-0.84 ± 0.15	18.4 ± 5.5

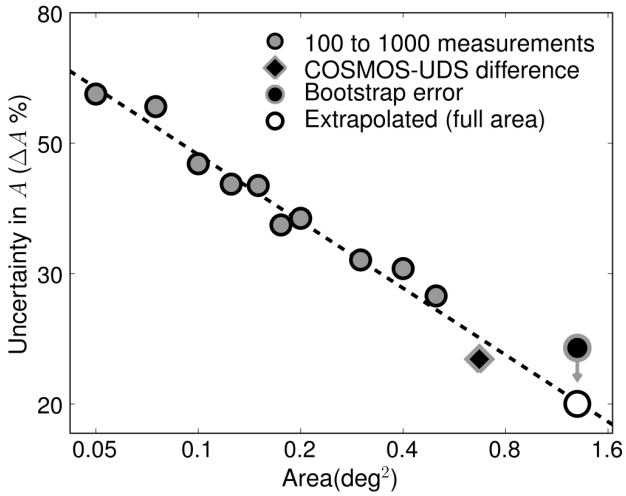

Figure 4.3: The uncertainty in A (per cent; $\Delta A = \sigma/A \times 100$, with $\beta = -0.8$) derived from 100-1000 $\omega(\theta)$ measurements on sub-samples spanning different areas within the complete 1.3 deg^2 (up to 0.5 deg^2) – which is considered to be mostly due to cosmic variance. This reveals that ΔA decreases with increasing area and this trend is very well fitted by a simple power-law ($20 \times \theta^{-0.35}$ per cent, with θ in deg^2, shown by the dashed line). The simple standard deviation between results from COSMOS and UDS is also shown for comparison. The error estimated from the bootstrap analysis and that given by extrapolating the fitted power-law are also shown for the full area.

between COSMOS and UDS (see Figure 4.3). Furthermore, this suggests that one requires areas of $\sim 7\,\mathrm{deg}^2$ (the HiZELS survey target) or more to reduce the effects of cosmic variance to less than 10 per cent.

These estimates could still slightly underestimate the errors, mostly because at larger areas the

number of approximately independent areas is strongly reduced. An alternative estimate of the clustering uncertainty can be derived using a bootstrap analysis. Since this often leads to a slight over-estimation of the errors, it can be combined with the previous analysis to give an approximate range for the expected error. The analysis is done by naturally dividing the complete sample into 26 regions of $\sim$0.05 deg^2 each (these are the minimum individual probed areas as these are covered by one WFCAM chip) and computing $\omega(\theta)$ with 26 randomly picked regions each time for 10000 times. Fitting all realizations with a power law (fixing $\beta = -0.8$) results in a distribution with a standard deviation of 23 per cent in the clustering amplitude, A. When compared and combined with the previous estimation ($\approx$ 18 per cent error), it suggests an error of $\sim$ 20 per cent in the clustering amplitude; this will be added in quadrature to the directly calculated errors in A.

4.3.3 AGN contamination

Some of the Hα emitters are likely to contain an AGN. By using emission-line ratio diagnostics for a small subset of emitters in *z*COSMOS, one can estimate a contamination of $\sim$15 per cent AGN in the sample. More recently, Garn et al. (2010) performed an extended search for AGN within the sample using several methods for identifying those sources, such as radio, X-rays and mid-infrared colours. This resulted in the identification of a maximum of 74 AGN (40 in COSMOS and 34 in UDS). From these, 34 are classified as likely AGN and the remaining 40 as possible AGN – this corresponds to an estimated $\sim$5-11 per cent AGN contamination within the sample.

The AGN may well have different clustering properties from the star-forming population. However, the nature of these potential AGN contaminants is very unclear, particularly the origin of the detected Hα emission. For example, they are mostly morphologically classified as irregulars and mergers and they span the entire luminosity range; it thus seems that although some of them might have their Hα emission powered by the AGN, they may well be undergoing significant star-formation. Indeed, recently, Shi et al. (2009b) presented a study of unambiguous AGN at $z \sim 1$, showing that at least half of the sample shows clear signatures of intense star-formation.

In order to understand how AGN contaminants might affect the clustering measurements, the angular correlation function was calculated after removing all the potential AGN contaminants. This results in no statistical change in either A or β for the entire sample (see Table 4.1). Removing only the likely AGN leads to an identical result. However, the true AGN contaminants (and the possible bias they may introduce) might well have a larger effect on the results when studying the clustering as a function of host galaxy properties (presented in Section 4.4), since for certain host galaxy properties the AGN contamination may be significantly higher than in the sample as a whole.

To ensure that the analysis is really tackling the AGN contamination and to robustly determine the clustering properties of each sample being studied (and test trends), all the clustering properties in this Chapter (for the $z = 0.84$ sample and sub-samples) are derived from a combination of measurements from samples with and without possible AGN contaminants. In practice, $\omega(\theta)$ is computed 500 times each using i) all the emitters in the sample, ii) removing likely AGN, and iii) removing all (likely

plus possible) AGN. χ^2 fits are obtained for each realization of each sample and the total resulting distribution is used for the analysis. This also allows to carefully confirm that there is a good degree of consistency between the 3 different distributions and in no case is the difference between samples with and without AGN larger than the 1σ errors. This mostly results in estimating larger errors than those which would be obtained from either simply excluding all AGN or not dealing with AGN contamination, and therefore represents a conservative approach.

4.3.4 Real-space correlation

First order approximation: Limber's equation

The real-space correlation, r_0, is a very useful description of the physical clustering of galaxies when the spatial correlation function is well-described by $\xi = (r/r_0)^{\gamma}$. The inverse Limber transformation (Peebles, 1980) can be easily used to obtain an approximation of the spatial correlation function[2] from the angular correlation function, provided the redshift distribution is known. For narrow-band surveys, the expected redshift distribution depends solely on the shape of the narrow-band filter profile; this can be well approximated by a Gaussian[3], which, for the Hα emission-line, corresponds to a redshift distribution centered at $z = 0.845$ with $\sigma = 0.0075$. This can be compared with the redshift distribution from Hα emitters confirmed by *z*COSMOS (93 sources) which has a mean redshift of 0.844 and $\sigma = 0.0076$; the excellent agreement reveals that the real redshift distribution should be very close to the one assumed.

In order to calculate the real space correlation length, r_0, and when performing the de-projection analysis, it is assumed that the redshifts are drawn from this Gaussian distribution and that the real-space correlation function is independent of redshift [c.f. Geach et al. (2008) or Kovač et al. (2007)] over the redshift range probed; this is a very good approximation, since the redshift distribution is extremely narrow. Contamination by sources which are not Hα emitters at $z = 0.84$ could have a significant effect on r_0, since the real redshift distribution will be different from the one assumed. Nevertheless, in Chapter 3 the sample was studied to find that only 2 out of 90 sources with spectroscopic redshifts that had been photometrically selected as Hα emitters were not real Hα emitters (one [SII]6717 emitter at $z = 0.79$ and a [OIII] 5007 emitter at $z = 1.42$, which were then removed from the sample). This conclusion is drawn from the analysis of limited spectroscopic data ($\sim$ 20 per cent of the HiZELS sample in COSMOS), but contamination at that level will only lead to underestimating r_0 by a maximum of 6 per cent[4]. Throughout this Chapter, a 5 per cent correction is applied when

[2] Limber's equation is an approximation that breaks down for large angular separations when one uses a narrow filter, but can still be used to obtain at least a first approximation of r_0 within $\approx$ 15 per cent for the NB_J filter used; see Section 4.3.2 for details.

[3] A simpler way to model the narrow-band filter is to assume it is a top-hat; this results in a Hα redshift distribution: 0.845 ± 0.015. The two approaches produce results for different r_0 determinations which are consistent within 5 per cent.

[4] Assuming that contaminants will not cluster significantly, the contamination fraction of f will result in a maximum underestimation of A given by $(1\text{-}f)^2$, and an underestimation of r_0 given by $\sim(1\text{-}f)^{2/|\gamma|}$.

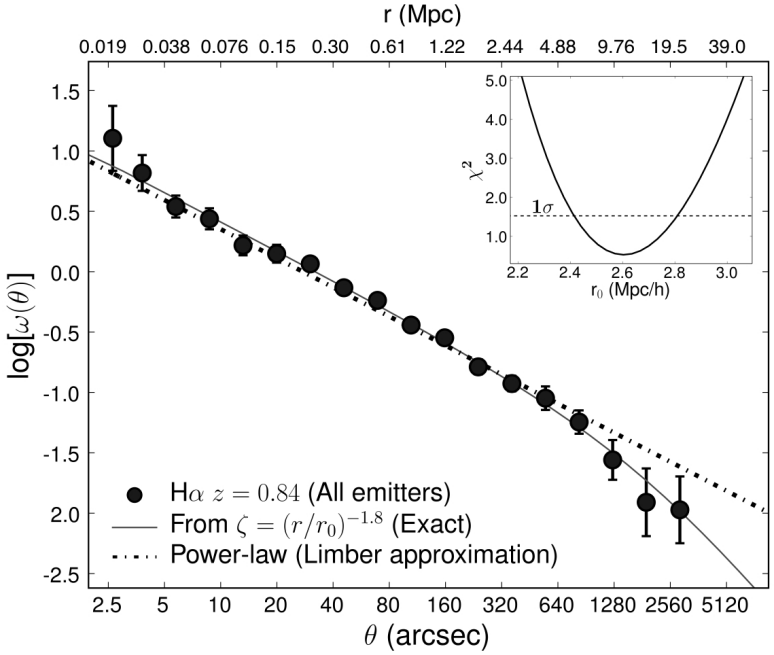

Figure 4.4: The two-point angular correlation function for the entire sample, compared with the simple power-law fit expected from the Limber's approximation. These are compared with the best (from a χ^2 fit – shown in the figure) exact angular correlation function obtained with the narrow-band filter profile for a spatial correlation function given by the power-law $\xi = (\mathrm{r}/\mathrm{r}_0)^{\gamma}$, with $\gamma = -1.8$ and $\mathrm{r}_0 = 2.61 \pm 0.13\,\mathrm{h}^{-1}\,\mathrm{Mpc}$ (not corrected for contamination; errors directly from χ^2), revealing an excellent agreement with the data. This also reveals the regime for which the Limber's approximation breaks for this particular case (~ 600 arcsec for a ~ 15 per cent difference; c.f. Simon 2007 for a general analysis of the typical separation at which Limber's approximation breaks down).

computing r_0 to account for the expected contamination.

Computing r_0 for each realization of $\omega(\theta)$ fitted with a power-law with $\beta = -0.8$ results in $r_0 = 2.5 \pm 0.3\,\mathrm{h}^{-1}\,\mathrm{Mpc}$ for the entire sample, or $r_0 = 2.6 \pm 0.3\,\mathrm{h}^{-1}\,\mathrm{Mpc}$ when accounting for 5 per cent contamination. Note that the 20 per cent error in A due to cosmic variance results in an error of 11 per cent in r_0, and this is added in quadrature. However, as mentioned before, Limber's equation is only an approximation which can potentially result in significant errors for narrow-band surveys at high redshift. Section 4.3.4 describes how r_0 is robustly calculated by fully de-projecting $\omega(\theta)$.

Accurate determination of r_0 for narrow-band surveys

The errors introduced by the Limber's approximation are tackled by numerically integrating the exact equation connecting the spatial and angular correlation functions (following Simon, 2007). This relation implies that spatial correlation functions described by $\xi = (\mathrm{r}/\mathrm{r}_0)^{\gamma}$ are projected as angular correlation functions with slopes $\beta = \gamma + 1$ for small scales and $\beta = \gamma$ for large angular separations when using a narrow filter – see full discussion in Simon (2007).

Here, it is assumed that the spatial correlation function is given by the power-law $\xi = (\mathrm{r}/\mathrm{r}_0)^{\gamma}$ (as this is able to reproduce the observed $\omega(\theta)$ very well with $\gamma = -1.8$), and that the narrow-band

filter profile is described by a Gaussian as detailed in Section 4.3.4. The following is then numerically integrated for the same angular separations as for the data and a χ^2 fit is done for $\omega(\theta)$ around the value of r_0 obtained in the previous Section:

$$\Delta\omega(\theta) = \psi^{-1} \int_0^{+\infty} \int_{s\sqrt{2\phi}}^{2s} \frac{2\mathrm{f_S}(s-\Delta)\mathrm{f_S}(s+\Delta)}{\mathrm{R}^{-\gamma-1} r_0^{\gamma} \Delta} \mathrm{d}\mathrm{R}\mathrm{d}s, \tag{4.3}$$

where $\psi = 1+\cos\theta$, $\phi = 1-\cos\theta$, $\Delta = \sqrt{(\mathrm{R}^2 - 2s^2\phi)/(2\psi)}$ and $\mathrm{f_S}$ is the profile of the filter being used in co-moving distance (assumed to be a Gaussian distributed value with an average of $2036.3\,\mathrm{h}^{-1}\,\mathrm{Mpc}$ and $\sigma = 14.0\,\mathrm{h}^{-1}\,\mathrm{Mpc}$). The χ^2 fitting results in a much more robust estimate of r_0 and allows the use of $\omega(\theta)$ up to larger angular separations than 600 arcsec, a regime for which a single power-law starts to become inadequate (as β changes from $\gamma+1$ to γ, c.f. Figure 4.4). For the entire sample, however, this leads to little change: $\mathrm{r}_0 = 2.7 \pm 0.3\,\mathrm{h}^{-1}\,\mathrm{Mpc}$ (this includes a 5 per cent correction for contamination, while the errors also include cosmic variance – this error estimation has been discussed in Section 4.3.2). Indeed, whilst Limber's equation breaks down for large galaxy separations, it is shown to do well as long as only smaller angular distances are considered. Note that real-space correlations for different samples (see Table 4.2) are computed in the following sections using the same procedure described here.

The dependence of the z distribution on limiting line luminosity for NB surveys

Since the narrow-band filter profile is not a perfect top-hat, emitters with different Hα luminosities are detected over a slightly different range of redshifts. As the exact relation between $\xi(\mathrm{r})$ and $\omega(\theta)$ depends on the redshift distribution (given by the filter profile), assuming the same redshift distribution for different luminosity limits can lead to biases, especially when looking at a possible relationship between the clustering amplitude and Hα luminosity.

This potential bias is studied by performing the same simulations described in Chapter 3. Briefly, the Hα luminosity function presented in Chapter 3 is used to generate a fake population of emitters equally distributed over a wider range of redshifts than those probed by the narrow-band filter and this is used to look at the recovered redshift distribution of sources as a function of measured luminosity. The redshift distribution is found to become continuously narrower with increasing Hα luminosity limit[5], although all the distributions can be equally well-fitted by a Gaussian. The variation can be written as a function of observed Hα flux as:

$$\sigma = -\eta \times (\log F_{\mathrm{H}\alpha(\mathrm{limit})} - \log F_0) + \sigma_0, \tag{4.4}$$

where F_0 is a flux limit at which the redshift distribution is relatively well understood and σ_0 is the width of the redshift distribution at that flux limit; for the NB_J filter, $\eta = 0.00117$, as derived from simulations.

[5] Although intrinsically more luminous sources are detectable over a wider redshift range, their detection in the wings of the filter leads to an under-estimation of their luminosity; galaxies are only measured to be luminous in Hα when the emission line is being detected near the peak of the filter profile.

Over the luminosity range of the sample (and for the assumed luminosity function and the real filter profile), neglecting this effect results in a maximum over-estimation of 8 per cent; this is only found when computing r_0 for a sample containing the brightest 5 per cent emitters (the ≈ 40 brightest emitters, for which $\sigma \approx 0.0065$). Nevertheless, narrow-band surveys which span a much wider luminosity range will be much more sensitive to this and line-luminosity trends could naturally arise from this bias.

This luminosity dependence is fully taken into account when computing r_0 for sub-samples defined by different Hα luminosity/SFR limits. For the analysis of other sub-samples, if the Hα luminosity distribution does not present any clear offset from that of the entire survey, it is assumed that the redshift distribution of those sub-samples is very well approximated by the complete redshift distribution.

4.4 The clustering dependences on galaxy properties

As discussed in the introduction, in the local Universe the clustering has been shown to depend on several host galaxy properties. At $z = 0.24$, Shioya et al. (2008) have shown that the clustering of Hα emitters seems to be stronger for the most Hα luminous sources, but so far testing and quantifying that clustering dependence at higher redshifts for Hα emitters has not been possible, as surveys have lacked area and sample size. The HiZELS sample is large enough to achieve this.

The complete sample is divided into several sub-samples in order to investigate the clustering as a function of fundamental observable host galaxy properties. These include i) Hα luminosity corrected for extinction as in Chapter 3 (1 mag), ii) rest-frame K luminosity (M_K), iii) rest-frame B luminosity (M_B) and iv) morphological class (discs, irregulars; non-mergers, mergers). The $\omega(\theta)$ correlation function is computed for each sub-sample (a single example is shown in Figure 4.5, presenting $\omega(\theta)$ for the brightest and faintest halves of the sample with respect to Hα luminosity). The approach detailed in the previous sections is then used by firstly computing r_0 using Limber's approximation power-law fit to $\omega(\theta)$ (fixing $\beta = -0.8$ and restricting the analysis to $5 < \theta < 600$ arcsec), and then using the exact relation between the space and angular correlation functions to improve the r_0 estimation determined. This analysis also accounts for the potential AGN contamination in the sample, following the procedures described at the end of Section 4.3.1 (computing $\omega(\theta)$ with and without the possible AGN contaminants and using the obtained distribution). The results obtained when splitting the sample into different sub-samples are presented in Table 4.2, Figure 4.6 and Figure 4.7. For sub-samples obtained from the complete survey area, an error of 11 per cent in r_0 is added in quadrature to the 1 σ errors (see Section 4.3.1), while for sub-samples derived based on morphology an extra 14 per cent error is added in Δr_0 (for the COSMOS field only).

4.4.1 Hα luminosity/ Star-formation rate

Following previous studies, such as Shioya et al. (2008), one can do a simple splitting of the sample in two halves with the same number of emitters (367 with $41.95 < \log L_{H\alpha} < 43.18$ erg s^{-1} and equal

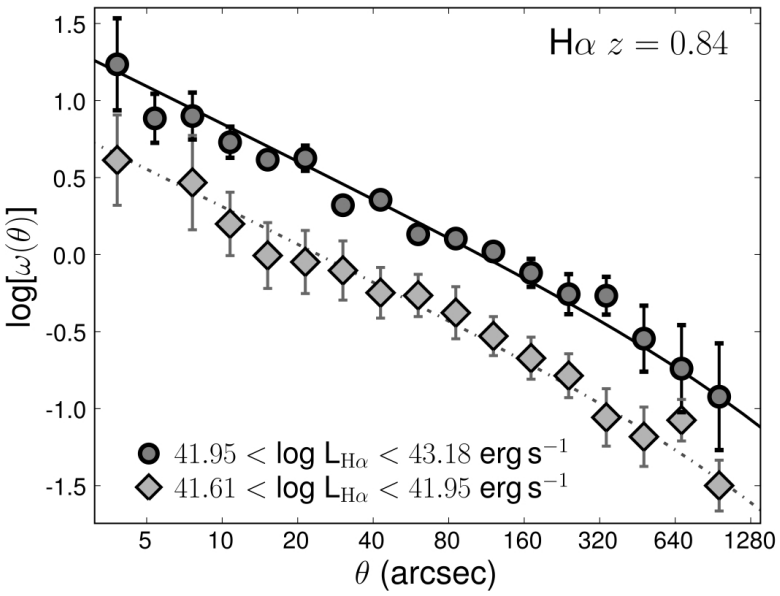

Figure 4.5: The two-point angular correlation function for sub-samples obtained by splitting the sample in 2 halves based on Hα luminosity/SFR. These clearly show that the clustering amplitude is higher for galaxies with higher Hα luminosities, implying that the most active star-forming galaxies are more clustered than the least active. Lines show the best χ^2 to the exact relation between $\xi(r)$ and $\omega(\theta)$ by fixing $\gamma = -1.8$, which (after applying all corrections already detailed) result in $r_0 = 4.84 \pm 0.58\,h^{-1}$ Mpc for the brightest emitters and $2.52 \pm 0.41\,h^{-1}$ Mpc for the faintest half (in Hα luminosity) of the sample.

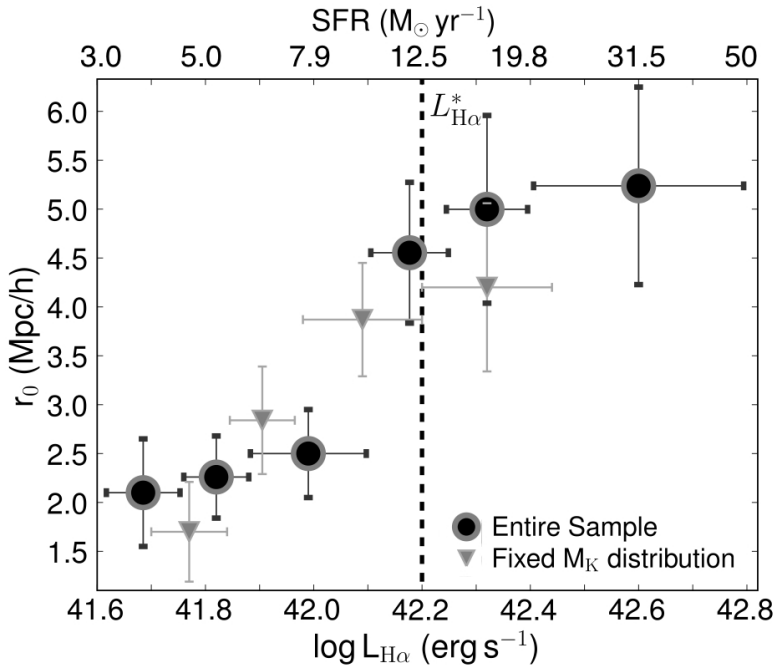

Figure 4.6: The dependence of the clustering length, r_0, with Hα luminosity at $z = 0.84$. This clearly reveals that galaxies presenting higher Hα luminosities/SFRs are more clustered, and that galaxies above the break in the Hα luminosity function ($L^*_{H\alpha}$) are much more clustered than those below. This dependence is not a result of the known correlation between SFR (Hα luminosity) and stellar mass (M_K), as r_0 correlates as well with Hα luminosity for sub-samples with the same M_K.

Table 4.2: The correlation length (fixing $\gamma = -1.8$ and corrected by 5 per cent for contamination) for Hα emitters at $z = 0.84$. Samples with fixed M_K have $-24.44 < M_K < -22.68$ (AB) and those with fixed $\log \mathrm{L_{H\alpha}}$ have $41.71 < \log \mathrm{L_{H\alpha}} < 42.44$ ($\mathrm{erg\,s^{-1}}$). Hα luminosities are given in $\mathrm{erg\,s^{-1}}$, M_K and M_B are AB rest-frame luminosities. Unclassified sources or those with no data available were not considered. Errors include cosmic variance (11 per cent of $\mathrm{r_0}$ for the entire sample and 14 per cent of $\mathrm{r_0}$ for samples of each individual field).

Sub-sample (**H**α $z = 0.845$)	**Number** #	$\mathbf{r_0}$ ($\mathrm{h^{-1}\,Mpc}$)
All Emitters	734	2.74 ± 0.29
Pure Star-forming	660	2.61 ± 0.28
COSMOS	477	2.67 ± 0.37
UDS	257	3.13 ± 0.52
$41.95 < \log \mathrm{L_{H\alpha}} < 43.18$ $\mathrm{erg\,s^{-1}}$	367	4.84 ± 0.58
$41.61 < \log \mathrm{L_{H\alpha}} < 41.95$ $\mathrm{erg\,s^{-1}}$	367	2.52 ± 0.41
$42.40 < \log \mathrm{L_{H\alpha}} < 42.80$	46	5.24 ± 1.01
$42.25 < \log \mathrm{L_{H\alpha}} < 42.40$	55	5.03 ± 0.96
$42.10 < \log \mathrm{L_{H\alpha}} < 42.25$	92	4.55 ± 0.72
$41.88 < \log \mathrm{L_{H\alpha}} < 42.10$	243	2.50 ± 0.45
$41.75 < \log \mathrm{L_{H\alpha}} < 41.88$	173	2.26 ± 0.42
$41.62 < \log \mathrm{L_{H\alpha}} < 41.75$	125	2.13 ± 0.55
$42.20 < \log \mathrm{L_{H\alpha}} < 42.44$ (fixed M_K)	56	4.20 ± 0.86
$41.98 < \log \mathrm{L_{H\alpha}} < 42.20$ (fixed M_K)	117	3.87 ± 0.58
$41.83 < \log \mathrm{L_{H\alpha}} < 41.98$ (fixed M_K)	125	2.84 ± 0.55
$41.71 < \log \mathrm{L_{H\alpha}} < 41.83$ (fixed M_K)	117	1.70 ± 0.51
$-26.1 < M_K < -24.5$	82	3.74 ± 0.69
$-24.5 < M_K < -24.0$	116	4.24 ± 0.63
$-24.0 < M_K < -23.5$	145	3.08 ± 0.51
$-23.5 < M_K < -23.0$	145	2.72 ± 0.43
$-23.0 < M_K < -22.5$	117	2.65 ± 0.54
$-22.5 < M_K < -20.5$	116	2.31 ± 0.49
$-24.44 < M_K < -24.02$ (fixed $\log \mathrm{L_{H\alpha}}$)	90	3.85 ± 0.72
$-24.02 < M_K < -23.62$ (fixed $\log \mathrm{L_{H\alpha}}$)	104	3.33 ± 0.60
$-23.62 < M_K < -23.16$ (fixed $\log \mathrm{L_{H\alpha}}$)	119	2.25 ± 0.59
$-23.16 < M_K < -22.69$ (fixed $\log \mathrm{L_{H\alpha}}$)	99	3.08 ± 0.62
$-23.23 < M_B < -21.61$	96	4.47 ± 0.77
$-21.61 < M_B < -21.11$	186	2.97 ± 0.44
$-21.11 < M_B < -20.61$	246	2.25 ± 0.30
$-20.61 < M_B < -20.11$	145	3.92 ± 0.63
$-20.11 < M_B < -18.71$	59	2.54 ± 0.92

Table 4.3: The correlation length (fixing $\gamma = -1.8$ and corrected by 5 per cent for contamination) for different morphological classes of Hα emitters at $z = 0.84$. Samples with fixed M_K have $-24.44 < M_K < -22.68$ (AB) and those with fixed $\log \mathrm{L_{H\alpha}}$ have $41.71 < \log \mathrm{L_{H\alpha}} < 42.44$ ($\mathrm{erg\,s^{-1}}$). Hα luminosities are given in $\mathrm{erg\,s^{-1}}$ and errors include cosmic variance (11 per cent of $\mathrm{r_0}$ for the entire sample and 14 per cent of $\mathrm{r_0}$ for samples of each individual field).

Sub-sample (**H**α $z = 0.845$)	**Number** #	$\mathbf{r_0}$ ($\mathrm{h^{-1}\,Mpc}$)
Discs (COSMOS)	363	2.52 ± 0.32
Irregulars (COSMOS)	68	5.12 ± 0.88
Discs (SFR & M_K match)	109	2.59 ± 0.45
Irregulars (SFR & M_K match)	46	2.96 ± 0.80
Non-mergers (COSMOS)	298	2.30 ± 0.31
Mergers (COSMOS)	111	3.75 ± 0.50
Non-mergers (SFR & M_K match)	128	2.35 ± 0.42
Mergers (SFR & M_K match)	100	2.87 ± 0.56
Bulge-dominated discs (COSMOS)	97	2.72 ± 0.54
Disc-dominated discs (COSMOS)	204	2.51 ± 0.39

number with $41.61 < \log \mathrm{L_{H\alpha}} < 41.95$ $\mathrm{erg\,s^{-1}}$), and study the clustering properties of each of those samples. Figure 4.5 presents the angular correlation function obtained for the brightest and faintest halves of the sample, revealing that the brightest Hα emitters are much more clustered than the faintest ones. This is also very clear when one compares the spatial correlations obtained for each sample: while the brightest emitters present $\mathrm{r_0} = 4.84 \pm 0.58\,\mathrm{h^{-1}\,Mpc}$, for the faintest emitters one finds $2.52 \pm 0.41\,\mathrm{h^{-1}\,Mpc}$. It should also be noted that because γ is fixed, the significant difference in $\mathrm{r_0}$ for the two samples can not be a result from the degeneracy between γ and $\mathrm{r_0}$ (see Figure 4.2 for a similar degeneracy between β and A), contrarily to studies such as Shioya et al. (2008), which allow for both γ and $\mathrm{r_0}$ to vary; such note is valid throughout this Chapter.

With the large sample of Hα emitters obtained by HiZELS at $z = 0.84$, it is possible to perform a much more detailed investigation into the relation between $\mathrm{r_0}$ and Hα luminosity by separating the emitters into a larger number of sub-samples. Figure 4.6 and Table 4.2 show that $\mathrm{r_0}$ increases by a factor of almost 3 from the faintest Hα galaxies to the most active star-forming galaxies found above the break in the Hα luminosity function, $L^*_{\mathrm{H\alpha}}$ ($10^{42.2}\,\mathrm{erg\,s^{-1}}$).

Whilst the increase of $\mathrm{r_0}$ with $\mathrm{L_{H\alpha}}$ can be reasonably well-described by a straight-line fit ($\chi^2 = 1.4$), there are hints that there might be a stronger increase in $\mathrm{r_0}$ around $L^*_{\mathrm{H\alpha}}$. This provides a quantitative description which is in line with previous studies, but provides an unprecedented degree of detail of the relation between $\mathrm{r_0}$ and Hα luminosity/star-formation rate. Moreover, the robustness of these results is also increased by including the small correction for the fact that samples with different

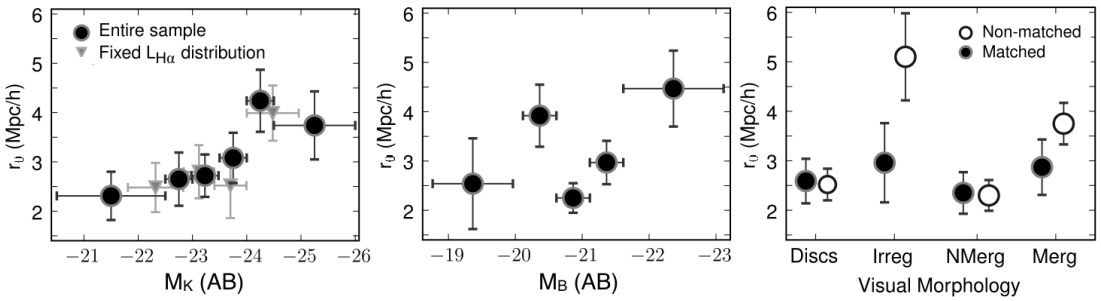

Figure 4.7: The real-space correlation length as a function of rest-frame K luminosity (left panel), rest-frame B luminosity (middle panel) and visual morphology (right panel). These results show that star-forming galaxies cluster more with increasing rest-frame K luminosity (which traces stellar mass), with this trend being maintained (but slightly weakened) even when one uses sub-samples that have the same Hα luminosity distribution. No statistically significant correlation between r_0 and rest-frame B luminosity is found. Morphologically classified irregulars and mergers cluster more strongly than discs and non-mergers, but this is due to a different Hα luminosity and M_K distribution within each population; matching these distributions results in a similar r_0.

luminosity limits will present a different redshift distribution just from considering the filter profile.

Recently, Orsi et al. (2008) made predictions for the clustering properties of Hα emitters using two different versions of the GALFORM galaxy formation model. At $z = 0.84$ and for the flux limit obtained in Chapter 3, Orsi et al. (2008) predicts $r_0 \approx 4-5\,\mathrm{h}^{-1}\,\mathrm{Mpc}$. This shows that the disagreement between the data and the models found at $z = 0.24$ and $z = 0.4$ in Orsi et al. (2008) is also found at $z = 0.84$. The model predictions would be consistent with the data for flux limits 2 times higher due to the strong clustering dependence with Hα luminosity at $z = 0.84$; however, none of the models is able to fully reproduce this r_0-$L_{H\alpha}$ relation at the moment.

4.4.2 Rest-frame continuum luminosity

Hα emitters presenting the highest rest-frame K band luminosities ($M_K < -24$) are strongly clustered, and a general trend of an increasing r_0 with K band luminosity is found (see left panel of Figure 4.7), similarly to what has been found for other populations of galaxies at different redshifts. This suggests that this correlation must be valid regardless of the population being observed – at least for the range of luminosities probed – and seems to simply imply that galaxies with the highest stellar masses (as these are expected to correlate very closely with K luminosity, although the contribution from the thermally pulsing asymptotic giant branch (TP-AGB) phase of stellar evolution can lead to some scatter in the M_K versus stellar mass relation; c.f. Maraston et al., 2006) reside in the most massive haloes. However, it is also clear that the increase of r_0 with rest-frame K luminosity, whilst continuous, is not as pronounced as the increase with star-formation rate.

In the local Universe, galaxies with higher B band luminosities (M_B) are more clustered than fainter galaxies. However, studying the clustering properties of Hα emitters at $z = 0.845$ as a function of rest-frame B luminosity reveals no statistically significant trend ($< 1\sigma$) (see middle panel of Figure

4.7). These results are in reasonable agreement with recent studies (e.g. Meneux et al., 2009), which did not find any significant dependence of galaxy clustering on B luminosity for a similar redshift range.

4.4.3 Morphological class

By splitting the sample into morphological classes (only for the COSMOS field [c.f. Chapter 3]), one finds that galaxies classified as irregulars are more clustered than those classified as discs; mergers have a measured r_0 which lies between these populations, but significantly above the non-mergers (see Table 4.3 and right panel of Figure 4.7 – open circles). However, Chapter 3 shows that irregulars and mergers are typically brighter in Hα and rest-frame K magnitude than discs (which completely dominate the faint-end of the Hα luminosity function at $z \sim 1$). Therefore, in order to understand if the clustering really does depend on the morphological class or if this is simply a secondary effect driven by star-formation rate and stellar mass dependencies, one needs to compare samples which are matched in $\log L_{H\alpha}$ and M_K. This is done by using the distribution of Hα emitters in the $\log L_{H\alpha}$-M_K plane and matching irregulars with discs and mergers with non-mergers. A $\Delta \log L_{H\alpha} < 0.02$ & $\Delta M_K < 0.02$ criteria is used: these values were chosen to ensure that the samples are very well-matched in both Hα luminosity and M_K while still retaining the sample sizes required for the analysis. The population match used still results in a severe reduction of the larger disc and non-merger samples (along with a smaller reduction of the number of irregulars and mergers), but by matching these on the basis of M_K and $\log L_{H\alpha}$ distribution, it is then possible to directly compare these populations on the basis of the morphological class only.

There is no significant difference in r_0 for the matched samples of irregulars and discs (see Figure 4.7 – filled circles) within 1σ. The r_0 difference between mergers and non-mergers is also greatly reduced, although mergers are still found to be slightly more clustered than non-mergers at $\sim 1\,\sigma$ level.

The sample of Hα emitters with disc morphologies has also been classified according to how much disc/bulge dominated each galaxy is (with ZEST; Scarlata et al., 2007). By computing the correlation length for disc dominated discs and bulge dominated discs, one finds that they present reasonably the same r_0 ($2.7 \pm 0.5\,h^{-1}$ Mpc for disc dominated and $2.5 \pm 0.4\,h^{-1}$ Mpc for bulge dominated galaxies). Therefore, the bulge-disk ratio of the studied star-forming disc galaxies does not have any significant effect on how these galaxies cluster at $z \sim 1$.

These results show that Hα luminosity and M_K (probing stellar mass) are the key host galaxy properties driving the clustering of star-forming galaxies at $z \sim 1$ and morphology is unimportant for the clustering of galaxies at high redshift, just as has been found in the local Universe (e.g. Skibba et al., 2009).

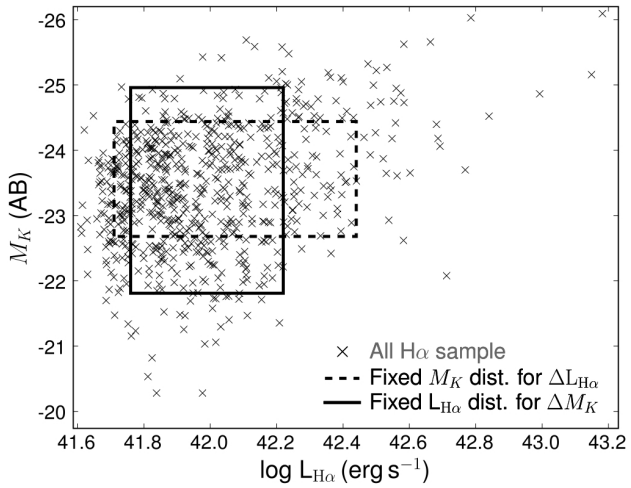

Figure 4.8: The complete 2-D M_K-log $L_{H\alpha}$ space, showing the correlation between rest-frame K luminosity and Hα luminosity, compared to the regions used to select sub-samples with the same M_K or $L_{H\alpha}$ distributions. This clearly shows that without using sub-regions of this 2-D space, samples defined only on either $L_{H\alpha}$ or M_K will present different M_K and $L_{H\alpha}$ distributions, respectively, since these quantities are correlated.

4.4.4 Hα luminosity versus rest-frame K luminosity

It has been shown that r_0 is very well correlated with both Hα luminosity (or star-formation rate) and rest-frame K luminosity (tracing stellar mass). On the other hand, star-forming galaxies both in the local Universe and at high redshift reveal a correlation between both, with star-formation rate typically being higher for galaxies with higher stellar masses (see Figure 4.8). Thus, how much is the correlation between r_0 and Hα luminosity driven by different rest-frame K luminosity distributions, and vice-versa?

In order to clearly test if both relations hold – or whether they are a result of a single strong relation between r_0 and either Hα luminosity of rest-frame K luminosity – new sub-samples are derived. To do this, two sub-regions are defined in the 2-D $L_{H\alpha}$–M_K space (see Figure 4.8). To test the r_0-$L_{H\alpha}$ correlation at a fixed M_K, the region $-24.44 < M_K < -22.68$ (AB) and $41.71 < \log L_{H\alpha} < 42.44$ erg s^{-1} (corresponding to $4.1 < SFR < 21.8$ M$_\odot$ yr^{-1}) is considered (see Figure 4.8). This region contains 409 Hα emitters, which can be divided into 4 sub-samples on the basis of Hα luminosities with the same distribution of M_K (means of -23.6, -23.7, -23.6 and -23.7 with standard deviations of 0.5 in all instances; ordered from highest to lowest in respect to Hα luminosity). Similarly, in order to test the r_0-M_K correlation, the sample is restricted to Hα emitters within the region defined by $-24.96 < M_K < -21.81$ (AB) and $41.76 < \log L_{H\alpha} < 42.22$ erg s^{-1} (see Figure 4.8) in which sub-samples split on the basis of their M_K have the same $L_{H\alpha}$ distributions (means of 41.97, 41.95, 41.95 and 41.97 and standard deviations of 0.12 in all instances; ordered from highest to lowest in M_K) – c.f. Table 4.2. The angular correlation functions of these matched sub-samples are then computed and values of r_0 derived as fully described before.

The results are presented in Table 4.2 and in Figures 4.6 and 4.7. These reveal that both Hα luminosity and rest-frame K luminosity are relevant for the clustering of star-forming galaxies, since

for a fixed distribution of one of these, a variation in the other one leads to a change in r_0. However, it should be noted that the correlation between r_0 and Hα luminosity (for a fixed M_K distribution) is maintained as highly statistically significant, while the statistical significance of the correlation between r_0 and M_K at a fixed $L_{H\alpha}$ distribution is slightly reduced.

4.5 The Clustering of Hα emitters across cosmic time

The clustering properties of the Hα emitters at $z = 0.84$ can be compared with those of the HiZELS sample at $z = 2.23$ (Geach et al. 2008) and with results derived from lower redshift surveys of Hα emitters at $z = 0.24$ and $z = 0.4$ (Shioya et al., 2008; Nakajima et al., 2008). This can then be interpreted in the context of the ΛCDM cosmological model.

4.5.1 The clustering of Hα emitters at z = 0.24

With the motivation of reliably comparing the clustering measurements at different redshifts, and since the Shioya et al. (2008) sample is publicly available, $\omega(\theta)$ is carefully re-computed for this sample.

Shioya et al. (2008) used galaxy colours to identify ~ 1000 candidate $z = 0.24$ Hα emitters within their narrow-band excess sample. For this analysis, the sample is restricted to 492 sources by limiting it to a very robust completeness limit ($L_{H\alpha} > 10^{39.8}\,\mathrm{erg\,s^{-1}}$, corresponding to $\mathrm{SFR} > 0.05\,M_\odot\,\mathrm{yr^{-1}}$). The robustness of this sample can be tested and improved taking advantage of a large set of spectroscopic data recently made available in the COSMOS field by the *z*COSMOS project. There are 75 Hα candidates with a spectroscopic redshift available from *z*COSMOS and 69 are identified as Hα emitters at $0.236 < z < 0.252$. The remaining 6 sources are identified as [SII] 6717 emitters at $0.229 < z < 0.231$ (contamination by SII emitters is even more significant at lower line fluxes, as pointed out recently by Westra et al., 2010). With the robust luminosity cut used here, this corresponds to a contamination of 8 per cent, and by removing the 6 confirmed contaminants from the sample of Hα emitters, the contamination is estimated to be 7 per cent for the remaining sample of 486 emitters. This results in underestimating r_0 by a maximum of 8.4 per cent and r_0 will be corrected by 7 per cent to account for contamination in the sample at $z = 0.24$; this is 80 per cent of the maximum correction, consistent with the approach used for $z = 0.84$.

Finally, in order to obtain r_0 (following the same procedures as for the $z = 0.84$ sample, except AGN contamination), two redshift distributions are considered: the one assumed in Shioya et al. (2008; a top-hat characterized by $z = 0.242 \pm 0.009$), and a redshift distribution derived from the distribution of the 69 spectroscopically confirmed Hα emitters, which can be well-described by a Gaussian with an average of $z = 0.245$ and a standard deviation of $\sigma = 0.006$. In practice, the values derived from both distributions agree well, but for consistency in determining r_0, the Gaussian distribution will be assumed.

The correlation length results in $r_0 = 1.8 \pm 0.2\,h^{-1}\,\mathrm{Mpc}$, with the error including random errors (from the standard deviation obtained after 1000 measurements of $\omega(\theta)$) and cosmic variance (assumed

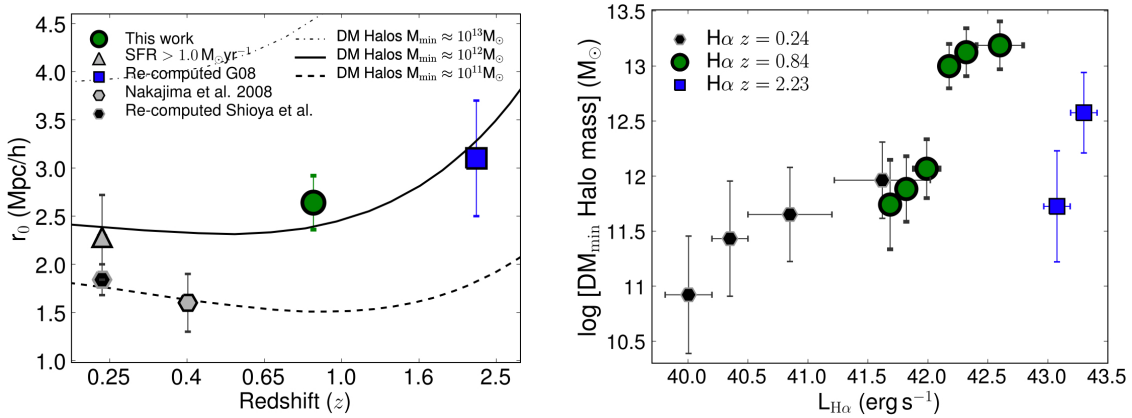

Figure 4.9: *Left*: The clustering length (r_0) as a function of redshift for Hα emitters selected by narrow-band surveys. This reveals that the Hα emitters at $z = 0.84$ studied by HiZELS reside in typical dark matter haloes of $M_{min} \approx 10^{12}\,M_\odot$, consistent with being the progenitors of Milky-Way type galaxies. The lower luminosity Hα emitters found in smaller volumes at $z = 0.24$ and $z = 0.4$ reside in less massive haloes; however, the most luminous Hα emitters at $z = 0.24$ cluster more strongly, and seem to reside in $M_{min} \approx 10^{12}\,M_\odot$, while H$\alpha$ emitters at $z = 2.23$ reside in haloes just slightly less massive. *Right*: The minimum mass of host dark matter haloes as a function of Hα luminosity; this reveals that more luminous emitters reside in more massive haloes, at any given cosmic time, but it also shows that the relation between halo mass and Hα luminosity/SFR evolves across cosmic time, with $M_{min} \approx 10^{12}\,M_\odot$ being much more effective (in respect to SFRs) at $z \sim 2$ than at $z < 1$.

to affect r_0 by 11 per cent for this area). Only separations of $5 < \theta < 800$ arcsec are used when obtaining a power-law fit: angular separations lower than 5 arcsec are not used as $\omega(\theta)$ becomes steeper, deviating from the power law; this is simply interpreted as the transition between the two-halo and one-halo clustering, happening at ≈ 20 kpc. It should also be noted that the Limber equation works well for this case, with the differences between using such approximation and integrating the full relation between $\omega(\theta)$ and $\xi(r)$ being lower than 5 per cent for $\theta < 800$ arcsec.

4.5.2 The clustering of Hα emitters at z = 2.23

It has been mentioned that Limber's equation breaks down for large angular separations and for very narrow filters. Indeed, at $z = 2.23$ the co-moving space width of the filter is extremely narrow, presenting $\sigma = 7.3\,h^{-1}$ Mpc, and representing only ≈ 0.2 per cent of the total co-moving distance to $z = 2.23$; this means that if the spatial correlation function of the Hα emitters is a power-law $\xi = (r/r_0)^{-1.8}$, then $\omega(\theta)$, measured at $5 < \theta < 1000$ arcsec can not be fitted by a power-law with $\beta = -0.8$, since this regime is probing the exact change between $\beta = \gamma + 1$ and $\beta = \gamma$.

The correlation length r_0 is therefore re-computed. This is done by using the $\omega(\theta)$ data points presented in Geach et al. (2008) and by doing a χ^2 fit to the obtained $\omega(\theta)$ from Equation 3. This assumes that the spatial correlation function is a power-law with $\gamma = -1.8$ (which is shown to reproduce the data very well) and only r_0 is allowed to vary. This procedure results in $r_0 =$

$2.6 \pm 0.5\,h^{-1}$ Mpc, with the error being derived directly from the χ^2 fit. Note that this implies a best fit $\omega(\theta)$ with $\beta \approx -1$ (for $\gamma = -1.8$) over the separations studied, agreeing well with the Geach et al. (2008) best β fit to $\omega(\theta)$ of $\beta = -1$. The value of r_0 is notably lower than the value of $r_0 = 3.6 \pm 0.4\,h^{-1}$ Mpc derived by Geach et al. (2008) from using the Limber approximation and their fitted values for A and β. A further correction is applied to account for a 15 per cent known contamination (the confirmed contaminants are all at different redshifts; this results in underestimating r_0 by 20 per cent) based on limited spectroscopic data available at the moment (J. Geach et al. in prep.); this finally results in $r_0 = 3.1 \pm 0.7\,h^{-1}$ Mpc (this also assumes a 14 per cent error in r_0 due to cosmic variance based on the area of the survey, but such uncertainty is likely to be under-estimated).

4.5.3 The clustering evolution of Hα emitters since z = 2.23

Figure 4.9 presents r_0 as a function of redshift for Hα emitters; this is the first combination of self-consistent clustering measurements for Hα emitters spanning more than half of the history of the Universe (≈ 8 Gyrs) whilst probing 4 different well-defined epochs. For comparison, the $r_0(z)$ predictions for dark matter haloes with a fixed *minimum* mass of $M_{min} > 10^{11-13}\,M_\odot$ (Matarrese et al., 1997; Moscardini et al., 1998) are also shown. A ΛCDM cosmology is assumed, together with an evolving bias model $b(z)$ from Moscardini et al. (1998) and the values from that study are used for various fixed minimum mass haloes (c.f. Geach et al. 2008).

The results show that Hα emitters found in the HiZELS survey at $z = 0.84$ (SFRs $> 3 M_\odot\,yr^{-1}$) reside in Milky-Way type haloes of $M \approx 10^{12}\,M_\odot$ – the typical haloes where $L^*_{H\alpha}$ galaxies in the local Universe reside. This contrasts with the low-Hα-luminosity galaxies for the samples at $z = 0.24$ and $z = 0.4$ (presenting SFRs $> 0.05 M_\odot\,yr^{-1}$). These seem to reside in much less massive haloes ($M_{min} \approx 10^{11}\,M_\odot$). These low redshift emitters also present very low stellar masses and low luminosities in all available bands and are therefore likely to be small, young, dwarf-like galaxies, very different from the already much more massive and active star-forming galaxies found at $z = 0.84$.

Nevertheless, motivated by the correlation between r_0 and $L_{H\alpha}$ found both at $z = 0.24$ and $z = 0.84$, it is found that if one considers only the ≈ 5 per cent highest Hα-luminosity emitters at $z = 0.24$ (a rough match in $L_{H\alpha}$ to the $z = 0.84$ sample), then these are much more clustered than the complete sample, presenting $r_0 \approx 2.4\,h^{-1}$ Mpc; this is consistent with these emitters residing in dark matter haloes of $M_{min} \approx 10^{12}\,M_\odot$. These emitters also present stellar masses closer to those presented by the $z = 0.84$ Hα-selected population, suggesting that the brightest $z = 0.24$ Hα emitters and part of the sample at $z = 0.84$ might be related.

At higher redshift ($z = 2.23$), one finds Hα emitters residing in the dark matter haloes around $M_{min} \approx 10^{12}\,M_\odot$, and it is therefore possible that at least a fraction of the very actively star-forming Hα emitters found at $z = 2.23$ (SFRs $> 70\,M_\odot\,yr^{-1}$) by Geach et al. (2008) with HiZELS will turn into the typical Hα emitters at $z = 0.84$ with a strong $L^*_{H\alpha}$ decrease.

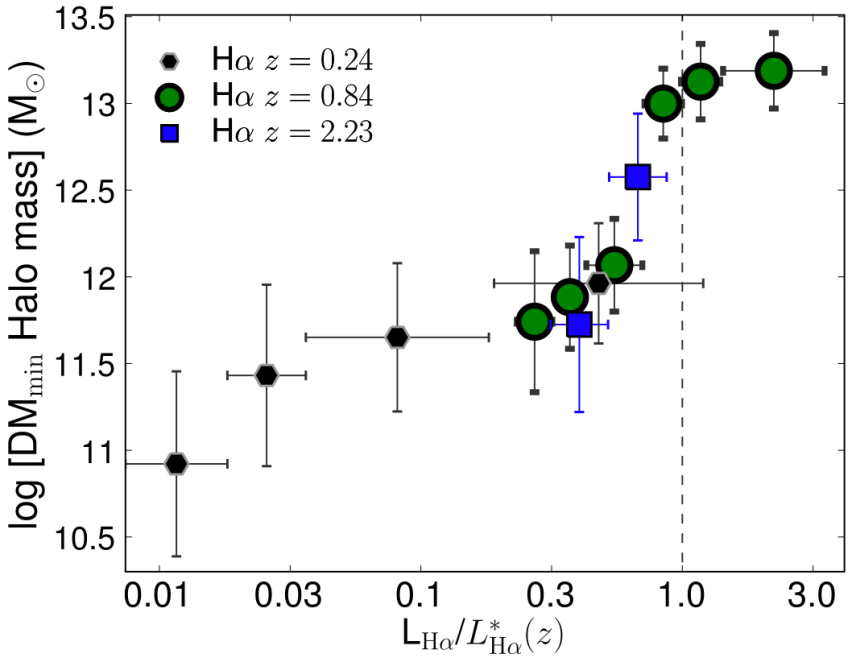

Figure 4.10: The minimum mass of host dark matter haloes as a function of $L_{H\alpha}/L^*_{H\alpha}(z)$ ($L^*_{H\alpha}(z)$ is the break in the Hα luminosity function, shown to evolve greatly from the local Universe up to $z = 2.23$ – see Chapter 3 for more details). This reveals a good agreement between the data at 3 very distinct epochs of the history of the Universe. This shows that luminous Hα emitters reside in more massive haloes, but also that across 8 billion years, emitters at the same fraction of $L^*_{H\alpha}$ seem to reside in haloes of typically the same mass.

4.5.4 The dark matter host halo-$L^*_{H\alpha}$ relation

The right panel of Figure 4.9 presents how the minimum mass of the host dark matter halo changes with measured Hα luminosity (all luminosities are derived assuming a constant 1 mag of extinction, as in Chapter 3). This shows that while the host halo mass increases with luminosity at any given redshift, there seems to be a different relation for each redshift/epoch. For a given dark matter halo mass, one finds that star-formation is tremendously more effective at high-redshift than at lower-redshift; this difference is especially pronounced from $z = 0.84$ to $z = 2.23$. On the other hand, Chapter 3 demonstrates that there is a clear evolution in the Hα luminosity function, showing that the characteristic luminosity, $L^*_{H\alpha}$, evolves by a factor of 20 from the local Universe to $z = 2.23$; the $L^*_{H\alpha}$ evolution is also most pronounced from $z = 0.84$ to $z = 2.23$. This suggests that there could be a relation between the host dark matter halo and $L^*_{H\alpha}$ found at different epochs.

In order to investigate this, the results from the right panel of Figure 4.9 are shown in Figure 4.10 after scaling the measured luminosities by $L^*_{H\alpha}$ found at each individual redshift[6]. Remarkably, this scaling reveals a clear relation between the typical dark matter halo host of Hα emitters and the

[6]The best-fit values for $L^*_{H\alpha}$ are taken from Shioya et al. (2008) at $z = 0.24$, from Chapter 3 at $z = 0.84$, and from the recent determination of Hayes et al. (2010) at $z = 2.23$. The Hayes et al. measurement combines the results of Geach et al. (2008) with deeper HAWK-I observations, and suggests a ~ 0.2 dex higher value of $L^*_{H\alpha}$ than Geach et al. (2008) derived, but within the errors of that study.

value of $L_{H\alpha}/L^*_{H\alpha}$, removing essentially all of the evolution seen in Figure 4.9. Even though there is a significant evolution in the Hα emitters population from $z = 2.23$ to the present epoch, at $L^*_{H\alpha}$, Hα emitters seem to reside in $M_{min} \approx 10^{13}\,M_\odot$ dark matter haloes, independently of cosmic time. Galaxies below the luminosity function break reside in least massive haloes, while (at least for $z = 0.84$), Hα emitters above $L^*_{H\alpha}$ seem to reside in haloes just slightly more massive than $M \approx 10^{13}\,M_\odot$.

As these results suggest an epoch-independent constancy between $L^*_{H\alpha}$ and the minimum mass of the dark matter halo host of Hα emitters, it seems plausible to suggest a simple connection between the two properties. Indeed, it is possible that the strong evolution in the break of the Hα luminosity function is being driven by the quenching of star-formation for galaxies residing in haloes much more massive than $M \approx 10^{12}\,M_\odot$, either because such haloes favour very intense and fast bursts of star-formation, capable of using the majority of the gas, or because such halo masses create the necessary conditions for AGN feedback to become important.

4.6 Summary and Conclusions

The clustering properties of Hα emitters at $z = 0.84$ have been fully detailed. These emitters are moderately clustered, with their angular correlation function $\omega(\theta)$ being very well fitted by a power law $A\theta^{-\beta}$ with $A = 15.5 \pm 4.1$ (for θ in arcsec) and $\beta = -0.81 \pm 0.05$ out to 600 arcsec (4.5 Mpc). The exact relation between the spatial and angular correlation funtion is used to show that the Hα emitters at $z = 0.84$ present $r_0 = 2.7 \pm 0.3\,h^{-1}\,$Mpc for a spatial correlation function given by $\xi = (r/r_0)^{-1.8}$, with the errors accounting for cosmic variance.

A strong dependence of the correlation length on Hα luminosity is found, with the most actively star-forming galaxies presenting $5.2 \pm 1.0\,h^{-1}\,$Mpc, while the lower Hα luminosity galaxies present a spatial correlation as low as $2.1 \pm 0.6\,h^{-1}\,$Mpc. The correlation length also depends on rest-frame K luminosity (broadly tracing stellar mass) for star-forming galaxies at $z \sim 1$ but not with rest-frame B luminosity (or only very weakly).

The r_0 correlation with $L_{H\alpha}$ is fully maintained at a fixed rest-frame K luminosity, clearly revealing that it is not a simple result of the $L_{H\alpha}$-M_K correlation; the r_0-M_K correlation is also maintained at a fixed $L_{H\alpha}$ distribution, but slightly weakened.

Irregular galaxies and mergers are found to cluster more strongly than discs and non-mergers, respectively. This, however, seems to be driven by the different Hα luminosity and M_K distribution of the distinct populations; once they are matched on the two properties, irregulars and discs present the same r_0 and mergers and non-mergers are consistent within $\approx 1\sigma$. Bulge-to-disc fraction is also shown not to be important to the clustering of star-forming galaxies at $z \sim 1$, and morphology seems to be as unimportant for the clustering at high redshift as it is in the local Universe.

Hα emitters at $z = 0.84$ found by HiZELS reside in minimum dark matter haloes of $\approx 10^{12}\,M_\odot$ similar to those of Milky Way type galaxies in the local Universe. Those are roughly the same as the haloes hosting the brightest Hα emitters at $z = 0.24$, and just slightly higher mass haloes than

the hosts of Hα emitters at $z = 2.23$. Furthermore, the minimum dark matter halo mass hosting Hα emitters increases with Hα luminosity, and a $L^*_{\mathrm{H}\alpha}$ scaling is able to combine observational results probing the last 8 billion years of the age of the Universe in one single relation. This also suggests a connection between the strong $L^*_{\mathrm{H}\alpha}$ evolution of the Hα luminosity function and star-formation being truncated in galaxies residing within dark matter haloes with masses much higher than $\approx 10^{12}\,\mathrm{M}_\odot$.

The results presented in this study provide important details on the clustering and evolution of Hα-selected star-forming galaxies at $z = 0.84$, which are mostly discs, but with a significant population of irregular and mergers above $L^*_{\mathrm{H}\alpha}$. Besides identifying and quantifying clustering relations with fundamental galaxy observables at $z \sim 1$ for the first time, the results clearly show that the highest star-formations at any epoch only occur in galaxies residing within very massive haloes. Dark matter haloes of a given mass seem to be more effective at providing the conditions for intense star-bursts at higher redshift. On the other hand, the fact that the brightest Hα emitters become rarer with cosmic time down to the present (seen by the strong evolution in the Hα luminosity function) suggests that the most massive haloes not only provide the conditions and the environment required for the highest SFRs to take place, but they also seem to be the sites in which the quenching of star-formation in galaxies occurs across cosmic time.

Chapter 5

The Roles of Mass and Environment on Star Formation at $z \sim 1$

5.1 Introduction and Motivation

At the present epoch, star formation activity is strongly dependent on environment (e.g. Lewis et al., 2002; Gómez et al., 2003; Tanaka et al., 2004; Mahajan et al., 2010): while clusters of galaxies seem to be primarily populated by passively-evolving galaxies, star-forming galaxies are mainly found in low-density environments (Dressler, 1980). It is well-established (e.g. Gómez et al., 2003; Kauffmann et al., 2004; Best, 2004) that the typical star formation rates of galaxies – and the star-forming fraction – decrease with local galaxy density (often projected local density, Σ) both in the local Universe and at moderate redshift (e.g. Kodama et al., 2004). Indeed, at $z \sim 0.2 - 0.3$, studies such as Couch et al. (2001) or Balogh et al. (2002) found that the Hα luminosity function in rich clusters, whilst having roughly the same shape as in the field, has a much lower normalisation ($\sim$ 50 per cent), consistent with a significant suppression of star formation in such environments.

Typically, active star-forming galaxies in the local Universe are also found to have lower masses than passive galaxies and, indeed, the most massive galaxies are mostly non-star-forming (an observational result often known as mass-downsizing; Cowie et al., 1996); this implies that the most massive galaxies assembled their stellar mass quicker and have not formed a significant amount of stars since then. Massive galaxies are predominantly found in high density environments, but the mass-downsizing trend is not simply a consequence of the environmental dependence, nor vice-versa. Recent studies such as Mahajan et al. (2010) – and references therein – show that the environment trends hold for both massive and dwarf galaxies, and that the mass trends also hold for both field and cluster

environments. Peng et al. (2010) also finds that the effects of mass and environment are completely separable (see Figure 1.14).

When did the environment and mass dependences of star-forming galaxies start to be observable, and how did they affect the evolution of galaxies and clusters? Clearly, in order to properly answer such questions it is mandatory to conduct observational surveys at high redshift, which can then be used to test theoretical models of galaxy evolution. By $z \sim 1$, some authors have claimed to have found a flattening or even a definitive reverse of the relation between star formation activity and local galaxy density, either by studying how the average/median star formation rates of galaxies change with local density (e.g. Elbaz et al., 2007; Cooper et al., 2008) or by looking at the star-forming fraction as a function of density (e.g. Ideue et al., 2009). Similar trends have also been suggested at $z \sim 2$ by Kodama et al. (2007), and recently Hayashi et al. (2010) found that the fraction of star-forming galaxies seems to remain constant up to the highest densities in a cluster environment at $z \sim 1.5$. These results would be naturally interpreted as a sign of a clear evolution if other studies (e.g. Finn et al., 2005; Patel et al., 2009; Koyama et al., 2010) had not indicated the opposite result. The latter studies argue that even at $z \sim 1$, and for the richest/cluster environments, both star formation rate and the star-forming fraction decline with increasing local density. Nevertheless, Koyama et al. (2010) also found that the Hα luminosity function of a rich cluster at $z \sim 0.8$ has roughly the same shape as the field luminosity function from Chapter 3, but with a higher normalisation; this implies that even if the environment is already suppressing star formation by $z \sim 1$, there is still a considerable population of star-forming galaxies in high-redshift clusters (c.f. Butcher and Oemler, 1984).

Part of the discrepancies in environmental trends between different studies may well be connected with possible mass dependences already in place at high redshift. While at $z \sim 0$ the large and deep surveys can now probe very different mass regimes with large enough samples within each environment to confirm and distinguish mass and environment trends individually (c.f. Peng et al., 2010), that is clearly not the case at high redshift, where luminosity limits inevitably bias samples towards higher mass galaxies. Thus, if mass-downsizing is already in place at high redshift, and massive galaxies are preferentially found in high density regions, samples with different luminosity limits and/or based on different selections may find contradictory results. Indeed, such downsizing trends have now been identified out to $z \sim 1.5$, by revealing that the most massive galaxies are undergoing very little or no star formation, or by finding a population of massive galaxies already in the red sequence (e.g. Bauer et al., 2005; Marchesini et al., 2009; Santini et al., 2009; Fontanot et al., 2009; Cirasuolo et al., 2010). Therefore, in order to identify and distinguish the separate roles of mass and environment on star formation at high redshift, one really requires clean, robust and large samples of star-forming galaxies residing in a wide range of environments and with a wide range of masses, together with samples of the underlying population found at the same redshift.

Narrow-band Hα surveys are one of the most effective ways to gather representative samples of star-forming galaxies at different epochs, and the scientific potential of these is now being widely explored, following the development of wide-field cameras in the near-infrared. Combined with a

wealth of high-quality multi-wavelength data in the targeted fields, wide narrow-band surveys like HiZELS can be fully explored to detail the roles of "nature" and "nurture" in galaxy evolution, by unveiling the importance of the environment on a well-defined star-forming population at a single epoch.

This Chapter presents a detailed study of the dependencies of star formation on environment and mass, and their relations with galaxy morphology, using a large sample of narrow-band selected Hα emitters at $z = 0.84$. Using this sample, it is possible to reconcile many of the apparently contradictory results in the literature. The results presented in this Chapter have been published in Sobral et al. (2011a).

5.2 Samples and Properties

5.2.1 The sample of robust Hα emitters at z = 0.84

This study uses the large sample of Hα emitters at $z = 0.84$ from HiZELS presented in Chapter 3, only slightly modified in three ways:

(i) Following Chapter 4 (and Sobral et al., 2010), the Hα sample is slightly changed on the basis of the new photometric redshifts, incorporating a higher number of bands, deeper data and accounting for possible emission-line flux contamination of the broad-bands (c.f. Ilbert et al., 2009, Cirasuolo et al. in prep.). In particular, the revised sample in UDS contains 257 Hα emitters over 0.52 deg^2, whilst that in COSMOS is unchanged (477 emitters over 0.76 deg^2).

(ii) Some of the Hα emitters may contain an AGN, which can be responsible for a significant fraction of the Hα flux and are capable of changing the host galaxy spectral energy distribution. Within the Hα sample, AGN candidates have been identified by Garn et al. (2010) using a wide range of methods. The analysis led to the identification of a maximum of 74 AGN (40 in COSMOS and 34 in UDS). From these, 40 are classified as possible AGN and the remaining 34 as likely AGN – implying $5 - 11$ per cent AGN contamination of the Hα sample at $z = 0.84$. For the analysis presented in this Chapter all 74 AGN candidates (possible and likely) are excluded from the star-forming Hα sample (though they are kept in the underlying population sample), but it has been checked that if these are retained then none of the results or conclusions of this Chapter are altered. This results in a robust sample of 660 star-forming Hα emitters at $z = 0.84$.

(iii) Finally, as detailed in §2.3, the sample is also modified to include potential Hα emitters with low equivalent widths.

5.2.2 The underlying population samples

As the samples were obtained in two of the best-studied square degree areas of equatorial sky, a wealth of multi-wavelength data are available. These include deep intermediate and broad-band imaging from the ultra-violet (UV) to the infrared (IR), making it possible for excellent photometric redshifts (photo-

zs) to be determined. These data are fundamental to test downsizing and environmental trends, since these trends can only be investigated by selecting an underlying population of galaxies within the same redshift range as the Hα population. Whilst the underlying population will never be as clean as the Hα sample, the high quality photometric redshifts at $z \sim 0.8$ available in COSMOS and UDS are good enough to do a first-pass cut at emulating the narrow-band filter selection. For the COSMOS field, the zCOSMOS DR2 secure (> 99 per cent confidence) spectroscopic redshifts can then be used to study the completeness and the contamination of various photometric-redshift selected samples (as well as to improve both, by taking out confirmed contaminants and introducing spectroscopically confirmed galaxies missed by the photometric redshifts). These results provide appropriate corrections to the photometric redshift selection. In Appendix A, a range of different initial photo-z cuts are considered and the resultant correction factors based on the contamination and completeness are calculated; these are used to show that the results in the Chapter are robust to changes in the photometric redshift cut.

The analysis in this Chapter is carried out using the background population sample with $0.82 < z_{photo} < 0.87$ for COSMOS (where photo-zs are very precise; the sample is also corrected and improved using spectroscopic redshifts), estimated to be 77 per cent complete and with a contamination of 59 per cent (when compared with the redshift range covered by the narrow-band top hat filter profile, $0.83 < z < 0.86$). For UDS, the underlying sample is obtained with galaxies having $0.79 < z_{photo} < 0.9$. Reliable contamination and completeness estimates are not available due to the lack of large spectroscopic data-sets, but the completeness can still be roughly estimated based on the recovery of Hα emitters (see Appendix A), yielding ~ 60 per cent. Also, given the uncertainty on the photo-zs, a ~ 75 per cent contamination is expected and this is assumed throughout the analysis. This, of course, results in a higher uncertainty in the following analysis for UDS, but as the next sections will fully detail, similar trends are recovered both in COSMOS and UDS.

A common $K < 23$ (observed, corresponding to rest-frame J at $z = 0.84$) cut is applied (prior to the completeness and contamination studies) to match the K completeness of the Hα emitters sample and minimize potential biases towards lower luminosity, lower stellar mass galaxies; this also guarantees that both the Cirasuolo et al. (in prep.) and the Ilbert et al. (2009) catalogues are more than 90 per cent complete and that the photometric redshifts perform to their best at the studied redshift, avoiding introducing extra biases into the analysis. Sources clearly classified as stars are also rejected. The final underlying sample in COSMOS contains 3656 sources (≈ 4800 per square degree) including all Hα emitters, while the equivalent sample in UDS contains 2688 galaxies (≈ 5100 per square degree).

5.2.3 The potential Hα emitters at z = 0.84 with EW< 50 Å

The equivalent width (EW) limit was adopted in Chapter 3 to improve the selection of emission-line objects and, in particular, Hα emitters at $z = 0.84$. It helps to avoid contamination both from bright sources, which can have an apparently significant narrow-band excess due to small colour terms, and

from weak (low EW) emission lines, which may be close in wavelength to Hα and thus difficult to distinguish with photo-zs. However, the EW limit can lead to neglecting galaxies which have emission-line fluxes above the limit of the survey but have a relatively luminous stellar continuum in the J band (rest-frame R at $z = 0.84$). In Chapter 3, this is dealt with by conducting detailed simulations which replicate the selection criteria. Simulations are used to compute a completeness correction as a function of luminosity for deriving the Hα luminosity function (c.f. Chapter 3 or Sobral et al. 2009a). These estimate that a total of ≈ 10 per cent of all Hα emitters above the flux limit may be missed by the EW> 50 Å selection in both COSMOS and UDS. However, they do not provide information about how this varies as a function of mass or environment.

Motivated by the need to provide a fair comparison of the Hα selected sample with the underlying population at the same redshift, the latter samples are used (in COSMOS and UDS). For all photo-z selected galaxies, data from Chapter 3 are used and the EW > 50 Å requirement is waived. Galaxies within the photo-z sample that present emission line fluxes (colour excesses $\Sigma > 2.5$) above the survey limit are considered to be potential additional low EW Hα emitters.

This approach results in selecting 76 additional sources in COSMOS and 42 in UDS above a flux limit of $8 \times 10^{-17}\,\mathrm{erg\,s^{-1}\,cm^{-2}}$ (these sources have EW $= 35 \pm 11$ Å, with the lowest EW being 13 Å). For COSMOS, 25 of the 76 recovered sources have high quality spectroscopic redshifts and 17 are indeed confirmed to be Hα emitters at $z = 0.84$[1], implying a contamination of 32 per cent (clearly demonstrating the initial motivation for the EW limit). After removing the confirmed contaminants, the sample is reduced to 68 Hα emitters. Furthermore, inspection of zCOSMOS spectra of the confirmed Hα emitters reveals [OII] emission lines with fluxes $\approx 1 \times 10^{-17}\,\mathrm{erg\,s^{-1}\,cm^{-2}}$, consistent with the estimated weak Hα emission for these sources. None of the sources present Hβ or [OIII] with $S/N > 1$, although 2 of these sources present a red, detectable continuum, with strong absorption lines such as H and K. Only one source is detected as a strong 24 μm source; this is flagged as an AGN in the general COSMOS catalogue.

For the UDS field, the lack of spectroscopic data does not allow for a similar investigation to be conducted, and with a wider photo-z cut being used, a 40 per cent contamination (by both lines close enough to Hα and others, as found in COSMOS) is assumed for the low EW Hα sample in UDS.

A sample containing a total of 770 Hα emitters will be used in this Chapter, but the estimated contamination rates of the samples of potential Hα emitters are taken into account by using those as relative weights in the analysis. Hα luminosities and SFRs for all Hα emitters are derived as in Chapter 3, accounting for dust extinction as in Garn et al. (2010), but it should be noted that the results remain unchanged if no, or a uniform extinction is applied to the sample.

[1]The data also reveal 1 [ArIII] emitter at $z = 0.69$, 2 [SII] emitters at $z = 0.79$, 1 [NII] emitter ($z = 0.82$), and 3 [OI] emitters at $z = 0.89$, while 1 source is not identified ($z \approx 0.99$).

Table 5.1: Parameters used to generate the SED templates using the Bruzual & Charlot (2003) package and the new Bruzual (2007) models.

τ **(Gyr)**	**E(B-V)**	Z
0.1	0	0.004
0.3	0.1	0.008
0.5	0.2	0.02 ($Z_\odot$)
1.0	0.3	
3.0	0.4	
5.0	0.5	
10.0		

5.2.4 Morphological classification with *HST* imaging

The COSMOS field has sensitive *Hubble Space Telescope* (*HST*) ACS F814W coverage, providing detailed morphological information for all samples. Automated classifications obtained by ZEST (Scarlata et al. 2007) are publicly available for the entire COSMOS field, which classifies galaxies in 3 morphological classes: 1) Early-types, 2) Disks/spirals and 3) Irregulars. Reliable estimates exist for 88 per cent of the complete underlying sample in COSMOS at $0.82 < z_p < 0.87$. Visual classifications have been obtained for Hα emitters at $z = 0.84$. Here, the same criteria are used to extend this classification to galaxies in the sample of potential Hα emitters with EW$<$ 50 Å. These sources are found to be mostly discs (65 per cent), with 15 per cent irregulars and 20 per cent early-type galaxies (the significant increase in the fraction of early-type galaxies is the most noticeable difference between the populations with different EWs, as the sample with lower EWs is able to probe much lower specific star formation rates); 33 per cent of the sample shows evidence of potential merging activity.

5.2.5 Stellar mass estimates

Deep multi-wavelength data are available for all Hα emitters and galaxies within the underlying populations and these data are used to compute stellar masses. The multi-wavelength data are used to perform a full SED χ^2 fit – normalised to one solar mass – to each galaxy; the stellar-mass is the factor needed to re-scale the luminosities in all bands from the best model to match the observed data. This method is similar to that used by Fontana et al. (2004) and Ilbert et al. (2010). The SED templates are generated with the stellar population synthesis package developed by Bruzual and Charlot (2003), but the models are drawn from Bruzual (2007). SEDs are produced assuming a universal initial mass function (IMF) from Chabrier (2003) and an exponentially declining star formation history with the form $e^{-t/\tau}$, with τ in the range 0.1 Gyrs to 10 Gyrs. The SEDs were generated for a logarithmic grid of 200 ages (from 0.1 Myr to 6.5 Gyr – the maximum age at $z = 0.84$). Dust extinction was applied to the templates using the Calzetti et al. (2000) law with $E(B-V)$ in the range 0 to 0.5 (in steps of 0.1). The models are generated with three different metallicities, including solar; the reader is referred

to Table 5.1 for a list of the parameters used (a wider range of metallicities, dust extinction and star formation histories were also tested, showing that all the results remain unchanged).

For the SED fitting, it is assumed that all Hα emitters are at $z = 0.845$ (the mean redshift for detecting Hα with the narrow-band filter)[2] and the full filter profiles are convolved with the generated SEDs for a direct comparison with the observed total fluxes. Up to 36 wide, medium and narrow bands (from the *GALEX* far ultra-violet and near ultra-violet bands to *Spitzer* 4 IRAC bands, c.f. Ilbert et al., 2010) are used for the COSMOS field, after applying all of the necessary corrections to obtain the total fluxes, as suggested and fully detailed in Capak et al. (2007) and Ilbert et al. (2009); Ilbert et al. (2010): individual aperture corrections, average systematic offsets per band and individual galactic extinction per band. For the UDS field, fewer bands are available (medium band imaging is not available), up to a total of 16, from CFHT U band in the near-ultra-violet to the 4 IRAC bands, but with the advantage of very deep and matched J, H and K data from UKIRT/UKIDSS DR5 (c.f. Cirasuolo et al. in prep.). The appropriate corrections (equivalent to those used for COSMOS) are applied to obtain total fluxes in each band for the UDS field. Once all corrections are applied, the COSMOS and UDS magnitude/flux distributions are very well matched.

Stellar masses are similarly derived for all galaxies within the underlying population at $z = 0.84$, assuming that they are all at $z = 0.845$ for simplicity (and that they are also representative of galaxies at $z \sim 0.8$); this thus provides a direct comparison with the masses estimated for the Hα population (after taking into account the completeness and contamination of the underlying sample – see Appendix A).

Finally, the reader should note that even with a large number of photometric data points available, the stellar mass estimate of each individual source is found to be affected by a 1σ error (from the multi-dimension χ^2 distribution) of ~ 0.15 dex, which results from degeneracies between the star formation time-scale τ, age, extinction and, to a smaller extent, metallicity. However, these are the typical errors found in other literature estimates at $z \sim 1$, and tests show that the results of this Chapter are robust against the uncertainties in the stellar mass estimates.

Other stellar mass estimates in COSMOS have been presented by Mobasher et al. (2007) [3]. However, these have been obtained using a much less sophisticated method[4] and are insufficiently accurate to undertake the analysis presented in this Chapter. Although the mass estimates of Cirasuolo et al. in UDS have been obtained using the same fitting method, there are some differences in the adopted photometric corrections and the SED templates used, so they are re-calculated here to ensure complete consistency between UDS and COSMOS. The reader is referred to Appendix B for a direct comparison between the stellar masses obtained in this Chapter and those from Mobasher et al. (2007) and Cirasuolo et al. (in prep.).

[2]The uncertainties in the luminosity distance (and the location of main spectral features) due to the filter profile are random and lead to much smaller uncertainties (~ 2 per cent) than other errors and degeneracies in the models.

[3]Improved mass estimates have been obtained by Ilbert et al. (2010) using the similar spectral energy distribution (SED) fitting method used here, but these are not publicly available.

[4]These were obtained from rest-frame V luminosities, M_V, and their expected relation with stellar mass using colours drawn from the best spectral-type fit (c.f. Mobasher et al., 2007).

5.2.6 Local density estimates

Local densities for each source (Hα emitters and galaxies in the underlying population samples) are estimated by conducting a 10th nearest neighbour analysis. Briefly, for each source, the angular distances to all other nearby sources are computed. These are then used to determine the projected distance to the 10th-nearest neighbour (in Mpc, using a scale of 7.64 kpc/arcsec at $z = 0.845$) and hence to estimate the local projected surface density. Sources near the edges of the fields and/or near masked regions will naturally be biased towards lower local density estimates ($\sim$5 per cent of them are in this situation). Where possible, this is fully tackled by using high-quality photo-z catalogues which exist well beyond the HiZELS NB$_J$ coverage. For regions where that is not possible ($\sim$ 4 per cent of the UDS emitters are found near the edges of the photo-z data-set or large masked regions, and $<$ 1 per cent of the COSMOS galaxies lie near masked regions), a simple correction is applied based on the fraction of area lost to the 10th nearest neighbour. Tests show that this does not introduce any bias.

Local density estimates derived using the underlying (photo-z) sample are corrected by assuming the contamination and completeness fractions derived in Appendix A. In general, given a contamination fraction, Co, a completeness fraction C, and a measured projected surface density Σ, the corrected local surface density is estimated as:

$$\Sigma_{\rm c} = \Sigma \times \frac{1 - {\rm Co}}{\rm C}. \tag{5.1}$$

When Equation 5.1 is used to correct densities estimated using different background populations (selected on the basis of photometric redshifts – see Section 5.2.2) the different estimations are found to agree very well, albeit that the scatter increases for wider (in photo-z cut) underlying population samples (as contamination becomes increasingly dominant). However, the scatter between density measurements obtained using different photo-z samples, or derived using different density estimators (e.g. 5th versus 10th nearest neighbour), is always significantly smaller ($<$ 0.18 dex) than the bin sizes used in this work ($\approx$ 0.30 dex). Thus, as Appendix A demonstrates, the main results of the Chapter do not depend on the choice of the underlying population; the samples used for the analysis are the ones presented in Section 5.2.2.

5.2.7 The clustering-density relation and interpretation

Estimating local surface densities can quantitatively distinguish higher density regions from lower density regions: but how do the derived surface densities relate to qualitative environments such as fields, groups or even clusters? Here, an attempt to associate qualitative environments with ranges of $\Sigma_{\rm c}$ will be presented, by using the real space correlation length, r_0.

Following the procedures fully detailed in Chapter 4, the entire sample of Hα emitters[5] is split

[5]The sample of Hα emitters is used instead of the photometric-redshift-selected population as the real-space correlation length can be well estimated (as detailed in Chapter 4) without major errors being introduced by the uncertainty in the exact redshift distribution and contamination.

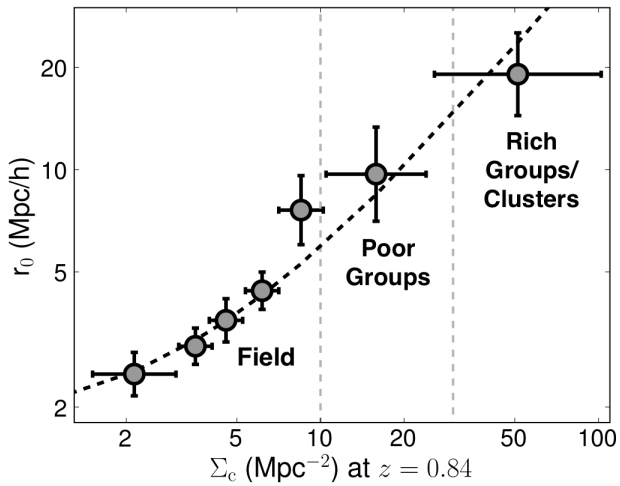

Figure 5.1: The empirical relation between the correlation length, r_0, and local density (corrected local projected density), derived for the Hα emitters. This provides an intuitive interpretation of both local densities and r_0, giving a better insight into the nature of the regions being probed and studied by the survey. This is found to be well fitted by a simple linear fit, given in Section 5.2.7. Bin sizes are chosen to guarantee that sub-samples have the same number of galaxies.

based on corrected local surface density, Σ_c, in order to compute the correlation length[6] of each sub-sample (using the exact relation between the angular and spatial correlation functions; see Chapter 4).

Figure 5.1 shows how r_0 correlates with Σ_c. The trend is found to be very well approximated (for r_0 in h^{-1} Mpc and Σ_c in Mpc^{-2}; see Figure 5.1) by $r_0 \approx 0.4 \times \Sigma_c + 1.6$.

Having been able to find an empirical link between Σ_c and the correlation length of the Hα emitters, one can associate different qualitative environments with local surface density (based on r_0). Studies such as Yang et al. (2005) found that galaxies in the poorest group environments typically have $r_0 \approx 6\,h^{-1}$ Mpc, while the rich groups have $r_0 \approx 15\,h^{-1}$ Mpc; for cluster environments, studies such as Mo et al. (1996) find typical correlation lengths of $r_0 > 15\,h^{-1}$ Mpc. For the purposes of the analysis, three main environments will be considered: field (including poor and rich field), poor groups and rich groups/clusters. Field environments are defined to be those with $\Sigma_c < 10$ Mpc^{-2} as these correspond to $r_0 < 6\,h^{-1}$ Mpc. Poor group environments are considered to be those for which $\Sigma_c = 10 - 30$ Mpc^{-2}, as samples with these densities yield the range of r_0 found for such groups ($6 < r_0 < 15\,h^{-1}$ Mpc). Rich groups/clusters are considered to be those at even higher densities, corresponding to $r_0 > 15\,h^{-1}$ Mpc, for which $\Sigma_c > 30$ Mpc^{-2}.

Of course, these simple classifications do not attempt to be fully accurate, nor do they aim to identify the exact transitions between what should be considered field, groups or cluster environments on their own. Nevertheless, they provide a valuable tool to associate the estimated local densities

[6]The analysis was carried out fixing $\gamma = -1.8$, since individual sub-samples are too small to accurately determine it. This value of γ provides a good fit to the overall sample (though note that, as discussed in Chapter 4, for narrow-band surveys this does not necessary translate to $\beta = -0.8$ as the Limber approximation would imply, and that the exact transformation between the angular and the 3-D correlation function is used).

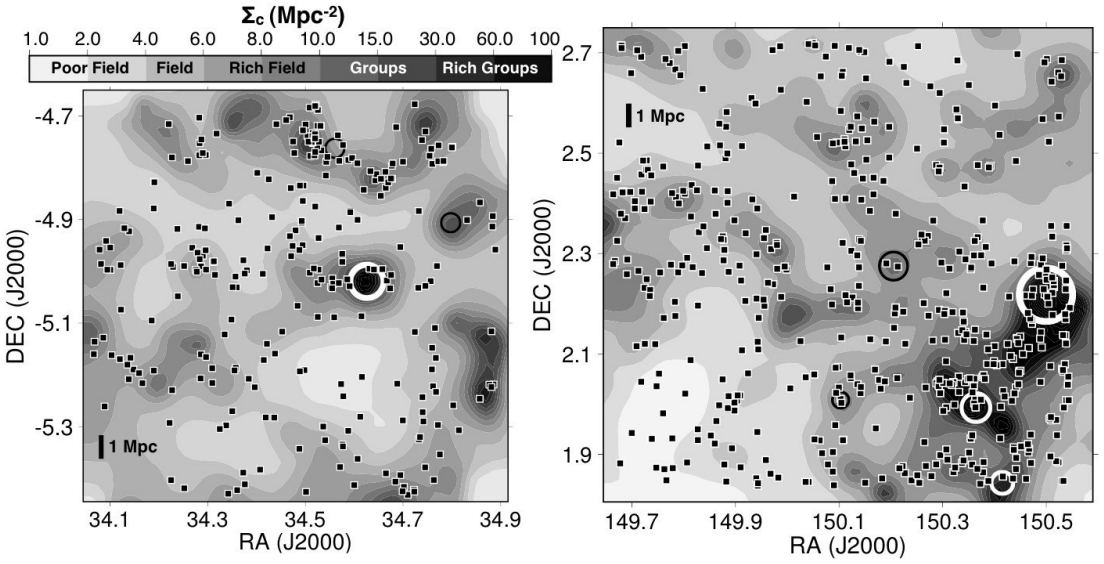

Figure 5.2: The on-sky distribution of the star-forming Hα emitters found at $z = 0.84$ in the UDS (left panel) and COSMOS (right panel) fields when compared with the local projected density field which can be linked with qualitative environments – c.f. Section 5.2.7. Sources classed as likely and potential AGN in Garn et al. (2010) are not shown. Circles mark the position of extended X-ray emission from confirmed groups and clusters (from Finoguenov et al., 2007, 2010) within the narrow-band redshift range, and are scaled to reflect the measured X-ray luminosity (in a log scale). Some lower X-ray luminosity groups are identified with black circles, while richer X-ray groups are plotted in white for good contrast. Note the very rich structure in the COSMOS field (see Section 5.2.8), providing a unique opportunity to probe the densest environments.

with different qualitative environments.

5.2.8 Confirmed clusters and groups in COSMOS and UDS

The on-sky distribution of Hα emitters can be seen in Figure 5.2, together with the different densities in which they reside in both the UDS (left panel) and the COSMOS (right panel) fields. By probing a very wide area, the Hα survey is able to target a relatively wide range of densities. Particularly, by chance, the survey is able to probe a luminous and massive ($M_{500} \approx 10^{14.3}\,M_{\odot}$) X-ray selected cluster in COSMOS at $z = 0.835$ (see Figure 5.2), along with other nearby lower luminosity X-ray groups at $z = 0.85$ which have already been reported by the COSMOS team (Finoguenov et al., 2007; Leauthaud et al., 2010). These confirmed group/cluster regions are identified as high local projected density regions, with the calibration from Section 5.2.7 clearly classifying them as group/cluster regions: this not only confirms that this study is able to probe a very wide range of environments, from the poorest fields up to rich groups/clusters, but it also backs-up the qualitative environment calibration used.

Finoguenov et al. (2010) reports on a search for groups and clusters in the UDS field; their catalogue is used to confirm a reasonably rich X-ray group in the UDS field, along with 2 other lower luminosity selected groups within the narrow-band redshift coverage of Hα (see Figure 5.2). This further confirms the wide range of densities probed by the survey, not only in the COSMOS field, but also in the UDS

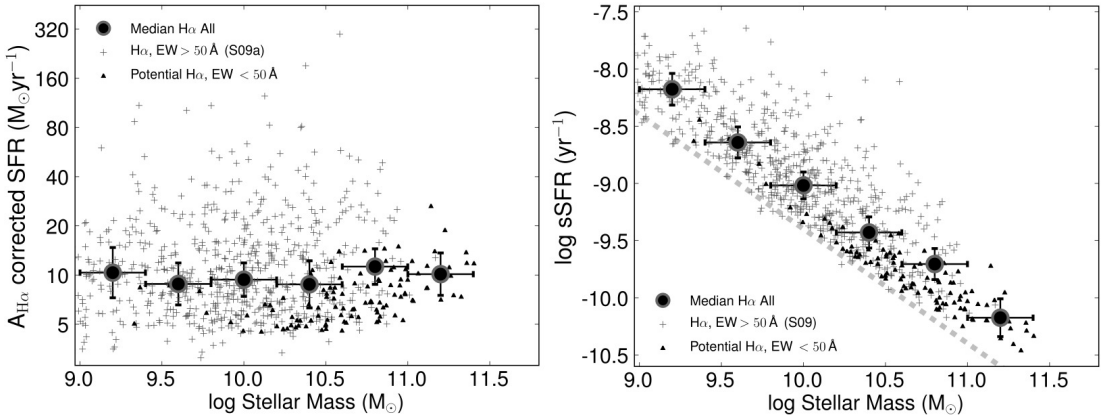

Figure 5.3: *Left*: The dust-extinction corrected SFR (Hα, SFRs obtained after applying the dust extinction from Garn et al., 2010) as a function of stellar mass for both the Hα sample presented in Chapter 3 (EW $>$ 50 Å) and the possible Hα emitters with EW $<$ 50 Å, showing that the median SFR (corrected for extinction in this way) is uncorrelated with stellar mass. Error bars present the 1 σ Poissonian errors ($\pm\sigma_m/\sqrt{\mathrm{N}}$). *Right*: the specific SFR (sSFR; SFR divided by stellar mass) falls with stellar mass, for both samples, although the steepness of such fall at the lowest masses is at least partially driven by the flux limit of the survey (dashed line; see discussion in main text). Both panels show very clearly how the nature of the samples with different EWs differs, with the sample presented in Chapter 3 being made of galaxies with lower stellar masses, higher SFRs and thus much higher sSFRs at all masses, while the lower EW sample is mostly made of massive galaxies, presenting low sSFRs.

field.

5.3 Mass-dependences and downsizing

The complete sample of Hα emitters at $z = 0.84$ present typical stellar masses of M$= 10^{10.1}$ M$_\odot$, while the general population of galaxies at the same redshift are redder in the rest-frame U-V, and present a wider range of stellar masses.

As the left panel of Figure 5.3 shows, the median Hα star formation rate (corrected for dust extinction following Garn et al., 2010) for the entire sample does not correlate with stellar mass. The latter also reveals that the lower EW Hα emitters are typically much more massive and less active. This is further confirmed by computing the specific star formation rates (sSFR, SFR per unit stellar mass) of the entire sample: as the right panel of Figure 5.3 reveals, there is a significant decrease in sSFR with stellar mass for the two samples of Hα emitters, with the lower EW Hα emitters presenting the lowest sSFRs (stressing the importance of including these, since they allow for a much wider range of masses and sSFRs to be studied).

The observed sSFR-mass trend is similar to the one found by studies such as Feulner et al. (2005), but is contrary to other determinations which suggest a much flatter relation between mass and sSFR (e.g. Daddi et al., 2007; Dunne et al., 2009; Rodighiero et al., 2010). One reason for this relates to a selection bias of the current sample due to the fixed SFR limit (dashed line in Figure 5.3): at the

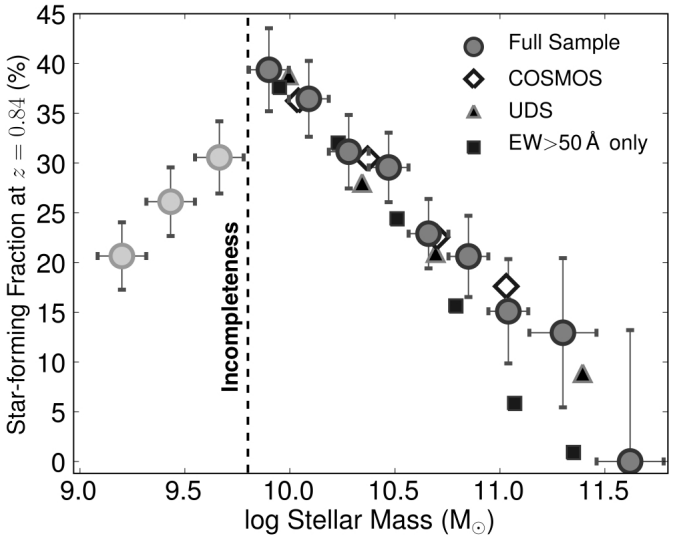

Figure 5.4: The fraction of galaxies forming stars with SFRs $> 3\,M_\odot\,yr^{-1}$ when compared to the underlying population as a function of stellar mass for the entire sample, separately for the COSMOS and UDS fields, and for the Chapter 3 sample only. The figure shows that the fraction of star-forming galaxies with SFRs above the survey limit (SFR $> 3\,M_\odot\,yr^{-1}$) is $\approx$ 40 per cent at $\sim 10^{10}\,M_\odot$, but falls sharply to 0 as a function of stellar masses. The EW cut used in Chapter 3 results in a sharper decline of the star-forming fraction, mostly because it misses the most massive galaxies with low specific star formation rates. Errors are Poissonian, but they also include a 20 per cent contribution from the contamination and completeness corrections applied.

lowest masses probed, low sSFR galaxies fall below the Hα selection limit, biasing upwards the median sSFR determined. To estimate the mass below which this bias becomes significant, the survey limit of SFR $> 3\,M_\odot\,yr^{-1}$ can be combined either with the typical median sSFR $\sim 10^{-9}\,yr^{-1}$ argued in the above studies, or with the 6 Gyr age of the Universe at $z \sim 0.8$, by considering galaxies which form stars at a fairly constant rate across their cosmic history. These both suggest that a detection bias will set in below $\sim 10^{10}\,M_\odot$ (a value confirmed by the analysis later in this section). At lower masses, the galaxies that are detected are mostly those with unusually high sSFRs (i.e., bursty).

This selection bias will therefore explain some or all of the steeper slope at low masses in Figure 5.3, but it cannot explain the strong trend at higher masses. Here, the difference from (and between) previous literature determinations largely arises from the definition of "star-forming galaxies". In the current work, all galaxies with Hα detections are classified as star-forming (SF) galaxies, leading to a clean selection cut in SFR. In contrast, previous works have often applied additional criteria to select the SF population. For example, Daddi et al. analyse 24 μm and ultra-violet data (i.e. broadly a SFR-selection, as in the current work) for a population of BzK-selected galaxies, but then they remove from consideration the galaxies classified as 'passive BzKs' (a simple colour cut). This colour cut broadly corresponds to a cut in sSFR of their galaxy population, and has the effect of excluding the high-mass low-sSFR galaxies from their sample: it is not surprising that this then leads to a relatively flat mass-sSFR relation. Thus, the nature of the "mass-sSFR relation for star-forming galaxies", which has been widely debated in the literature, is critically dependent on exactly which

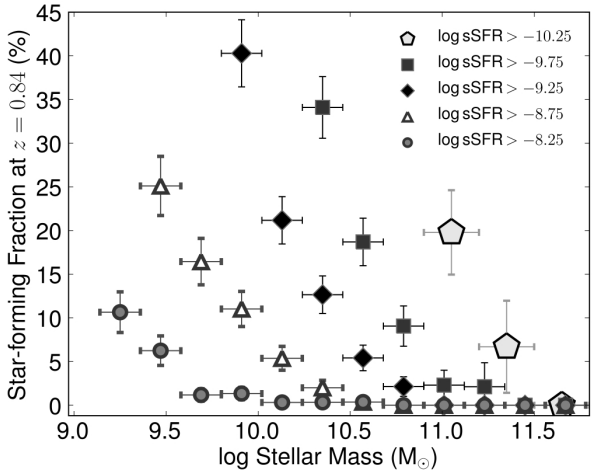

Figure 5.5: The fraction of star-forming galaxies as a function of stellar mass with a specific star formation rate greater than a given cut-off (corrected for completeness and contamination as a function of mass). This shows that the downsizing trend presented in Figure 5.4 is recovered regardless of the sSFR cut-off used, and allows for lower masses to be probed. Errors are Poissonian and take into account the contamination and completeness from the photometric redshift selected population. Points are only plotted if above the SFR$> 3\,\mathrm{M}_{\odot}\,\mathrm{yr}^{-1}$ survey limit.

galaxies one considers to be star-forming.

By comparing the sample of Hα emitters (star-forming population) with the underlying galaxy population it is possible to determine the fraction of star-forming galaxies as a function of stellar mass, which can provide an important insight into where most of the star formation is occurring at $z \sim 1$. Figure 5.4 presents the results (after correcting the underlying population for contamination and completeness as a function of mass; see Appendix A). It reveals that while for $\mathrm{M} \approx 10^{10}$ $\mathrm{M}_{\odot}$ the fraction of star-forming galaxies is $\approx$ 40 per cent, it continuously drops as a function of increasing stellar mass, effectively reaching 0 per cent just below $10^{11.5}\,\mathrm{M}_{\odot}$; the same results are independently recovered for COSMOS and UDS. Using the sample presented in Chapter 3 produces a sharper decline as a function of mass, mostly because the EW selection misses massive galaxies with very low sSFRs.

Figure 5.4 also reveals an apparent drop in the fraction of star-forming galaxies at lower masses ($< 10^{9.8}\mathrm{M}_{\odot}$). This is simply a result of the SFR limit in the Hα sample that was discussed above[7]. Nevertheless, specific star formation rate cuts can provide a view which broadly avoids this bias at the low mass end. Figure 5.5 presents the fraction of star-forming galaxies presenting sSFR above a certain value (points are only plotted if they are above the SFR limit of the survey, which avoids biases from the flux limit). The results reveal that the trend of a decreasing star-forming fraction with increasing stellar mass is recovered for galaxies with a wide range of specific star formation rates, implying that the results are not simply biased by more passive-like, massive galaxies, dominating the very massive end of the star-forming fraction-mass relation. This analysis is also able to probe to lower masses, where the same trend is recovered. Nevertheless, it should be noted that the trends

[7]In order to properly probe star-forming galaxies with lower masses one requires a much deeper survey such as ROLES (Gilbank et al., 2010b).

recovered for different sSFR cuts are not simple linear functions and, particularly for high sSFR cuts, the fraction of star-forming galaxies above a certain stellar mass is effectively zero up to the highest masses probed.

These results indicate that mass-downsizing is already in place at $z \sim 1$, with a sharp decrease of the star-forming fraction as a function of stellar mass for the highest masses. Therefore, the most massive galaxies at $z \sim 1$ are mostly non-starforming, and even those that are forming stars present very low sSFRs.

5.4 The Environment of Hα emitters

In this Section, the star-forming fraction is studied as a function of corrected surface density at $z = 0.84$. The main result can be seen in the left panel of Figure 5.6, which reveals that the star-forming fraction is relatively flat with density up to $\Sigma_c \sim 10\,\mathrm{Mpc}^{-2}$ (with hints of a slight rise, but only at a $\approx 1.5\sigma$ level), but then falls sharply for much higher densities. This seems to be associated with the qualitative transition between environments: the star-forming fraction (for galaxies producing stars at a rate higher than $3\,\mathrm{M}_\odot\,\mathrm{yr}^{-1}$) decreases with increasing density once group regimes are reached, approaching zero for the highest densities; this is in good agreement with the results presented by Koyama et al. (2010) at a similar redshift. The trend is the same in both COSMOS and UDS fields (even though the UDS field is not able to probe the highest densities found in the COSMOS X-ray cluster), revealing that this is not caused by a bias in one of the fields, nor due to the selection of the underlying population (this is very unlikely since the COSMOS and UDS photometric redshift catalogues are completely independent, obtained with different codes, and by different teams). It should be noted that the narrow-band filter is not a perfect top-hat and that some group/cluster members may have their Hα line being detected towards the wings of the filter, affecting the likelihood of detecting them as star-forming. However, particularly because two independent fields are considered in the analysis, this effect is likely to even out in the statistics, with different groups detected at all points on the filter profile. Furthermore, as detailed in Appendix A, the trend is recovered regardless of the choice of underlying populations: only small differences are found once one applies the completeness & contamination corrections given by Equation 5.1.

The right panel of Figure 5.6 shows that the median star formation rate of Hα emitters rises with increasing local density, at least up to group densities, although there are hints that this relation does not hold for highest (rich groups/cluster) densities, consistent with previous results which find that, for rich environments, the typical SFR decreases with Σ (e.g. Poggianti et al., 2008). The results in this Chapter are also consistent with Chapter 4, where the correlation length of star-forming galaxies was shown to rise with Hα luminosity. The relation between the median SFR and density is seen in both COSMOS and UDS, and is also observed for different Hα luminosity limits adopted or when the analysis is restricted to spectroscopically confirmed Hα emitters.

Moreover, as Figure 5.7 shows, the connections between environment and star formation activity

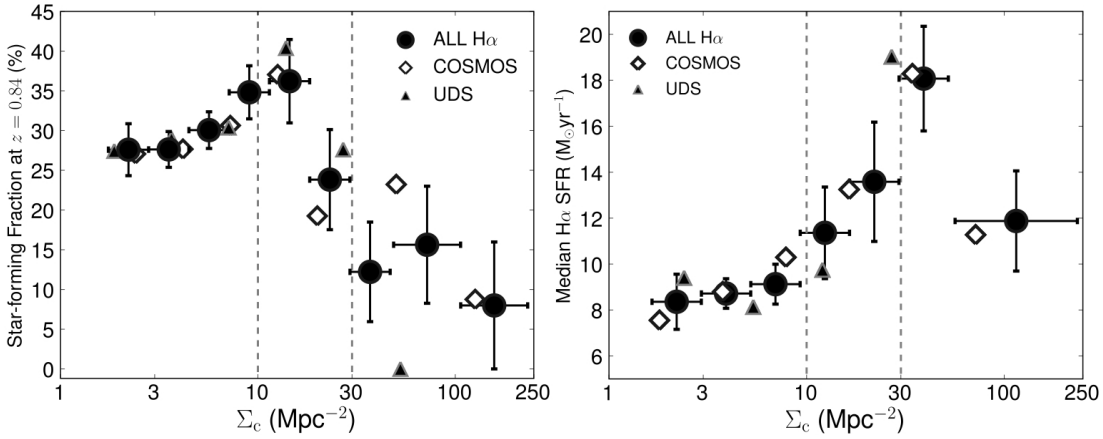

Figure 5.6: The fraction of the Hα-emitting galaxies when compared to the underlying population at the same redshift (left panel) and the median Hα star formation rate of Hα emitters (right panel), as a function of local projected galaxy surface density (for Hα emitters with SFRs $> 3\,M_\odot\,yr^{-1}$). The error bars present the Poissonian uncertainty for each bin and in the left panel also include a 20 per cent contribution from the completeness and contamination corrections applied. At the lowest densities, the star-forming fraction is relatively constant and only increases slightly, from $\sim$ 30 per cent at the lowest field densities probed to $\sim$ 35 per cent across the field environment. However, for higher densities, $\Sigma_c > 10\,Mpc^{-2}$, there is a steep decline of the star-forming fraction down to the highest (rich groups/cluster) densities probed, where the star-forming fraction is only $\approx$ 5 per cent. The results also show that the typical (median) star formation rate of Hα emitters increases continuously from the lowest densities to $\Sigma_c \sim 50$ Mpc^{-2}, although it appears to fall again in the very richest environments. This corresponds to emitters residing in groups and cluster outskirts presenting typical SFRs which are about 2 times higher than those residing in the field.

are likely to be related with the star formation mode: while star formation in the field is dominated by non-interacting galaxies, at rich group and cluster densities, the star formation seen at $z = 0.84$ in Hα is dominated by potential mergers; with this correlation being found at a 2.4σ level. In fact, Hα star-forming galaxies found in the X-ray core of the massive cluster in COSMOS are all mergers.

The environment seems to be connected with a change in the star-forming fraction, the typical star formation rate and the nature of Hα emitters at $z = 0.84$; how are these changes manifested in the Hα luminosity function? While it is nearly impossible to accurately determine the volume occupied by galaxies residing in different environments, one can arbitrarily normalise any obtained Hα luminosity function to investigate changes in $L^*_{H\alpha}$ and the faint-end slope, α: this approach can provide the insight that one needs to further investigate the relation between star formation and environment.

Figure 5.8 presents the normalised Hα luminosity functions[8] appropriately weighted as discussed in Section 5.2.3) for different local projected densities. By fixing ϕ^*, both $L^*_{H\alpha}$ and the faint-end slope, α, are allowed to vary in order to obtain the best Schechter function fit to each luminosity function. The results reveal that while the value of $L^*_{H\alpha}$ is consistent within the errors for all environments probed by the HiZELS survey at $z = 0.84$ ($\log L^*_{H\alpha} = 42.47 \pm 0.05, 42.44 \pm 0.07, 42.45 \pm 0.09\,erg\,s^{-1}$

[8]Hα luminosity functions are computed using the entire sample of Hα emitters, which includes the low EW sample. Conclusions remain unchanged even if the low EW sample is excluded.

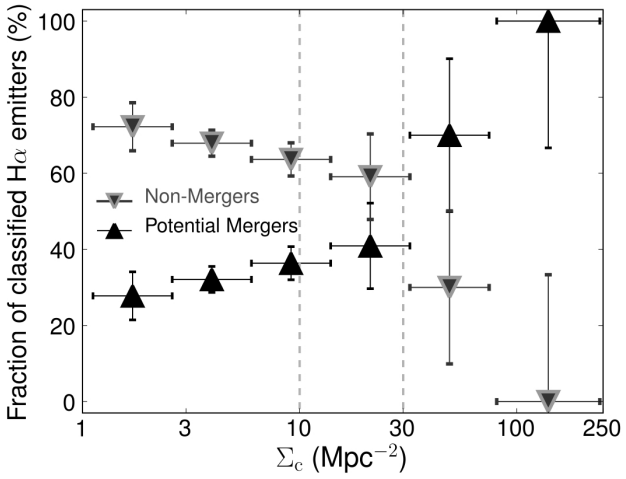

Figure 5.7: The potential merger and non-merger fractions as a function of projected local surface density (errors are Poissonian). This reveals that the fraction of potential mergers is reasonably flat at ~ 33 per cent for field densities but is then found to increase continuously with density, reaching ≈ 100 per cent at rich groups/cluster densities.

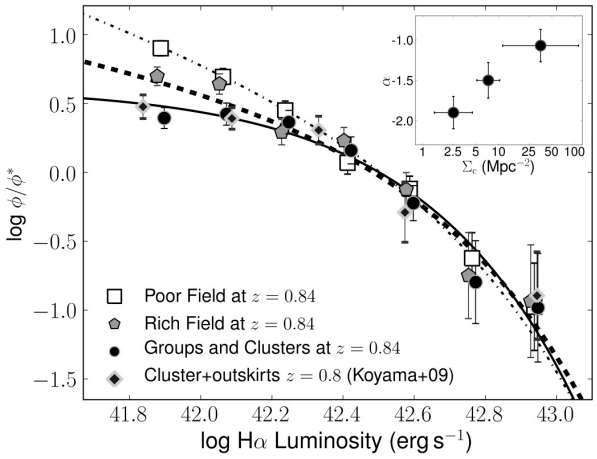

Figure 5.8: The normalised Hα luminosity function for different environments, with the best-fit Schechter functions. While the characteristic luminosities, $L^*_{\mathrm{H}\alpha}$, of the different luminosity functions are in very good agreement within the errors, the results show a significant difference in the faint-end slope, α, as a function of local surface density. As shown in the inset, this is found to be very steep ($\alpha \approx -1.9$) for the lowest densities (poor field, $\Sigma < 5\,\mathrm{Mpc}^{-2}$), shallower for medium densities (rich field, $5 < \Sigma < 10\,\mathrm{Mpc}^{-2}$, with $\alpha \approx -1.5$) and very shallow for groups and clusters ($\Sigma > 10\,\mathrm{Mpc}^{-2}$), with $\alpha \approx -1.1$. Recent results from Koyama et al. (2010), which studied one cluster and its outskirts at $z = 0.8$ (therefore equivalent to group and cluster densities) fully agree with the Hα luminosity function derived for the ≈same local projected densities.

for poor fields, rich fields and groups and clusters, respectively), there is a strong difference in the steepness of the faint-end (see the inset of Figure 5.8). The faint-end of the LF becomes continuously shallower with increasing density, from $\alpha = -1.9 \pm 0.2$, for the lowest densities, to $\alpha = -1.5 \pm 0.2$ for rich fields and $\alpha \approx -1.1 \pm 0.2$ for groups and clusters. This clearly implies that the enhancement in the typical SFRs with environment directly results from the strong depletion of the faint-end and the

shallow α in rich environments relative to the field, rather than an increase in the bright-end. This also reveals that the steepness of the faint-end of the Hα LF seen in Chapter 3 is completely driven by field galaxies. Section 5.6.2 presents a discussion and possible interpretations of these results.

Figure 5.8 also provides a direct comparison with results from Koyama et al. (2010); these authors studied a high density region at $z \sim 0.8$, probing densities which are directly comparable with groups and cluster densities. The data are corrected for extinction using the relation presented in Garn et al. (2010) for a direct comparison. Koyama et al. found their data to be reasonably consistent within the errors with the total Sobral et al. (2009a) LF (which contained all environments), but their data fully support the difference in the faint-end of the luminosity function between field and group/cluster environments found here, and completely agrees with the results derived for the same densities, supporting the results which show that the environment seems to be responsible for setting the faint-end slope of the LF, at least at $z = 0.84$. A qualitatively similar result has been found for the 0024 super-cluster by Kodama et al. (2004) at $z = 0.4$; however, studies at even lower redhift (see e.g. Balogh et al., 2002) have found different and mostly discrepant results regarding α. It is clear that a comprehensive and large local study is still needed to really detail the role of the environment on the faint-end of the Hα LF in the local Universe, to provide the low-redshift benchmark that can be used to look for any cosmic evolution..

5.5 The nature of star formation and the mass-environment view

5.5.1 The star-forming fraction in the 2-D mass-environment space

It has been shown that star formation has strong dependences on both mass and environment at $z \sim 1$. Nevertheless, with environment and stellar mass expected to be somewhat correlated, how related are the dependences of star formation on mass and environment and are these intrinsically connected? Figure 5.9 presents the mass-environment 2-D space for Hα emitters and for the entire underlying population. This reveals the expected trend of an increase in the typical stellar mass with increasing local projected density for both populations of galaxies (with a change of ≈ 0.5 dex in the median mass from low to high densities).

To attempt to distinguish any potential inter-dependence of the roles of mass and environment on star formation at $z \sim 1$, the analysis presented in the previous 2 sections is repeated in the 2-D space of mass and Σ_c. The right panel of Figure 5.9 presents the star-forming fraction evaluated within this space, in regions where this can be calculated (see caption for details). While this clearly illustrates the overall behaviour which has already been presented, the fine details suggest significant connections between the dependence of the star-forming fraction on mass and environment. In particular, the

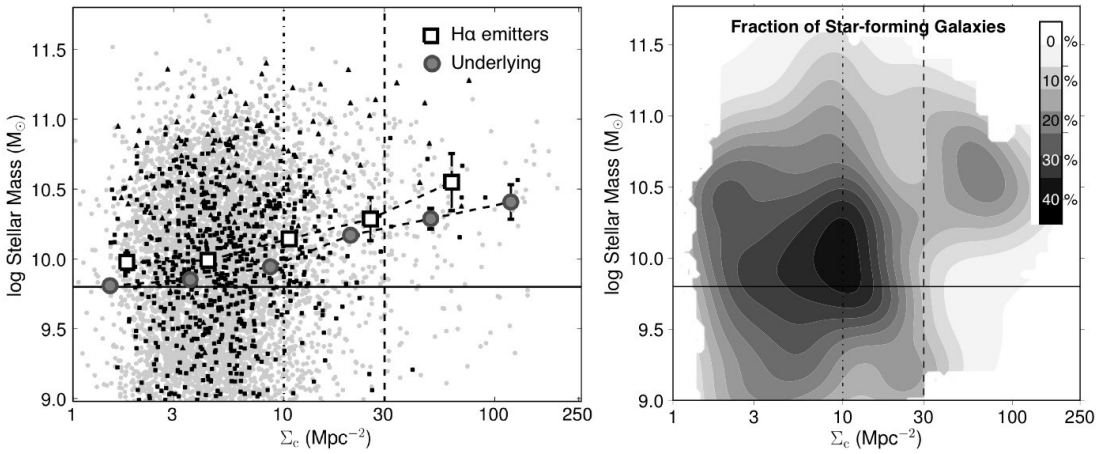

Figure 5.9: *Left*: The distribution of both Hα emitters (filled squares: emitters with EW > 50 Å; filled triangles: emitters with EW < 50 Å) and galaxies within the underlying population (dots) in the 2D mass-environment plane. Vertical lines represent the qualitative transitions between field, groups and rich groups/cluster environments, while the filled horizontal line indicates the approximate mass for which the star-forming population becomes significantly incomplete due to its star formation rate limit (see Section 3). This reveals the expected correlation between median stellar mass and local density (larger symbols). Note that the median of the underlying population is evaluated over all galaxies, while the star-forming population is incomplete below the horizontal line, hence the apparently higher median mass for star-forming galaxies. *Right*: The fraction of galaxies that are forming stars as a function of both stellar mass and environment. This is calculated in regions of the 2-D space for which it is possible to gather 5 or more background galaxies in a (Gaussian) smoothing radius up to 1σ of the typical errors in mass and environment – regions with less than 5 background galaxies are not shown. The latter reveals that the overall behaviour of the star-forming fraction as a function of stellar mass or environment depends, to some extent, on the environment or stellar mass, respectively.

results show that the weak increase of the star-forming fraction with density within the field regime and its subsequent sharp decline at higher densities is predominantly driven by galaxies of typical mass ($\approx 10^{10} - 10^{10.5}\,\mathrm{M}_{\odot}$) in the sample (please note that, as described in Section 5.3, there is a significant incompleteness effect at the lowest masses; this is indicated by the horizontal filled line in the figures). Interestingly, whilst the mass-downsizing trend is driven by galaxies in the dominant field and group environments, the results reveal an increase in the fraction of star-forming galaxies with density at the highest masses and, equivalently, an apparent reversal of the mass-downsizing trend in the richest environments.

Earlier, it was shown that the fraction of potential mergers increases with local density. To investigate whether this change in the potential nature of star formation can shed some light onto understanding what is happening at relatively high masses and high densities, the left panel of Figure 5.10 presents how the fraction of star-forming galaxies that are classified as potential mergers (in the COSMOS field) varies within the 2D mass-environment space. It clearly reveals a strong increase in the fraction of potential mergers with environment, and, particularly, that star formation at the

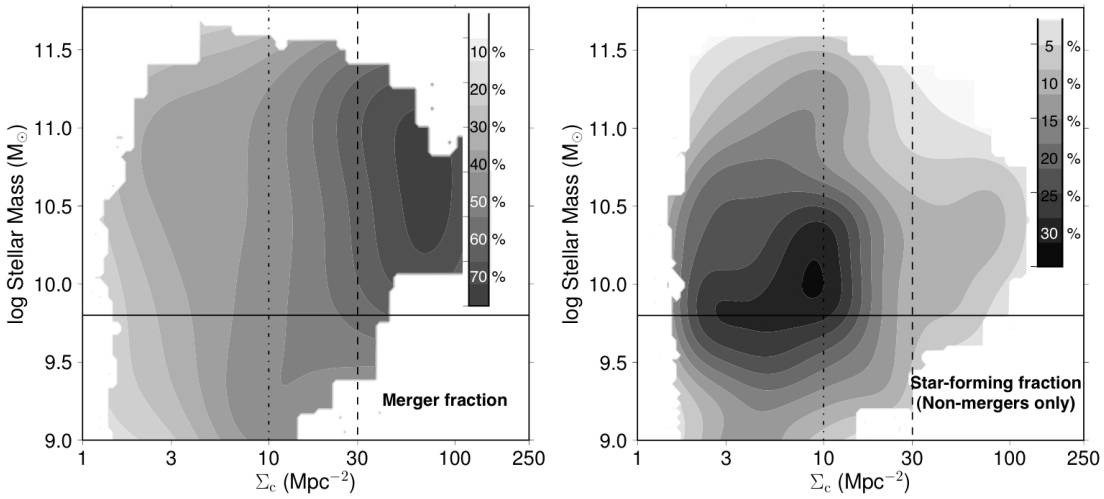

Figure 5.10: *Left*: The fraction of potential mergers within the star-forming population of galaxies (in COSMOS). This reveals that star formation occurring at the densest environments is potentially merger-driven. *Right*: The non-merger driven star-forming fraction, revealing that the trends with environment and mass become even stronger once potential mergers are removed from the sample. This is calculated in regions of the 2-D space (COSMOS only) for which it is possible to gather 5 or more background galaxies in a (Gaussian) smoothing radius up to 1σ of the typical errors in mass and environment – regions with less than 5 background galaxies are not shown.

highest densities is mostly driven by potential mergers, regardless of mass. It is therefore clear that the behaviour of the star-forming fraction within the studied 2D space reflects the role of potentially merger-driven star formation for very high densities, where merging events are more likely to happen. This is shown more clearly in the right panel of Figure 5.10, which repeats the analysis of Figure 5.9, but now restricted to isolated star-forming galaxies only (i.e. excluding all potential mergers). It is found that the fraction of non-merging star-forming galaxies peaks roughly at the mass completeness limit (for the SFR limit of the current sample, $\approx 10^{9.8}\,\mathrm{M}_{\odot}$), and in the transition between fields and groups, but shows strong general declining trends with both increasing mass for all environments and with increasing local density for all masses. This reveals that non-merger driven star formation is strongly suppressed in both rich groups/cluster environments and for high stellar masses, implying that once potential mergers are neglected, stellar mass and environment both play separate and important roles.

5.5.2 The mass-SFR-environment dependence

Section 5.4 showed that the typical SFR increased with density at least up to groups/cluster outskirts densities. Here this is investigated further, by examining how the median star-formation rates vary with environment for sub-samples of star-forming galaxies with different stellar masses. Figure 5.11 reveals that while a strong SFR-environment trend is seen in low to moderate stellar mass galaxies, it does not hold for the most massive galaxies ($\mathrm{M} > 10^{10.6}\,\mathrm{M}_{\odot}$), for which the median SFR seems to

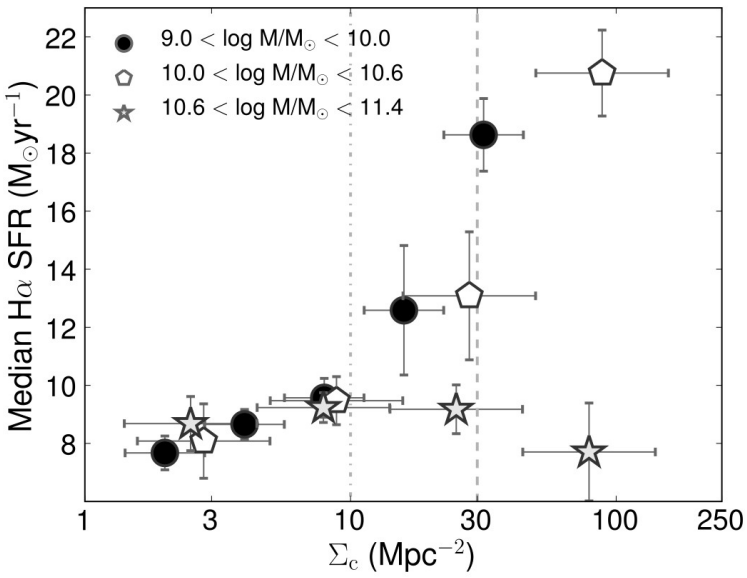

Figure 5.11: The dependence of the median SFR on environment (Σ_c) for star-forming galaxies with different stellar masses. Error bars present the $1\,\sigma$ Poissonian uncertainty ($\pm\sigma_m/\sqrt{\mathrm{N}}$). The results show that while the increase of the median Hα SFR with environment is valid for galaxies with stellar masses in the range $\approx 10^{9.0-10.6}\,\mathrm{M}_\odot$, the most massive galaxies in the sample (stellar masses $> 10^{10.6}\,\mathrm{M}_\odot$) do not have their typical SFR enhanced with environment.

remain unchanged with increasing local density. Since the typical stellar mass of galaxies increases with density, in terms of sSFRs one finds that for the most massive galaxies, the median sSFR decreases with increasing local density (at a 2σ significance level), whilst this trend is continually reversed with decreasing stellar mass, becoming a significant positive correlation (3.5σ) at the lowest masses probed. It should be noted that although the most pronounced difference in the SFR-Σ behaviour is in the densest environments, where the merger fraction is high, the same trends are recovered (albeit weakened by $\sim 0.6\sigma$) if the analysis is conducted using only non-merger star-forming galaxies. Therefore, merging activity by itself is not enough to explain the enhancement of SFR in low-to-medium mass star-forming galaxies. These results imply that there is some inter-dependence in the influence of mass and environment on galaxy evolution.

5.5.3 The colours of star-forming galaxies in the 2-D mass-environment space

The nature of the Hα emitters occupying different regions in the 2D space being probed can be made even clearer by looking at the colours of emitters. For $z \sim 0.8$, this can be simply done using $(R-z)$ because these roughly span the 4000 Å break, and are sufficiently close so that dust extinction is unlikely to be a significant problem. Figure 5.12 (left panel) presents how the median colours of the Hα emitters vary across environment for different stellar masses. The results suggest that stellar mass is the most important quantity for determining the 4000 Å break colour (and whether the Hα emitter

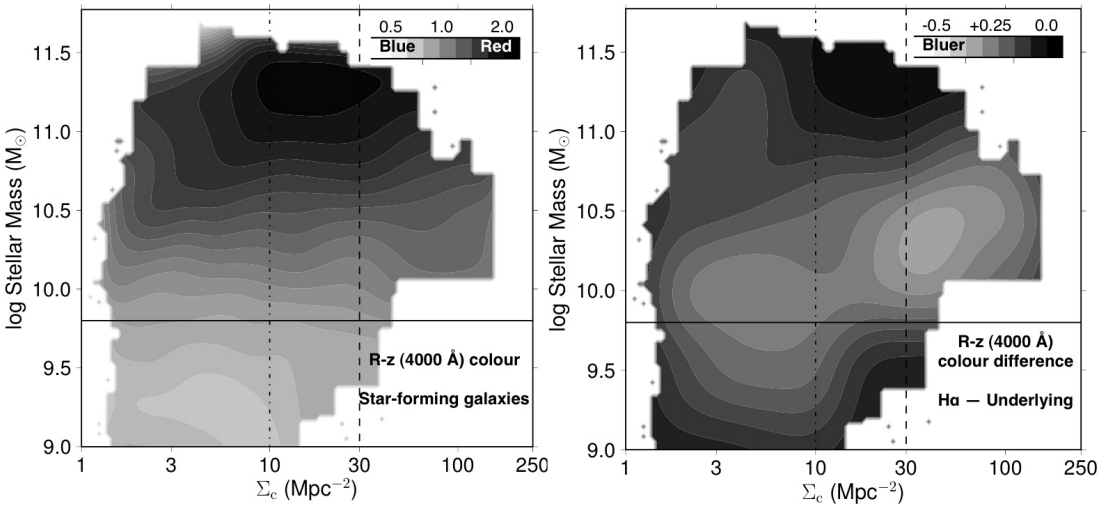

Figure 5.12: *Left*: The distribution of the median R-z colour (probing the 4000 Å break at $z = 0.84$) within the mass-density 2D space for the Hα star-forming galaxies, revealing that stellar mass is the main colour predictor as the environment only correlates weakly with colour. *Right*: The difference in the median R-z colour between the population of star-forming galaxies and the complete underlying population, revealing that although star-forming galaxies are consistently bluer than the underlying population, the colour difference is a clear function of mass and also depends on the environment.

is consistent with already being in the red sequence or still occupying the blue cloud) of star-forming galaxies. Figure 5.12 also reveals that the environment plays a much weaker role for determining the colour of star-forming galaxies, even though the reddest Hα emitters are found in group environments (but those are also very massive). The 2-D colour distribution is found to be qualitatively the same for both potential mergers and non-merging galaxies, showing the same trends, although potential mergers are consistently bluer (by ≈ 0.2 in colour) than the non-mergers throughout the 2-D space studied.

Further information can be obtained by comparing the colour distribution of the star-forming galaxies with that of the underlying population. As the right panel of Figure 5.12 shows, the star-forming population is bluer than the underlying population at all masses and environments. However, the results indicate that even though the main colour predictor for star-forming galaxies is stellar mass, the difference in colour between the star-forming population and the underlying population of galaxies depends on both mass and environment. Particularly, the colour difference is greatest at lower masses (above the mass completion limit – see Section 5.3), where the underlying population contains a mix of blue and red galaxies, while the star-forming population has very few red ones, thus leading to the difference. However, such difference is negligible at the very highest masses, where even star-forming galaxies are very red. Moreover, the fraction of redder galaxies at moderate masses is found to be higher in denser environments for the underlying population (the underlying galaxy population has a weak trend of colour with increasing density), but the star-forming population has essentially no trend with environment for a fixed mass (see left panel of Figure 5.12), thus resulting in the environmental trend of the colour difference.

5.6 Discussion

It is clear that the bulk of the most massive galaxies that are already in place at $z = 0.84$ are non-star-forming (star formation rates lower than the HiZELS limit, $3\,M_\odot\,yr^{-1}$) and many of those which are star-forming have low sSFRs and have stronger 4000 Å breaks (are redder) than lower mass galaxies. These results clearly point towards mass downsizing already being in place for the general population of star-forming galaxies studied at $z \sim 1$, although potential merging activity (which becomes more likely at higher densities) can be responsible for triggering some star formation even in massive, apparently red-sequence galaxies.

In addition to this, the environment has a significant role in the nature and evolution of star-forming galaxies at $z \sim 1$. For local surface densities associated with the field regime, and for moderate stellar masses, the fraction of star-forming galaxies is relatively flat with increasing environmental density, while the median star formation rate of Hα emitters is found to increase with density. However, for higher densities, the star-forming fraction falls sharply towards ~ 0 per cent for the highest rich group/cluster densities. The environment is also found to play an important role in setting the faint-end slope of the Hα luminosity function, with the results showing that under-dense regions have Hα LFs with very steep faint-end slopes, while the highest densities have a shallow faint-end slope – this confirms analytic predictions such as those presented by Trenti and Stiavelli (2008). If this holds at different epochs (particularly, at higher redshift), then it suggests that the steepening of the faint-end slope with redshift that has been argued by many authors (for both Hα and UV selected samples, e.g. Hopkins et al., 2000; Bouwens et al., 2007; Reddy and Steidel, 2009), may be mostly a consequence of structure formation, since at high redshift groups and clusters of galaxies become rarer and rarer and the field environment dominates. At lower redshift, on the other hand, the discrepancies in the faint-end slope discussed in Chapter 3 are likely to be caused by cosmic variance, with different surveys targeting regions with different densities.

When one combines the dependences of star formation on mass and environment, a sharper picture arises: this shows that the increase in the star-forming fraction in the field regime is dominated by median mass ($\approx 10^{10} - 10^{10.5}\,M_\odot$), essentially non-merging galaxies, and that the bulk of star-forming galaxies in high density environments are red, massive galaxies undergoing a merger episode. It is also found that the fraction of non-merging star-forming galaxies strongly declines in rich groups/cluster densities for all masses, and for high masses for all environments, implying that both mass and environment independently suppress non-merging star-formation. However, this also shows that the enhancement of the typical SFRs with increasing density is only happening at $z \sim 1$ for galaxies with masses lower than $10^{10.6}\,M_\odot$ – for the most massive star-forming galaxies the environment does not seem to alter the typical SFRs and their properties seem to be mostly set by their stellar mass.

5.6.1 Comparison with other studies

Studies at $z \sim 1$ and above have found apparent discrepant results for the relation between star formation and environment, with some authors claiming to have found an inversion in that relation when compared to the local Universe. In particular, Elbaz et al. (2007) study the star formation rate-density relation at $z \sim 1$ and find that, instead of declining, SFRs of star-forming galaxies are enhanced with local projected density; Cooper et al. (2008) find similar results. These studies typically probe field to poor group environments. On the other hand, Poggianti et al. (2008) presents a detailed study of a large sample of relatively high redshift groups and clusters (up to $z \sim 1$). Contrarily to Elbaz et al. (2007) and Cooper et al. (2008), Poggianti et al. (2008) find that SFRs decrease with environment in the high density regime (but the results agree with a rise in the mean SFRs – which are [OII] based – with density up to $\Sigma \sim 30\,\mathrm{Mpc}^{-2}$, and with the fall after that).

Patel et al. (2009) studied a $z \sim 0.8$ cluster and the surrounding regions (using a mass limited sample, but selecting only relatively massive galaxies, and making use of MIPS 24 μm data) to show that the specific star formation rate decreases with increasing density at $z \sim 1$ and argued that star formation is suppressed with density even at that epoch. The authors comment on the big discrepancy of their results when compared to Cooper et al. (2008) or Elbaz et al. (2007), and, whilst they argue that the differences could be arising from a combination of different effects, they are not able to reach a definitive answer. Feruglio et al. (2010) also study the role of the environment on star-formation and, using a sample of luminous and ultra-luminous infrared galaxies (LIRGs and ULIRGs) in COSMOS, find that for such massive galaxies there is not an increase in SFR with density up to $z \sim 1$.

Fortunately, the large sample and the wide range of environments and stellar masses within the HiZELS sample provides an ideal opportunity to attempt to reconcile these results. Indeed, one finds, just like Elbaz et al. (2007), that the environment enhances SFRs at least up to groups/cluster outskirts environments, but then decreases at higher densities as found by Poggianti et al. Furthermore, if one looks at how the sSFR of massive galaxies (comparable to those studied by Patel et al. 2009) varies with environment, the same trend is recovered: sSFRs of massive galaxies decrease with Σ, mostly because median SFRs of massive galaxies are largely insensitive to environment, but the median mass increases at higher densities, leading to a lower median sSFR. Note that such a trend is reversed for lower mass galaxies, where the increase in SFR with density is fully valid; this reveals that the results from Patel et al. (a mass-selected sample), or Feruglio et al. (2010) (a sample of massive LIRGs and ULIRGs) are highly dependent on the stellar mass selection, and that these do not agree with results from Elbaz et al. (2007) mostly because galaxies in the later study are selected from their star formation emission lines (therefore bluer, less massive galaxies).

Furthermore, Poggianti et al. (2008) also finds that the fraction of star-forming galaxies falls continuously for densities significantly larger than $\Sigma \sim 10\,\mathrm{Mpc}^{-2}$ (the study is not sensitive to field densities). Similar results are recovered by Koyama et al. (2010), who studied a cluster at $z = 0.8$ and found that the star-forming fraction (Hα emitters) falls from groups to the cluster core, while Feruglio et al. (2010) finds that the fraction of LIRGs and ULIRGs also decreases with increasing density up

to $z \sim 1$. These are the same trends found in this Chapter, but the current work extends this to much lower densities and, overall, probes a wider range of densities.

Together, the results in this Chapter are able to simultaneously agree with previously apparently contradictory results, revealing that such discrepancies are caused by the studies focusing on galaxies with significantly different masses and, most importantly, residing in different environments.

The analysis presented here contributes towards improving our understanding of galaxy evolution and the key epochs for significant transitions. While the median SFR is enhanced with density up to moderate densities, for a star-forming selected population, it has also been shown that the behaviour of that relation depends on stellar mass. Furthermore, while merging does become important at the highest densities, it is also found that the SFR-Σ relation is still recovered even when considering non-mergers only. This surely implies that the physical processes through which the environment enhances the typical SFRs cannot be fully explained by (major) mergers. Therefore, galaxy harassment, or the acceleration of the intergalactic gas infall in rich groups and cluster outskirts are likely to play a significant role in enhancing star-formation at high densities. Since these processes are more likely to affect galaxies with higher gas contents, it may be understandable that the trends are seen most strongly at low and medium masses.

Furthermore, the star-forming fraction drops from fields to groups and clusters, revealing no qualitative evolution from the local Universe: very rich environments already have a low star-forming fraction even at $z = 0.84$ (and the star formation activity occurring at high densities is potentially merger-dominated). Particularly when one excludes potential mergers, the environmental trend of a declining star-forming fraction for high densities is recovered at all masses, revealing that the environment plays an important role which is roughly independent from that of stellar mass. This is in good agreement with the results presented by Cooper et al. (2010), at a similar redshift, and qualitatively similar to the clear independence of the quenching roles of stellar mass and environment found by Peng et al. (2010) using SDSS. Since HiZELS is able to agree with previous results and provide a much broader view, it further confirms that the densest regions at $z \sim 1$ are already the sites where one finds predominantly red sequence galaxies and low star-forming fractions, as found in previous cluster studies. However, with studies such as Hayashi et al. (2010) showing that the star-forming fraction does not drop with increasing density even for the densest regions at $z \sim 1.5$ (but that some of [OII] emitters within the cluster core are already in the red sequence), it seems likely that the latter stages of the environment transformation happen between $z \sim 0.8$, where one finds red Hα emitters at cluster cores, but a fraction of star-forming galaxies which already declines steeply, and $z \sim 1.5$, where such fraction seems to hold up to the highest densities; the same view seems to be recovered by using 24 μm data (Hilton et al., 2010).

5.6.2 The role of the star formation mode: potential mergers vs. non-mergers

In Chapter 3, the results show that non-merging galaxies (mostly disc galaxies) dominate the star formation rate density of the Universe at $z \sim 0.8$, and it is now clear that the bulk activity of such galaxies is occurring in the field and poor groups.

Nevertheless, while the fraction of non-merger driven star-forming galaxies falls sharply at high densities, there is still some star formation found in the richest environments. The latter is merger dominated, and this is linked with the increase in the median SFRs of Hα emitters and, to some extent, with the fall of the star-forming fraction with environment.

Indeed, in group and cluster environments, $\sim$ 80 per cent of star-forming galaxies are potential mergers. This is somewhat expected, as mergers are more likely to happen in dense environments. However, merger-driven star formation at $z = 0.84$ is likely to result in starbursts which quickly exhaust the available gas (which, for the most massive galaxies that are already reasonably red, is likely to be low), and are expected to produce elliptical galaxies. This would then further drive the decline of the overall star-forming fraction with environment and would be consistent with a significant population of mergers at high densities at slightly higher redshifts, as argued in Chapter 3 to explain the evolution of the Hα luminosity function. Thus, as the densest regions increase the merger chances, they can lead to a much quicker migration of blue cloud galaxies into the red sequence. This would then establish a higher fraction of passive galaxies in the densest regions much earlier than in the field, where potential merging events are not dominant.

At higher redshift ($z = 1.2$), Ideue et al. (2009) presented an environment analysis using [OII] 3727 emitters selected from a narrow-band survey, assessing the potential role of interacting galaxies as a function of environment in the COSMOS field (but instead of morphologically classifying the galaxies, they looked at the fraction of isolated against non-isolated galaxies). The authors find an increase in the fraction of non-isolated galaxies with density. However, while this is fully consistent with the results presented in this Chapter and with the interpretation, it should be noted that Ideue et al. (2009) define non-isolated galaxies as galaxies separated by distances of less than 80 kpc. Whilst this is not a robust criteria for identifying a merger, it also strongly correlates with the local density estimate, even if the merger fraction does not go up with density; therefore, an increase with density may be expected as a bias, regardless of the nature of the galaxies (real mergers or non-mergers).

The results of this Chapter can also be used to interpret the influence of the environment on the Hα luminosity function. In Chapter 3, the Hα luminosity function derived for just potentially merging sources was found to have a shallow faint-end slope, α. With this study it seems likely that the low α is a consequence of a higher density environment: galaxies in high densities will increase their merging chances and reside in potentially gas-rich regions at $z \sim 1$, making it hard to maintain low, isolated star formation rates.

The results imply that higher densities enhance star formation in star-forming galaxies and that seems to be valid at all cosmic times; that's why denser regions have the most massive galaxies;

however, because star formation has been enhanced, galaxies form stars quicker and sooner, and this leads to the mass downsizing observed since $z = 1$ down to the local Universe.

5.7 Summary and Conclusions

The conclusions of this study can be summarised as follows:

- The well-defined HiZELS sample of Hα emitters at $z = 0.845 \pm 0.015$ down to SFRs $> 3\,\mathrm{M_{\odot}yr^{-1}}$ covering a large sky area has been used to conduct a detailed study of the dependence of star formation on mass and environment. This is able to reconcile previous results and provide an integrated, clearer view of galaxy evolution at $z \sim 1$, particularly by taking advantage of the excellent underlying data in the COSMOS and UDS fields, but also because the survey probes significantly massive, rich groups/clusters, providing a truly panoramic Hα survey over a very wide range of environments.

- The star-forming fraction is found to strongly decline with stellar mass, from ≈ 40 per cent for $10^{10}\,\mathrm{M_{\odot}}$ galaxies to effectively zero above $10^{11.5}\,\mathrm{M_{\odot}}$. Specific star-formation rates also decline continuously with stellar mass. Mass downsizing is therefore fully in place at $z = 0.84$.

- The median SFRs of Hα emitters at $z = 0.84$ increases as a function of local surface density for both field and group environments, but the trend is stopped for the highest densities, where it is likely to fall. This trend is driven by star-forming galaxies with stellar masses up to $\approx 10^{10.6}\,\mathrm{M_{\odot}}$; higher-mass galaxies seem to have median SFRs which are mostly independent of the environment they reside in. With this result being recovered even when one excludes potential merger-driven star-formation, it is likely that at least part of the environmental enhancement must come from other physical processes, such as galaxy harassment, or the acceleration of intergalactic gas infall in groups and cluster outskirts.

- The fraction of galaxies that are forming stars is relatively flat with density within the field regime, but there is a clear, continuous decline once group densities are reached, resulting in the fall of the star-forming fraction from fields to rich groups/clusters, as seen in the nearby Universe and in studies focusing on the highest densities at $z \sim 1$.

- The environment is responsible for shaping the faint-end of the Hα luminosity function: the faint-end slope, α is found to be very steep ($\alpha = -1.9 \pm 0.2$) for the poorest regions, becoming shallower ($\alpha = 1.5 \pm 0.2$) for rich fields and even shallower ($\alpha = -1.1 \pm 0.2$) for groups and clusters.

- Star formation at the highest densities is dominated by potential mergers, with likely implications on the nature and duration of the star formation activity, and suggesting that at least part of the environment quenching of star formation seen in the local Universe is driven by merging events at higher redshift. Neglecting potential merger-driven star formation results in stronger and

mostly independent trends of a declining fraction of star-forming galaxies with both increasing mass and environment.

- The 4000 Å colour of star-forming galaxies correlates strongly with stellar mass, but only weakly with environmental density. Massive star-forming galaxies residing in groups are mostly in the red sequence, while lower mass galaxies residing in the field occupy the blue cloud.

These results show that both mass and environment play significant, inter-dependent roles in galaxy evolution, although such roles may become more independent if one neglects potential merger-driven star-forming galaxies. High density regions are linked with triggering high SFRs (for moderate mass galaxies), but this is likely to result in a quicker quenching of star formation as the gas is rapidly consumed, thus quickly transforming groups and cluster environments into the predominant sites for gas-poor, passive galaxies. On the other hand, the quenching processes linked with stellar mass (e.g. AGN) must also play an important role which is distinct from that of environment. It seems that the combination of high masses and high densities is the recipe for very effective and early galaxy formation, as even at z$\sim$ 1 the star-forming galaxies found with such combination are already on the red sequence, with very low sSFRs (even though most of them are potential mergers).

Chapter 6

Star formation at z = 1.47: the Hα-[OII] stereoscopic view

6.1 Introduction and Motivation

It is now clear that the "epoch" of galaxy formation occurs at $z > 1$, as surveys measuring the star formation rate density ($\rho_{\rm SFR}$) as a function of epoch show that $\rho_{\rm SFR}$ rises steeply out to $z \sim 1$ (e.g. Lilly et al., 1996), but determining the redshift where $\rho_{\rm SFR}$ peaked at $z > 1$ is more difficult.

Ideally, the use of different tracers of recent star formation would provide a consistent view, but in reality, because they have different selection biases, and require different assumptions/extrapolations, measurements are often significantly discrepant (see Chapter 1). An additional complication comes from surveys at different epochs making use of different indicators due to instrumentation and detection limitations. Indeed, while for $0 < z \lesssim 0.4$ the evolution of $\rho_{\rm SFR}$ is typically estimated using Hα luminosity, because it is easily targeted in the optical (e.g. Ly et al., 2007; Shioya et al., 2008; Dale et al., 2010), at higher redshifts the line is redshifted into the near-infrared, and [OII] 3727 – hereafter [OII] – luminosity (much more affected by extinction than Hα, and also a metallicity-dependent indicator) is used instead (e.g. Zhu et al., 2009; Bayliss et al., 2011).

The [OII] emission line can be traced in the optical window up to $z \sim 1.5$ and many authors have attempted to measure the evolution of [OII] luminosity function up to such look-back times (e.g. Hogg et al., 1998b; Gallego et al., 2002; Takahashi et al., 2007; Zhu et al., 2009). Such studies have identified a strong evolution from $z = 0$ to $z > 1$ (e.g. Gallego et al., 2002; Zhu et al., 2009), although the evolution seems to be slightly different from that seen in the Hα luminosity function. Part of the differences may well arise from the difficulty in using [OII] luminosity density directly

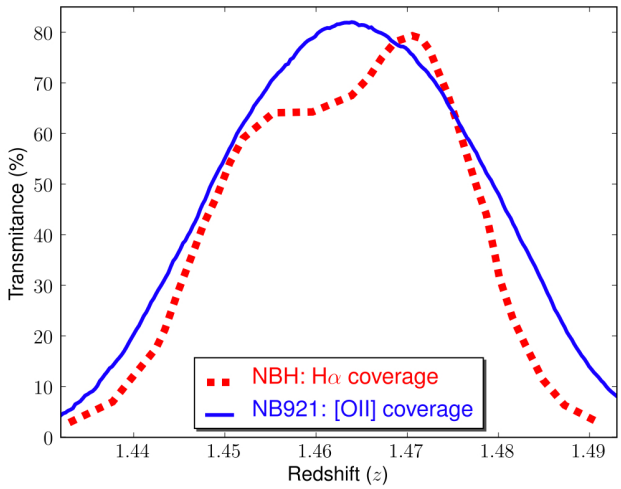

Figure 6.1: A comparison between the NB_H redshift coverage of the Hα emission line and the NB921 redshift coverage of the [OII] emission-line, revealing that the two filters are extremely well matched and ideal for a double Hα-[OII] narrow-band survey. The [OII] coverage is only slightly wider (in redshift) than the Hα coverage – but this is shown to have little to no effect on the analysis (c.f. Section 6.4.5).

as a star-formation rate density indicator: [OII] luminosity is calibrated locally using Hα (see e.g. Aragón-Salamanca et al., 2003; Mouhcine et al., 2005, for a comparison between both emission-lines at low-z), but the actual calibration depends on metallicity and dust-extinction (c.f. Jansen et al., 2001; Kewley et al., 2004). These issues have been reported by many studies, mostly using data from the local Universe or low redshift (see e.g. Gilbank et al., 2010a, for a comparison between both lines and other indicators in the Sloan Digital Sky Survey), for which it is possible to measure both Hα and [OII]. However, so far it has not been possible to directly compare the Hα and [OII] indicators at $z > 1$ using large-enough samples to test, extend and improve our understanding.

As discussed in Chapter 2, the development of wide-field near-infrared cameras made it possible to conduct large area surveys (necessary to overcome cosmic variance), tracing the Hα emission-line up to $z \approx 2.5$. In Chapter 3, the Hα luminosity function is shown to evolve significantly, mostly due to an increase by more than one order of magnitude in $L^*_{H\alpha}$, the characteristic Hα luminosity, from the local Universe to $z = 2.23$. Moreover, Chapter 5 shows that at $z = 0.84$ the faint-end slope of the luminosity function is strongly dependent on the environment, with the Hα luminosity function being much steeper in poorer field regions and much shallower in the group/cluster environments. Whether this is also found at higher redshifts remains unknown, as current samples do not provide the size, robustness and the wide range of parameters needed.

Indeed, while it is now possible to detect Hα emission over very wide areas up to $z > 2$, distinguishing between Hα and any other emission line at any redshift is a challenge, particularly over (large) areas where it is unfeasible to assemble ultra-deep multi-wavelength data over dozens of bands. Double matched narrow-band surveys offer an outstanding solution to the problem; in particular, since the NB921 narrow-band filter on Subaru is able to probe the [OII] emission line for the same redshift range ($z \sim 1.47$) as the narrow-band H filter on UKIRT probes Hα (see Figure 6.1), a matched and

Table 6.1: Observation log for the NB_H observations of the UDS field, taken using WFCAM on UKIRT, during 2008, 2009 and 2010. Limiting magnitudes ($3\,\sigma$) are the average of the four frames which constitute a field, based on the measurements of 10^6 randomly placed $2''$ apertures in each frame. Integration times given in brackets present the total integration times obtained at the telescope prior to rejection of data taken in poorer conditions (see §6.2.1).

Field	R.A. (J2000)	Dec. (J2000)	Int. time (ks)	FHWM ($''$)	Dates	m_{lim} (H) (3σ)
SXDF/UKIDSS-UDS NE	02 18 29	−04 52 20	18.2 (18.2)	0.8	Sep(08), Aug(09), Jul(10)	21.2
SXDF/UKIDSS-UDS NW	02 17 36	−04 52 20	17.1 (18.3)	0.9	Sep(08), Jul(10)	20.9
SXDF/UKIDSS-UDS SE	02 18 29	−05 05 53	28.0 (28.0)	0.8	Sep(08), Aug(09)	21.4
SXDF/UKIDSS-UDS SW	02 17 38	−05 05 34	18.3 (19.1)	0.8	Oct(08), Aug (09), Jul (10)	21.2

sufficiently deep survey would not only provide a simple, clean selection ($z = 1.47$ sources will be detected as emitters in both data-sets), but also provide a means of directly comparing Hα and [OII] at $z \sim 1.5$ for very large samples for the first time.

This Chapter presents deep narrow-band imaging using the NB_H filter at $\lambda = 1.617\mu$m, as part of HiZELS, over $0.79\,\mathrm{deg}^2$ in the UDS field and combines the data with ultra-deep NB921 data taken using Suprime-Cam on the Subaru telescope, to explore an extremely well-matched Hα-[OII] narrow-band survey over $0.70\,\mathrm{deg}^2$. The results presented in this Chapter are presented in Sobral et al. (2011b).

6.2 Data and Samples

6.2.1 Near-infrared NB_H imaging with UKIRT

The UKIDSS UDS field was observed with WFCAM on UKIRT using a set of custom narrow-band H filters (NB_H, $\lambda = 1.617\,\mu$m, $\Delta\lambda = 0.021\,\mu$m), on 25–29 September, 2008, 25–26 November, 2008, 16–17 August, 2009 and 18, 22 July, 2010. WFCAM's standard "paw-print" configuration of four 2048×2048 ($0.4''\,\mathrm{pixel}^{-1}$) detectors offset by $\sim 20'$ was macrostepped four times to cover a contiguous region of $\sim 55' \times 55'$ (Casali et al., 2007), with individual narrow-band exposures of 100 s. The seeing varied between $0.7''$–$0.8''$ during the observing nights, and conditions were mostly photometric. The Non Destructive Read (NDR) mode was used for all narrow-band observations to minimise the effects of cosmic rays in long exposures. The observations were obtained by jittering around 14 different positions in each of the 4 pointings. Details of the observations are given in Table 6.1. The NB_H survey is made up of a mosaic of four WFCAM pointings, i.e., $4 \times 4 \times 13.7' \times 13.7'$ tiles. The UKIDSS UDS H-band image (24 AB, 5σ) overlaps entirely with the full narrow-band image, yielding a total overlapping area of $0.79\,\mathrm{deg}^2$.

Data were reduced using the dedicated pipeline that has been developed for HiZELS (PfHiZELS, c.f. Chapter 2 for more details). Narrow-band images were photometrically calibrated (independently)

by matching ~ 70 stars with $m_H = 11 - 16$ per frame from the 2MASS All-Sky catalogue of Point Sources (Cutri et al., 2003) which are unsaturated in the narrow-band frames.

6.2.2 NB_H Source Extraction and Survey Limits

Sources were extracted using SExtractor (Bertin and Arnouts, 1996). Photometry was done using apertures of $2''$ diameter. In order to clean spurious sources from the catalogue (essential to remove cross-talk artifacts), the final images were visually inspected. Cross-talk sources and detections in the halo regions were removed from the catalogue separately for each frame, which greatly simplifies their identification (see discussion in Chapter 2).

The average $3\,\sigma$ depth of the entire set of NB_H frames is 21.18 mag; this is measured using a set of 10^6 randomly placed apertures per frame. Above the $3\,\sigma$ threshold in each frame, the narrow-band imaging detects a total of 23394 sources (5904, 4533, 6946 and 6011 in the NE, NW, SE and SW pointings, respectively) in UDS across $0.78\,\mathrm{deg}^2$ (after removal of regions in which cross-talk and other artifacts caused by bright objects are located).

6.2.3 Optical NB921 imaging with Subaru

Archival Subaru/Suprime-Cam NB921 data of the UDS field are available, taken by Ouchi et al. (2009, 2010). The field was observed with Suprime-Cam on Subaru as part of the Subaru/XMM-Newton Deep Survey (SXDS, Ouchi et al., 2008) during 2005–2007. The NB921 filter is centered at 9196 Å with a FWHM of 132 Å, and was used to cover the field with 5 pointings with a total integration of 45.1 hours (individual exposures ranging from 8 to 10 hours) – see Ouchi et al. (2010). The raw NB921 data were downloaded from the archive and reduced with the Suprime-Cam Deep field REDuction package (SDFRED, Yagi et al., 2002; Ouchi et al., 2004) and IRAF. The combined images were aligned to the public z'-band images of Subaru-XMM Deep Survey (SXDS; Furusawa et al., 2008) and PSF matched (FWHM= $0.8''$). The NB921 zero points were determined using z' data, so that the z'-NB921 colour distributions of SXDS would be consistent with that of Subaru Deep Field data (SDF; Kashikawa et al., 2004). Source detection and photometry were performed using SExtractor (Bertin and Arnouts, 1996). Sources were detected on each individual NB921 image and magnitudes measured with $2''$ diameter apertures. The average NB921 3σ limiting magnitude is estimated to be 26.3 (AB) by randomly placing 10^6 $2''$ apertures in each frame; down to that depth, 347341 sources are detected over the entire $1\,\mathrm{deg}^2$ area (5 Suprime-Cam pointings). Note that NB921 and z' magnitudes are given in the AB system.

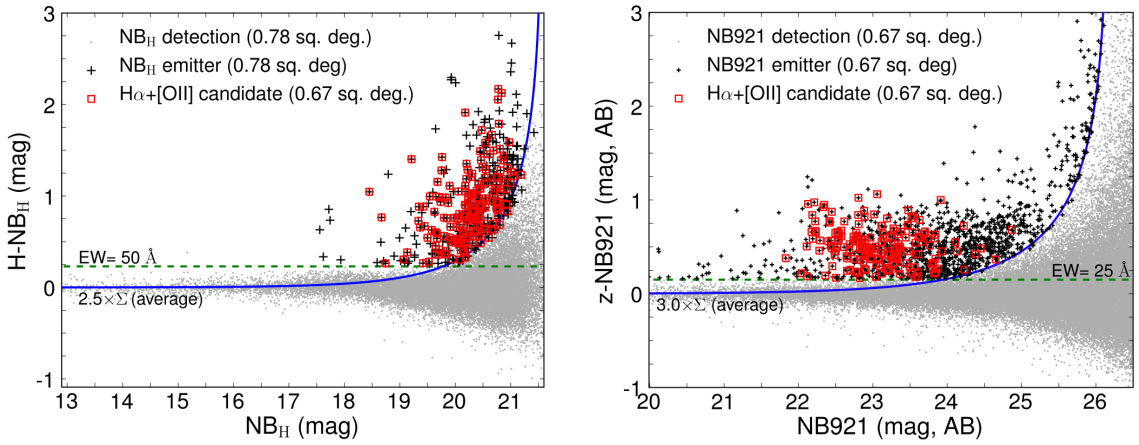

Figure 6.2: Narrow-band excess as a function of narrow-band magnitude for $\mathrm{NB_H}$ (left panel, Vega magnitudes) and NB921 (right panel, AB magnitudes) data. These show $> 3\sigma$ detections in narrow-band imaging and the lines present the average $2.5\,\Sigma$ and $3.0\,\Sigma$ colour significances for $\mathrm{NB_H}$ and NB921, respectively (for the average depth, but note that the analysis is done individually for each frame). Also, due to the very high number of detected sources in NB921, only 1 in every 5 sources is shown. The horizontal dashed lines present the equivalent width cuts used for $\mathrm{NB_H}$ and NB921 data – these correspond to $z = 1.47$ rest-frame EW limits of 20 Å for Hα and 10 Å for [OII]. Narrow-band excess sources in both $\mathrm{NB_H}$ and NB921 (double-emitters) are shown, and constitute a robust sample of Hα/[OII] candidate emitters – see Figure 6.3 for a visualisation of one such emitters.

6.3 SELECTION

6.3.1 Narrowband excess selection

Potential line emitters ($\mathrm{NB_H}$ and NB921) are selected according to the significance of their broad-band − narrow-band ($BB - NB$) colour, as they will have ($BB - NB$) > 0.

Neither of the narrow-band filters falls at the center of the broad-band filters and thus objects with redder colours will tend to have a negative $H - \mathrm{NB_H}$ colour, and a positive z'−NB921 colour, while bluer sources will have $H - \mathrm{NB_H} > 0$ and z'−NB921< 0. This can be broadly corrected by considering the broad-band colours of each source, as in Chapter 3. For the $\mathrm{NB_H}$ data, this is done by studying $H - \mathrm{NB_H}$ as a function of $J - H$ colour for all sources detected in the $\mathrm{NB_H}$ frames. A linear fit is derived[1] and is used to correct the initial H magnitudes to produce an effective H' magnitude appropriate for estimation of the continuum contribution at the wavelength of the $\mathrm{NB_H}$ filter. This assures a mean zero $H' - \mathrm{NB_H}$ as a function of $J - H$, and also results in no significant trend as a function of $H - K$. The correction is given by:

$$H' - \mathrm{NB_H} = (H - \mathrm{NB_H}) - 0.1(J - H) - 0.03. \quad (6.1)$$

[1]Only sources within $\pm 2\sigma$ of the general scatter around the median $H - \mathrm{NB_H}$ are used. Furthermore, in order to improve the fit for galaxies, potential stars (selected as sources satisfying $B - z' > 13.5(H - K) + 2.0$, AB) are excluded and a separate fit is done just for the latter.

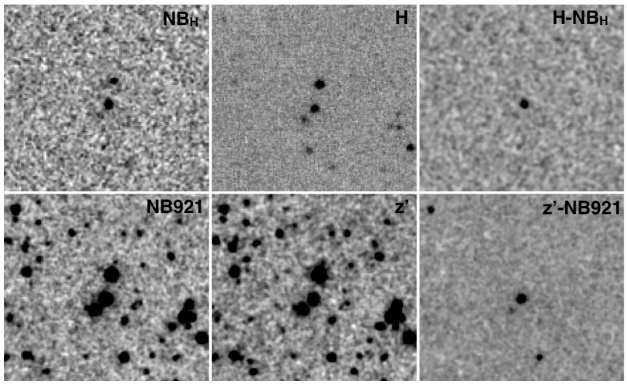

Figure 6.3: The top panels show a strong NB_H emitter, clearly revealed after subtracting the H continuum. The bottom panels show the same sky area ($\sim 30'' \times 30''$) in NB921 and z', revealing that the NB_H emitter is also a strong NB921 emitter (and thus a Hα+[OII] $z \sim 1.47$ emitter). Note the depth difference, and how non-emitters disappear when the continuum estimated flux is subtracted from the narrow-band flux (other fainter NB921 emitters are also revealed).

For the NB921 data, a similar approach is taken, but using $z' - J$ colours instead[2]. Colours are corrected by using the best linear fit:

$$z'' - \text{NB921} = (z' - \text{NB921}) - 0.05(z' - J') + 0.15. \quad (6.2)$$

Emission line fluxes, F_{line}, and equivalent widths, EW_{line}, are computed following Chapter 2.

The selection of emission-line candidates is done following Chapters 2 and 3 (see also Ouchi et al., 2010). Narrow-band sources in the H band (NB_H) are selected as line emitters if they present a colour excess significance of $\Sigma > 2.5$ (which broadly corresponds to a flux limit), and an observed EW > 50 Å (corresponding to EW > 20 Å rest-frame for the Hα line at $z = 1.47$). NB921 sources are selected as potential emitters if they present a colour excess significance of $\Sigma > 3.0$ (as the data are much deeper, a higher significance cut can be applied) and EW > 25 Å (corresponding to EW > 10 Å for [OII] emitters at $z = 1.47$). The EW cuts are applied to avoid including bright foreground objects with a large significance and a steep continuum across the H or z' bands, and were chosen to reflect the general scatter around the zero colour at bright magnitudes (thus the difference between NB_H and NB921) and to allow a good selection of both Hα and [OII] emitters. Figure 6.2 presents the corrected broad-band − narrow-band colours as a function of narrow-band magnitude, including the selection criteria and the sample of NB_H and NB921 emitters. Figure 6.3 presents examples of emitters drawn from the samples (for each filter).

6.3.2 The samples of narrow-band emitters

Narrow-band detections below the $3\,\sigma$ threshold were not considered. Due to the depth of the UKIDSS-UDS data (DR5), all extracted NB_H sources have $> 3\,\sigma$ broad-band H detections (down to ≈ 24.9 AB);

[2]For sources with no clear J detection, a statistical correction of +0.05 is applied.

for the much deeper NB921 data, only sources with $> 3\sigma$ detections in z' ($z' < 26.7$) are considered[3]. The average $3\,\sigma$ line flux limit is $7 \times 10^{-17}\,\mathrm{erg\,s^{-1}\,cm^{-2}}$ for the $\mathrm{NB_H}$ data and $7 \times 10^{-18}\,\mathrm{erg\,s^{-1}\,cm^{-2}}$ for the NB921 data. The first-pass $\mathrm{NB_H}$ sample of potential emitters contains 439 excess candidates out of all 23394 $\mathrm{NB_H}$ detections in the entire $\mathrm{NB_H}$ area ($0.78\,\mathrm{deg^2}$), while the NB921 sample has 8865 potential emitters out of 347341 NB921 individual detections over the entire NB921 area coverage.

All $\mathrm{NB_H}$ potential emitters are visually inspected in both the broad-band and narrow-band imaging. Twenty six (26) sources were removed from the sample as they were flagged as likely spurious. The majority of these (15) correspond to artifacts caused by bright stars that are on the edges of two or more frames simultaneously. The remaining 11 sources removed were low S/N detections in noisy regions of the $\mathrm{NB_H}$ image.

Visual inspection and star exclusion

All $\mathrm{NB_H}$ potential emitters are visually inspected in both the broad-band and narrow-band imaging. Twenty six (26) sources were removed from the sample as they were flagged as likely spurious. The majority of these (15) correspond to artifacts caused by bright stars that are on the edges of two or more frames simultaneously. The remaining 11 sources removed were low S/N detections in noisy regions of the $\mathrm{NB_H}$ image. After this visual check, the sample of potential $\mathrm{NB_H}$ is reduced to 413.

Even by applying a conservative EW cut, the sample of potential emitters can be contaminated by stars. Fortunately, stars can be easily identified by using the high-quality, multi-wavelength colour information available for the SXDF-UDS field. In particular, an optical colour vs. near-infrared colour (e.g. $B - z$ vs. $H - K$) is able to easily separate stars from galaxies. Here, sources satisfying $(B-z) > 13.5(H-K)+2.0$ (AB) are classed as stars. By doing this, 2 potential stars are identified in the sample of potential emitters selected from the $\mathrm{NB_H}$ data, and 118 (out of 5623 emitters) from the NB921 data (the higher number of stars in the NB921 sample is driven both by a much larger sample size and, more importantly, because of the lower EW cut used to probe down to weak [OII] EWs). These are excluded from the following analysis. It should be noted that all these sources present $B-z$ colours significantly larger than $13.5(H-K)+2.0$ (AB), and therefore the identification of these as potential stars is not affected by small changes in the separation criteria. One of the potential $\mathrm{NB_H}$ emitters flagged as a star is likely to be a cool T-dwarf (see Chapter 7).

The final sample of $\mathrm{NB_H}$ emitters over the entire $\mathrm{NB_H}$ area contains 411 sources, of which 135, 69, 136 and 71 are found over the NE, NW, SE and SW fields, respectively ($\approx 530\,\mathrm{deg^{-2}}$ over the entire field down to the average $\mathrm{NB_H}$ UDS depth). Note that by restricting the analysis to the UKIDSS-UDS area coverage (matched to the $\mathrm{NB_H}$ and NB921 simultaneous coverage), which will be mostly used throughout this paper, the survey covers $0.67\,\mathrm{deg^2}$; the sample of $\mathrm{NB_H}$ emitters is reduced to 295 sources (the rest of the sources are outside this area), while the sample of NB921 emitters has 5505

[3]This results in rejecting 5 per cent of the total number of potential emitters, but it should be noted that visual inspection of a sub-sample of these sources show that the majority are likely to be spurious, due to the combination of a faint detection in NB921 and a $< 3\,\sigma$ in z. Furthermore, the results in this paper remain unchanged even if these sources are included in the analysis.

sources.

6.3.3 Distinguishing between different line emitters

There are many possible emission-lines which can be detected individually by the NB_H and the NB921 filters. For $z < 1$ galaxies, the NB_H filter is sensitive to lines such as Paβ at $z = 0.26$ or Paγ and HeI at $z = 0.49$ or HeII at $z = 0.96$, while at $z > 1$ the (main) possible emission lines are Hα at $z \sim 1.47$, [OIII]/Hβ at $z \sim 2.25$ and [OII] at $z = 3.34$, among others. The NB921 filter is mostly sensitive to Hα at $z \sim 0.4$, [OIII]/Hβ at $z \sim 0.83$, [OII] at $z \sim 1.47$ and Lyα at $z \sim 6.6$. Hα–[OII] line emitters at $z = 1.47$ can be selected with a significant narrow-band excess in both bands, and thus simultaneous excess sources provide an extremely robust means of selecting a $z = 1.47$ sample. This is explained in Section 6.3.4. First, in order to select [OII] emitters below the Hα flux limit (see Figure 6.2), to assess the robustness and contamination of different selections, to investigate the range of different emitters, and to allow the selection in sky areas where coverage is not available in both filters, alternative approaches are considered.

Photometric redshift analysis

Multi-wavelength data can be used to effectively distinguish between line-emitters at different redshifts (different emission lines) and separately obtain Hα and [OII] selected samples of galaxies at $z = 1.47$ from the NB_H and NB921 data-sets. Out of 5505 NB921 potential emitters (excluding stars) within the UKIDSS UDS area, 2715 ($\approx 50\,\%$) have a $> 3\,\sigma$ detection in the near-IR UKIDSS data ($K \lesssim 25\,\mathrm{AB}$), while all NB_H emitters are detected in K. Robust photometric redshifts[4] are only available over a matched $0.64\,\mathrm{deg}^2$ area, mostly due to the overlap with the Subaru data and the deep Spitzer coverage (SpUDS), and for sources with $K < 23$. Photo-zs are available for 257[5] NB_H potential line emitters and 1021 NB921 excess sources.

Figure 6.4 shows the photometric redshift distribution for the selected narrow-band emitters in NB_H (left panel) and NB921 (right panel) with available photometric redshifts in UDS, demonstrating the common peak at $z \sim 1.4 - 1.5$, associated with the Hα/[OII] lines being detected in each narrow-band filter. In addition to this, the other peaks are easily identified as Hα at $z = 0.4$ and [OIII]/Hβ at $z = 0.83$ for the NB921 emitters.

Spectroscopic redshift analysis

Although an extensive spectroscopic sample is not yet available in the UKIDSS-UDS field (Almaini et al. in prep.; Pearce et al. in prep.), matching the samples of emitters with all the spectroscopic

[4]The latest photometric redshifts for UDS present $\sigma(\Delta z) = 0.015$, where $\Delta z = (z_{phot} - z_{spec})/(1 + z_{spec})$. The fraction of outliers, defined as sources with $\Delta z > 3\sigma(\Delta z)$, is lower than 2%. These photometric redshifts were used in Chapters 4 and 5.

[5]The area reduction by itself results in the loss of 297 NB921 emitters and reduces the sample of NB_H line emitters from 411 to 297. It should be noted, nonetheless, that faint sources (with no reliable photo-z information) and those outside the photo-z area can still be further investigated by using colour-colour criteria.

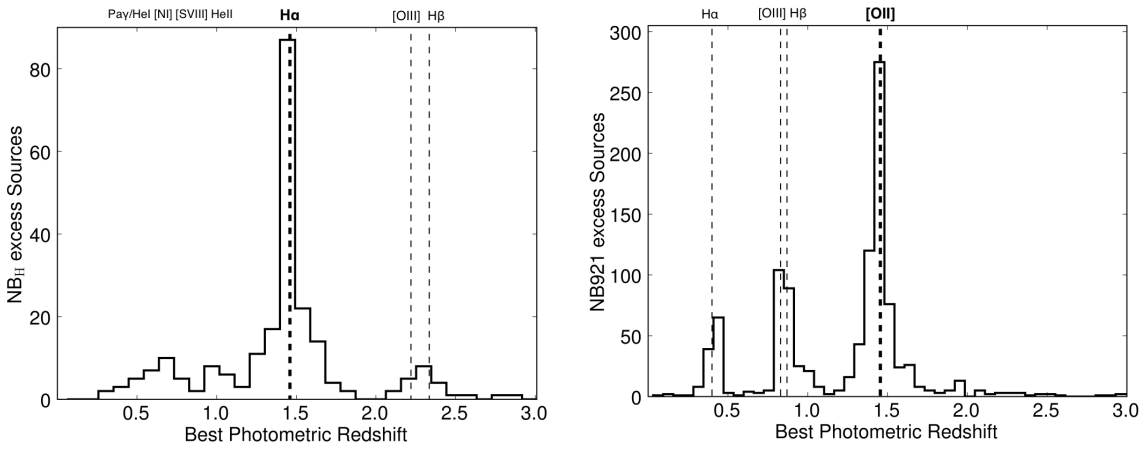

Figure 6.4: *Left*: photometric redshift distribution (peak of the probability distribution function for each source) for the NB_H emitter candidates. *Right*: the equivalent distribution for NB921 emitter candidates. Both distributions peak at $z \sim 1.47$, corresponding to Hα and [OII] emitters, respectively, but other populations of emitters are also found, such as Hα at $z = 0.4$ and Hβ/[OIII] at $z \sim 0.83$ for the NB921 data and Paschen-lines at $z < 1$, [OIII] at $z \sim 2.2$ and [OII] at $z \sim 3$ for the NB_H data. Lyα emitter candidates in the NB921 dataset (51 with reliable photometric redshift within the SpUDS coverage) with photo-z of $z \sim 6 - 7$ are not shown.

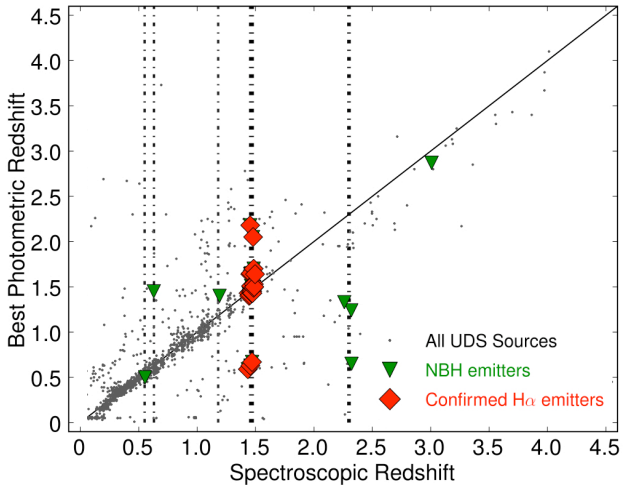

Figure 6.5: A comparison between the best photometric redshifts in the UDS field and the robust spectroscopic redshift for such sources in UDS with spectroscopic redshift. NB_H excess sources with spectroscopic redshifts are all identified with a known emission line falling into the NB_H filter. It is noteworthy that the limited (and very biased towards the strongest line emitters and AGN) spectroscopic sample reveals that some confirmed Hα emitters have photo-zs which place them at a higher and lower redshift – the use of NB921 data is able to identify these emitters which the photo-zs could miss. Vertical lines indicate the redshifts of the main emission lines detected by the NB_H filter, specifically [NI] at $z = 0.545$, [SVIII] 9914 at $z = 0.625$, [OII] 7625 at $z = 1.125$, Hα at $z = 1.47$, [OIII] 5007 at $z = 2.23$ and Hβ at $z = 2.33$.

redshifts published in the literature in this field (Yamada et al., 2005; Simpson et al., 2006; **?**; van Breukelen et al., 2007; Ouchi et al., 2008; Smail et al., 2008; Ono et al., 2010)[6] allows the spectroscopic confirmation of 17 Hα emitters at $z = 1.455-1.48$ (over the full 0.78 deg^2 area), two [OIII] 5007 emitters at $z = 2.23$, an Hβ emitter at $z = 2.33$, and three lower redshift emitters ([NI] at $z = 0.545$, [SVIII] 9914 at $z = 0.625$ and [OII] 7625 at $z = 1.125$), for the NB_H data (see Figure 6.5). Furthermore, follow-up spectroscopy with SINFONI on the VLT of 6 Hα candidates has resulted in confirming all those sources, with spectroscopic redshifts $1.45 - 1.47$ (M. Swinbank et al. in prep.), and observations with FMOS on Subaru have confirmed a further 8 Hα emitters (E. Curtis-Lake et al., in prep.), resulting in a total of 31 confirmed $z \sim 1.47$ Hα emitters.

For NB921 emitters, the limited spectroscopy confirms nine $z = 0.4$ Hα emitters, 12 $z = 0.83$ [OIII] 5007 emitters, a $z = 1.1$ Hγ emitter, ten 4000Å breaks (in which the NB921 filter probed light just to the red of the break, while the z' band is dominated by emission shortward of the break, resulting in an excess in NB921), eight [OII] emitters at $z = 1.47$, nine $z = 2.31$ MgII emitters (AGN) and a $z = 3.87$ CIII] emitter, among others.

Colour-colour separation of emitters

Colour-colour diagnosis can be valuable tools to explore the extremely deep broad-band photometry available, particularly for sources with no photometric redshift information (either because they are faint in the K band, or because they are found outside the matched Subaru-Spitzer area). In S09, the $BR - iK$ colour-colour diagram is shown to isolate $z \sim 0.8$ emitters from lower and higher redshift emitters. As Figure 6.6 shows, the same colour-colour separation is also suited to separate $z \sim 1.5$ emitters from lower redshift emitters. Such colour-colour space is found to be particularly suited to distinguish between the bulk of the NB921 emitters, as Figure 6.6 shows, clearly isolating Hα, [OIII]/Hβ and [OII] emitters. Based on the spectroscopic confirmations and the reliable photometric redshifts, empirical colour-colour selection criteria are defined (see Figure 6.6) to distinguish between emitters. The same separation line produces relatively clean samples of $z > 1.3$ emitters for the NB_H sample. However, for this filter the Hα emitters at $z \sim 1.5$ and the [OIII]/Hβ emitters at $z \sim 2 - 3$ have similar $BR - iK$ colour-colour distributions, and a new set of colours needs to be explored to separate $z \sim 1.5$ and $z > 2$ emitters, after using the $BR - iK$ technique to remove low-z emitters. As Figure 6.7 shows, $i - z$ vs. $z - K$ colours provide a good separation between $z \sim 1.5$ and $z > 2$ emitters (the selection is similar to the widely used BzK method, but can separate $z \sim 1.5$ galaxies from those at $z \sim 2$ and higher much more effectively), defining a colour-colour sub-space where Hα emitters at $z = 1.47$ should be found.

These results demonstrate that a relatively good selection of $z \sim 1.5$ emitters can be obtained using just 5-band ($BRiz'K$) photometry. The $BR - iK$ selection can be used to remove low-z emitters, and a further izK analysis is capable of removing higher redshift emitters (although there's little contamination of the latter in the NB921 sample).

[6] See UKIDSS UDS website for a redshift compilation by O. Almaini.

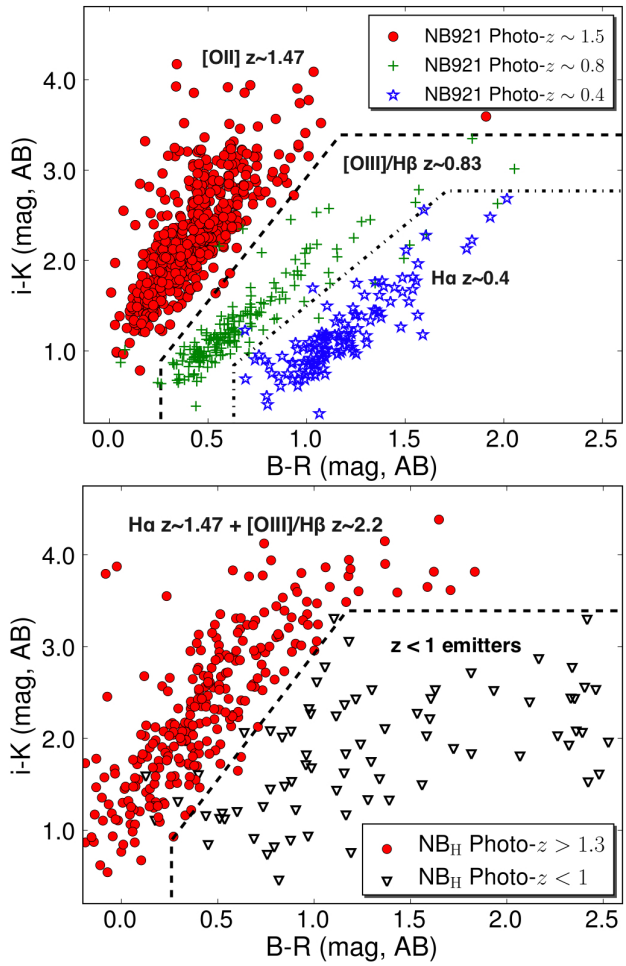

Figure 6.6: *Top*: The $i-$K vs. B$-R$ (AB) colour-colour distribution of NB921 emitters, clearly separating the 3 types of emitters that make the bulk of the sample of emitters. Simple lines for distinguishing these emitters – supported by evolution tracks – are also shown. *Bottom*: An equivalent plot for the NB$_H$ emitters (AB), again demonstrating that lower redshift emitters can be easily isolated from the $z = 1.47$ Hα emitters. Higher redshift emitters, however, occupy a similar region, and can not be robustly isolated with this set of colours alone. The two pivot points for the $z \sim 0.4$ and $z \sim 0.8$ separation are [0.63,0.84] and [1.71,2.77]; while the two pivot points used to separate $z \sim 0.8$ from $z \sim 1.5$ are [0.26,0.89] and [1.17,3.39].

6.3.4 The dual narrow-band approach at $z = 1.47$

As Figure 6.1 demonstrates, the two narrow-band filter profiles are extremely well matched in redshift (although the NB921 filter probes a slightly wider range in redshift). The match can be fully explored to select robust Hα emitters at $z = 1.47$, as these should be detected as [OII] emitters in NB921 (because of the depth of those data). Within the matched NB$_H$-NB921 area (out of a sample of 297 NB$_H$ emitters), a sample of 178 dual-emitter sources is recovered. Figure 6.8 shows the photometric redshift distribution of the double emitters, compared with the distribution of all NB$_H$ emitters with photo-zs (for roughly the same area). The results clearly suggest that the dual-emitter candidate criteria is able to recover essentially the entire population of $z = 1.47$ Hα emitters. Moreover, the dual-emitter selection also recovers some sources with photometric redshifts which are higher and

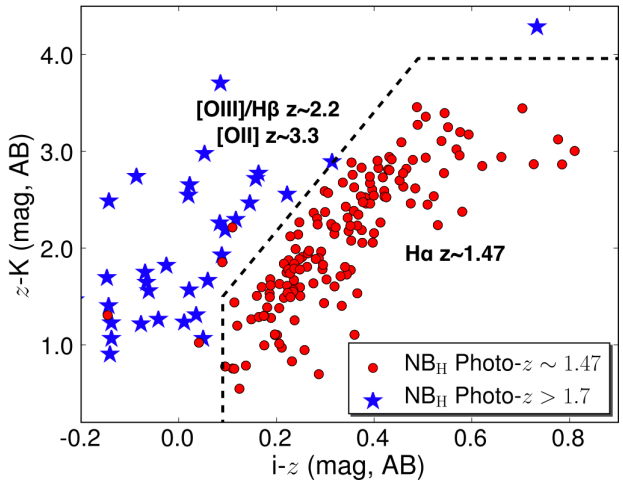

Figure 6.7: The $z-$K vs. i$-z$ (AB) colour-colour distribution of NB$_H$ emitters, demonstrating a method to distinguish between the population of $z \sim 1.47$ Hα emitters, which dominate the sample, and higher redshift emitters such as [OIII] and Hβ emitters at $z \sim 2.2$. The dashed line presents the simple separation used (in combination with the removal of lower redshift emitters using the criteria in Figure 6.6) for sources with no photometric redshifts. The colour separation is similar to the BzK selection, but by using the $i-z$ colour it better picks up the 4000Å break for $z = 1.47$ galaxies, thus separating them better from $z \sim 2$ galaxies than using $B-z$. The two pivot points for the $z \sim 2.2$ and $z \sim 1.47$ separation are [0.09,1.50] and [0.49,3.96].

lower than $z = 1.47$ and that would have been missed by a simple photo-z selection. Interestingly, some of these are confirmed to be $H\alpha$ emitters at $z = 1.47$ by the available spectroscopic redshifts (see Figure 6.5), indicating that their selection by the dual-emitter technique is reliable.

Searching for low [OII] EWs Hα emitters

Figure 6.9 shows the distribution of [OII]/Hα line ratios for the emitters selected in both narrow-band filters. In order to ensure maximum completeness at the faintest [OII] fluxes, and minimise any possible biases, a search for extra Hα emitters with significant ($\Sigma > 3$) NB921 colour-excess but low [OII] EWs (i.e. waiving the 25Å EW requirement), is conducted. This yields 12 additional sources above the NB921 flux limit. All of these additional sources present colours and photometric redshifts consistent with being genuine $z \sim 1.47$ sources and probe down to the lowest [OII]/Hα line fractions (see Figure 6.9); their colours are consistent with being sources affected by higher dust extinction. These 12 sources are included in the robust double-emitter sample.

The completeness of the Hα-[OII] double selection

The completeness limit on the [OII]/Hα flux ratio (see Figure 6.9) indicates that the deep NB921 flux limit guarantees a very high completeness of the dual-emitter sample, and suggests that the small number of sources that photo-zs indicate as being at $z \sim 1.47$, but which are not NB921 excess sources, are actually at other redshifts. To test this further, the photometric redshift and colour-colour selections are applied in the same matched sky area. These identify 32 Hα candidate sources which

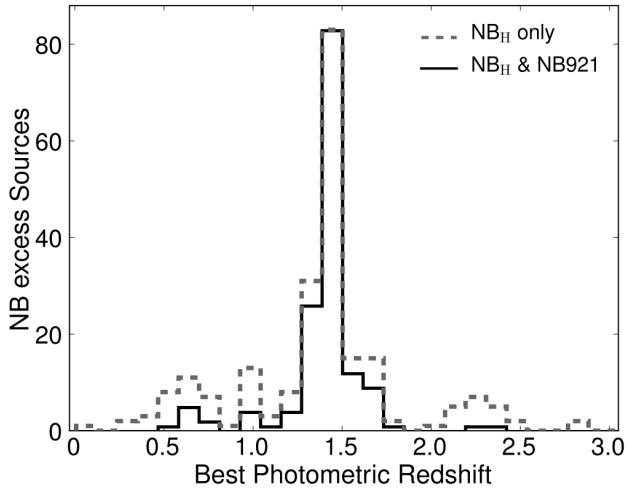

Figure 6.8: The photometric redshift distribution of simultaneous NB_H & NB921 narrow-band emitters when compared to all NB_H emitters within the NB921 imaging area. By matching both samples, it is possible to define a robust sample of Hα&[OII] emitters without the need for colour or photometric redshift selection. Note that emitters with $K > 23$ AB are not found in the photo-z catalogue, and therefore not shown in the figure.

are not selected by the dual-emitter approach. Four of these sources have spectroscopic redshifts available, and all four of these are indeed spectroscopically confirmed to lie at different redshifts (cf. Figure 6.5). Of the remaining 28, 18 sources have significantly negative excesses in NB921, and the remaining 10 have $< 3\Sigma$ excesses which would correspond to a range of NB921 line fluxes from $\sim 0.1 - 1 \times 10^{-18}\,\mathrm{erg\,s^{-1}\,cm^{-2}}$. If real, these line fluxes would imply very low [OII]/Hα flux ratios, indicating that the sources must be highly extinguished; however, their UV and optical colours appear inconsistent with such high extinction (see Section 6.5.6). Thus, these sources are likely to be a mixture of other line emitters of weaker emission lines close to Hα (e.g. [NII], [SII]), which the photometric redshifts are not sufficiently accurate to distinguish (see Chapter 3).

6.3.5 Selecting Hα and [OII] z = 1.47 emitters

Hα emitters at $z = 1.47$

Section 6.3.4 shows that with the flux limits of this study, the NB_H-NB921 is clearly a clean and highly complete means of selecting $z = 1.47$ Hα emitters. The sample of robust Hα emitters at $z = 1.47$ is therefore derived solely by using the dual-emitter selection, within the matched area. This results in the selection of very robust 190 Hα-[OII] sources at $z = 1.47$.

[OII] emitters at $z = 1.47$

In order to select [OII] emitters, in addition to the dual-emitter selection at bright fluxes, both photo-zs and(or) colours are used. In particular, the $z = 1.47$ [OII] candidates are defined to be narrow-band excess sources with $z_{min} < 1.47 < z_{max}$ (where z_{min} and z_{max} are the 3-σ redshift limits of the

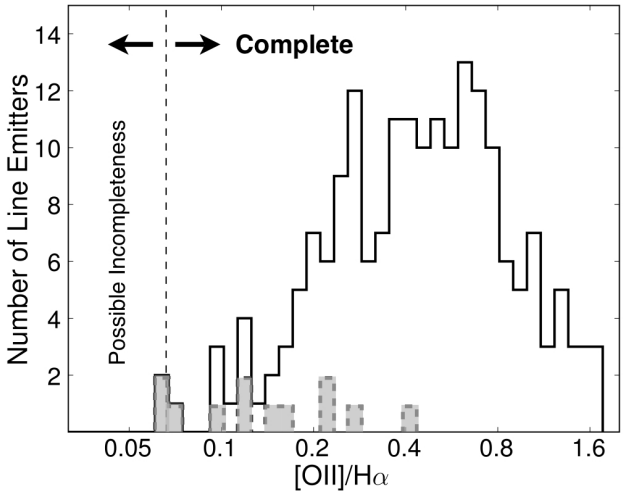

Figure 6.9: The distribution of the [OII]/Hα line ratios for the robust sample of 190 simultaneous Hα-[OII] line emitters at $z = 1.47$ (the shaded region represents the 12 sources with the low [OII] EWs). The vertical dashed line represents the lowest line ratio that the combined survey is able to probe at the lowest Hα fluxes; this shows that the [OII] survey is deep enough to recover essentially all Hα emitters and that the line flux distribution is not a result of a bias caused by insufficient sensitivity at the lowest line flux ratios.

principle peak in the photometric redshift probability distribution – photo-zs of emitters have a typical Δz of ≈ 0.13) or those that are found within the defined $BR - iK$ colour-colour space ($B - R < 0.26$ or $i - K > 4.92$ or $i - K > 4.121(B - R) + 1.349$; see Figure 6.6). Even though the contamination from higher redshift ($z > 1.5$) emitters (such as MgII) is likely to be low, the colour-colour selection presented in Figure 6.7 is also applied ($i - z < 0.24$ or $z - K > 5.33$ or $z - K > 6.15(i - z) + 1.394$), to remove potential higher redshift ($z > 1.5$) emitters. This results in a sample of 1379 [OII] selected emitters down to the flux limit of the survey. However, as noted before, many faint NB921 emitters are not detected in at least one of the bands necessary for the colour-colour identification, and therefore are not included directly in the [OII] sample. Section 6.4.3 investigates how this can bias the determination of the faint-end of the luminosity function and derives a correction to account for the sources which are missed.

6.4 Hα and [OII] Luminosity functions

6.4.1 Contribution from adjacent lines

While the NB921 filter can measure the [OII] emission line (which, in fact, is a doublet) without contamination from any other line, this is not the case for NB_H and the Hα line. The nearby [NII] emission lines can contribute to the NB_H emission flux, and therefore both EWs and fluxes will be a sum of [NII] and Hα. The limited spectroscopic follow-up in the H band with SINFONI (M. Swinbank et al. in prep.) provides good enough S/N and spectral resolution to compute individual [NII] fractions/corrections. The data show a range of [NII] fractions between 0.1–0.4 and, despite

being a limited sample, the results are broadly consistent with Equation 3.3, which estimates the [NII] contamination as a function of total rest-frame EW_0([NII]+Hα). For the analysis presented in this work, the polynomial approximation used in Chapter 3 has been re-computed using a higher order polynomial which is able to reproduce the full SDSS relation between the average, log([NII]/Hα) (f), and logEW_0([NII]+Hα), E: f=-0.924+4.802E-8.892E^2+6.701E^3-2.27E^4+0.279E^5. This relation is used to correct all Hα fluxes in this work. The average correction for the $z = 1.47$ sample is 0.22 (average rest-frame EW_0(Hα+[NII]) of 130Å).

6.4.2 Individual line completeness

It is fundamental to understand how complete the samples are as a function of line flux. This is done using simulations, as described in Chapter 3. Briefly, the simulations consider two major components driving the incompleteness fraction: the detection completeness (which depends on the actual imaging depth and the apertures used) and the incompleteness resulting from the selection (both EW and colour significance). The first component is studied individually per frame, by adding a set of fake galaxies with a given input magnitude to each frame and obtaining both the recovery fraction and the recovered magnitude. The second component is studied by using non-selected emitters, and adding an emission line with a given flux to all those in order to study the fraction recovered. In an improvement to Chapter 3, sources classed as stars and those occupying the $z < 1$ region of the BR-iK diagram are not used in this simulation – this results in a set of galaxies with an input magnitude distribution which is very well-matched to the $z = 1.47$ population, providing a more realistic sample to study the line completeness of the survey for $z = 1.47$ Hα emitters. By taking this approach, the observed H band magnitude distribution is quite different from that of all detections, as can be seen in Figure 6.10. Indeed, by using the entire population of detections, the number of bright sources with low equivalent widths is over-estimated, and thus an overall lower completeness fraction is derived. Figure 6.11 compares the completeness fraction as a function of input line flux for simulations using all sources and for those using only $z > 1$ galaxies (rejecting potential stars and using the BR-iK colour-colour selection).

For each recovered source, a detection completeness is associated, based on its new magnitude. The results (survey average) can be found in Figure 6.11, but it should be noted that because of the differences in depth, simulations are conducted for each individual frame, and the appropriate completeness corrections applied accordingly when computing the luminosity function.

A similar procedure is followed for the NB921 data (average results are also shown in Figure 6.11); corrections are also derived and used individually for each field, although the differences in depth are not as significant as for the NB_H data. Similarly to the NB_H analysis, non-emitter sources which are classed as stars and low redshift ($z < 1$) are rejected when studying how the completeness of the survey varies with line flux in order to better estimate how complete the survey is specifically for $z = 1.5$ line emitters.

For any completeness correction applied, an uncertainy of 20% of the size of the correction is added

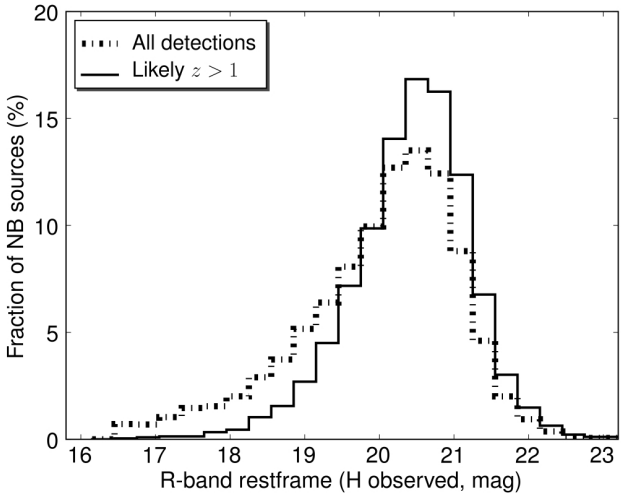

Figure 6.10: Observed H band magnitude (R rest-frame at $z = 1.47$) distributions for the two samples used in the completeness simulations. Note the difference between the samples at bright magnitudes: while the sample of likely $z > 1$ galaxies presents a strong peak at faint magnitudes and a relatively sharp decline for brighter magnitudes, the sample containing all detections presents a much broader distribution, including a much shallower decay at bright magnitudes.

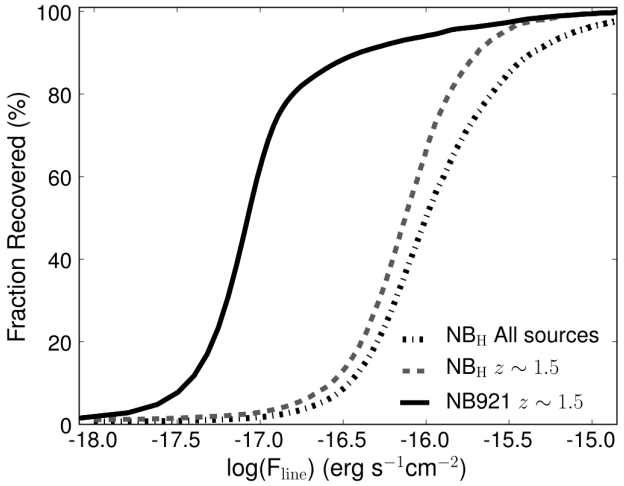

Figure 6.11: A study of the completeness fraction (defined as the fraction of sources with a given flux recovered by the selection against the actual number of sources with that flux) in order to address incompleteness as a function of line flux for both NB_H and NB921 samples in the SXDF-UKIDSS-UDS field. Note that both image detection and colour-magnitude selection are taken into account as these are *both* sources of incompleteness, and that sources identified as stars or at $z < 1$ are not included in the studies. For comparison, for the NB_H filter the completeness fraction as a function of input line flux is also shown when calculated using the entire sample. The results confirm the flux limit computed for both bands (down to $\sim 3\,\sigma$), and allow to compute individual completeness corrections that will be used when evaluating the luminosity functions.

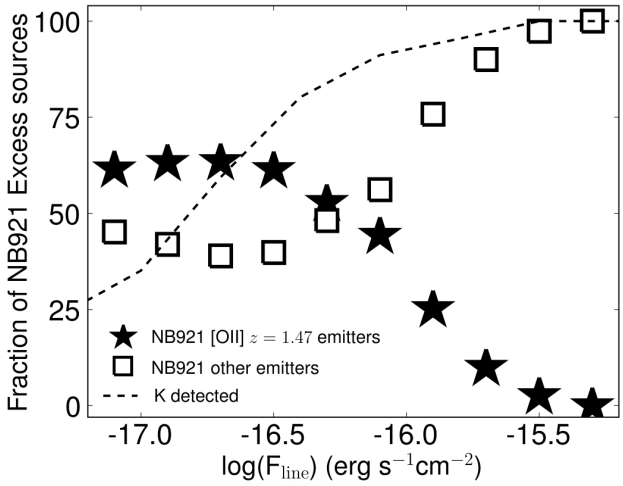

Figure 6.12: Fraction of [OII] and non-[OII] NB921 emitters (amongst those with K detections, allowing for a colour-colour separation) as a function of emission line flux. A significant number of potential line emitters are not in the final [OII] colour-selected sample as they are not detected in the K band imaging; the fraction of all emitters with a K detection is also shown.

in quadrature to the other uncertainties to account for possible inaccuracies in the simulations.

6.4.3 [OII] selection completeness

A significant fraction of NB921-selected emitters do not have photometric redshifts (79%), and half of the sample is undetected in K above the 3σ limit. Therefore, these cannot be robustly classified, implying they are not included in the [OII] sample, even though at least some of them may well be genuine [OII] emitters at $z = 1.47$. This can cause a potentially significant incompleteness in the [OII] sample, resulting in an underestimation of the luminosity function. In order to investigate this source of incompleteness and its effect in the determination of the luminosity function, the fraction of emitters with K detections (which generally sets the limit for colour-colour selection, as the other bands used are significantly deeper - though even in the optical bands typically 33% of the sources are undetected) is studied as a function of line flux. As Figure 6.12 shows, the fraction of NB921 excess sources with K detections falls as a function of decreasing line fluxes, suggesting that the incompleteness is higher at the lowest fluxes. This can have implications for determinations of the faint end slope of the luminosity function. Note that other studies at this redshift do not discuss, or appear to take account of, this potential bias.

Figure 6.12 also shows that, for the classifiable sources, the fraction of [OII] emitters rises with decreasing flux at the highest fluxes, and then seems to remain relatively flat at $\sim 60\%$ down to the lowest fluxes. Assuming that this same distribution is true for the unclassified sources (which is likely, since the [OII] fraction also remains roughly constant with K–band magnitude for the faintest K magnitudes probed), it is possible to estimate a correction at a given flux that is given by the ratio of the classifiable sources to all sources at that flux. This is equivalent to including unclassified emitters

in the luminosity function calculation with a weight that is given by the fraction of [OII] emitters at that flux. An uncertainty corresponding to 20% of this correction is added in quadrature to the other uncertainties.

6.4.4 Volume: Hα and [OII] surveys

Assuming the top-hat (TH) model for the NB_H filter (FWHM of 211.1 Å, with $\lambda_{min}^{TH} = 1.606\,\mu$m and $\lambda_{max}^{TH} = 1.627\,\mu$m), the Hα survey probes a volume of $2.667 \times 10^5\,\mathrm{Mpc}^3$. When matched to the NB921 coverage, this is reduced to $2.2872 \times 10^5\,\mathrm{Mpc}^3$ due to the reduction in area – the matched FWHM is the same. While this is the total volume probed for the common flux limit over the entire coverage, each pointing reaches a slightly different flux limit, and therefore at the faintest fluxes the volume is smaller (as only one pointing is able to probe those). This is taken into account when determining the luminosity function: only areas with a flux limit above the flux (luminosity) bin being calculated are actually taken into account. In practice, this results in only using $\sim$ one quarter of the total area for the faintest bin (with this being derived from the deeper WFCAM pointing).

Assuming a top-hat model for the NB921 filter, (FHWM of 132 Å, with $\lambda_{min}^{TH} = 0.9130\,\mu$m and $\lambda_{max}^{TH} = 0.9262\,\mu$m), the [OII] survey probes a volume (over $0.67\,\mathrm{deg}^2$) of $2.5102 \times 10^5\,\mathrm{Mpc}^3$ when assuming a single line at 3727Å, and a volume of $2.6363 \times 10^5\,\mathrm{Mpc}^3$ using the fact that the [OII] line is actually a doublet; 3726.1Å and 3728.8Å. For simplicity, because the change in volume is less than 5 per cent (and therefore much less than the errors), and for consistency with other authors (allowing a better comparison), the volume used assumes a single line.

6.4.5 Filter Profiles: volume and line ratio biases

Neither NB_H or NB921 filter profiles are perfect top-hats. Figure 6.1 presents the filter profiles and how they compare. In order to evaluate the effect of this bias on estimating the volume (luminous emitters will be detectable over larger volumes – although, if seen in the filter wings, they will be detected as fainter emitters), a series of simulations is done. Briefly, a top-hat volume selection is used to compute a first-pass (input) luminosity function and derive the best Schechter Function fit. The fit is used to generate a population of simulated Hα emitters (assuming they are distributed uniformly across $1.40 < z < 1.52$); these are then folded through the true filter profile, from which a recovered luminosity function is determined. Studying the difference between the input and recovered luminosity functions shows that the number of bright emitters is underestimated, while faint emitters are slightly over-estimated (c.f. Chapter 3 for details). This allows correction factors to be estimated – these are then used to obtain the corrected luminosity function.

Figure 6.1 also shows how the NB_H and NB921 filters are very well matched, although the [OII] coverage is slightly wider than the Hα coverage. In order to evaluate how this might affect the results on line ratios, a series of simulations is done. Simulated [OII]+Hα emitters are distributed uniformly in a volume defined by $1.40 < z < 1.52$, which contains the entire transmission regions of both profiles.

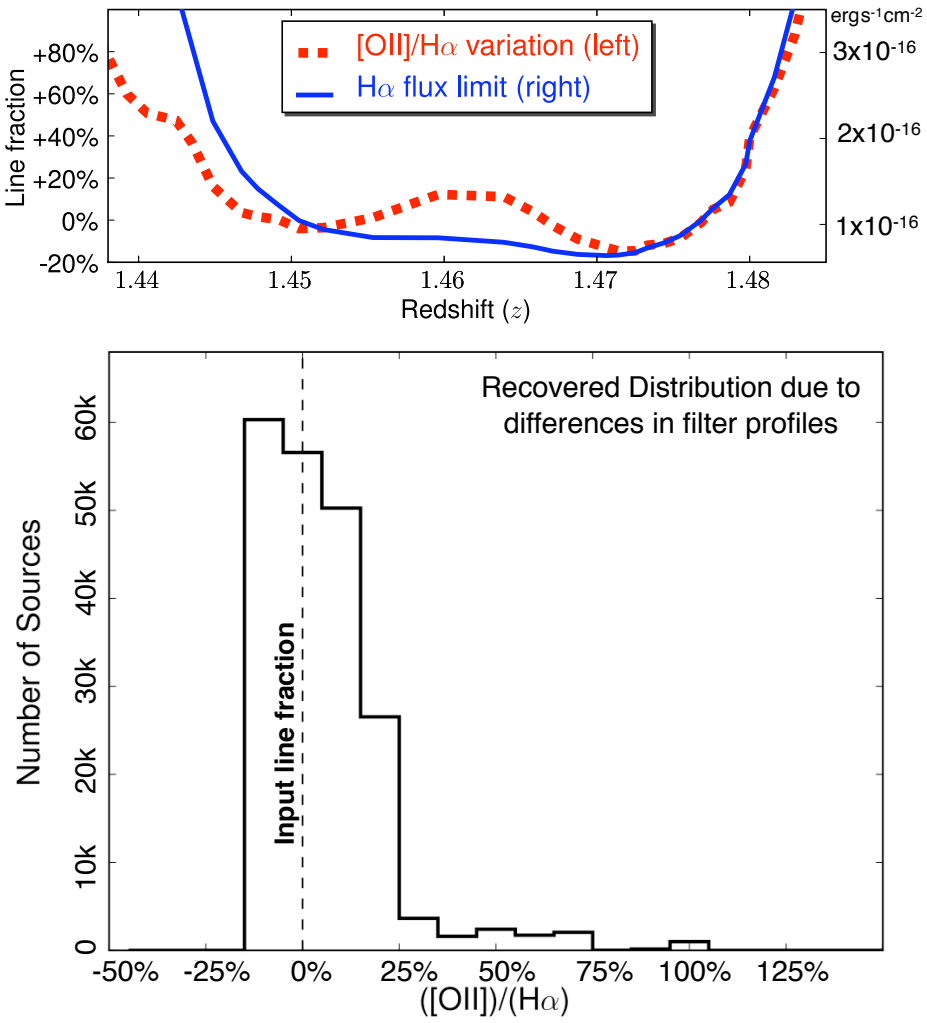

Figure 6.13: *Top*: the variation of the measured [OII]/Hα line ratio as a function of galaxy redshift due to the small differences in the transmission function of both filter profiles. Note that the flux limit (in units of erg s^{-1} cm^{-2}) also varies very significantly as a function of redshift, and thus line ratios are likely to be correct to within less than 20% for the large bulk of the sample. *Bottom*: by using the Hα luminosity function to produce a population of galaxies distributed over a wider redshift range than the filter profile, it is possible to use both NB_H and NB921 filter profiles to study in a simple way the distribution of the ratio between the recovered and input line fractions. The results recover the input line fraction with 17% standard deviation and with less than 1% recovered with a line fraction increased by more than +50%.

Emitters are given a wide range of Hα fluxes based on the observed Hα luminosity function, and [OII] fluxes corresponding to [OII]/Hα line ratios between 0.1 and 1.0. The real filter profiles are then used to recover, for each emitter, both the [OII] and Hα fluxes, and therefore allow the study of both the recovered line fluxes and the recovered line ratios. Based on these results – presented in Figure 6.13 – the line ratios should be accurate within $\sim 20\%$.

6.4.6 Extinction Correction

The Hα emission line is not immune to dust extinction, although it is considerably less affected than the [OII] emission line. Measuring the extinction for each source can in principle be done by several methods, ranging from spectroscopic analysis of Balmer decrements to a comparison between Hα and far-infrared determined SFRs, but such data are currently not available.

In this Section, the analysis of the Hα luminosity function is done using $A_{H\alpha} = 1$ mag of extinction at Hα[7], as this allows an easy comparison with the bulk of other studies which have used the same approach. Some studies have used a Hα dependent extinction correction – either derived from Garn et al. (2010), or the one derived from Hopkins et al. (2001). However, Section 6.5 suggests that at least the overall normalization of such a relation at $z \sim 1.5$ is significantly lower (dust extinction is not as high as predicted for the very high luminosities probed) and that this therefore over-predicts dust-extinction corrections by ~ 0.5 mag. Finally, the [OII] luminosity function is presented without any correction for extinction, in order to directly compare it with the bulk of other studies. Detailed extinction corrections and a discussion regarding those are presented in Section 6.5.

6.4.7 Hα Luminosity Function at $z = 1.47$ and Evolution

By taking all Hα selected emitters, the luminosity function is computed. As previously described, it is firstly assumed that the NB_H filter is a perfect top-hat, but the method fully described in Chapter 3 is applied to correct for the real profile (see Section 6.4.5). Candidate Hα emitters are assumed to be all at $z = 1.47$ (as far as luminosity distance is concerned). Results can be found in Figure 6.14. The luminosity function is fitted with a Schechter function defined by three parameters α, ϕ^* and L^*:

$$\phi(L)\mathrm{dL} = \phi^* \left(\frac{L}{L^*}\right)^{\alpha} e^{-(L/L^*)} \mathrm{d}\left(\frac{L}{L^*}\right). \tag{6.3}$$

In the log form the Schechter function is given by:

$$\phi(L)\mathrm{dL} = \ln 10\, \phi^* \left(\frac{L}{L^*}\right)^{\alpha} e^{-(L/L^*)} \left(\frac{L}{L^*}\right) \mathrm{d}\log \mathrm{L}. \tag{6.4}$$

A Schechter function is fitted to the Hα luminosity function, with the best fit resulting in:

$$\log L^*_{H\alpha} = 42.50 \pm 0.23\,\mathrm{erg\,s^{-1}}; \quad \log \phi^*_{H\alpha} = -2.44 \pm 0.33\,\mathrm{Mpc^{-3}}; \quad \alpha_{H\alpha} = -1.6 \pm 0.4$$

The best-fit function is also shown in Figure 6.14, together with the luminosity functions determined by Ly et al. (2007) – extending the work by Gallego et al. (1995) – at $z \approx 0$ and that from Shioya et al. (2008) at $z = 0.24$. Also presented on Figure 6.14 are luminosity functions from the other HiZELS redshifts. In order to guarantee a fully consistent view, the $z = 0.84$ luminosity function displayed here has been re-computed from that in Chapter 3. The new luminosity function uses the revised catalogues presented in Chapters 4 and 5, and uses new completeness corrections, re-computed fluxes and the rest-frame EW dependent [NII] correction. The changes to the luminosity function are only

[7] Corresponding to ~ 1.76 mag of extinction at [OII] for a Calzetti et al. (2000) extintion law.

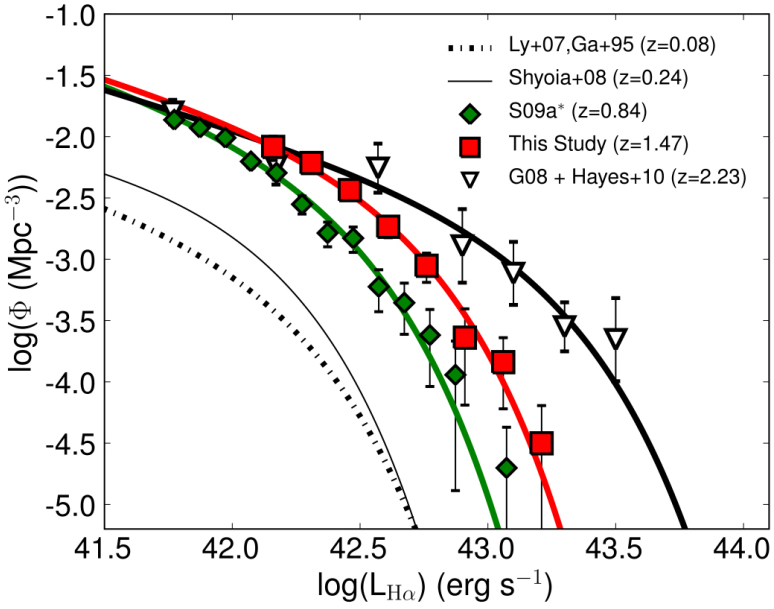

Figure 6.14: The Hα luminosity function evolution, determined with unprecedented detail up to $z \sim 2.3$. The new measurement at $z = 1.47$ is combined with re-computed measurements from Chapter 3 and other narrow-band studies (Gallego et al., 1995; Ly et al., 2007; Shioya et al., 2008; Geach et al., 2008; Hayes et al., 2010; Tadaki et al., 2011). This confirms the strong $L^*_{H\alpha}$ evolution from $z = 0$ to $z = 2.23$.

minor. At $z = 2.23$, the luminosity function has also been re-calculated by combining the results from Geach et al. (2008), with new ultra-deep measurements of the faint end by Hayes et al. (2010) – using HAWK-I on VLT – and Tadaki et al. (2011) – using MOIRCS on Subaru. Best fits for the HiZELS luminosity functions at $z = 0.84$, $z = 1.47$ and $z = 2.23$ are presented in Table 6.2.

The results confirm the strong evolution from the local Universe to $z = 2.23$ and provide further insight. In particular, while there is significant evolution up to $z \sim 0.8$, the Hα luminosity functions at $z \sim 0.8$, $z \sim 1.47$ and $z \sim 2.23$ (including the ultra-deep measurement by Hayes et al., 2010) seem to agree well at the lowest luminosities probed (below $\log L_{H\alpha} \sim 42.0\,\mathrm{erg\,s^{-1}}$) in normalisation and slope – all consistent with a relatively steep value of $\alpha \sim -1.6$. A similar α is found by Ly et al. (2011). In contrast, at the bright end, $L^*_{H\alpha}$ is clearly seen to continue to increase from $z = 0.84$ to $z = 1.47$ and to $z = 2.23$, with $\log L^* \propto 0.6z$. This implies that the bulk of the evolution from $z = 2.23$ to $z \sim 1$ is happening for the most luminous Hα emitters ($L_{H\alpha} > 10^{42}\,\mathrm{erg\,s^{-1}}$), which greatly decrease their number density as the Universe ages: the faint-end number densities seem to remain relatively unchanged.

6.4.8 The [OII] Luminosity function at $z = 1.47$ and Evolution

The [OII] luminosity function at $z = 1.47$ (not corrected for dust extinction) is shown in Figure 6.15. Note that this includes corrections for i) incompleteness in both detection and flux selection, ii) incompleteness in the redshift selection of [OII] emitters and iii) correction for the filter profile not

Table 6.2: The luminosity function and star-formation rate density evolution at the peak of the star formation history as seen by HiZELS at $z = 0.84$, $z = 1.47$ and $z = 2.23$; assuming 1 mag extinction at Hα. Columns present the redshift, break of the luminosity function, $L^*_{H\alpha}$, normalisation, $\phi^*_{H\alpha}$ and faint-end slope of the luminosity function, α. The 3 right columns present the star formation rate density at each redshift based on integrating the luminosity function down to the given luminosity limit (in log $\mathrm{erg\,s^{-1}}$). Star formation rate densities include a correction for AGN contamination of 10% at $z = 0.84$ (c.f. Garn et al. 2010) and 15% at both $z = 1.47$ and $z = 2.23$.

Epoch (z)	$L^*_{H\alpha}$ $\mathrm{erg\,s^{-1}}$	$\phi^*_{H\alpha}$ $\mathrm{Mpc^{-3}}$	$\alpha_{H\alpha}$	$\rho_{SFRH\alpha}$ 42 $\mathrm{M_\odot\,yr^{-1}\,Mpc^{-3}}$	$\rho_{SFRH\alpha}$ 40 $\mathrm{M_\odot\,yr^{-1}\,Mpc^{-3}}$	$\rho_{SFRH\alpha}$ All $\mathrm{M_\odot\,yr^{-1}\,Mpc^{-3}}$
$z = 0.84 \pm 0.02$	42.25 ± 0.16	-2.36 ± 0.29	-1.66 ± 0.34	0.03 ± 0.01	0.12 ± 0.04	0.13 ± 0.06
$z = 1.47 \pm 0.02$	42.50 ± 0.23	-2.44 ± 0.33	-1.6 ± 0.4	0.06 ± 0.02	0.15 ± 0.06	0.16 ± 0.05
$z = 2.23 \pm 0.02$	43.07 ± 0.24	-2.93 ± 0.41	-1.60 ± 0.21	0.12 ± 0.06	0.20 ± 0.09	0.22 ± 0.10

being a perfect tophat. The fully-corrected [OII] luminosity function is found to be well-fitted by a Schechter function, with the best fit resulting in:

$$\log L^*_{[\mathrm{OII}]} = 41.71 \pm 0.09\,\mathrm{erg\,s^{-1}}; \quad \log \phi^*_{[\mathrm{OII}]} = -2.01 \pm 0.10\,\mathrm{Mpc^{-3}}; \quad \alpha_{[\mathrm{OII}]} = -0.9 \pm 0.2$$

The results are compared with other studies at different redshifts (Hogg et al., 1998b; Gallego et al., 2002; Takahashi et al., 2007; Ly et al., 2007; Bayliss et al., 2011) – all uncorrected for dust extinction – and shown in Figure 6.15. The comparison reveals a significant evolution in the [OII] luminosity function from $z \approx 0$ to $z = 1.47$. Such evolution seems to be simply described by a ϕ^* and L^* evolution up to $z \sim 0.9$ and a continuing L^* evolution from $z \sim 0.9$ up to $z \sim 2$, in line with the results for the evolution of the Hα luminosity function. It should also be noted that there is good agreement with the Ly et al. (2007) luminosity function at the same redshift derived from a smaller area, but at a similar depth.

The correction for redshift/emitter selection is found to be particularly important at faint fluxes, setting the slope of the faint-end of the luminosity function (although it has little effect on the values of L^* and ϕ^*). If no correction for unclassified sources is applied, the best-fit Schechter function yields $\alpha \approx -0.2$ (compared to the corrected best-fit of $\alpha \approx -0.9$). In the extreme case where all the non-selectable emitters are assumed to be [OII], it would yield $\alpha \approx -1.8$. This makes it clear that the crucial data that one needs in order to improve the determination of the faint-end slope is not new, deeper NB921 data, but rather significantly deeper multi-wavelength (or spectroscopic) data, which will enable to completely distinguish between different line emitters at faint fluxes (or at least provide a more robust correction by classifying a much higher fraction of emitters).

6.4.9 Evolution of the Hα and [OII] Luminosity Functions

Robust measurements of the evolution of both the Hα and [OII] luminosity functions up to $z \sim 2$ have been presented. The results reveal that there is a strong, and consistent, evolution of both luminosity functions. Moreover, while the evolution up to $z \sim 1$ can be described as both an increase of the

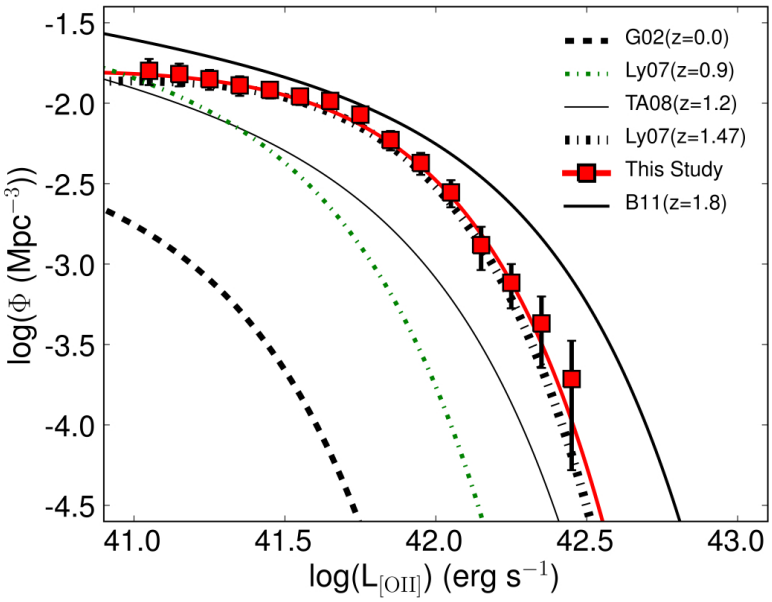

Figure 6.15: The [OII] luminosity function derived from this study, at $z = 1.47$ and a comparison with measurements at different redshifts from Gallego et al. (2002); Takahashi et al. (2007); Ly et al. (2007); Bayliss et al. (2011) and with a measurement at the same redshift (using the same narrow-band filter, but on a different field) by Ly et al. (2007). There is a clear evolution in the [OII] luminosity function, at least up to $z \sim 2$.

typical luminosity (L^*) and an increase of the overall normalization of the luminosity functions (ϕ^*), at $z > 1$ the bulk of the evolution is driven by a continuous increase in L^*. The current results also show that the faint-end slope (and the number density of the faintest star-forming galaxies probed) seems to remain relatively unchanged during the peak of the star formation history ($z \sim 1 - 2$). Of course, the latter does not imply, at all, that the faint population is not evolving. Furthermore, particularly beyond $z \sim 1$, AGN contamination at the highest luminosities could still be polluting the view of the evolution of the star-forming population.

6.4.10 The star formation rate density at $z = 1.47$

The best-fit Schechter function fit to the Hα luminosity function can be used to estimate the star formation rate density at $z = 1.47$. The standard calibration of Kennicutt (1998) is used to convert the extinction-corrected Hα luminosity to a star formation rate:

$$\mathrm{SFR}(\mathrm{M_\odot yr^{-1}}) = 7.9 \times 10^{-42}\ \mathrm{L_{H\alpha}\ (erg\,s^{-1})}, \tag{6.5}$$

which assumes continuous star formation, Case B recombination at $T_e = 10^4$ K and a Salpeter initial mass function ranging from 0.1–100 $\mathrm{M_\odot}$. A constant 1 magnitude of extinction is assumed for the analysis, as this is a commonly adopted approach which is a good approximation at least for the local Universe. Section 6.5 will investigate this further based on the analysis of emission-line ratios, revealing that $\mathrm{A_{H\alpha}} \sim 1.0$ mag for the sample presented in this Chapter. A 15% AGN contamination is

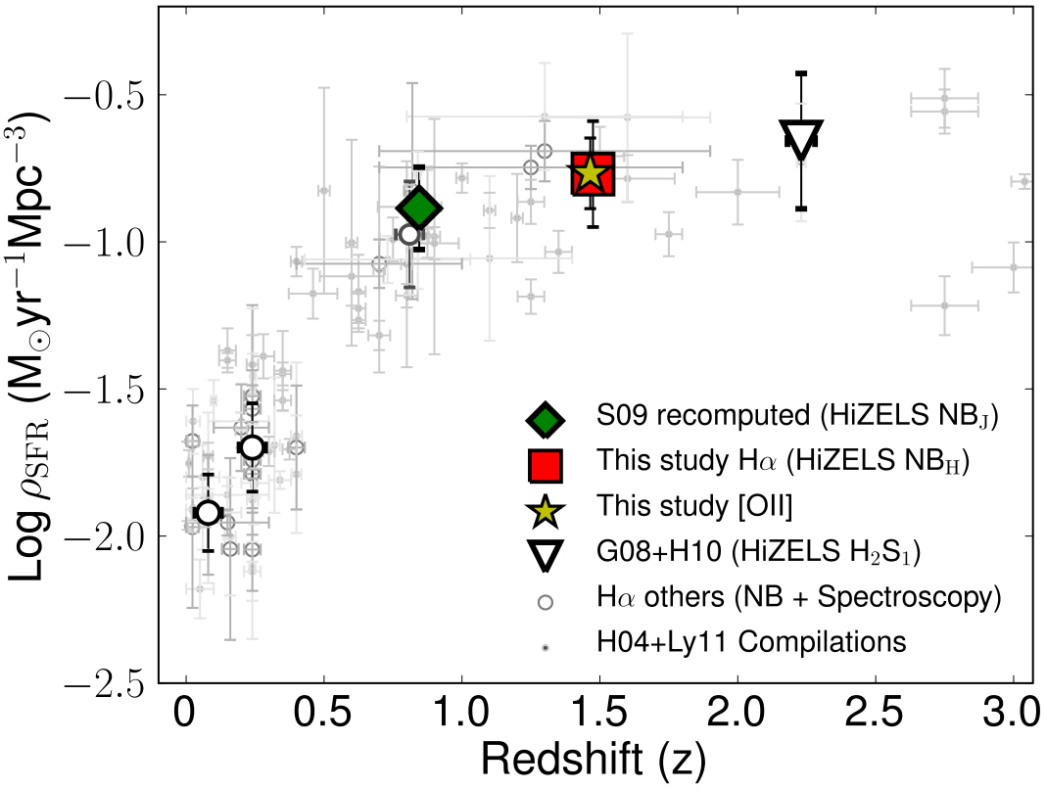

Figure 6.16: The star formation rate density and its evolution with redshift up to $z \sim 2.3$ using Hα only, but also including the [OII] measurement presented in this paper (assuming 1 magnitude of extinction at Hα) and compared to estimates at different redshifts from the literature. Darker circles represent the results from Hα studies which are also shown in Figure 13. This confirms a strong evolution in the star formation rate density over the last ~ 10 Gyrs, with a flattening or slow decline over $1 < z < 2$ and a sharp decrease from $z \sim 1$ to $z \sim 0$.

also assumed (Garn et al. 2010 found AGN $\sim 10\%$ contamination at $z = 0.84$, but the contamination is likely to be higher at higher redshift and the slightly higher flux limit of this sample). Down to the survey limit (after extinction correction, $L_{H\alpha} = 10^{42} \mathrm{erg\,s^{-1}}$), one finds $\rho_{SFR} = 0.07 \pm 0.01\, M_\odot\, yr^{-1}$ Mpc^{-3}; a complete integration extrapolating to zero luminosity yields $\rho_{SFR} = 0.16 \pm 0.05\, M_\odot\, yr^{-1}$ Mpc^{-3}. Furthermore, by using the standard Kennicutt (1998) calibration of [OII] as a star formation tracer (calibrated using Hα),

$$SFR(M_\odot year^{-1}) = 1.4 \times 10^{-41}\ L_{[OII]}\ (ergs\,s^{-1}), \tag{6.6}$$

it is also possible to derive an [OII] estimate of the star formation rate density at the same redshift, by using the complete integral of the [OII] luminosity function determined at $z = 1.47$, and assuming the same 1 magnitude of extinction at Hα. This yields $\rho_{SFR} = 0.17 \pm 0.04\, M_\odot\, yr^{-1}$ Mpc^{-3}, in very good agreement with the measurement obtained from Hα.

By taking advantage of the other HiZELS measurements, and other Hα based measurements, it is possible to construct a full and consistent view of the Hα-based star formation history of the Universe. This is done by integrating all derived luminosity functions down to a ∼common luminosity

limit of $L_{H\alpha}$=$10^{41.5}$erg s^{-1}. The results are presented in Figure 6.16, revealing a strong rise in the star formation activity of the Universe up to $z \sim 1$ and a flattening or a small continuous increase beyond that out to $z > 2$.

6.5 The matched Hα-[OII] view

This section presents a detailed comparison of [OII] and Hα luminosities and line flux ratios (observed and corrected for dust-extinction) as a function of galaxy colour, mass and luminosity for the sample of matched Hα and [OII] emitters at $z = 1.47$. These are compared with equivalent results for a similarly-selected sample at $z \sim 0.1$ drawn from the SDSS.

6.5.1 A SDSS sample at z $\sim$ 0.1

In order to compare the $z = 1.47$ Hα+[OII] sample with a large local sample and provide a further insight into any important correlations between line fractions and dust-extinction, mass and colour, an SDSS sample was used. Data were extracted from the MPA SDSS derived data products catalogues[8]. The sample was defined to emulate a narrow-band slice at $0.07 < z < 0.1$ (chosen to be distant enough so that the fibers capture the majority of the light – typically $\sim 3 - 4$ kpc diameter, but not too far out in redshift to guarantee that the sensitivity is still very high and the measurements are accurate). The sample was selected by further imposing a requirement that $L_{H\alpha} > 10^{40.6}$ erg s^{-1} (observed, not aperture or dust extinction corrected); this guarantees high S/N line ratios and that the vast majority of sources are detected in [OII] as well, allowing unbiased estimates of the line ratio distribution, as well as the detection of other emission lines ([OIII], Hβ and [NII]) that can be used to distinguish between AGN and star-forming galaxies (c.f. Rola et al., 1997; Brinchmann et al., 2004). Among 17354 SDSS $z \sim 0.1$ Hα emitters, 498 were classified as AGN, implying a ~ 3 per cent contamination. Potential AGN were removed from the sample. Emission line fluxes are aperture corrected following a similar procedure as in Garn & Best (2010) – i.e., by using the ratio between the fiber estimated mass and the total mass of each galaxy. For 32 galaxies where the catalogued fiber mass is higher than the catalogued total mass, an aperture correction factor of 1.0 was assigned. For those in which the fiber mass had not been determined, the average correction for the total mass of that galaxy was assigned. The median fraction of flux within the SDSS apertures is 32%. Note that the even though these aperture corrections change the total fluxes, line ratios remain unchanged. Finally, in order to provide a more direct comparison with the sample at $z = 1.47$, an EW cut of 20 Å in Hα was applied (to mimic the selection done at $z = 1.47$), and galaxies with lower EWs were excluded (1701 galaxies). The final SDSS sample contains 14451 star-forming Hα selected galaxies at $0.07 < z < 0.1$.

[8]See http://www.mpa-garching.mpg.ed/SDSS/

6.5.2 Calibrating [OII]/Hα line ratio as a dust extinction probe

Due to the difference in rest-frame wavelength of the [OII] and Hα emission lines, and both emission-lines being tracers of recent star-formation, the [OII]/Hα line ratio is sensitive to dust-extinction, even though metallicity can affect the line ratio as well. After correcting for dust extinction (using the Balmer decrement), several studies find a [OII]/Hα average of $\approx 1.0 - 1.4$ in the local Universe (c.f. Kewley et al., 2004).

The Hα/Hβ line ratio (Balmer decrement) is widely used as an extinction estimator, particularly up to $z \sim 0.4$, as it is relatively easy to obtain both emission lines. As the SDSS-derived sample is able to obtain reliable fluxes for the [OII], Hβ and Hα emission lines, it is possible to investigate (and potentially calibrate) [OII]/Hα as a dust-extinction indicator, using the Balmer decrement directly. As Figure 6.17 shows, [OII]/Hα is relatively well correlated with Hα/Hβ, indicating that it is possible to use [OII]/Hα to probe dust extinction within the observed scatter. For each galaxy in the SDSS-derived sample at $z \sim 0.1$, Hα/Hβ line fluxes are measured and used to estimate the extinction at Hα, $A_{H\alpha}$, by using:

$$A_{H\alpha} = \frac{-2.5 k_{H\alpha}}{k_{H\beta} - k_{H\alpha}} \log_{10}\left(\frac{2.86}{H\alpha/H\beta}\right), \tag{6.7}$$

where 2.86 is the assumed intrinsic Hα/Hβ line flux ratio, appropriate for Case B recombination, temperature of $T = 10^4$ K and an electron density of $n_e = 10^2$ cm^{-3} (Brocklehurst, 1971). The Calzetti et al. (2000) dust attenuation law is used to calculate the values of $k_\lambda \equiv A_\lambda / E(B-V)$ at the wavelengths of the Hα and Hβ emission lines, resulting in:

$$A_{H\alpha} = 6.531 \log_{10} H\alpha/H\beta - 2.981. \tag{6.8}$$

By using the Calzetti law, it is also possible to write a similar relation by using [OII]/Hα:

$$A_{H\alpha} = -2.296 \log_{10}[OII]/H\alpha + 2.29 \log_{10}(R_0), \tag{6.9}$$

where R_0 is the unknown intrinsic [OII]/Hα, but the slope of the relation is fully determined. Figure 6.17 shows that the Calzetti law matches the global trend well, but fails to predict the fine details. The failure to match the data perfectly results from a combination of different factors. The Calzetti et al. law does not include important variations of the intrinsic [OII]/Hα line fraction with e.g. metallicity. The Calzetti et al. extinction law is also based on a relatively small number of local galaxies, and, most of all, it is based on continuum light, and not on emission-lines. However, it is possible to obtain a much better fit to the relation between [OII]/Hα (Ψ) and Balmer decrement with a 4th order polynomial (shown in Figure 16), and to derive an empirical relation between $A_{H\alpha}$ directly from Hα/Hβ:

$$A_{H\alpha} = -4.30\Psi^4 - 11.30\Psi^3 - 7.39\Psi^2 - 2.94\Psi + 0.31 \tag{6.10}$$

with a scatter of 0.28 mag (in $A_{H\alpha}$). The scatter may be driven by the range of metallicities within the sample, as galaxies will have slightly different intrinsic [OII]/Hα line ratios.

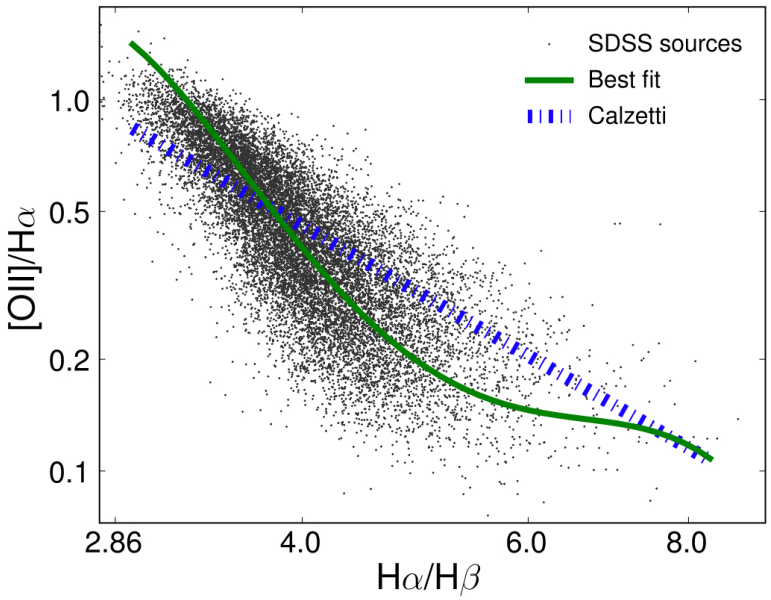

Figure 6.17: The variation of [OII]/Hα line ratios as a function of Hα/Hβ ratios for SDSS (Balmer decrement), showing that they correlate well, and therefore it is possible to calibrate the observed [OII]/Hα line ratio as a dust extinction indicator. Binned median values and the best polynomial fit are also shown, together with the prediction from the Calzetti et al. extinction law.

The SDSS data can be used to investigate how the offset of a galaxy from the [OII]/Hα vs Hα/Hβ relation depends upon metallicity, and thus it is possible to measure the extent to which the [OII]/Hα line ratio can be used to probe extinction, without metallicity biases. Here, the O3N2 indicator (Pettini and Pagel, 2004) is used as a tracer of metallicity (the gas-phase abundance of oxygen relative to hydrogen), computed by using:

$$12 + \log 10(\mathrm{O/H}) = 8.73 - 0.32 \times \log_{10}(\mathrm{O3H}\beta/\mathrm{N2H}\alpha), \tag{6.11}$$

where O3Hβ is the line flux ratio [OIII]5007/Hβ and N2Hα is the line flux ratio [NII]6584/Hα. This indicator has the main advantages of i) using emission lines which have very similar wavelengths, thus being essentially independent of dust attenuation and ii) having a unique metallicity for each line flux ratio. Figure 6.18 shows the difference between $A_{H\alpha}$ computed with the empirical [OII]/Hα and $A_{H\alpha}$ estimated directly from the Balmer decrement, as a function of metallicity. For comparison, the Calzetti law prediction is also shown, emphasizing that the mismatch between the latter law and the observational data is mostly due to the the effect of metallicity on the [OII]/Hα ratio, which is not taken into account by Calzetti, but is incorporated in the empirical calibration presented in this work. The results suggest that even if galaxies at $z = 1.47$ have different metallicities from those in SDSS, no significant offset (within the scatter, ± 0.3 mag) is expected when estimating $A_{H\alpha}$ from [OII]/Hα for a wide range of metallicities.

For the remaining of the analysis, $A_{H\alpha}$ is computed as in equation 12, both for the $z = 1.47$ and the SDSS samples. It should be noted that the qualitative and quantitative results remain unchanged if Balmer decrements are used instead to estimate $A_{H\alpha}$ for the SDSS galaxies, and that qualitative

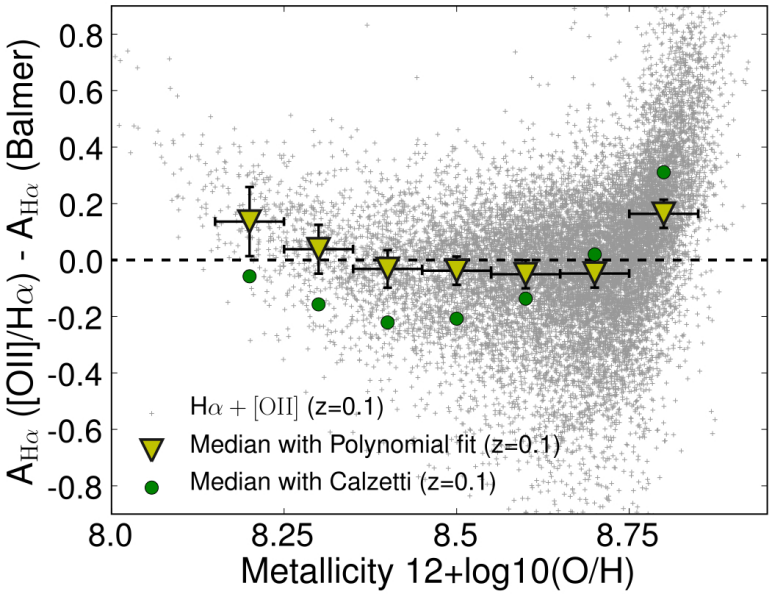

Figure 6.18: The difference between $A_{H\alpha}$ estimated using equation 12 and directly using the Balmer decrement, as a function of a metallicity (from Equation 13). The results show that the empirical calibration derived is able to use [OII]/Hα line ratios as dust extinction probe without any significant bias for a relatively wide range of metallicities/abundances. A comparison with what would be obtained using the Calzetti law directly is also shown, highlighting that the polynomial fit is able to provide a calibration of [OII]/Hα which is less affected by metallicities. Solar metallicity corresponds to 12+log 10 of 8.66; the figure presents metallicities varying from ≈ 0.2 to ≈ 2.2 solar metallicities. Note that while Equation 12 provides reliable results (without any significant systematics/biases) for galaxies with abundances (12+log 10) from 8.2 to 8.75, it will overestimate the median $A_{H\alpha}$ by about +0.2 mag for very sub-solar and very super-solar metallicity galaxies.

results also remain unchanged if the Calzetti law/best linear fit is used instead of the polynomial fit. The sample of Hα emitters at $z = 0.1$ presents $A_{H\alpha} = 0.97 \pm 0.42$, while the sample of H$\alpha$ emitters at $z = 1.47$ presents $A_{H\alpha} = 1.0 \pm 0.6$.

6.5.3 [OII]-Hα luminosity correlation at $z = 1.47$ and $z \sim 0.1$

Figure 6.9 presents the distribution of [OII]/Hα line ratios for the $z = 1.47$ sample. While it reveals a relatively wide range within the sample, ($\approx 0.08 - 1.2$), it also shows that down to the Hα flux limit, the line ratio distribution peaks at ≈ 0.5 (a bit above the median value, ≈ 0.45). In the SDSS-derived sample, the line ratios show a similar range from $0.1 - 1$ (c.f. Hopkins et al., 2003) and the median observed line ratio is found to peak at ≈ 0.4. Thus, even though the Hα and [OII] luminosities in the $z = 1.47$ sample are much higher than those probed locally, the typical line ratio, if anything, is higher, indicating lower extinction.

This is investigated in more detail in Figure 6.19, which shows how the Hα and [OII] luminosities (not corrected for extinction) correlate over the range of luminosities probed by SDSS at $z \sim 0.1$ and HiZELS at $z = 1.47$. Lines of constant extinction (in Hα) are also shown. It is noteworthy that at

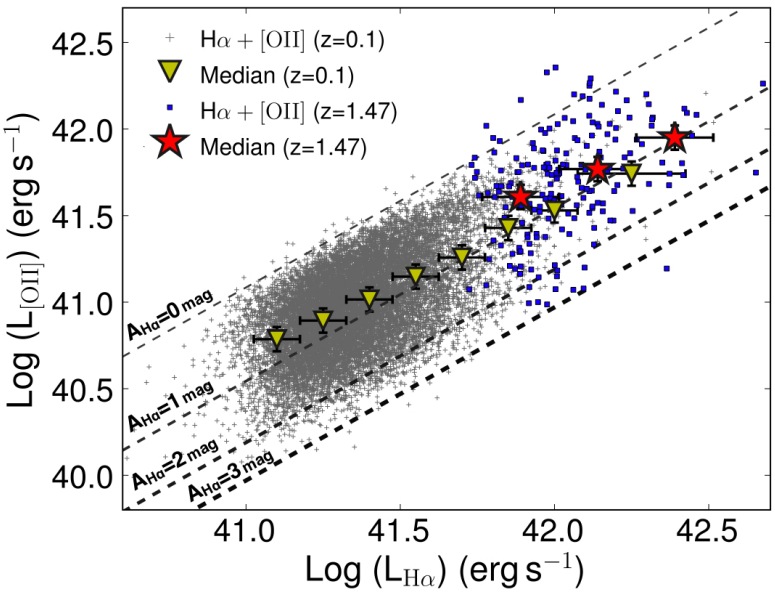

Figure 6.19: A comparison between observed [OII] and Hα luminosities (not corrected for dust-extinction) for samples at $z \sim 0.1$ and $z \sim 1.5$. The correlation between observed luminosities seem to evolve very little in the last ~ 9 Gyrs, revealing a typical 1 mag of extinction at Hα for the probed luminosities. Lines of constant extinction are also shown – note that these are not evenly spaced due to the use of the non-linear relation (Equation 12).

a given observed Hα luminosity, the median [OII] luminosities are slightly higher (indicating lower median extinction) at the higher redshift. Both samples show weak trends for increasing extinction with increasing luminosity. Furthermore, it should be noted that the simple assumption that both samples present a typical constant extinction of 1 magnitude is a relatively good approximation.

Hopkins et al. (2001) find that there is a correlation between SFR and $A_{H\alpha}$, and so argue that it is possible to estimate (statistical) dust extinction corrections based on observed SFRs, particularly for Hα (but also for the [OII]-derived SFRs); their relation has been used to apply statistical corrections to the observed Hα luminosities in many studies at low and high redshift. On the other hand, the Hopkins SFR-$A_{H\alpha}$ relation, whilst derived with a relatively small sample in the local Universe, seems to be roughly valid at $z \sim 0.84$, as found by Garn et al. (2010) (which presents a similar analysis to Hopkins et al., i.e. comparing mid-infrared SFRs with Hα), although it slightly overestimates the amount of dust extinction of the sample. Nevertheless, it is unclear whether a similar result can be found when studying $A_{H\alpha}$ as a function of SFRs at $z = 1.47$, or if the result from Hopkins et al. (2001) can be recovered when using emission-line ratios (e.g. Balmer decrement, or the [OII]/Hα calibration) at $z \sim 0.1$.

Figure 6.20 presents the results of investigating the dependence of dust-extinction on observed Hα SFR for both samples. The results show a relatively weak correlation between $A_{H\alpha}$ and observed Hα SFRs at both $z = 0.1$ and $z = 1.47$; an offset in the median extinction for a given SFR between both epochs is also found.

The figure also shows the Hopkins et al. (2001) relation between $A_{H\alpha}$ and observed SFRs, with

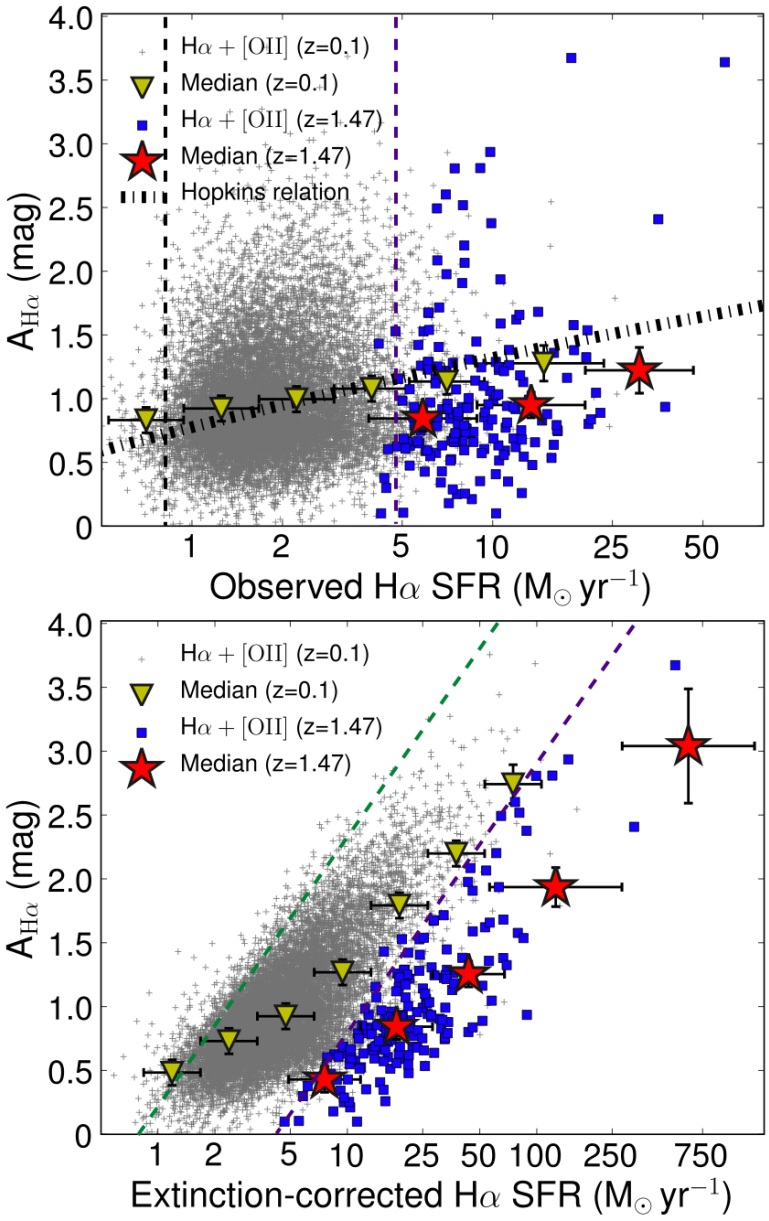

Figure 6.20: The relation between dust extinction and star formation rates (uncorrected and corrected for dust extinction) based on the Hα emission lines for both $z = 1.47$ and $z = 0.1$. The *top* panel shows the relation between dust extinction at Hα and observed Hα SFRs. The figure also shows the Hopkins et al. (2001) relation; this consistently over-predicts the dust extinction correction of the $z = 1.47$ sample by ~ 0.5 mag and, although it agrees better with the $z = 0.1$ sample, it over-predicts the slope of the correlation. The *bottom* panel presents the relation between $A_{H\alpha}$ and dust extinction-corrected SFRs for both redshifts. Note that because both samples are Hα selected, there are strong selection biases affecting the Hα analysis (dashed lines, resulting from the approximate selection limit in the two samples), but the trends are still recovered even when accounting for such biases. The results show that even though the trends are similar at both $z = 0.1$ and $z = 1.47$, the normalisation is different, and the trends have evolved between $z \sim 1.5$ and $z \sim 0$.

the results showing that it consistently over-predicts the dust extinction correction of the $z = 1.47$ sample by ~ 0.5 mag ($\sim 1.6\times$) and, although it agrees better with the $z = 0.1$ sample (in the

normalisation), it over-predicts the slope of the correlation. Note that $A_{H\alpha}$ at $z = 1.47$ are potentially overestimated for extremely metal-poor or metal-rich galaxies, so the offset is robust and, if anything, is underestimated. The SDSS results remain completely unchanged when using the Balmer decrement $A_{H\alpha}$. Therefore the use of the Hopkins et al. relation to correct observed Hα SFRs as a function of observed SFRs/luminosity results in a clear overestimation of the dust-extinction correction at $z = 1.47$; re-normalising it by ~ 0.5 mag is able to solve this.

Nevertheless, there seems to be a correlation between SFR and $A_{H\alpha}$ at $z \sim 1.5$, which is more clearly revealed after correcting SFRs for dust extinction, as can be seen in Figure 6.20. It should however be noted that such relation is in part a result of a bias (as indicated in Figure 6.20), as for a given flux limit and a (wide) distribution of dust extinction corrections, one easily recovers a relation between extinction and corrected SFRs. The relation between extinction and SFR is clear at the highest Hα luminosities where such selection biases are negligibly small. The offset between the $A_{H\alpha}$ vs corrected-SFR relations between $z = 0.1$ and $z = 1.47$ is also clear at these high SFRs, and is still recovered even when a common Hα luminosity limit is applied to both samples. These results indicate that although there does appear to be a relationship between dust extinction and SFR, this relation appears to evolve with redshift and should not be used as a reliable way of estimating statistical dust extinction corrections for samples of galaxies at different redshifts.

6.5.4 Mass as a dust-extinction indicator

Recently, Garn and Best (2010) performed a detailed investigation of the correlations between dust extinction ($A_{H\alpha}$) and several galaxy properties (e.g. metallicity, star formation rate, stellar mass) using large SDSS samples. The authors find that although $A_{H\alpha}$ roughly correlates with many galaxy properties, stellar mass seems to be the main predictor of dust extinction in the local Universe (see also Gilbank et al., 2010a, for a similar analysis). The authors derive a polynomial fit to the observed trend, which can be used to estimate dust extinction corrections for galaxies with a given stellar mass in the local Universe. Nonetheless, so far no study has been conducted in order to test whether such relation exists at high redshift and whether it evolves significantly.

Estimating stellar masses at $z = 1.47$

In order to investigate any potential correlation between dust extinction and stellar mass at $z \sim 1.5$, stellar masses are obtained for the entire $z = 1.47$ sample, following the methodology fully described in Chapter 5. Very briefly, the multi-wavelength data available for the $z = 1.47$ sources are used to perform a full SED χ^2 fit with a range of models – normalised to one solar mass – to each galaxy; the stellar-mass is the factor needed to re-scale the luminosities in all bands from the best model to match the observed data. As in Chapter 5, the SED templates are generated with the stellar population synthesis package developed by Bruzual and Charlot (2003), but the models are drawn from Bruzual (2007). SEDs are produced assuming a universal initial mass function (IMF) from Chabrier (2003) and an exponentially declining star formation history with the form $e^{-t/\tau}$, with τ in the range 0.1

Gyrs to 10 Gyrs. The SEDs were generated for a logarithmic grid of 220 ages (from 0.1 Myr to 4.3 Gyr – the maximum age at $z = 1.47$). Dust extinction was applied to the templates using the Calzetti et al. (2000) law with $E(B-V)$ in the range 0 to 0.8 (in steps of 0.1). The models are generated with a logarithmic grid of 6 different metallicities, from sub-solar to super-solar metallicity. It is assumed that all Hα emitters are at $z = 1.47$ and the complete filter profiles are convolved with the generated SEDs for a direct comparison with the observed total fluxes. Up to 16 bands are used, spanning from the CFHT U band in the near-ultra-violet to the 4 IRAC bands. The appropriate corrections (c.f. Chapter 5) are applied to obtain total fluxes in each band.

Stellar mass estimates of each individual source are found to be affected by a 1σ error (from the multi-dimension χ^2 distribution) of ~ 0.30 dex, which results from degeneracies between the star formation time-scale τ, age, extinction and, to a smaller extent, metallicity. As the analysis uses a Chabrier IMF, stellar masses are directly comparable with SDSS masses (which are the ones used by Garn and Best, 2010), but note that there is a systematic offset when compared to Salpeter (see Chapter 5). It should also be noted that the $E(B-V)$ from the best fits correlate well with the $A_{H\alpha}$ determined for each individual galaxy.

Mass-Extinction relation

The sample of $z = 1.47$ emitters presents a median stellar mass of $10^{9.9}\,M_\odot$. Figure 6.21 shows the observed relation between $A_{H\alpha}$ and stellar mass, for both $z = 0.1$ and $z = 1.47$ samples, together with the Garn and Best (2010) relation. The results reveal that not only is there a correlation between stellar mass and dust extinction at $z = 1.47$, just like the one at $z \sim 0$, but, even more importantly, that the Garn and Best (2010) relation seems to be valid at least up to $z \sim 1.5$ as a dust extinction estimator for most masses. As shown above, this is in contrast with SFR-dependent extinction corrections, which must at least be re-normalised when being applied to $z \sim 1.5$ or $z \sim 0$, and provides an important insight into what is important in determining the dust properties of galaxies. Table 6.3 presents the Garn and Best (2010) relation for predicting $A_{H\alpha}$ as a function of stellar mass, which can be applied, at least within the studied range of masses, to derive statistical corrections for samples of galaxies up to $z \sim 1.5$.

Although the relation between stellar mass and $A_{H\alpha}$ seems to hold across redshift for most masses probed, there is tentative evidence of an offset at the highest masses, in the sense that the most massive $z = 1.47$ star-forming galaxies appear to be affected by significantly less dust extinction that those with comparable masses at $z = 0.1$. The sample at high masses remains relatively small, however, and also since these massive star-forming galaxies are all of very low Hα EWs (see Chapter 5), there is the possibility that selection effects are driving this result. Until this can be investigated with an improved sample, however, caution should be taken in applying the mass-extinction relation at high redshifts for masses above $\sim 10^{10.75}\,M_\odot$.

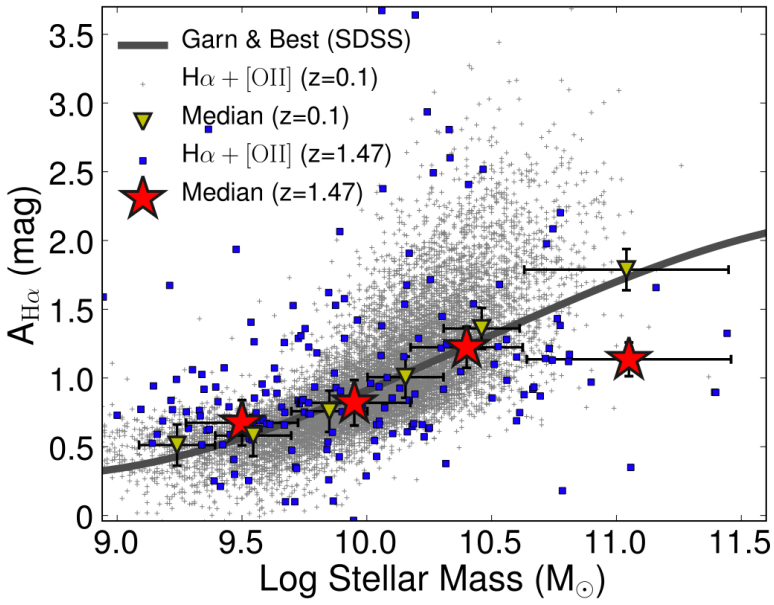

Figure 6.21: The relation between dust extinction ($A_{H\alpha}$) and stellar mass for the samples at $z = 0.1$ and $z = 1.47$. Individual galaxies from both samples and the median are presented. The relation derived by Garn and Best (2010) is also shown, which is found to describe the relation very well for $z = 0.0 - 1.5$ at least for low and moderate masses, indicating that stellar mass is likely a fundamental property for predicting dust-extinction corrections. The most massive star-forming galaxies (log Mass> 10.75) seem to have different extinction properties at $z = 0.1$ and $z = 1.5$, even though the sample of such galaxies at $z = 1.5$ is still small.

6.5.5 Predicting $A_{H\alpha}$ dust-extinction with colours

Stellar mass seems to be a relatively reliable (and important) non-evolving dust-extinction predictor which can therefore be applied both in the local Universe and at higher redshift ($z \sim 1.5$), at least within a range a masses. However, computing reliable stellar masses requires obtaining a significant number of observations at different wavelengths, relies on the validity of the stellar population models used to compute mass to light ratios, and it is, in general, a difficult quantity to estimate, particularly at high redshift. There is therefore the need to investigate more direct observables as a way to predict the median dust extinction of a population of galaxies that could be applied out to $z \sim 1.5$. Rest-frame optical colours are expected to correlate with dust extinction, and are therefore investigated and calibrated as dust-extinction tracers. All colours presented in this Section are given in the AB system and are rest-frame colours computed using the SDSS filters.

Figure 6.22 presents $A_{H\alpha}$ as a function of rest-frame $u - z$ for both $z = 0.1$ and $z = 1.47$. For the $z = 1.47$, the observed $z' - K$ colours[9] can be used, as the redshifted z' and K filter profiles broadly match u and z SDSS filters and a simple statistical correction of $+0.15$[10] on the $z - K$ colour (which accounts for a small K correction and the differences in the filter profiles) is able to match the colours

[9] z'-band data from Suprime-cam/Subaru; K from WFCAM/UKIRT.

[10] This statistical correction was computed by using the range of best-fit SED models to the z=1.47 sources and measuring the $z' - K$ colours with the z' and K filters on Subaru and UKIRT, respectively, following by measuring the $u - z$ rest-frame colours of the same sources, using the u and z SDSS filters.

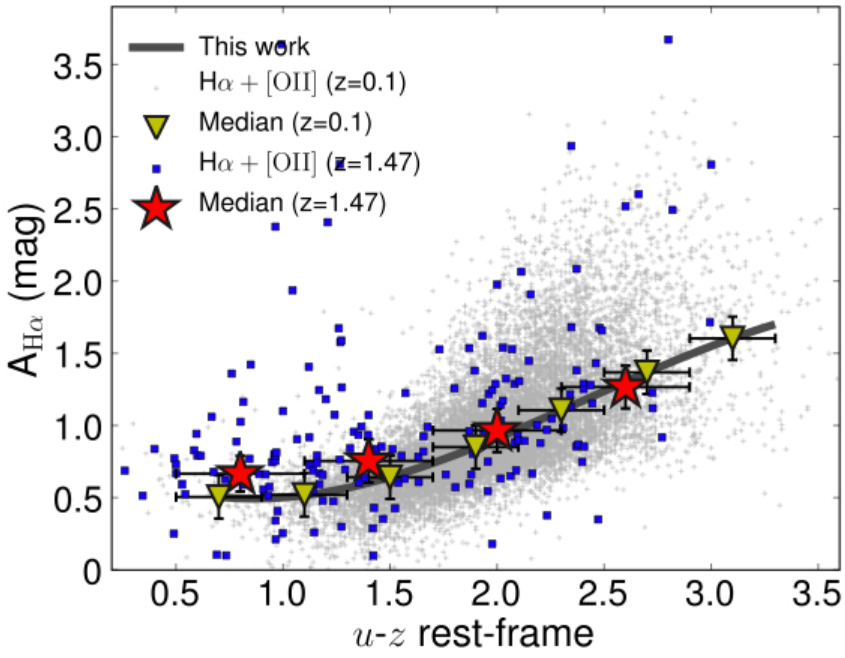

Figure 6.22: The relation between dust extinction and rest-frame $u-z$ colour for the samples at $z = 0.1$ (SDSS) and $z = 1.47$. The data are used to derive an empirical relation which is valid for Hα emitters both at $z = 0.1$ and $z = 1.47$ and predicts median dust extinction corrections ($A_{H\alpha}$) based on $u-z$ colours. Table 6.3 presents the best-fit polynomial relations based on other rest-frame colours which also correlate well with $A_{H\alpha}$.

very well.

The results presented in Figure 6.22 show that there is a significant correlation between galaxy colour and dust-extinction and suggest that, despite galaxies in the sample at $z = 1.47$ being bluer (on average), a single relation seems to hold across epochs (at least out to $z \sim 1.5$). Indeed, a simple polynomial fit to the median extinction for galaxies with a given rest-frame $u-z$ colour ($\approx$ observed $z' - K + 0.15$ colour at $z \sim 1.5$) is valid at both $z = 0.1$ and $z = 1.47$, and is given by:

$$A_{H\alpha} = -0.092(u-z)^3 + 0.671(u-z)^2 - 0.952(u-z) + 0.875 \quad (6.12)$$

Relations between $A_{H\alpha}$ and various other optical rest-frame colours are also investigated; these can be a valuable tool to estimate dust-extinction of galaxy populations at different redshfits where only a simple colour is available. Table 6.3 presents the best fits to the data that are valid at least up to $z \sim 1.5$, together with the limits within the relations are valid. The scatter is also quantified for each fit (see Table 6.3).

6.5.6 Discussion of emission-line ratios

The mean dust extinction properties of the sample of star-forming galaxies at $z \sim 1.5$ seem to be very similar to those in the local Universe (a simple 1 mag of extinction at Hα for the entire population of $z \sim 0.1$ and $z \sim 1.5$ galaxies is a relatively good approximation), as a whole, even though galaxies at

Table 6.3: Predicting median dust-extinction ($A_{H\alpha}$, mag) corrections using rest-frame colours and mass for galaxies at $z \sim 0-1.5$. Best-fit relations are based on 3rd order polynomials: $y = Ax^3 + Bx^2 + Cx + D$. Lower and upper limits of validity of the fits are also presented. Note that the photometry is in the AB system and using SDSS filters and that $Mass$ is given in units of $\log(M_\odot/10^{10})$. The scatter of the data relative to the best fit is also given.

Property	A	B	C	D	Validity	Scatter
$Mass$	−0.09	0.11	0.77	0.91	[−0.4,0.3]	0.33
$u-g$	−1.31	4.59	−4.15	1.68	[0.4,1.5]	0.35
$g-r$	−2.63	5.00	−0.78	0.51	[0.0,0.8]	0.28
$r-i$	−27.29	29.83	−7.64	1.10	[0.1,0.55]	0.35
$u-z$	−0.092	0.671	−0.952	0.875	[0.5,3.2]	0.30

$z \sim 1.5$ seem to be slightly less extinguished. Even more interesting is the fact that dust extinction presents the same dependence on stellar mass in the last 9 Gyrs, at least for star-forming galaxies with low and moderate stellar masses. In contrast, while dust extinction correlates with SFRs at both z=0 and $z \sim 1.5$, the normalization of the relations clearly evolves, with differences of ~ 0.5 mag in Hα for the same (corrected) SFR.

As extinction-corrected SFRs correlate reasonably well with stellar mass and dust extinction also correlates with (corrected) SFRs, it is possible that the relation simply evolves as sSFRs evolve. Physically, the normalization of the relation could be driven by the gas reservoirs in galaxies; allowing them to reach much higher SFRs at $z \sim 1.5$ than locally, for a fixed stellar mass. This conclusion is in line with Garn and Best (2010) and has important consequences towards understanding galaxy evolution in the last 9 Gyrs and how little dust properties seem to have changed.

6.6 Conclusions

This Chapter presented the results from the first panoramic matched Hα+[OII] dual narrow-band survey at $z \sim 1.5$. This is a very effective way of assembling large robust samples of simultaneous Hα and [OII] at $z = 1.47$. It provides a large, robust sample of Hα emitters at $z = 1.47$, together with a large sample (~ 1400) of [OII] emitters at the same redshift. The survey has allowed for the first statistical direct comparison of Hα and [OII] emitters at $z \sim 1.5$ and a direct comparison with an equivalent sample in the local Universe to look for evolution. The main results are:

- The well-defined samples of emitters were used to compute the Hα and [OII] luminosity functions at the same redshift. For the Hα luminosity function at $z = 1.47$, the best-fit Schechter function parameters are: $\log L^*_{H\alpha} = 42.5 \pm 0.2\,\mathrm{erg\,s^{-1}}$, $\log \phi^*_{H\alpha} = -2.4 \pm 0.3\,\mathrm{Mpc^{-3}}$ and $\alpha_{H\alpha} = -1.6 \pm 0.4$, while for the [OII] luminosity function at the same redshift the best-fit parameters are: $\log L^*_{[OII]} = 41.71 \pm 0.09\,\mathrm{erg\,s^{-1}}$, $\log \phi^*_{[OII]} = -2.01 \pm 0.10\,\mathrm{Mpc^{-3}}$ and $\alpha_{[OII]} = -0.9 \pm 0.2$.
- Both Hα and [OII] luminosity functions show a strong and consistent evolution in ϕ^* and L^* from

$z \sim 0$ to $z \sim 1$ and a continued L^* evolution to $z \sim 1.5$ and beyond. By combining the results with other HiZELS measurements and other estimates from the literature, our understanding of the star-formation history of the Universe is improved. Using a single well-calibrated indicator, the star-formation rate density is shown to rapidly increase out to $z \sim 1$, and to probably continue rising (although much more weakly) out to $z \sim 2$, due to the steep faint-end now measured at $z = 2.2$. At $z = 1.47$, the Hα analysis yields $\rho_{\rm SFR} = 0.16 \pm 0.05\,{\rm M}_\odot\,{\rm yr}^{-1}\,{\rm Mpc}^{-3}$, while the [OII] analysis yields $\rho_{\rm SFR} = 0.17 \pm 0.04\,{\rm M}_\odot\,{\rm yr}^{-1}\,{\rm Mpc}^{-3}$, in excellent agreement.

- By using SDSS, the [OII]/Hα line fraction is calibrated as a dust-extinction probe against the Balmer decrement. The relation is shown to be accurate within ≈ 0.3 dex.

- Hα and [OII] luminosities correlate well at $z = 1.47$, similarly to those at $z \sim 0.1$, but the sources at higher redshifts appear less dust extinguished for a given observed Hα luminosity. A relatively weak correlation between observed SFR and dust extinction is found for both $z = 0.1$ and $z = 1.47$, but with a different normalisation. It is also shown that the Hopkins relation consistently over-predicts dust extinction corrections for $z \sim 1.5$ by ~ 0.5 mag in Hα.

- Stellar mass is shown to be a good dust-extinction predictor, at least for low and moderate mass galaxies, with the relation between dust extinction and mass being the same in the last 9 Gyrs for such star-forming galaxies. The relation between mass and dust extinction from Garn & Best (2010) is shown to be fully valid with no evolution at $z = 1.47$.

- Optical or UV colours are shown to be a simple observable extinction predictor which can be applied for $z \sim 0 - 1.5$ star-forming galaxies; the best-fit relations based on several colours are derived and presented.

The results presented in this paper are a significant contribution to understanding the nature and evolution of star-forming galaxies at the likely peak of the star-formation history of the Universe, particularly by showing an effective and clean way of selecting large samples of these galaxies and by investigating, for the first time, the evolution using both the Hα and [OII] emission lines at $z \sim 1.5$ at the same time. The results show a very good agreement between the Hα and [OII] view. Moreover the results reveal that the typical necessary extinction corrections for the probed Hα luminosities at $z = 1.5$ is $A_{\rm H\alpha} \approx 0.9 - 1.0$; this is what has been found for a range of luminosities in the local Universe, therefore revealing no significant evolution (if anything, sources at higher redshift are less extinguished). Extinction corrections blindly applied as a function of Hα luminosity (e.g. using the local Hopkins relation) over-predict the dust extinction correction for the $z = 1.47$ sample and would lead to significant biases. New relations based on the analysis presented in this paper are given, providing statistical corrections for dust extinction based on colours and stellar mass.

Chapter 7

Bright Lyα emitters at $z \sim 9$

7.1 Motivation and background

Accurately determining and understanding the star formation history of the Universe is fundamental for our understanding of galaxy formation and evolution, but such knowledge will undeniably be incomplete without extending it to the earliest epochs of galaxy formation. Therefore, finding and characterizing populations of galaxies at the highest redshifts $z > 8$ is extremely important.

Presently, there are three relatively effective methods for searching for very distant galaxies: the broad-band drop-out technique, "blind" spectroscopic searches and narrow-band imaging surveys. The widely-used drop-out technique (pioneered at $z \sim 3$ by Steidel et al., 1996) requires very deep broad-band imaging, and can identify $z > 7$ galaxies as z-band drop-outs (e.g. Bouwens et al., 2008; Richard et al., 2008; Bouwens et al., 2010; McLure et al., 2010). This method is efficient for identifying candidates, but requires detailed spectroscopic follow-up to confirm the candidates, especially to rule out contributions from other populations with large z$-J$ breaks, such as dusty or evolved $z \sim 2$ galaxies and ultra-cool galactic stars (e.g. McLure et al., 2006). Thus, while studies such as Richard et al. (2008) identify a couple to a few $z \sim 8-10$ candidates by either taking advantage of the lensing magnification of a high mass cluster, or probing wider areas, spectroscopic follow-up is usually inconclusive, with no emission lines detected. The recent exception is a galaxy that has been spectroscopically confirmed at $z = 8.55$ (Lehnert et al., 2010), although still at a relatively low signal-to-noise. "Blind" spectroscopic surveys can potentially provide spectra directly. They are always limited to very small areas, although Stark et al. (2007) targetted the critical lensing lines of clusters and were able to identify 6 potential $z \sim 9$ objects. Finally, the narrow-band imaging technique has the advantage of potentially probing very large volumes, but can only detect sources with relatively strong emission lines, whilst it still

depends on the Lyman-break technique to isolate very high-redshift emitters.

Narrow-band Lyα searches at lower redshifts have been extremely successful in detecting and confirming emitters (e.g. Hu et al., 1998), including what was, until very recently, the detection of the most distant (spectroscopically confirmed) galaxy at $z = 6.96$ (Misawa et al., 2006). There have been attempts to detect Lyα at higher redshift and searches at $z = 7.7$ (e.g. Hibon et al., 2010; Tilvi et al., 2010) are now providing a handful of robust candidates. Studies looking for Lyα emission at even higher redshift, and particularly at $z \sim 9$ (e.g. Willis and Courbin, 2005; Cuby et al., 2007; Willis et al., 2008), have, until now, been unsuccessful, although they have only surveyed very small areas (a few tens of square arcmins at most). With the advent of wide-field near-IR detectors, however, it is now possible to increase the sky areas studied by over 2 to 3 orders of magnitude and reach the regime where one can realistically expect to detect $z \sim 9$ objects. This is a key aim of, for example, the narrow-band component of the UltraVISTA Survey (c.f. Nilsson et al., 2007). It is also an aim of HiZELS, the Hi-Z Emission Line Survey (c.f. Geach et al., 2008; Sobral et al., 2009a), described in Chapter 2. Indeed, the NB_J filter ($\lambda = 1.211 \pm 0.015 \mu$m) is sensitive to Ly$\alpha$ emission at $z = 8.96 \pm 0.06$ (assuming a top-hat filter shape), probing a co-moving volume of 1.12×10^6 Mpc^3 – by far the largest probed by a narrow-band survey at these wavelengths. This will be used to search for very-high redshift Lyα emitters. This Chapter presents the results of a search for such emitters; these have been presented in Sobral et al. (2009b).

7.2 Search for Candidates

For a source to be considered a candidate $z \approx 9$ Lyα emitter it is required to: i) be selected as a narrow-band emitter as in Chapter 3 (this required it to be clearly detected in NB_J ($\sigma > 3$) with a J-NB_J colour excess significance of $\Sigma > 2.5$ and observed equivalent width EW$>$ 50 Å – see Chapter 3 or Sobral et al. (2009a) for details in which it is shown that these criteria are very robust); ii) have at least one other detection $> 3\sigma$ in the near-infrared; iii) be visually believable in NB_J and the other band(s), avoiding noisy areas; and iv) be undetected ($< 3\sigma$ and direct visual analysis) in the available visible band imaging (B,V,r,i,z) – SUBARU and ACS/HST).

The sample presented in Chapter 3 was used to search for potential Lyα emitters at $z \approx 9$. However, the investigation was also extended to a slightly larger area in the UKIDSS UDS field to include areas where deep SUBARU and near-infrared imaging data were available – this corresponds to re-including areas which were conservatively masked for SED fitting purposes, and increases the total area probed to 1.4 deg^2.

7.3 Candidates, testing and follow-up observations

No candidates were found in the UKIDSS UDS field, with all emitters that passed tests i) to iii) being clearly detected in z-band imaging. In COSMOS, however, 2 candidates were found that satisfied all

criteria. Both sources are absent in all optical bands down to the 3σ level (e.g. I = 28.1 mag, z = 25.8 mag). They are both detected in NB_J and J, with Cand 1 having $NB_J = 20.8$ mag (5σ) and $J = 21.5$ mag (9σ) and a drop $z - J > 4.2$ mag, while Cand 2 presents $NB_J = 20.8$ mag (5σ) and $J = 22.1$ mag (6σ) and a drop $z - J > 3.6$ mag. They are both undetected in all other infra-red bands.

These two sources were then subjected to a series of further tests and follow-up observations. Splitting the data into subsets confirmed the detections across observations conducted on different nights (timescale from one day up to one month), with no evidence for variability or proper motion; they were also clearly excluded as potential cross-talk artifacts. Cand1 was followed-up spectroscopically using the CGS4 instrument on UKIRT in January 2009 – these data failed to confirm an emission line. Both candidates were then re-observed using WFCAM (further J imaging in February 2009), resulting in the non-detection of both candidates. Also, J imaging from the COSMOS public archive (which has become publicly available very recently) fails to detect the candidates. It is therefore clear that these sources are not Lyα emitters at $z \sim 9$. Further investigation shows that the sources are likely to be artifacts; they are located at almost the same pixel position on WFCAM4 in 2 different paw-prints (later investigation showed that similar artifacts were also found at similar pixel positions in the remaining 2 paw-prints, although at a lower level, and thus were not selected). They seem to be caused by an unfortunate coincidence of a set of slightly hot pixels (not sufficient to be flagged as bad pixels) which, combined with the ditter pattern, produced a few σ excess at one location on the combined image. No other artifacts like these were found either in UDS (which used a different dither pattern) or in other cameras for COSMOS data.

7.4 Lyα luminosity function at $z \sim 9$

After conducting the widest survey for bright ($L > 7.6 \times 10^{43}\,\mathrm{erg\,s^{-1}}$) Ly$\alpha$ emitters at $z \sim 9$, probing a co-moving volume of $1.12{\times}10^6$ Mpc^3 (1.4 deg^2), only 2 sources passed the selection criteria and even those were ruled out after follow-up observations. This result allows the tightest constraint on the bright end of the $z \sim 9$ Lyα luminosity function, as previous surveys (Willis and Courbin, 2005; Cuby et al., 2007; Willis et al., 2008) have only covered very small areas (a factor ∼1000 smaller). However, those surveys have gone significantly deeper (up to a factor of ∼100). Thus, by combining all the results from the literature, the luminosity function of LAEs at $z \sim 9$ can be constrained across a wide range of luminosities: $10^{42} < L < 10^{45}\,\mathrm{erg\,s^{-1}}$. Figure 7.1 presents the constraints from Willis and Courbin (2005), Cuby et al. (2007), Willis et al. (2008) and from this work, indicating the inverse of the volume selection function for each survey. These are compared to the measured Lyα luminosity functions from $z \sim 3$ to $z \sim 7$ from recent studies. Although the samples of Lyα emitters may suffer from significant biases due to the selection, cosmic variance and possible contamination, Figure 7.1 reveals that there is little evolution in the bright end of the luminosity function between $z \sim 3$ and $z \sim 5.7$. However, those bright emitters seem to become much rarer at $z = 6.5$ (Kashikawa et al., 2006), indicating that L^* is not increasing from $z \sim 6$ onwards. The results presented in this Chapter

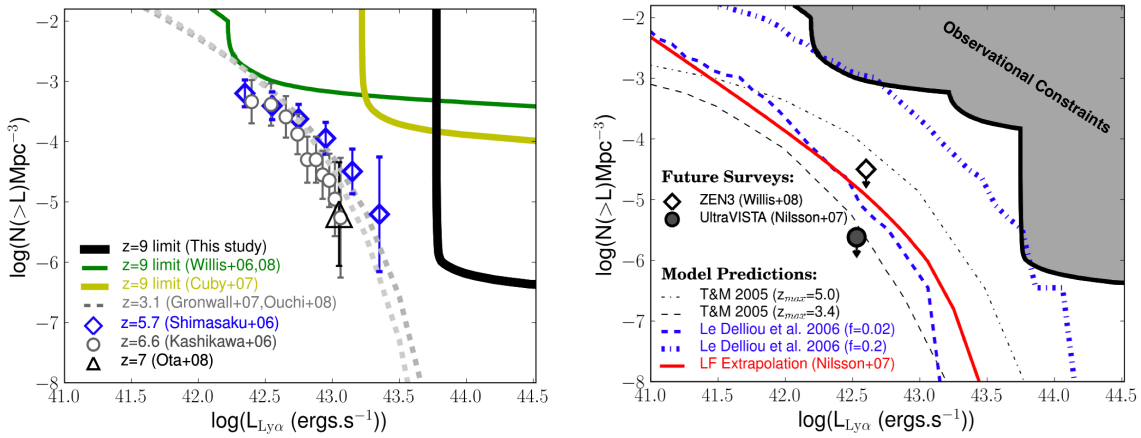

Figure 7.1: *Left*: Comparison between the measured Lyα luminosity function at $z \sim 3$ (dotted lines; Gronwall et al., 2007; Ouchi et al., 2008) with data from $z \sim 6-7$ (Kashikawa et al., 2006; Shimasaku et al., 2006; Ota et al., 2008). Other typically smaller $z \sim 6$ surveys give consistent results within the error bars. No evidence of significant evolution is found, especially when accounting for cosmic variance. Limits for the $z \sim 9$ LF from Willis and Courbin (2005), Cuby et al. (2007) and Willis et al. (2008) are also presented, together with the one presented in this Chapter, which is inconsistent with a strong evolution in L* up to $z \sim 9$. *Right*: The observational limits on the $z \sim 9$ Lyα luminosity function compared to different model predictions and proposed future surveys. The most recent models agree well with the data limits, and only the most extreme ones can be ruled out. Also, according to these models, the UltraVISTA survey will have a clear chance of detecting a few of these Lyα emitters, while ZEN3 may get a detection and will at least be able to rule out more models.

are also consistent with no evolution in L^* (Δlog(L*)<0.5) from $z = 5.7$ to $z \sim 9$.

7.5 Comparison with models and future surveys

Several authors have tried to predict the Lyα luminosity function at $z \sim 9$, either by extrapolating the luminosity function of these emitters from lower redshift, or by using numerical or semi-analytical models (Thommes and Meisenheimer, 2005; Le Delliou et al., 2006; Nilsson et al., 2007). In this Section, different models are compared with the observational constraints: semi-analytical models, observational extrapolations and phenomenological models. The semi-analytical models discussed here are obtained from GALFORM (Baugh et al., 2005) – these are based on ΛCDM, having been successful in reproducing a wide range of galaxy properties at different redshifts, including Lyα emitters up to $z \sim 6$ (Le Delliou et al., 2006). GALFORM computes the build-up of dark matter halos by merging and the assembly of baryonic mass of galaxies and the semi-analytical approach allows the study of properties of the Lyα emission – the reader is referred to Baugh et al. (2005), Le Delliou et al. (2006) and Orsi et al. (2008) for more details on these. The observational approach, as in Nilsson et al. (2007), extrapolates the Schechter function parameters based on those obtained in the $3.1 < z < 6.5$ redshift range. In practice, this results in little L^* evolution but a significant negative ϕ^* evolution. Finally, the phenomenological approach in Thommes and Meisenheimer (2005) assumes that Lyα emitters at

high redshift are spheroids seen during their formation phase. These models are normalised to give the observed mass function of spheroids in the local Universe, and are combined with a phenomenological function that provides the distribution of spheroid formation events in mass and redshift. Each galaxy is assumed to be visible as a Lyα emitter during a starburst phase of fixed duration that occurs at a specific redshift, drawn from a broad distribution. The reader is referred to Thommes and Meisenheimer (2005) for details.

Figure 7.1 presents predictions from GALFORM (Le Delliou et al., 2006), the observational luminosity function extrapolation from Nilsson et al. (2007) and updated phenomenological predictions (Thommes and Meisenheimer, 2005) assuming peak redshifts of $z_{max} = 3.4$ and $z_{max} = 5.0$. Le Delliou et al. (2006) found that their model required an escape fraction of $f_{esc} = 0.02$ to fit the observed Lyα luminosity function at $3 < z < 6.5$, but they also presented predictions for $f_{esc} = 0.2$ to illustrate how the results might change if the escape fraction increased at very high redshift; we therefore show both predictions in Figure 7.1. While most predictions are consistent with the current limits, GALFORM models with high escape fractions are marginally rejected both at faint and bright levels. Earlier phenomenological models (e.g. the $z_{max} = 10$ model of Thommes and Meisenheimer, 2005, not shown in Figure 7.1) are also clearly rejected by the results presented here.

These results also show, observationally, that bright $L > 10^{43.8}\,\mathrm{erg\,s^{-1}}$ Lyα emitters are very rare. Although the area coverage is absolutely important, a depth+area combination is likely to be the best approach for gathering the first sample of these very high-redshift galaxies. In fact, that is the strategy of the narrow-band component of the UltraVISTA survey (c.f. Nilsson et al., 2007), using the VISTA telescope, which is mapping 0.9 deg^2 of the COSMOS field to a planned 5σ flux limit of $4 \times 10^{-18}\,\mathrm{erg\,s^{-1}\,cm^{-2}}$ (although in reality this is likely to be increased due to the narrow-band filter not performing exactly to specification); this corresponds to luminosity limit of $L = 10^{42.53}\,\mathrm{erg\,s^{-1}}$ and a surveyed volume of $5.41{\times}10^5$ Mpc^3 (see Figure 7.1) at $z = 8.8$. This combination lies below all current predictions for the $z \sim 9$ Lyα LF and the survey is expected to detect 2-20 Lyα emitters at $z = 8.8 \pm 0.1$.

7.6 High redshift Lyα searches and cool galactic stars

It has become widely realised in recent years that broad-band searches for $z > 6$ galaxies using the Lyman-break technique may suffer from significant contamination by cool Galactic L, T, and possibly Y-dwarf stars (e.g. McLure et al., 2006). These low-mass brown dwarfs display extremely red $z - J$ colours reaching as high as $z - J \approx 4$ (e.g. Burningham et al., 2008), coupled with relatively flat $J - K$ colours. Such colours can mimic very closely those expected of a $z > 6$ star forming galaxy with a strong Lyman-break.

It may be thought that narrow-band Lyα searches are immune to this contamination, since the initial emission-line galaxy selection relies on an excess flux observed in a narrow-band filter relative (usually) to a broad-band filter; only after that is the Lyman-break technique used to pick out the

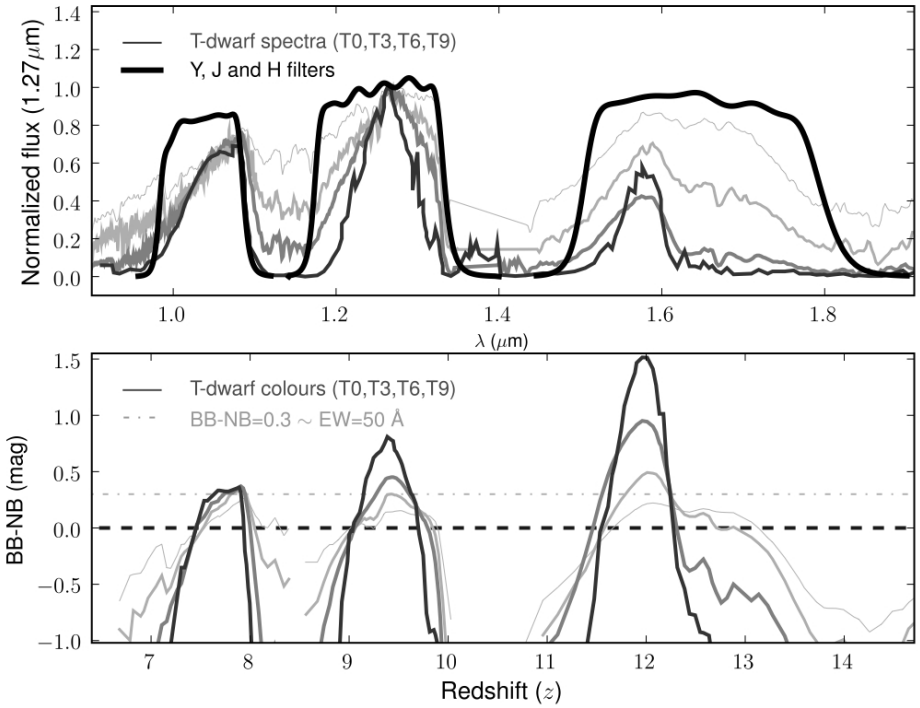

Figure 7.2: *Top panel:* the near-infrared spectra of T0, T3, T6 and T9 dwarf stars (T0 – lighter, T9 – darker, from Burningham et al., 2008)) compared to near-IR broad band filter profiles. *Lower panel:* the consequences for measured broad-band minus narrow-band (BB-NB) colours, clearly demonstrating the redshifts/wavelengths at which searches for Lyα emitters can be significantly contaminated by these very cool stars. For $7.7 < z < 8.0$ and $9.1 < z < 9.5$ searches, these stars can easily mimic Lyα emitters, with strong Y-z or J-z breaks and significant positive BB-NB colours. Searches at higher redshift $11.6 < z < 12.2$ in the H band can detect T9s with BB-NB$\sim$1.5, although the lack of strong H-J or H-Y breaks will make it easier to distinguish T-dwarfs from Lyα emitters.

high-redshift Lyα candidates from amongst the emission-line objects. However, the near-infrared continuum spectra of low mass brown dwarfs show considerable structure due to broad molecular absorption features (especially methane and ammonia; e.g. Leggett et al., 2007), as shown in the top panel of Figure 7.2. The lower panel of Figure 7.2 shows very clearly that T-dwarfs can easily produce a positive broad-band minus narrow-band (BB-NB) colour if the narrow-band filter is located within one of the spectral peaks (note that this is much less of an issue for surveys which difference two closely-located narrow-band filters). Lyα narrow-band surveys in the redshift ranges $7.7 < z < 8.0$, $9.1 < z < 9.5$ and $11.7 < z < 12.2$ may therefore be prone to contamination by cool Galactic stars – this includes the $z = 7.7$ and $z = 9.4$ atmospheric windows for narrow-band searches of Lyα emitters. Narrow-band surveys at redshifts $z < 7.7$, or between $8.0 < z < 9.1$ – which includes both HiZELS ($z = 8.96$) and the narrow-band component of the UltraVISTA Survey ($z = 8.8$; e.g. Nilsson et al 2007) – will be free of such contamination. Indeed, such surveys could potentially select very cool T-dwarf stars via a narrow-band *deficit* due to the strong methane absorption feature at these wavelengths.

With this result in mind, a T-dwarf search was conducted among narrow-band *deficit* sources in S09. These *deficit* sources were selected using equivalent criteria as for emitters (with a change in sign). None of the $deficit$ sources has z(AB)$-J > 3$, as expected for T-dwarfs (e.g. Leggett et al. 2007, Burningham et al. 2008), and even a selection imposing z(AB)$-J > 2$ results in a sample of only 9 sources which are all very well SED-fitted as galaxies with $z_{\rm photo} \sim 1.4-1.5$. These sources also present slightly higher J and H fluxes when compared to the best SED fit, but this can be explained by the Hβ and [OIII] contributing to the J band and Hα to the H band, which also explains the NB$_J$ deficit. No T-dwarf candidate was found in our survey.

7.7 Summary

- Deep narrow-band imaging in the J band ($\lambda = 1.211; \Delta\lambda = 0.015\mu$m) has been used to search for bright Lyα emitters at $z = 8.96$ over an area of 1.4 deg^2. No Lyα emitter was found brighter than L $\approx 7.6 \times 10^{43}\,{\rm erg\,s^{-1}}$.

- The Lyα luminosity function constraints at $z \sim 9$ have been improved for $10^{42} < L < 10^{45}\,{\rm erg\,s^{-1}}$ emitters. The results rule out significant positive evolution of the Lyα LF beyond $z \sim 6$; they are in line with recent semi-analytic & phenomenological model predictions, rejecting some extreme models.

- It has been shown that for narrow-band searches, T-dwarfs can mimic Lyα emitters at $7.7 < z < 8.0$, $9.1 < z < 9.5$ and $11.7 < z < 12.2$; they will not contaminate the future UltraVISTA narrow-band survey (and can even be identified via a narrow-band *deficit*), but they may contaminate narrow-band Lyα searches within the $z = 7.7$ and $z = 9.4$ atmospheric windows.

Chapter 8

Conclusions and Future Work

This thesis presented results from the HiZELS survey (see Chapter 2), a Campaign Project using WFCAM on UKIRT which exploits specially-designed narrow-band filters in the J and H bands (NB_J and NB_H), along with the H_2S1 filter in the K band, to undertake deep, wide surveys for line emitters. HiZELS is primarily targeting the Hα emission line at $z = 0.84$, $z = 1.47$ and $z = 2.23$, covering ~ 7 deg^2 and reaching limiting Hα SFRs of $\sim 3-20\,M_\odot\,yr^{-1}$. This thesis demonstrates the great potential of near-IR Hα narrow-band surveys as a route for significant progress in our understanding of galaxy formation and evolution.

The Star formation history of the universe: the Hα view at $0 < z < 2.23$

Until recently, samples of Hα emitters above $z \sim 0.5$ only contained a handful of objects (e.g. Moorwood et al. 2000) – and simply could not measure the fine evolution of the Hα luminosity function. In Chapters 3 and 6, the largest sample of distant Hα emitters (~ 1000 and ~ 200) in thin redshift slices were presented, with the widest and deepest narrow-band survey ever carried out at $z \sim 1-2$. Archival spectroscopic redshifts for a fraction of the emitters confirm the high completeness and reliability of the photometric selection (samples are $> 95\%$ reliable and complete). Moreover, for $z = 1.47$, a new selection technique has been used, by noting that the Subaru/Suprime-cam NB921 filter is perfectly matched for detecting the $[OII]_{3727}$ emission line for NB_H detections of Hα at $z = 1.47$. The double narrow-band selection provides a very effective and complete means of selecting $z = 1.47$ line emitters (Chapter 6). Further time has been awarded on Subaru as PI to extend this effective survey to the COSMOS field, and proposed to extend it to the remaining HiZELS fields.

This thesis presents the first fully self-consistent measurement of the evolution of the Hα luminosity function from $z = 0$ to $z \sim 2.2$ (see Chapter 6). This work also shows that ρ_{SFR} rises steeply up to

$z \sim 1$ and then continues to rise, but with a weaker evolution (see Chapter 3 and 6), using one single star formation indicator for the first time. The bulk of the evolution of the Hα luminosity function is seen as an evolution of $L^*_{\rm H\alpha}$ up to $z \sim 2.23$, while the faint-end of the LF seems to be evolving very little at the peak of the star-formation activity. The [OII] view at $z = 1.47$ and the evolution of the [OII] luminosity function provide a consistent view on the evolution (Chapter 6).

The Nature of Hα star-forming galaxies at z $\sim$ 1

The results presented in Chapter 3 show that the majority (80%) of Hα emitters at $z \sim 1$ are classed as disks; irregulars constitute a much smaller fraction of the sample. Moreover, a strong relation between morphology and Hα luminosity is found: the fraction of irregulars/mergers rises steadily with luminosity, while the fraction of disks falls (Chapter 3). The break of the LF, $L^*_{\rm H\alpha}$, seems to define a switch-over luminosity between the two populations.

The work presented in this thesis shows that, out to $z \sim 1$, the integrated ρ_{SFR} is dominated by disk galaxies and it is their evolution (from $z \sim 0$) that drives the strong rise in ρ_{SFR} with z. The continued evolution of $L^*_{\rm H\alpha}$ between $z = 0.84$ and $z = 2.23$ suggests an increasing importance of merger-driven star formation activity beyond $z \sim 1$; this will be possible to detail with large samples of $z \sim 1.5$ and $z = 2.23$ Hα emitters over the COSMOS field. Preliminary analysis indicates that a similar Hα-morphology relation is recovered at $z \sim 1.5$, shifted by $L^*_{\rm H\alpha}$, but with a much higher $\sim 50\%$ overall fraction of mergers.

The clustering of Hα star-forming galaxies at z $\sim$ 1 and evolution

Using the large sample of Hα emitters obtained in Chapter 3 and the exact relation between the spatial and angular correlation function, Chapter 4 is able to show that Hα emitters are moderately clustered at all redshifts, with a correlation length of $\rm r_0 = 2.6 \pm 0.2\, \mathit{h}^{-1}\, Mpc$ at $z \sim 1$. Moreover, the results show a strong dependence of the clustering on Hα luminosity ($L_{\rm H\alpha}$): at $z \sim 1$, the most actively star-forming galaxies present $\rm r_0 \sim 5\, \mathit{h}^{-1}\, Mpc$, while the lower H$\alpha$ luminosity galaxies present $\rm r_0 \sim 2\, \mathit{h}^{-1}\, Mpc$. The correlation length also depends on rest-frame K-band luminosity ($M_{\rm K}$, tracing stellar mass) for star-forming galaxies at $z \sim 1$, but the $L_{\rm H\alpha}$-$\rm r_0$ dependence remains at fixed rest-frame K luminosity. Irregular galaxies and mergers are found to cluster more strongly than discs and non-mergers, respectively, but once they are matched in $L_{\rm H\alpha}$ and $M_{\rm K}$, they yield comparable clustering amplitudes. Morphology is as unimportant for the clustering at high redshift as it is in the local Universe.

Hα emitters at $z = 0.84$ found with the HiZELS survey reside in dark matter haloes of minimum mass $\sim 10^{12}\, \rm M_\odot$ (similar to those of Milky Way type galaxies in the local Universe) and the minimum dark matter halo mass hosting Hα emitters correlates with Hα luminosity all the way up to $z \sim 2.3$. Furthermore, it is found that an $L^*_{\rm H\alpha}$ luminosity scaling is able to combine observational results probing the last 11 billion years of the age of the Universe in one single relation (see Chapter 4). This suggests a connection between the strong $L^*_{\rm H\alpha}$ evolution of the Hα luminosity function and star

formation being truncated in galaxies residing within dark matter haloes with masses much higher than $\sim 10^{12}\,\mathrm{M}_{\odot}$.

The dependence of star formation activity on environment and stellar mass

By probing a very wide range of environments (from fields to clusters) and masses with the first truly Hα panoramic survey at $z \sim 1$, this work (Chapter 5) provided a sharp picture of the roles and inter-dependences of mass and environment at $z \sim 1$ and reconciled the contradictory results in the literature, greatly adding to our understanding. The results show that both the fraction of star-forming galaxies and specific star formation rates decline strongly with stellar mass, confirming that mass downsizing is fully in place at $z = 0.84$.

The fraction of galaxies that are forming stars (above the HiZELS limit) is relatively flat with local environmental density at the lowest densities, but there is continuous fall of the star-forming fraction from fields to rich groups/clusters. The environment is also found to change the faint-end slope (α) of the Hα LF: it is very steep ($\alpha \sim -2$) for the poorest regions, and shallow ($\alpha \sim -1$) for groups and clusters (see Chapter 5).

This thesis robustly demonstrates that mass is the main SF predictor at $z \sim 1$, but environment also plays a significant role in galaxy evolution. High-density regions are linked with triggering high SFRs (for moderate mass galaxies), but this likely to result in a faster gas consumption, quickly transforming groups and cluster environments into the predominant sites for gas-poor, passive galaxies.

The double [OII]-Hα view at $z = 1.47$ and evolution to $z = 0$

Chapter 6 presented results from the first wide and deep double narrow-band survey for both Hα and [OII] line emitters at $z = 1.47 \pm 0.02$, using UKIRT, Subaru and extremely well matched narrow-band filters in the H and z' bands. The combined survey resulted in the identification of ~ 200 robust simultaneous Hα and [OII] emitters at $z = 1.47$. Both Hα and [OII] luminosity functions were presented and both were shown to evolve significantly from $z \sim 0$ in a consistent way; the star formation rate density of the Universe at $z = 1.47$ was evaluated, with the Hα and the [OII] analysis agreeing extremely well ($\rho_{\mathrm{SFR}} = 0.17 \pm 0.04\,\mathrm{M}_{\odot}\,\mathrm{yr}^{-1}\,\mathrm{Mpc}^{-3}$). The measurements are combined with other studies, providing a self-consistent measurement of the star formation history of the Universe for the last ~ 11 Gyrs. By taking advantage of the large sample of reliable Hα-[OII] emitters, and by using a large comparison sample at $z \sim 0.1$, derived from the Sloan Digital Sky Survey, [OII]/Hα line ratios were calibrated as probes of dust-extinction. Hα emitters at $z \sim 1.47$ present $\mathrm{A}_{\mathrm{H}\alpha} \approx 1$, similarly to those found by SDSS in the local Universe. Chapter 6 showed that although dust extinction correlates with SFR, the relation evolves by about ~ 0.5 mag from $z \sim 1.5$ to $z \sim 0$, with local relations over-predicting dust extinction corrections at high-z by that amount. This work also found that stellar mass is much more fundamental, with the same relation between mass and dust-extinction being valid at both $z \sim 0$ and $z \sim 1.5$. The evolution in the extinction-SFR relation is therefore interpreted as being due to the evolution in median specific SFRs over cosmic time. Dust extinction corrections as

a function of observed optical colours were also derived and shown to be broadly valid at both $z \sim 0$ and $z \sim 1.5$, offering a simpler mechanism for estimating extinction.

Bright Lyα emitters

Parallel to the Hα survey using the NB$_J$ filter, the HiZELS survey has has been explored to look for bright Lyα emitters at $z = 8.9$, when the Universe was only ~ 0.5 Gyr old. Two candidates were isolated, but follow-up observations showed that these cannot be Lyα emitters. It has therefore been possible to set by far the tightest constraint to date on the bright end of the $z \sim 9$ Lyα LF (Chapter 7). It has also been shown that for narrow-band searches, T-dwarfs can mimic Lyα emitters at $7.7 < z < 8.0$, $9.1 < z < 9.5$ and $11.7 < z < 12.2$; they will not contaminate the future UltraVISTA narrow-band survey (and can even be identified via a narrow-band *deficit*), but they may contaminate narrow-band Lyα searches within the $z = 7.7$ and $z = 9.4$ atmospheric windows.

8.1 On-going and Future Research

Our detailed understanding is still limited beyond $z \sim 1$ because current samples lack the depth, size and/or volume and are still affected by large or uncertain contamination fractions. Obtaining robust samples of ~ 1000 Hα emitters at both $z = 1.47$ and $z = 2.23$ over $\sim 7 - 10$ deg^2 will therefore be fundamental to expand and detail our understanding.

Reducing Contamination: towards larger, clean and robust samples at z ∼ 1.5 and z ∼ 2.3

Obtaining large, robust and reliable samples of Hα emitters at $1 < z < 2$ (the so-called redshift desert) is particularly hard. For $z = 1.47$, the approach taken in Chapter 6 has been show to work remarkably well and will now be extended to all HiZELS fields. Data have already been successfully obtained in COSMOS (selection of over 150 double emitters is on-going), and will be extended to the remaining HiZELS fields soon, which will lead to a robust sample of ~ 1000 emitters at $z \sim 1.5$ without depending on high-quality photometric-redshifts. For $z = 2.23$, there is a clear need to develop and use effective colour selections – building on the colour selection techniques studied and used in Chapter 6 – and taking advantage of on-going and future high-quality spectroscopic follow-up in the optical and near-IR, and propose further spectroscopic follow-up with the VLT.

Tackling the low-luminosity incompleteness at 1 < z < 3

HiZELS does not probe to low enough luminosities to accurately probe the faint-end of the population; this becomes particularly important at $z = 1.47$ and even more so at $z = 2.23$. Understanding the peak of the star formation history requires us to obtain large samples at both high and low luminosities. *Is the faint-end slope of the luminosity function evolving with cosmic time? Are faint emitters fundamentally different from the luminous emitters?* This limitation can addressed by using very deep narrow-band surveys at $z \sim 0.8$, $z \sim 1.5$ and $z = 2.23$ (with VISTA, WFCAM/UKIRT and

HAWK-I/VLT) – with these targeting at least two different fields at each redshift, in order to tackle cosmic variance. The data should probe SFRs similar to the Milky Way, guaranteeing large samples of ~ 500 Hα emitters below L^* all the way up to $z \sim 3$, and to determine the faint-end slope, α, with an accuracy of ~ 0.05 for all epochs. This future research will provide an even more detailed Hα-based star formation history of the Universe without the need for large extrapolations, and allow a direct comparison between large populations of the same luminosity over a wide range of look-back times for the first time. It will also be possible to address the detailed clustering evolution of Hα star-forming galaxies across the bulk of the age of the Universe and provide some of the strongest constraints on semi-analytical models.

The roles of environment, mass and galaxy properties using a super-cluster at z $\sim$ 0.84

Chapter 5 presented a truly panoramic Hα map at $z \sim 1$, covering $\sim 1.3\,\mathrm{deg}^2$, providing a much sharper picture of the roles and inter-dependences of mass and environment at $z \sim 1$ and reconciling the contradictory results in the literature. In order to obtain an even sharper view of the role of the environment at $z \sim 1$, overcoming current limitations (from the use of photo-zs), the VLT is being and will be used (with VIMOS, PI, ~ 40 hours awarded for 2011) to accurately map in 3-D a super-structure at $z = 0.84$ in the COSMOS field ($10 \times 13\,\mathrm{Mpc}$), containing 3 confirmed massive X-ray clusters/groups and showing a striking filamentary structure in the Hα map (see Chapter 5). Accurate redshifts, independent mass estimates from the absorption lines, and SFRs down to $10\times$ deeper than the Hα coverage will be obtained. Post-starburst galaxies (K+As) will be detected and it will be possible to map their fraction in the cluster, group, filament and field environments over the entire structure, thus revealing *exactly where* star formation activity is being enhanced/quenched, disentangling the roles of mass and environment.

The roles of mass, environment, galaxy dynamics and their evolution up to z $\sim$ 3

The detailed studies at $z = 0.84$ (Chapters 3, 4 and 5) should now be extended to $z \sim 1.5$ and $z \sim 2.2$. It is absolutely fundamental to both look for inter-dependences between mass, environment, Hα luminosity, morphology and other galaxy properties at a given epoch and, most of all, to seek to understand the potential evolution of such relations. *Is the role of the environment the same at all epochs? Is it all simply stellar-mass driven? Is mass-downsizing already in place at* $z \sim 1-3$*?* Downsizing is fully in place at $z \sim 1$ (Chapter 5), and on-going analysis points towards a similar result at $z = 1.47$, while by $z = 2.23$, the fraction of star-forming galaxies appears to remain constant up to the highest masses. This suggests that massive galaxies are still actively forming stars at $z \sim 2.3$ and that downsizing sets in at $z \sim 1.5 - 2$. Blank fields will be complemented with over-dense regions (by mapping high-z clusters in Hα). For $z = 1.47$, my NB921 data will also enable unique simultaneous [OII]-Hα science, further investigating the role/evolution of dust extinction/metallicity in line emitters at $z \sim 1.5$ and $z \sim 2.2$ and any possible differences from $z \sim 0$ and $z \sim 0.84$ as a function of environment, mass, and other properties.

Further unprecedented insight into the nature and evolution of star-forming galaxies at $z \sim 1-3$ can be

gained by obtaining high S/N near-infrared spectra (e.g. NIRC2 & NIRSPEC on Keck, FMOS/Subaru, and also NICS/TNG for bright emitters). *Do they contain a significant AGN contribution?* What are the metallicities of active star-forming galaxies at $z \sim 1.5$ and $z \sim 2.2$? IFU observations with SINFONI/VLT of ~ 20 Hα emitters are being obtained, including sources from the sample presented in Chapter 6. For sources at $z = 1.47$, the majority of the sample presents disk-like dynamics, but two emitters are consistent with being mergers. The [NII]/Hα flux ratio in these galaxies is ~ 0.2–0.35, consistent with slightly sub-solar metallicity. Results will be published in Swinbank, Sobral et al. (2011). By using IFUs such as SINFONI and KMOS to target hundreds of sources, it will be possible to study the dynamics and line ratios of large samples of $z = 1.47$ and $z = 2.23$ emitters over a range of galaxy properties for the first time. Is stellar mass assembly occurring in secular isolation or via merger build-up? A further exciting research line is to detect the Hα emitters in CO (at $z = 0.84, 1.47, 2.23$) using ALMA (Early Science), and to obtain high-resolution CO maps of those sources (as soon as ALMA is able to provide sufficient resolution). The combination of the powerful Hα and CO $\sim$sub-kpc maps at 3 different redshifts will not only trace star formation laws at high redshift, but will also allow to robustly measure any evolution for the first time and provide some of the strongest constraints on models of galaxy formation and evolution.

Searching and Studying the First Galaxies: Wide-area Lyα Searches at z > 7

Understanding galaxy formation requires us to ask an even more fundamental question: *when did the first stars and galaxies form?* Over the last decade, considerable manpower and telescope time has been dedicated towards this goal: galaxies have been robustly identified out to redshift $z \sim 7$, just 750 Myr after the Big Bang (Iye et al. 2006), and a GRB has been confirmed at an even earlier epoch ($z \sim 8.2$, Tanvir et al. 2009). The refurbished HST/WFC3 has opened a window to even earlier epochs, allowing the selection of $z \sim 7 - 8$ very faint candidates (c.f. Bouwens et al. 2010), and Chapter 7 presents a search for $z \sim 9$ galaxies, placing strong constraints on their number density. However, despite the great progress, there are still strong limitations at the moment which should be addressed.

Obtaining larger samples over much larger areas

Current samples are derived from ultra-deep, small-area surveys and are likely to be strongly affected by cosmic variance. Arguably, one way of progressing is by conducting relatively deep, wide narrow-band surveys for Lyα emitters, taking advantage of NB921 data from Subaru and the VISTA telescope. VISTA has the largest field of view (~ 1 square degree) in the near-IR, and low-atmospheric emission narrow-band filters (used for the LASER and UltraVISTA projects), making it ideal to survey large areas and identify relatively luminous Lyα emitters very effectively. Observations will be carefully planned using the best constraints on the Lyα LF to securely provide samples of ~ 100 Lyα emitters at $z \sim 6.6$ (PI, Subaru) and $z \sim 7.1$ with VISTA over $\sim 5 - 10\,\mathrm{deg}^2$.

Selecting bright-enough candidates for detailed follow-up

Current $z > 7$ candidates are extremely faint to be followed up. Lehnert et al. (2010) obtained a very deep spectrum of a likely $z = 8.55$ Lyα emitter, but even with ~ 15 hrs integration time on the VLT the S/N is low. What we really require are brighter candidates. By conducting wide high-z narrow-band surveys, it should be possible to identify some of the most luminous Lyα emitters at $z > 7$ which are ideal targets for spectroscopic follow-up with 8-10 m telescopes. This will not only confirm their redshift, it will finally be possible to investigate their star formation rates, existing stellar mass content, and other properties for the first time. Taking advantage of the experience in searching for Lyα emitters at $z \sim 9$, a very wide area survey for Lyα at $z \sim 9$ will be conducted using CFHT and VISTA (combined with UltraVISTA, this will provide the best constraint of the shape of the $z \sim 9$ Lyα), with a large potential to detect Lyα emitters bright enough for the first robust $z = 8.8$ spectroscopic confirmation and follow-up, even before the era of JWST/TMTs.

Towards a complete understanding of galaxy formation and evolution

In summary, the work presented in this thesis constitutes an important contribution towards our understanding of galaxy formation and evolution. It presents the first fully self-consistent star formation history of the Universe and a robust measurement of the strong evolution of both the Hα and [OII] luminosity functions. Most importantly, this work goes beyond simply measuring the evolution in a detailed and robust way, and uses the large sample at $z = 0.84$ to investigate the clustering, morphologies, masses and environments of the star-forming galaxies, and the important inter-relations between these. The latter investigations are the observational keys that can lead us to understand the fundamental mechanisms that drive galaxy evolution. Nevertheless, a complete understanding can only be obtained if such studies are extended to higher redshifts and using even larger samples and over a wider range of luminosities and other galaxy properties, as many questions remain unanswered. The studies at $z = 1.47$ constitute the first efforts towards such goal, but larger samples at that redshift, and larger and reliable samples at even higher redshift will also be necessary if we are to solve many of the unsolved problems and questions. Such questions will strongly drive the future research, which will take full advantage of the results and techniques presented here, together with new observations, and will seek to confront new results with the most up-to-date models and theory.

Appendix A

The underlying populations

A.1 Completeness and contamination

State-of-the-art photometric redshifts (Ilbert et al., 2009, Cirasuolo et al. in prep.) can be used to obtain samples of galaxies found at roughly the same redshift as the Hα emitters. In this Appendix, the completeness and contamination of the different photometric-redshift-selected samples are investigated and, after correcting for these, the robustness of the results presented in Chapter 5 is demonstrated.

For COSMOS, where the photometric redshifts can be obtained more precisely (due to the availability of medium bands which can, for example, probe the 4000 Å break extremely well), samples are defined selecting galaxies with $0.845 \pm \Delta z$, with Δz ranging from 0.005 to 0.065 ($0.78 < z_{\rm photo} < 0.91$) in steps of 0.005. Similar samples are defined for the UDS, but in steps of 0.01. The samples are selected over the entire available area with the best photometric and spectroscopic data in both fields.

For the COSMOS field, the zCOSMOS DR2 secure (> 99 per cent confidence) spectroscopic redshifts are used to study the completeness (the number of galaxies selected by the photo-z cut that have spectroscopic redshifts within the top hat narrow-band redshift range for the Hα emission line [$0.83 < z_{\rm spec} < 0.86$] compared to the total number of galaxies with spectroscopic redshifts in that range over the same area) and the contamination (the fraction of galaxies in the photo-z sample with spectroscopic redshifts that are confirmed to lie outside the narrow-band redshift range). The photo-z samples are all ≈ 10 per cent spectroscopically complete and there are a total of 260[1] spectroscopically confirmed galaxies in the full NB$_J$ filter range (over the entire COSMOS field).

The results for different photo-z cuts can be found in Table A.1 and Figure A.1. These clearly reveal that adopting a photo-z cut matching the full spectroscopic redshift distribution of the narrow-band

[1] From these, 182 are found over the NB$_J$ imaging coverage, with roughly half of these being detected by HiZELS as Hα emitters.

Table A.1: A completeness and contamination study of the photometric redshift selected samples obtained in the full COSMOS field using z-COSMOS DR2 (Lilly et al., 2009). Completeness is estimated as the fraction of galaxies wich have spectroscopic redshifts in the narrow-band (top hat) filter range ($0.83 < z < 0.86$) which are recovered by the photo-z cut (and after accounting for introducing all confirmed galaxies into each sample). The contamination is calculated by computing the fraction of galaxies with spectroscopic redshifts for which the redshifts are not within the narrow-band filter redshift range for Hα emitters at $z = 0.84$. Photometric-selected samples are all ≈ 10 per cent spectroscopically complete. The samples presented here include Hα emitters, but the completeness estimated from excluding the Hα emitters is found to be the same. The separating line represents the exact redshift range of the narrow-band filter when assumed to be a perfect top-hat function. Results are also presented in Figure A.1.

Sample	**Sources**	**Completeness**	**Contamination**
COSMOS	(Number)	C (%)	Co (%)
$0.780 < z_{\rm ph} < 0.910$	14812	88	73
$0.785 < z_{\rm ph} < 0.905$	14296	88	72
$0.790 < z_{\rm ph} < 0.900$	13262	87	70
$0.795 < z_{\rm ph} < 0.895$	11932	86	68
$0.800 < z_{\rm ph} < 0.890$	11205	85	66
$0.805 < z_{\rm ph} < 0.885$	10131	83	65
$0.810 < z_{\rm ph} < 0.880$	9670	83	64
$0.815 < z_{\rm ph} < 0.875$	8977	81	63
$0.820 < z_{\rm ph} < 0.870$	8047	77	59
$0.825 < z_{\rm ph} < 0.865$	6921	72	53
$0.830 < z_{\rm ph} < 0.860$	5636	65	46
$0.835 < z_{\rm ph} < 0.855$	3682	49	41
$0.840 < z_{\rm ph} < 0.850$	1492	41	36

filter ($0.825 < z_{\rm ph} < 0.865$) recovers 72 per cent of the total number of galaxies at those spectroscopic redshifts, missing a significant fraction of the population. On the other hand, while using a wider photo-z cut increases the completeness, it also raises the contamination quite considerably.

It should be noted that in the area covered by the NB$_J$ imaging there are 22 sources spectroscopically confirmed to be within the narrow-band redshift range which are missed by all the studied photo-z cuts (11 of these are Hα emitters). These present a median photometric redshift of 0.73 (although some of those have photo-zs of $1.3 - 1.4$), and are much bluer (U-K $\approx 0.4 - 3$) than sources recovered by the photo-zs (U-K $\approx 1.5 - 7.5$); this indicates that the photometric redshift selection is more likely to miss bluer, less massive galaxies than redder, more massive/luminous galaxies. This is mostly a consequence of the fact that blue, star-forming galaxies present weak 4000 Å break features, combined with a significant [OII]3727 emission and Balmer breaks which, combined, can mimic a 4000 Å at lower rest-frame wavelengths and result in lower photometric redshifts. In order to investigate

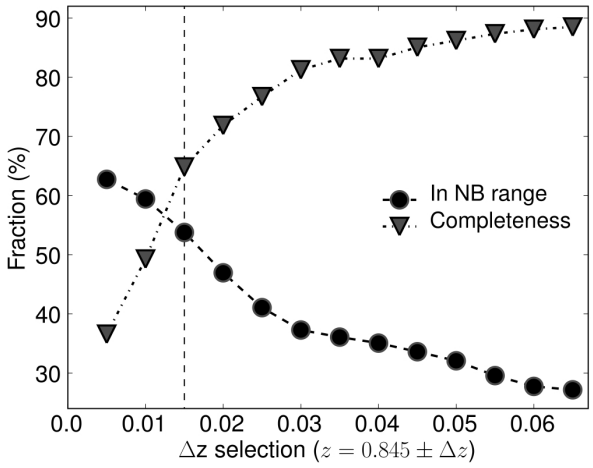

Figure A.1: The completeness fraction and the fraction of sources within the NB filter redshift range (1− contamination) as a function of photometric redshift width for the COSMOS field. The dashed line indicates the narrow-band filter cut-off assuming a perfect top-hat filter.

this further, the completeness and contamination are computed independently in different stellar mass bins. The results, presented in Table A.2, show that the completeness increases as a function of stellar mass; this increase can be well approximated by a 10 per cent increase in completeness per 1 dex in stellar mass for the current sample – between 9.5 and 11.5 in log $M_{\odot}$. It is also found that the contamination decreases with increasing stellar mass, by approximately 10 per cent per dex in stellar mass. These corrections are incorporated when computing the star-forming fraction as a function of mass.

For the UDS field, the lack of spectroscopic redshifts does not allow a detailed study of the completeness and contamination of the underlying samples; the completeness is therefore estimated using the HiZELS Hα sample and the recovery fraction of this sample as a function of the photometric redshift cut. In the COSMOS field, the completeness and contamination estimated using the Hα sample are found to be broadly comparable to those from using the population as a whole. Results are presented in Table A.3.

Completeness and contamination may vary as a function of environment as well, particularly because galaxies are spread rather uniformly in the field, but groups are clustered at certain redshifts. Nevertheless, currently the limited spectroscopic samples do not allow to reliably estimate how completeness and contamination may vary with environment, although any such variation is expected to be weak and to largely even out in the statistics, so any possible trends are ignored in the analysis.

A.2 The effect of varying photo-z cuts

The choice of the underlying population for estimating local densities can in principle play a significant role in such estimation in a number of ways: sources at significant different redshifts (photo-z outliers) will introduce extra scatter in the measurements; wider photo-z selected samples might pick up large

Table A.2: A completeness and contamination study as a function of stellar mass of the photometric redshift selected samples obtained in the COSMOS field. The results reveal that while completeness increases as a function of stellar mass, the contamination decreases as a function of mass.

COSMOS	$10^{9.5}\,\mathbf{M}_{\odot}$	$10^{10.0}\,\mathbf{M}_{\odot}$	$10^{10.5}\,\mathbf{M}_{\odot}$	$10^{11.0}\,\mathbf{M}_{\odot}$	$10^{11.5}\,\mathbf{M}_{\odot}$
Sample	C (%)	C (%)	C (%)	C (%)	C (%)
$0.790 < z_{\rm ph} < 0.900$	56	85	90	97	90
$0.800 < z_{\rm ph} < 0.890$	50	82	89	95	90
$0.810 < z_{\rm ph} < 0.880$	38	81	86	95	90
$0.820 < z_{\rm ph} < 0.870$	25	68	83	93	90
Sample	Co (%)	Co (%)	Co (%)	Co (%)	Co (%)
$0.790 < z_{\rm ph} < 0.900$	80	64	74	68	55
$0.800 < z_{\rm ph} < 0.890$	80	58	71	65	51
$0.810 < z_{\rm ph} < 0.880$	80	52	69	63	51
$0.820 < z_{\rm ph} < 0.870$	80	51	64	55	38

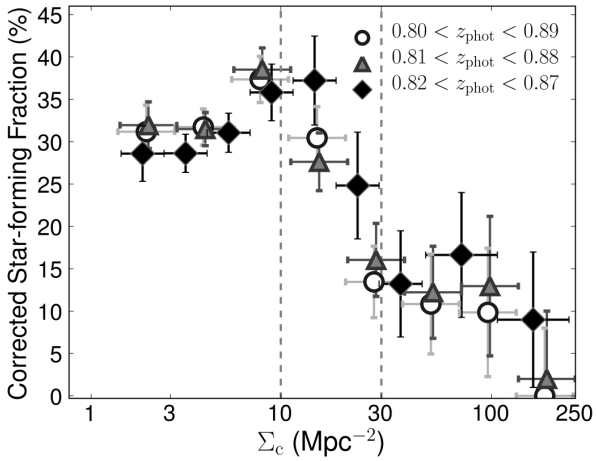

Figure A.2: The relatively small increase of the star-forming fraction within the field regime and fall for denser regions is recovered independently of the photometric redshift cut, once corrections for completeness and contamination are made. Both the underlying population and the estimated local densities are calculated and corrected appropriately for each photo-z sample, but the resultant behaviour of the star-forming fractions as a function of local density for each determination is essentially the same.

structures just outside the narrow-band filter range and bias certain regions; more importantly, a higher or lower number of sources could change the normalisation of the star-forming fraction. In principal, the latter issue can be avoided by using the completeness and contamination statistics for the underlying samples, calculated in Section A1 to correct the projected local densities (Σ) and star-forming fractions (SFF) using:

$$\Sigma_{\rm c} = \Sigma \times \frac{1 - {\rm Co}}{\rm C}, \qquad {\rm SFF_c} = {\rm SFF} \times \frac{\rm C}{1 - {\rm Co}}. \tag{A.1}$$

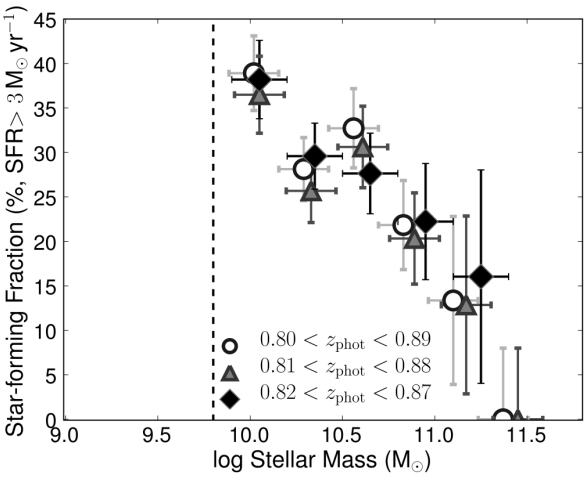

Figure A.3: The mass dependence of the star-forming fraction presented in CHapter 5 is clearly recovered independently of the choice of photometric redshift cut. Furthermore, correcting the star-forming fraction based on the mass-dependent completeness and contamination also shows that the normalisation, along with the trend, agrees very well between samples.

Table A.3: A completeness study of the photometric redshift selected samples obtained in the UDS field based on the Hα sample. Completeness is estimated as the fraction of Hα emitters recovered as compared with the total number.

Sample	**Sources**	**Completeness**
UDS	(Number)	C (%)
$0.780 < z_{ph} < 0.910$	3502	57
$0.790 < z_{ph} < 0.900$	3078	54
$0.800 < z_{ph} < 0.890$	2494	49
$0.810 < z_{ph} < 0.880$	1874	42
$0.820 < z_{ph} < 0.870$	1502	41
$0.830 < z_{ph} < 0.860$	1125	34

In order to assess any potential biases or errors, corrected local densities have been computed using all of the previously defined underlying populations. It is found that once the corrections are applied, the local density estimates using different underlying samples correlate very well with a slope of unity. Furthermore, as Figure A.2 shows, the trends presented in the analysis are independent of the choice of underlying population (within the photo-z range used).

Mass-downsizing trends have also been presented in Chapter 5 – these reveal that the fraction of star-forming galaxies decreases as a function of mass. It is fundamental to confirm that this is a consequence of galaxy formation and evolution, rather than a possible bias in either or both the selection of the underlying population and/or the mass estimates. As Figure A.3 fully details, the mass-downsizing trends are robust against the choice of the underlying population. They are also found to be equally robust against variations in the mass estimates (cf. Appendix B).

Appendix B

Stellar Mass Estimates

Stellar masses were computed for all Hα emitters and galaxies within the underlying population as fully detailed in Section 5.2.5. Here, further attention is given to the uncertainties and possible systematic errors.

Figure B.1 shows a comparison between the mass estimates for galaxies in the COSMOS field obtained in this work and those from Mobasher et al. (2007). There is a systematic offset from zero, but this is fully explained by the different Initial Mass Functions (IMF) used: using a Salpeter IMF, as in Mobasher et al. (2007) results in assuming a mass-to-light ratio higher by a factor of 1.8 when compared to the Chabrier (2003) IMF used here; this results in a difference of ≈ 0.17 dex in stellar mass. The additional scatter is mostly due to the simpler approach used by Mobasher et al. (2007) to estimate stellar masses from visible luminosities and artificial colours, together with their poorer photometric redshifts. Figure B.1 also compares the mass estimates for the UDS field with those derived by M. Cirasuolo et al. (in preparation), revealing a lower degree of scatter, which mostly arises from a different aperture correction (M. Cirasuolo et al. use a constant aperture correction assuming all sources are point sources, while in this work individual corrections are used; the constant aperture correction matches very well to the average of the individual corrections used in this work), and different stellar synthesis models (with different parameters). Overall, the scatter between the different determinations is relatively small and there are no systematic trends.

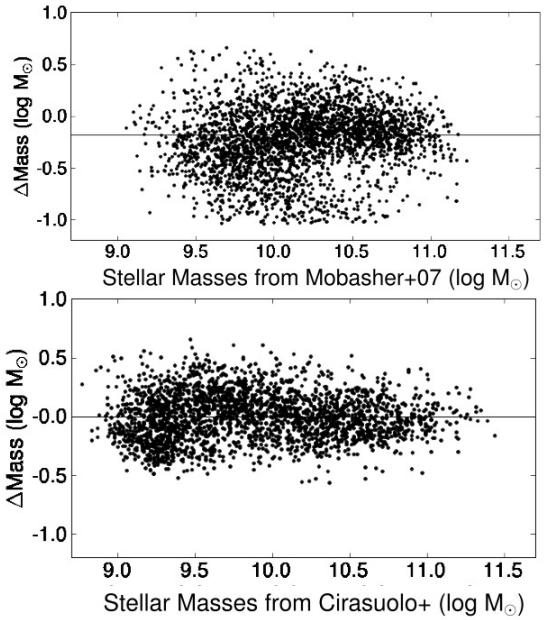

Figure B.1: Comparison between the determined stellar masses and those from Mobasher et al. (2007) and Cirasuolo et al. (in prep.). The ones computed in this study, by using a much larger number of bands and by taking a full SED fitting approach fixing the redshift are much more reliable than those estimated from rest-frame V luminosities combined with artificial rest-frame B-V colours by Mobasher et al. (2007) (those authors also use a Salpeter IMF; this results in estimating stellar masses which are +0.17 dex higher). Nevertheless, there is no significant offset between both estimates (once one corrects for the different IMFs), and the scatter is fully consistent with the errors expected from the Mobasher et al determinations. As for the comparison with the preliminary results from Cirasuolo et al., the differences (scatter) mostly arise from the use of different models, different aperture corrections and, to a lower extent, the use of $z = 0.845$ in this work instead of the best photo-z.

Bibliography

Adelberger, K. L. and Steidel, C. C.: 2000, *ApJ* **544**, 218

Afonso, J., Cram, L., and Mobasher, B.: 2000, *ApJ* **536**, 68

Amanullah, R., Lidman, C., Rubin, D., Aldering, G., Astier, P., Barbary, K., Burns, M. S., Conley, A., Dawson, K. S., and et al.: 2010, *ApJ* **716**, 712

Antonucci, R.: 1993, *ARA&A* **31**, 473

Aragón-Salamanca, A., Alonso-Herrero, A., Gallego, J., García-Dabó, C. E., Pérez-González, P. G., Zamorano, J., and Gil de Paz, A.: 2003, in *Star Formation Through Time*, Vol. 297 of *ASPCS*, p. 191

Ball, N. M., Loveday, J., and Brunner, R. J.: 2008, *MNRAS* **383**, 907

Balogh, M. L., Couch, W. J., Smail, I., Bower, R. G., and Glazebrook, K.: 2002, *MNRAS* **335**, 10

Barkana, R. and Loeb, A.: 2001, *Physics Review P* **349**, 125

Bauer, A. E., Drory, N., Hill, G. J., and Feulner, G.: 2005, *ApJL* **621**, L89

Baugh, C. M.: 2006, *Reports on Progress in Physics* **69**, 3101

Baugh, C. M., Cole, S., and Frenk, C. S.: 1996, *MNRAS* **283**, 1361

Baugh, C. M., Cole, S., Frenk, C. S., and Lacey, C. G.: 1998, *ApJ* **498**, 504

Baugh, C. M., Lacey, C. G., Frenk, C. S., Granato, G. L., Silva, L., Bressan, A., Benson, A. J., and Cole, S.: 2005, *MNRAS* **356**, 1191

Bayliss, K. D., McMahon, R. G., Venemans, B. P., Ryan-Weber, E. V., and Lewis, J. R.: 2011, *arXiv:1102.0229*

Begelman, M. C.: 2008, in *First Stars III*, Vol. 990 of *AIPCS*, pp 489–493

Beisbart, C. and Kerscher, M.: 2000, *ApJ* **545**, 6

Bennett, C. L., Banday, A. J., Gorski, K. M., Hinshaw, G., Jackson, P., Keegstra, P., Kogut, A., Smoot, G. F., Wilkinson, D. T., and Wright, E. L.: 1996, *ApJ Letters* **464**, L1

Benson, A. J.: 2010, *Physics Reports* **495**, 33

Benson, A. J., Cole, S., Frenk, C. S., Baugh, C. M., and Lacey, C. G.: 2000, *MNRAS* **311**, 793

Bertin, E. and Arnouts, S.: 1996, *A&AS* **117**, 393

Best, P. N.: 2004, *MNRAS* **351**, 70

Best, P. N., Kaiser, C. R., Heckman, T. M., and Kauffmann, G.: 2006, *MNRAS* **368**, L67

Blain, A. W., Chapman, S. C., Smail, I., and Ivison, R.: 2004, *ApJ* **611**, 725

Bouwens, R. J., Illingworth, G. D., Franx, M., and Ford, H.: 2007, *ApJ* **670**, 928

Bouwens, R. J., Illingworth, G. D., Franx, M., and Ford, H.: 2008, *ApJ* **686**, 230

Bouwens, R. J., Illingworth, G. D., Oesch, P. A., Stiavelli, M., van Dokkum, P., Trenti, M., Magee, D., Labbé, I., Franx, M., Carollo, C. M., and Gonzalez, V.: 2010, *ApJL* **709**, L133

Bower, R. G., Benson, A. J., Malbon, R., Helly, J. C., Frenk, C. S., Baugh, C. M., Cole, S., and Lacey, C. G.: 2006, *MNRAS* **370(2)**, 645

Brainerd, T. G., Smail, I., and Mould, J.: 1995, *MNRAS* **275**, 781

Brinchmann, J., Charlot, S., White, S. D. M., Tremonti, C., Kauffmann, G., Heckman, T., and Brinkmann, J.: 2004, *MNRAS* **351**, 1151

Brocklehurst, M.: 1971, *MNRAS* **153**, 471

Bromm, V. and Larson, R. B.: 2004, *ARAA* **42**, 79

Bruzual, G.: 2007, in A. Vallenari, R. Tantalo, L. Portinari, & A. Moretti (ed.), *From Stars to Galaxies: Building the Pieces to Build Up the Universe*, Vol. 374 of *ASPCS*, p. 303

Bruzual, G. and Charlot, S.: 2003, *MNRAS* **344**, 1000

Buat, V. and Xu, C.: 1996, *A&A* **306**, 61

Bunker, A. J., Warren, S. J., Hewett, P. C., and Clements, D. L.: 1995, *MNRAS* **273**, 513

Bunker, A. J., Wilkins, S., Ellis, R. S., Stark, D. P., Lorenzoni, S., Chiu, K., Lacy, M., Jarvis, M. J., and Hickey, S.: 2010, *MNRAS* **409**, 855

Burningham et al.: 2008, *MNRAS* **391**, 320

Butcher, H. and Oemler, Jr., A.: 1984, *ApJ* **285**, 426

Calzetti, D., Armus, L., Bohlin, R. C., Kinney, A. L., Koornneef, J., and Storchi-Bergmann, T.: 2000, *ApJ* **533**, 682

Capak, P., Aussel, H., Ajiki, M., McCracken, H. J., Mobasher, B., Scoville, N., Shopbell, P., and et al.: 2007, *ApJS* **172**, 99

Caplan, J., Ye, T., Deharveng, L., Turtle, A. J., and Kennicutt, R. C.: 1996, *A&A* **307**, 403

Caputi et al.: 2007, *ApJ* **660**, 97

Casali, M., Adamson, A., Alves de Oliveira, C., Almaini, O., Burch, K., Chuter, T., Elliot, J., and et al.: 2007, *A&A* **467**, 777

Cattaneo, A., Faber, S. M., Binney, J., Dekel, A., Kormendy, J., Mushotzky, R., Babul, A., Best, P. N., and et al.: 2009, *Nature* **460**, 213

Chabrier, G.: 2003, *PASP* **115**, 763

Cirasuolo, M., McLure, R. J., Dunlop, J. S., Almaini, O., Foucaud, S., and Simpson, C.: 2010, *MNRAS* **401**, 1166

Cohen, J. G.: 1976, *ApJ* **203**, 587

Colless, M., Dalton, G., Maddox, S., Sutherland, W., Norberg, P., and et al.: 2001, *MNRAS* **328**, 1039

Condon, J. J.: 1992, *ARAA* **30**, 575

Connolly, A. J., Szalay, A. S., Dickinson, M., SubbaRao, M. U., and Brunner, R. J.: 1997, *ApJL* **486(1)**, L11

Cooper, M. C., Coil, A. L., Gerke, B. F., Newman, J. A., Bundy, K., Conselice, C. J., Croton, D. J., and et al.: 2010, *MNRAS* **409**, 337

Cooper, M. C., Newman, J. A., Weiner, B. J., Yan, R., Willmer, C. N. A., Bundy, K., and et al.: 2008, *MNRAS* **383**, 1058

Couch, W. J., Balogh, M. L., Bower, R. G., Smail, I., Glazebrook, K., and Taylor, M.: 2001, *ApJ* **549**, 820

Cowie, L. L., Songaila, A., Hu, E. M., and Cohen, J. G.: 1996, *AJ* **112**, 839

Cram, L., Hopkins, A., Mobasher, B., and Rowan-Robinson, M.: 1998, *ApJ* **507**, 155

Cuby, J.-G., Hibon, P., Lidman, C., Le Fèvre, O., Gilmozzi, R., Moorwood, A., and van der Werf, P.: 2007, *AAP* **461**, 911

Cutri, R. M., Skrutskie, M. F., van Dyk, S., Beichman, C. A., Carpenter, J. M., Chester, T., Cambresy, L., and et al.: 2003, *2MASS All Sky Catalog of point sources.*, NASA/IPAC Infrared Science Archive

da Ângela et al.: 2008, *MNRAS* **383**, 565

Daddi, E., Dickinson, M., Morrison, G., Chary, R., Cimatti, A., Elbaz, D., Frayer, D., and et al.: 2007, *ApJ* **670**, 156

Dale, D. A., Barlow, R. J., Cohen, S. A., Cook, D. O., Johnson, L. C., Kattner, S. M., Moore, C. A., and et al.: 2010, *ApJL* **712**, L189

Dale et al.: 2008, *AJ* **135**, 1412

de Jong, T., Klein, U., Wielebinski, R., and Wunderlich, E.: 1985, *A&A* **147**, L6

De Lucia, G. and Blaizot, J.: 2007, *MNRAS* **375**, 2

Dickey, J. M. and Salpeter, E. E.: 1984, ApJ **284**, 461

Doherty, M., Bunker, A., Sharp, R., Dalton, G., Parry, I., and Lewis, I.: 2006, *MNRAS* **370(1)**, 331

Dressler, A.: 1980, *ApJ* **236**, 351

Dunkley et al.: 2009, *ApJS* **180**, 306

Dunne, L., Ivison, R. J., Maddox, S., Cirasuolo, M., Mortier, A. M., Foucaud, S., Ibar, E., and et al.: 2009, *MNRAS* **394**, 3

Efstathiou, G., Bernstein, G., Tyson, J. A., Katz, N., and Guhathakurta, P.: 1991, *ApJL* **380**, L47

Elbaz, D., Daddi, E., Le Borgne, D., Dickinson, M., Alexander, D. M., Chary, R., Starck, J., and et al.: 2007, *MNRAS* **468**, 33

Ellis, R. S.: 2008, *Observations of the High Redshift Universe*, pp 259–364, Loeb, A., Ferrara, A., & Ellis, R. S.

Feruglio, C., Aussel, H., Le Floc'h, E., Ilbert, O., Salvato, M., Capak, P., Fiore, F., and et al.: 2010, *arXiv:1007.1933*

Feulner, G., Goranova, Y., Drory, N., Hopp, U., and Bender, R.: 2005, *MNRAS* **358**, L1

Finn, R. A., Zaritsky, D., McCarthy, Jr., D. W., Poggianti, B., Rudnick, G., Halliday, C., and et al.: 2005, *ApJ* **630**, 206

Finoguenov, A., Guzzo, L., Hasinger, G., Scoville, N. Z., Aussel, H., Böhringer, H., Brusa, M., Capak, P., and et al.: 2007, *ApJS* **172**, 182

Finoguenov, A., Watson, M. G., Tanaka, M., Simpson, C., Cirasuolo, M., Dunlop, J. S., Peacock, J. A., and et al.: 2010, *MNRAS* **403**, 2063

Fisher, K. B., Davis, M., Strauss, M. A., Yahil, A., and Huchra, J.: 1994, *MNRAS* **266**, 50

Fontana, A., Pozzetti, L., Donnarumma, I., Renzini, A., Cimatti, A., Zamorani, G., Menci, N., Daddi, E., and et al.: 2004, *A&A* **424**, 23

Fontanot, F., De Lucia, G., Monaco, P., Somerville, R. S., and Santini, P.: 2009, *MNRAS* **397**, 1776

Fujita et al.: 2003, *ApJL* **586**, L115

Furusawa, H., Kosugi, G., Akiyama, M., Takata, T., Sekiguchi, K., Tanaka, I., Iwata, I., and et al.: 2008, *ApJS* **176**, 1

Gallego, J., García-Dabó, C. E., Zamorano, J., Aragón-Salamanca, A., and Rego, M.: 2002, *ApJL* **570**, L1

Gallego, J., Zamorano, J., Aragon-Salamanca, A., and Rego, M.: 1995, *ApJL* **455**, L1

Garn, T. and Best, P. N.: 2010, *MNRAS* **409**, 421

Garn, T., Sobral, D., Best, P. N., Geach, J. E., Smail, I., Cirasuolo, M., Dalton, G. B., Dunlop, J. S., McLure, R. J., and Farrah, D.: 2010, *MNRAS* **402**, 2017

Gavazzi, G., Boselli, A., and Kennicutt, R.: 1991, *AJ* **101**, 1207

Geach, J. E., Smail, I., Best, P. N., Kurk, J., Casali, M., Ivison, R. J., and Coppin, K.: 2008, *MNRAS* **388**, 1473

Giavalisco, M. and Dickinson, M.: 2001, *ApJ* **550**, 177

Gilbank, D. G., Baldry, I. K., Balogh, M. L., Glazebrook, K., and Bower, R. G.: 2010a, *MNRAS* **405**, 2594

Gilbank, D. G., Balogh, M. L., Glazebrook, K., Bower, R. G., Baldry, I. K., Davies, G. T., Hau, G. K. T., and et al.: 2010b, *MNRAS* **405**, 2419

Glazebrook, K., Tober, J., Thomson, S., Bland-Hawthorn, J., and Abraham, R.: 2004, *AJ* **128**, 2652

Gómez, P. L., Nichol, R. C., Miller, C. J., Balogh, M. L., Goto, T., Zabludoff, A. I., Romer, A. K., and et al.: 2003, *ApJ* **584**, 210

Gronwall et al.: 2007, *ApJ* **667**, 79

Gunawardhana, M. L. P., Hopkins, A. M., Sharp, R. G., Brough, S., Taylor, E., Bland-Hawthorn, J., Maraston, C., and et al.: 2011, *arXiv:1104.2379*

Guth, A. H.: 1981, *Physical Review D (Particles and Fields)* **23**, 347

Haarsma, D. B., Partridge, R. B., Windhorst, R. A., and Richards, E. A.: 2000, *ApJ* **544**, 641

Haiman, Z. and Cen, R.: 2005, *ApJ* **623**, 627

Hartley, W. G., Lane, K. P., Almaini, O., Cirasuolo, M., Foucaud, S., Simpson, C., Maddox, S., Smail, I., and et al.: 2008, *MNRAS* **391**, 1301

Hayashi, M., Kodama, T., Koyama, Y., Tanaka, I., Shimasaku, K., and Okamura, S.: 2010, *MNRAS* **402**, 1980

Hayes, M., Schaerer, D., and Östlin, G.: 2010, *A&A* **509**, L5

Helou, G., Soifer, B. T., and Rowan-Robinson, M.: 1985, *ApJL* **298**, L7

Hibon, P., Cuby, J.-G., Willis, J., Clément, B., Lidman, C., Arnouts, S., Kneib, J.-P., Willott, C. J., Marmo, C., and McCracken, H.: 2010, *A&A* **515**, A97

Hilton, M., Lloyd-Davies, E., Stanford, S. A., Stott, J. P., Collins, C. A., Romer, A. K., Hosmer, M., Hoyle, B., and et al.: 2010, *arXiv:1005.4692*

Hogg, D. W., Blandford, R., Cohen, J. G., and Pahre, M. A.: 1998a, in *BAAS*, Vol. 30, p. 888

Hogg, D. W., Cohen, J. G., Blandford, R., and Pahre, M. A.: 1998b, *ApJ* **504**, 622

Hopkins, A. M.: 2004, *ApJ* **615**, 209

Hopkins, A. M. and Beacom, J. F.: 2006, *ApJ* **651**, 142

Hopkins, A. M., Connolly, A. J., Haarsma, D. B., and Cram, L. E.: 2001, *AJ* **122**, 288

Hopkins, A. M., Connolly, A. J., and Szalay, A. S.: 2000, *AJ* **120**, 2843

Hopkins, A. M., Miller, C. J., Nichol, R. C., Connolly, A. J., Bernardi, M., Gómez, P. L., Goto, T., and et al.: 2003, *ApJ* **599**, 971

Hu, E. M., Cowie, L. L., and McMahon, R. G.: 1998, *ApJL* **502**, L99

Hubble, E.: 1929, *Proceedings of the National Academy of Science* **15**, 168

Hughes, D. H., Serjeant, S., Dunlop, J., Rowan-Robinson, M., Blain, A., Mann, R. G., Ivison, R., Peacock, J., Efstathiou, A., Gear, W., Oliver, S., Lawrence, A., and et al.: 1998, *Nature* **394**, 241

Ibar, E., Cirasuolo, M., Ivison, R., Best, P., Smail, I., Biggs, A., Simpson, C., Dunlop, J., Almaini, O., McLure, R., Foucaud, S., and Rawlings, S.: 2008, *MNRAS* **386**, 953

Ideue, Y., Nagao, T., Taniguchi, Y., Shioya, Y., Saito, T., Murayama, T., Sasaki, S., and et al.: 2009, *ApJ* **700**, 971

Ilbert, O., Salvato, M., Le Floc'h, E., Aussel, H., Capak, P., McCracken, H. J., Mobasher, B., and et al.: 2010, *ApJ* **709**, 644

Ilbert et al.: 2009, *ApJ* **690**, 1236

Ivison, R. J., Magnelli, B., Ibar, E., Andreani, P., Elbaz, D., Altieri, B., Amblard, A., Arumugam, V., and et al.: 2010, *A&A* **518**, L31

Iye, M., Ota, K., Kashikawa, N., Furusawa, H., Hashimoto, T., Hattori, T., Matsuda, Y., Morokuma, T., Ouchi, M., and Shimasaku, K.: 2006, *Nature* **443**, 186

Jansen, R. A., Franx, M., and Fabricant, D.: 2001, *ApJ* **551**, 825

Kashikawa, N., Shimasaku, K., Yasuda, N., Ajiki, M., Akiyama, M., Ando, H., Aoki, K., and et al.: 2004, *PASJ* **56**, 1011

Kashikawa et al.: 2006, *ApJ* **648**, 7

Kauffmann, G., White, S. D. M., Heckman, T. M., Ménard, B., Brinchmann, J., Charlot, S., Tremonti, C., and Brinkmann, J.: 2004, *MNRAS* **353**, 713

Kennicutt, R. C., Hao, C.-N., Calzetti, D., Moustakas, J., Dale, D. A., Bendo, G., Engelbracht, C. W., Johnson, B. D., and Lee, J. C.: 2009, *ApJ* **703**, 1672

Kennicutt, Jr., R. C.: 1983, *ApJ* **272**, 54

Kennicutt, Jr., R. C.: 1998, *ApJ* **498**, 541

Kennicutt, Jr., R. C. and Kent, S. M.: 1983, *AJ* **88**, 1094

Kennicutt, Jr., R. C., Tamblyn, P., and Congdon, C. E.: 1994, *ApJ* **435**, 22

Kewley, L. J., Geller, M. J., and Jansen, R. A.: 2004, *AJ* **127**, 2002

Kodama, T., Balogh, M. L., Smail, I., Bower, R. G., and Nakata, F.: 2004, *MNRAS* **354**, 1103

Kodama, T., Tanaka, I., Kajisawa, M., Kurk, J., Venemans, B., De Breuck, C., Vernet, J., and Lidman, C.: 2007, *MNRAS* **377**, 1717

Koekemoer et al.: 2007, *APJS* **172**, 196

Komatsu et al.: 2009, *ApJS* **180**, 330

Kong, X., Daddi, E., Arimoto, N., Renzini, A., Broadhurst, T., Cimatti, A., Ikuta, C., and et al.: 2006, *ApJ* **638**, 72

Kovač, K., Somerville, R. S., Rhoads, J. E., Malhotra, S., and Wang, J.: 2007, *ApJ* **668**, 15

Kowalski, M., Rubin, D., Aldering, G., Agostinho, R. J., Amadon, A., Amanullah, R., Balland, C., and et al.: 2008, *ApJ* **686**, 749

Koyama, Y., Kodama, T., Shimasaku, K., Hayashi, M., Okamura, S., Tanaka, I., and Tokoku, C.: 2010, *MNRAS* **403**, 1611

Kurczynski, P., Gawiser, E., Huynh, M., Ivison, R. J., Treister, E., Smail, I., Blanc, G. A., Cardamone, C. N., Greve, T. R., Schinnerer, E., Urry, M., van der Werf, P., and Walter, F.: 2010, *arXiv:1010.0290*

Lacey, C. and Cole, S.: 1993, *MNRAS* **262**, 627

Lacey, C. G., Baugh, C. M., Frenk, C. S., and Benson, A. J.: 2011, *MNRAS* **412**, 1828

Landy, S. D. and Szalay, A. S.: 1993, *ApJ* **412**, 64

Lawrence, A., Warren, S. J., Almaini, O., Edge, A. C., Hambly, N. C., Jameson, R. F., Lucas, P., Casali, M., and Adamson, A. e.: 2007, *MNRAS* **379**, 1599

Le Delliou, M., Lacey, C. G., Baugh, C. M., and Morris, S. L.: 2006, *MNRAS* **365**, 712

Le Févre, O., Hudon, D., Lilly, S. J., Crampton, D., Hammer, F., and Tresse, L.: 1996, *ApJ* **461**, 534

Leauthaud, A., Finoguenov, A., Kneib, J., Taylor, J. E., Massey, R., Rhodes, J., Ilbert, O., Bundy, K., and et al.: 2010, *ApJ* **709**, 97

Leggett, S. K., Marley, M. S., Freedman, R., Saumon, D., Liu, M. C., Geballe, T. R., Golimowski, D. A., and Stephens, D. C.: 2007, *ApJ* **667**, 537

Lehnert, M. D., Nesvadba, N. P. H., Cuby, J.-G., Swinbank, A. M., Morris, S., Clément, B., Evans, C. J., Bremer, M. N., and Basa, S.: 2010, *Nature* **467**, 940

Lemaître, G.: 1927, *Annales de la Societe Scietifique de Bruxelles* **47**, 49

Lewis, I., Balogh, M., De Propris, R., Couch, W., Bower, R., Offer, A., Bland-Hawthorn, J., and et al.: 2002, *MNRAS* **334**, 673

Li, C., Kauffmann, G., Jing, Y. P., White, S. D. M., Börner, G., and Cheng, F. Z.: 2006, *MNRAS* **368**, 21

Li, Y., Hernquist, L., Robertson, B., Cox, T. J., Hopkins, P. F., Springel, V., Gao, L., Di Matteo, T., Zentner, A. R., Jenkins, A., and Yoshida, N.: 2007, *ApJ* **665**, 187

Lilly, S. J., Le Fevre, O., Hammer, F., and Crampton, D.: 1996, *ApJL* **460**, L1

Lilly, S. J., LeBrun, V., Maier, C., Mainieri, V., Mignoli, M., Scodeggio, M., Zamorani, G., and et al.: 2009, *ApJS* **184**, 218

Lotz et al.: 2008, *ApJ* **672**, 177

Ly, C., Lee, J. C., Dale, D. A., Momcheva, I., Salim, S., Staudaher, S., Moore, C. A., and Finn, R.: 2011, *ApJ* **726**, 109

Ly, C., Malkan, M. A., Kashikawa, N., Shimasaku, K., Doi, M., Nagao, T., Iye, M., and et al.: 2007, *ApJ* **657**, 738

Madau, P., Ferguson, H. C., Dickinson, M. E., Giavalisco, M., Steidel, C. C., and Fruchter, A.: 1996, *MNRAS* **283**, 1388

Madau, P., Pozzetti, L., and Dickinson, M.: 1998, *ApJ* **498**, 106

Mahajan, S., Haines, C. P., and Raychaudhury, S.: 2010, *MNRAS* 404

Malhotra, S. and Rhoads, J. E.: 2004, *ApJL* **617**, L5

Maraston, C., Daddi, E., Renzini, A., Cimatti, A., Dickinson, M., Papovich, C., Pasquali, A., and Pirzkal, N.: 2006, *ApJ* **652**, 85

Marchesini, D., van Dokkum, P. G., Förster Schreiber, N. M., Franx, M., Labbé, I., and Wuyts, S.: 2009, *ApJ* **701**, 1765

Markevitch, M., Gonzalez, A. H., Clowe, D., Vikhlinin, A., Forman, W., Jones, C., Murray, S., and Tucker, W.: 2004, *ApJ* **606**, 819

Markevitch, M., Gonzalez, A. H., David, L., Vikhlinin, A., Murray, S., Forman, W., Jones, C., and Tucker, W.: 2002, *ApJ Letters* **567**, L27

Matarrese, S., Coles, P., Lucchin, F., and Moscardini, L.: 1997, *MNRAS* **286**, 115

McLure, R. J., Cirasuolo, M., Dunlop, J. S., Foucaud, S., and Almaini, O.: 2009, *MNRAS* **395**, 2196

McLure, R. J., Dunlop, J. S., Cirasuolo, M., Koekemoer, A. M., Sabbi, E., Stark, D. P., Targett, T. A., and Ellis, R. S.: 2010, *MNRAS* **403**, 960

McLure, R. J., Jarvis, M. J., Targett, T. A., Dunlop, J. S., and Best, P. N.: 2006, *MNRAS* **368**, 1395

McLure et al.: 2006, *MNRAS* **372**, 357

Meneux et al.: 2009, A&A **505**, 463

Meurer, G. R., Heckman, T. M., and Calzetti, D.: 1999, *ApJ* **521**, 64

Miller, G. E. and Scalo, J. M.: 1979, *ApJ* **41**, 513

Misawa, T., Kashikawa, N., Ohyama, Y., Hashimoto, T., and Iye, M.: 2006, *ApJ* **131**, 34

Mo, H. J., Jing, Y. P., and White, S. D. M.: 1996, *MNRAS* **282**, 1096

Mo, H. J. and White, S. D. M.: 1996, *MNRAS* **282**, 347

Mobasher, B., Capak, P., Scoville, N. Z., Dahlen, T., Salvato, M., Aussel, H., Thompson, D. J., and et al.: 2007, *ApJS* **172**, 117

Mobasher et al.: 2007, *ApJS S* **172**, 117

Moorwood, A. F. M., van der Werf, P. P., Cuby, J. G., and Oliva, E.: 2000, *A&A* **362**, 9

Morioka, T., Nakajima, A., Taniguchi, Y., Shioya, Y., Murayama, T., and Sasaki, S. S.: 2008, PASJ **60**, 1219

Moscardini, L., Coles, P., Lucchin, F., and Matarrese, S.: 1998, *MNRAS* **299**, 95

Mouhcine, M., Lewis, I., Jones, B., Lamareille, F., Maddox, S. J., and Contini, T.: 2005, *MNRAS* **362**, 1143

Nakajima, A., Shioya, Y., Nagao, T., Saito, T., Murayam, T., Sasaki, S. S., Yokouchi, A., and Taniguchi, Y.: 2008, *PASJ* **60**, 1249

Navarro, J. F., Frenk, C. S., and White, S. D. M.: 1996, *ApJ* **462**, 563

Nilsson, K. K., Orsi, A., Lacey, C. G., Baugh, C. M., and Thommes, E.: 2007, *A&A* **474**, 385

Norberg et al.: 2001, *MNRAS* **328**, 64

Ono, Y., Ouchi, M., Shimasaku, K., Akiyama, M., Dunlop, J., Farrah, D., and et al.: 2010, *MNRAS* **402**, 1580

Orsi, A., Lacey, C. G., Baugh, C. M., and Infante, L.: 2008, *MNRAS* **391**, 1589

Ota et al.: 2008, *ApJ* **677**, 12

Ouchi, M., Shimasaku, K., Akiyama, M., Simpson, C., Saito, T., Ueda, Y., Furusawa, H., and et al.: 2008, *ApJS* **176**, 301

Ouchi, M., Shimasaku, K., Akiyama, M., Simpson, C., Saito, T., Ueda, Y., Furusawa, H., and et al.: 2009, *VizieR Online Data Catalog* **217**, 60301

Ouchi, M., Shimasaku, K., Furusawa, H., Saito, T., Yoshida, M., Akiyama, M., Ono, Y., and et al.: 2010, *ApJ* **723**, 869

Ouchi, M., Shimasaku, K., Okamura, S., Furusawa, H., Kashikawa, N., Ota, K., Doi, M., and et al.: 2004, *ApJ* **611**, 660

Ouchi et al.: 2005, *ApJL* **635**, L117

Patel, S. G., Holden, B. P., Kelson, D. D., Illingworth, G. D., and Franx, M.: 2009, *ApJL* **705**, L67

Peebles, P. J. E.: 1975, *ApJ* **196**, 647

Peebles, P. J. E.: 1980, *The large-scale structure of the universe*, Princeton University Press

Peng, Y., Lilly, S. J., Kovac, K., Bolzonella, M., Pozzetti, L., Renzini, A., Zamorani, G., and et al.: 2010, *ApJ* **721**, 193

Percival, W. J., Nichol, R. C., Eisenstein, D. J., Weinberg, D. H., Fukugita, M., Pope, A. C., Schneider, D. P., Szalay, A. S., and et al.: 2007, *ApJ* **657**, 51

Pérez-González, P. G., Zamorano, J., Gallego, J., Aragón-Salamanca, A., and Gil de Paz, A.: 2003, *ApJ* **591**, 827

Perlmutter, S., Aldering, G., Goldhaber, G., Knop, R. A., Nugent, P., Castro, P. G., Deustua, S., and et al.: 1999, *ApJ* **517**, 565

Pettini, M. and Pagel, B. E. J.: 2004, *MNRAS* **348**, L59

Poggianti, B. M.: 1997, *AAPS* **122**, 399

Poggianti, B. M., Desai, V., Finn, R., Bamford, S., De Lucia, G., Varela, J., Aragón-Salamanca, A., Halliday, C., and et al.: 2008, *ApJ* **684**, 888

Reddy, N. A. and Steidel, C. C.: 2009, *ApJ* **692**, 778

Richard, J., Stark, D. P., Ellis, R. S., George, M. R., Egami, E., Kneib, J.-P., and Smith, G. P.: 2008, *ApJ* **685**, 705

Robertson, B. E., Ellis, R. S., Dunlop, J. S., McLure, R. J., and Stark, D. P.: 2010, *Nature* **468**, 49

Roche, N. D., Almaini, O., Dunlop, J., Ivison, R. J., and Willott, C. J.: 2002, *MNRAS* **337**, 1282

Rodighiero, G., Cimatti, A., Gruppioni, C., Popesso, P., Andreani, P., Altieri, B., Aussel, H., and et al.: 2010, *arXiv:1005.1089*

Rola, C. S., Terlevich, E., and Terlevich, R. J.: 1997, *MNRAS* **289**, 419

Romanishin, W.: 1990, *AJ* **100**, 373

Rozo, E., Wechsler, R. H., Rykoff, E. S., Annis, J. T., Becker, M. R., Evrard, A. E., Frieman, J. A., Hansen, S. M., and et al.: 2010, *ApJ* **708**, 645

Salpeter, E. E.: 1955, *ApJ* **121**, 161

Santini, P., Fontana, A., Grazian, A., Salimbeni, S., Fiore, F., Fontanot, F., Boutsia, K., and et al.: 2009, *A&A* **504**, 751

Scalo, J. M.: 1986, *Fundamentals of Cosmic Physics* **11**, 1

Scarlata, C., Carollo, C. M., Lilly, S., Sargent, M. T., Feldmann, R., Kampczyk, P., Porciani, C., and et al.: 2007, *ApJS* **172**, 406

Scoville et al.: 2007, *APJS* **172**, 1

Sheth, R. K., Mo, H. J., and Tormen, G.: 2001, *MNRAS* **323**, 1

Shi, Y., Rieke, G., Lotz, J., and Pérez-González, P. G.: 2009a, *ApJ* **697**, 1764

Shi, Y., Rieke, G. H., Ogle, P., Jiang, L., and Diamond-Stanic, A. M.: 2009b, *ApJ* **703**, 1107

Shim, H., Colbert, J., Teplitz, H., Henry, A., Malkan, M., McCarthy, P., and Yan, L.: 2009, *ApJ* **696**, 785

Shimasaku et al.: 2006, *PASJ* **58**, 313

Shioya, Y., Taniguchi, Y., Sasaki, S. S., Nagao, T., Murayama, T., and et al.: 2009, *ApJ* **696**, 546

Shioya, Y., Taniguchi, Y., Sasaki, S. S., Nagao, T., Murayama, T., Takahashi, M. I., Ajiki, M., and et al.: 2008, *ApJS* **175**, 128

Simon, P.: 2007, *A&A* **473**, 711

Simpson, C., Martínez-Sansigre, A., Rawlings, S., Ivison, R., Akiyama, M., Sekiguchi, K., Takata, T., Ueda, Y., and Watson, M.: 2006, *MNRAS* **372**, 741

Skibba, R. A., Bamford, S. P., Nichol, R. C., Lintott, C. J., Andreescu, D., Edmondson, E. M., and et al.: 2009, *MNRAS* **399**, 966

Smail, I., Sharp, R., Swinbank, A. M., Akiyama, M., Ueda, Y., Foucaud, S., Almaini, O., and Croom, S.: 2008, *MNRAS* **389**, 407

Smoot, G. F., Bennett, C. L., Kogut, A., Wright, E. L., Aymon, J., Boggess, N. W., Cheng, E. S., and et al.: 1992, *ApJ Letters* **396**, L1

Sobral, D., Best, P., Smail, I., Geach, J. E., Cirasuolo, M., Garn, T., and Dalton, G. B.: 2011a, *MNRAS* **411**, 675

Sobral, D., Best, P. N., Geach, J. E., Smail, I., Cirasuolo, M., Garn, T., Dalton, G. B., and Kurk, J.: 2010, *MNRAS* **404**, 1551

Sobral, D., Best, P. N., Geach, J. E., Smail, I., and et al.: 2009a, *MNRAS* **398**, 75

Sobral, D., Best, P. N., Geach, J. E., Smail, I., and et al.: 2009b, *MNRAS* **398**, L68

Sobral, D., Best, P. N., Matsuda, Y., Smail, I., Geach, J., and Cirasuolo, M.: 2011b, *MNRAS, arXiv:1109.1830*

Spergel, D. N., Bean, R., Doré, O., Nolta, M. R., Bennett, C. L., Dunkley, J., Hinshaw, G., and et al.: 2007, *ApJs* **170**, 377

Spergel, D. N., Verde, L., Peiris, H. V., Komatsu, E., Nolta, M. R., Bennett, C. L., Halpern, M., and et al.: 2003, *ApJs* **148**, 175

Springel, V., White, S. D. M., Jenkins, A., Frenk, C. S., Yoshida, N., Gao, L., Navarro, J., and et al.: 2005, *Nature* **435**, 629

Stark, D. P., Ellis, R. S., Chiu, K., Ouchi, M., and Bunker, A.: 2010, *MNRAS* **408**, 1628

Stark, D. P., Ellis, R. S., Richard, J., Kneib, J.-P., Smith, G. P., and Santos, M. R.: 2007, *ApJ* **663**, 10

Steidel, C. C., Adelberger, K. L., Giavalisco, M., Dickinson, M., and Pettini, M.: 1999, *ApJ* **519**, 1

Steidel, C. C., Giavalisco, M., Pettini, M., Dickinson, M., and Adelberger, K. L.: 1996, *ApJL* **462**, L17

Sullivan, M., Mobasher, B., Chan, B., Cram, L., Ellis, R., Treyer, M., and Hopkins, A.: 2001, *ApJ* **558**, 72

Sumiyoshi et al.: 2009, *arXiv:0902.2064*

Tadaki, K.-I., Kodama, T., Koyama, Y., Hayashi, M., Tanaka, I., and Tokoku, C.: 2011, *PASJ* **63**, 437

Takahashi, M. I., Shioya, Y., Taniguchi, Y., Murayama, T., Ajiki, M., Sasaki, S. S., Koizumi, O., and et al.: 2007, *ApJS* **172**, 456

Tanaka, M., Goto, T., Okamura, S., Shimasaku, K., and Brinkmann, J.: 2004, *AJ* **128**, 2677

Tanvir, N. R., Fox, D. B., Levan, A. J., Berger, E., Wiersema, K., Fynbo, J. P. U., Cucchiara, A., and et al.: 2009, *Nature* **461**, 1254

Tegmark, M., Eisenstein, D. J., Strauss, M. A., Weinberg, D. H., Blanton, M. R., Frieman, J. A., Fukugita, M., Gunn, J. E., and et al.: 2006, *Physical Review D* **74(12)**, 123507

Tegmark, M., Silk, J., Rees, M. J., Blanchard, A., Abel, T., and Palla, F.: 1997, *ApJ* **474**, 1

Thommes, E. and Meisenheimer, K.: 2005, *A&A* **430**, 877

Tilvi, V., Rhoads, J. E., Hibon, P., Malhotra, S., Wang, J., Veilleux, S., Swaters, R., Probst, R., Krug, H., Finkelstein, S. L., and Dickinson, M.: 2010, *ApJ* **721**, 1853

Trenti, M. and Stiavelli, M.: 2008, *ApJ* **676**, 767

Tresse, L. and Maddox, S. J.: 1998, *ApJ* **495**, 691

Tresse, L., Maddox, S. J., Le Fevre, O., and Cuby, J.-G.: 2002, *MNRAS* **337(1)**, 369

van Breukelen, C., Cotter, G., Rawlings, S., Readhead, T., Bonfield, D., Clewley, L., Ivison, R., Jarvis, M., Simpson, C., and Watson, M.: 2007, *MNRAS* **382**, 971

van der Werf, P. P., Moorwood, A. F. M., and Bremer, M. N.: 2000, *A&A* **362**, 509

Villar, V., Gallego, J., Pérez-González, P. G., Pascual, S., Noeske, K., Koo, D. C., Barro, G., and Zamorano, J.: 2008, *ApJ* **677**, 169

Vitores, A. G., Zamorano, J., Rego, M., Alonso, O., and Gallego, J.: 1996, *AAPS* **118**, 7

Wake et al.: 2008, *MNRAS* **387**, 1045

Weiß, A., Kovács, A., Coppin, K., Greve, T. R., Walter, F., Smail, I., Dunlop, J. S., and et al.: 2009, *ApJ* **707**, 1201

Westra, E., Geller, M. J., Kurtz, M. J., Fabricant, D. G., and Dell'Antonio, I.: 2010, *ApJ* **708**, 534

Westra, E. and Jones, D. H.: 2008, *MNRAS* **383**, 339

White, S. D. M. and Frenk, C. S.: 1991, *ApJ* **379**, 52

Wijesinghe, D. B., Hopkins, A. M., Sharp, R., Gunawardhana, M., Brough, S., Sadler, E. M., Driver, S., and et al.: 2011, *MNRAS* **410**, 2291

Willis, J. P. and Courbin, F.: 2005, *MNRAS* **357**, 1348

Willis, J. P., Courbin, F., Kneib, J.-P., and Minniti, D.: 2008, *MNRAS* **384**, 1039

Yagi, M., Kashikawa, N., Sekiguchi, M., Doi, M., Yasuda, N., Shimasaku, K., and Okamura, S.: 2002, *AJ* **123**, 66

Yamada, T., Kodama, T., Akiyama, M., Furusawa, H., Iwata, I., Kajisawa, M., Iye, M., Ouchi, M., and et al.: 2005, *ApJ* **634**, 861

Yan, L., McCarthy, P. J., Freudling, W., Teplitz, H. I., Malumuth, E. M., Weymann, R. J., and Malkan, M. A.: 1999, *ApJ Letters* **519(1)**, L47

Yang, X., Mo, H. J., van den Bosch, F. C., and Jing, Y. P.: 2005, *MNRAS* **357**, 608

York, D. G., Adelman, J., Anderson, Jr., J. E., Anderson, S. F., Annis, J., Bahcall, N. A., and et al.: 2000, *AJ* **120**, 1579

Yoshida, N., Omukai, K., and Hernquist, L.: 2008, *Science* **321**, 669

Yüksel, H., Kistler, M. D., Beacom, J. F., and Hopkins, A. M.: 2008, ApJ **683**, L5

Zehavi, I., Zheng, Z., Weinberg, D. H., Frieman, J. A., Berlind, A. A., Blanton, M. R., and et al.: 2005, *ApJ* **630**, 1

Zhu, G., Moustakas, J., and Blanton, M. R.: 2009, *ApJ* **701**, 86